Block Copolymer Assemblies of DNA and Gold Nanoparticles: Towards Applications in Photoinitiated Gene Delivery

Ph.D. Dissertation

by

Sundiata Kly

A Dissertation Submitted in Partial Fulfillment of the Requirements for the Degree of

DOCTOR OF PHILOSOPHY

In the Department of Chemistry

University of Victoria

We acknowledge and respect the lək̓ʷəŋən peoples on whose traditional territory the university stands and the Songhees, Esquimalt and W̱SÁNEĆ peoples whose historical relationships with the land continue to this day.

Block Copolymer Assemblies of DNA and Gold Nanoparticles: Towards Applications in Photoinitiated Gene Delivery

Ph.D. Dissertation

by

Sundiata Kly

Supervisory committee:

Dr. Mathew Moffitt (Department of Chemistry)

Supervisor

Dr. Jeremy Wulf (Department of Chemistry)

Co-supervisor

Dr. Alexander Brolo (Department of Chemistry)

Department member

Dr. Frank Van Veggel (Department of Chemistry)

Committee member

Dr. Francis Nano (Department of Biochemistry)

Outside member

Abstract

Gene therapies require transportation of fragile genetic material to the defective site within a body. Polymer-based micelles can provide protection while incorporated gold nanoparticles can add additional functionalities. This thesis investigates the incorporation of both nucleic acids and gold nanoparticles into block copolymer nanoparticles manufactured on gas - liquid segmented reactors. In the first of three studies plasmid DNA is incorporated into hydrophobic cores of polymer nanoparticles by the bench top mixing of plasmids and poly(2-vinylpyridine-*b*-polycaprolactone (P2VP-*b*-PCL) to create the polyplex and then incorporate the polyplex into larger polycaprolactone-*b*-poly(ethylene oxide) (PCL-*b*-PEO) micelles by microfluidics or benchtop mixing. The subsequent polyplex in hydrophobic core (PIHC) micelles are used to transform E. coli DH5α. The second study provides a route to incorporating gold nanoparticles (GNPs) of different shapes into PCL-*b*-PEO polymer nanoparticles (PNPs) to create GNP-PNPs while preventing coalescence of the GNPs within the larger PNPs. The study explores the limits of microfluidic shear on the GNP-PNPs as the chip is found to destroy GNPs at high flow rate. The cellular uptake of the gold was shown to increase when packaged into micelles. The technique used to discern the cellular uptake is novel and a more economic alternative to mass spectrometry. The final study explores the relation of plasmid size to on chip stability in aqueous and polar organic solvents. The study then shows how decoration of plasmids with P2VP-*b*-PCL can allow the plasmid to maintain fidelity at all flow rates. Three plasmids were used to test molecular weight effects on shear induced deformation. Ultimately only the smallest plasmid was able to survive the organic solvents and microfluidic shear.

TABLE OF CONTENTS

LIST OF FIGURES

Chapter 1

Chapter 2

Chapter 3

Chapter 4

Chapter 5

Appendix A

Appendix B

Appendix C

LIST OF TABLES

Chapter 3

Appendix A

Appendix B

Appendix C

List of Abbreviations

2VP	2-vinylpyridine
ACN	acetonitrile
ANSA	8-anilio-1-napthalenesulfonic acid
API	active pharmaceutical ingredient
b	block
CCMB	calcium chloride manganese buffer
CFU	colony forming unit
CT	computed tomography
CTAB	cetyl trimethylammonium bromide
CWC	critical water content
$d_{h,eff}$	effective hydrodynamic diameter
DAPI	4′,6-diamidino-2-phenylindole
DLS	dynamic light scattering
DMEM	Dulbecco’s modified eagles medium
DMF	N,N-dimethylformamide
EE	encapsulation efficiency
EtBr	ethidium bromide
EPR	enhanced permeability and retention
FBS	fetal bovine serum
FE	functionalization efficiency
GFAA	graphite furnace atomic absorption

GNP	gold nanoparticle
GNR	gold nanorod
mRNA	messenger ribonucleic acid
NIR	near infrared region
LCV	large compound vesicles
LN	linear
OC	open circular
P2VP	poly(2-vinylpyridine)
PAA	polyacrylic acid
PCL	polycaprolactone
pDNA	plasmid deoxyribonucleic acid
PDI	polydispersity index
PDMS	polydimethylsiloxane
PEI	polyethylenimine
PEO	poly(ethylene oxide)
PEG	poly(ethylene glycol)
PIHC	polyplex in hydrophobic core
PLL	poly-L-lysine
PNP	polymer nanoparticle
PPO	poly(propylene oxide)
PS	polystyrene
PUC18	plasmid of University of California 18
r	ratio

RN	ribonucleic
SA	self assembly
SiRNA	small interfering ribonucleic acid
SC	supercoiled circular
TEM	transmission electron microscopy
TGA	thermogravimetric analysis
THF	tetrahydrofuran
UV	ultraviolet
Vis	visible
wt	weight

Acknowledgments

The production of this thesis and the materials described within would never have manifest without the guidance and support from my committee, Professors Alexander Brolo, Francis Nano, Frank Van Veggel, Jeremy Wulff and Matthew Moffitt. Their patience, enthusiasm and knowledge has been an abundant resource throughout my graduate school journey. So I am incredibly grateful for the role they had in shaping my career.

My mother has given me unconditional love and support throughout this process, and I would never have made it this far without her unwavering and unrelenting support. I would like to thank my dad for giving me my hard work ethic and resourcefulness that made completing this degree possible. I imagine he would be very happy with this achievement.

I would like to thank some key members of the UVic BCMB staff: Barbara Curie, Janice Keliher, Val Kerr, Adrienne White, and Allison Maffey. All of these amazing women helped me acquire the materials and access the equipment that I needed to do the biological work on plasmids.

I would also like to thank some key members of the Chemistry staff: Rebecca Hof, Alex Wlasenko, Kelli Fawkes, Mehraveh Seyedalikhani, Professor David Harrington, Mark Evans, and Sean Adams. Without the assistance and support they provided I would not have been able to collect all the data I needed for my work. I would also like to give a huge thank you to Becky Luening for her assistance.

Finally, I would like to thank the reader for using some of their time to look through my work.

Chapter 1

General Introduction

1.1 Motivation of thesis

Genetic therapy using gene delivery is a promising strategy for treating the roughly 10,000 diseases that manifest as a result of single mutations and represent billions in healthcare costs.[1–3] Gene therapy requires nucleic acid delivery vectors for intravenous delivery of genes to the target cells. The gene delivery vectors should provide stability in the plasma, protection from opsonization, and successful translocation through the cell and nuclear membranes. Viral vectors work well because of their ability to administer nucleic acids to the nucleus, but immunogenicity and incorporation of larger genes into viral vectors remain challenging issues.[4] To overcome these issues, work on non-viral vectors (including polymers) has focussed on developing materials that encapsulate and protect the nucleic acid, deliver it to the target, then release the nucleic acid to transfect the cell.[5,6] Despite the growing interest in polymeric gene vectors, none of these have been widely accepted for therapeutic use and none have been approved by the FDA, indicating a need for new strategies for polymer-based gene delivery.[7,8] Our group has experience developing block copolymer self-assembly strategies for encapsulating inorganic nanoparticles and molecular therapeutic agents in polymer nanoparticles (PNPs) for nanomedicine applications.[9–18] Our group has also developed a microfluidic platform for controlling the morphology and drug delivery properties of nanomedicines based on flow-directed shear processing.[19,20] We were therefore

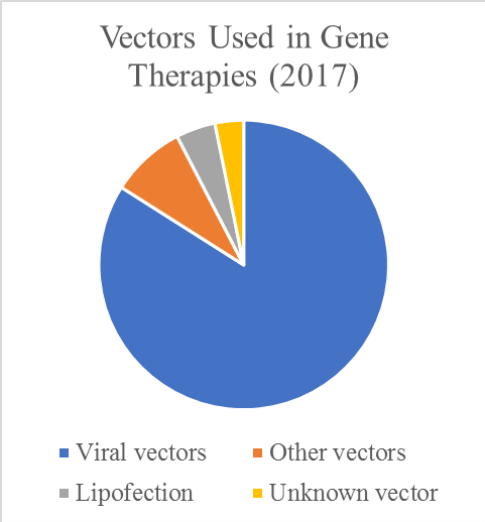

Figure 1.0 Vectors used in gene therapy as of 2017.

motivated to apply our methods and experience to develop an improved and versatile polymer nanoparticle platform for gene delivery.

1.2 Polymer nanoparticles for gene delivery

In developing new polymeric vectors for gene delivery, a number of requirements should be addressed. First, the polymer material must bind electrostatically with the nucleic acid. For example, the negative charge on the phosphodiester linkages of the plasmid backbone can be leveraged to condense with positive charges on the pendant groups of polycationic polymers.[21,22] Second, the polymer must protect the nucleic acid cargo; nucleic acids are identified as foreign invaders in the body and are therefore attacked and digested by enzymes called nucleases in the blood.[23] Therefore the polymer vector should shield nucleic acids from nuclease attack. Third, the polymeric vector must be sufficiently stable in the blood to allow the nucleic acid to reach the target cell.[6] If passive targeting is employed (e.g. the enhance permeability and retention (EPR) effect) then extra stability and blood residence time is needed.[6] Fourth, the vector must be taken up by the target cell, which usually results in the vector being trapped in the endosome.[24] Finally, the nucleic acid must escape from the polymeric vector and transform the cell, which may require endosomal escape[6,24,25] and transport across the nuclear barrier.[26–30]

Initial work on PNPs for gene delivery focussed on hydrophilic cationic polymers. Cationic polysaccharides like dextran, chitosan, or polyamines, including polyethylenimine (PEI), have been widely investigated.[21,25,31,32] These polymers bind to nucleic acids via electrostatic interactions between positively charged nitrogen atoms on the polymer and negatively charged phosphate groups on the nucleic acids to create a DNA-polycation complex called a “polyplex”. To increase the amount of DNA condensation, many groups have acetylated primary and secondary amines to give them a formal charge before binding DNA.[33] Additionally, others have made dendrimers of polycations such as poly-L-lysine (PLL) and PEI to condense and deliver nucleic acids more efficiently; the large concentration of positive charge on the surface of

dendrimers is thought to be more beneficial for DNA condensation.[34,35] Unfortunately, the positive surface charge on these polycationic gene delivery vectors has been shown to lead to binding of serum proteins and nucleases leading to their elimination from the blood via renal filtration.[6] It has been shown that modifying polycationic vectors by covalently attaching PEG (PEGylation) to these materials provides steric protection from protein adsorption (including nuclease attack), and also reduces cytotoxicity.[3136]

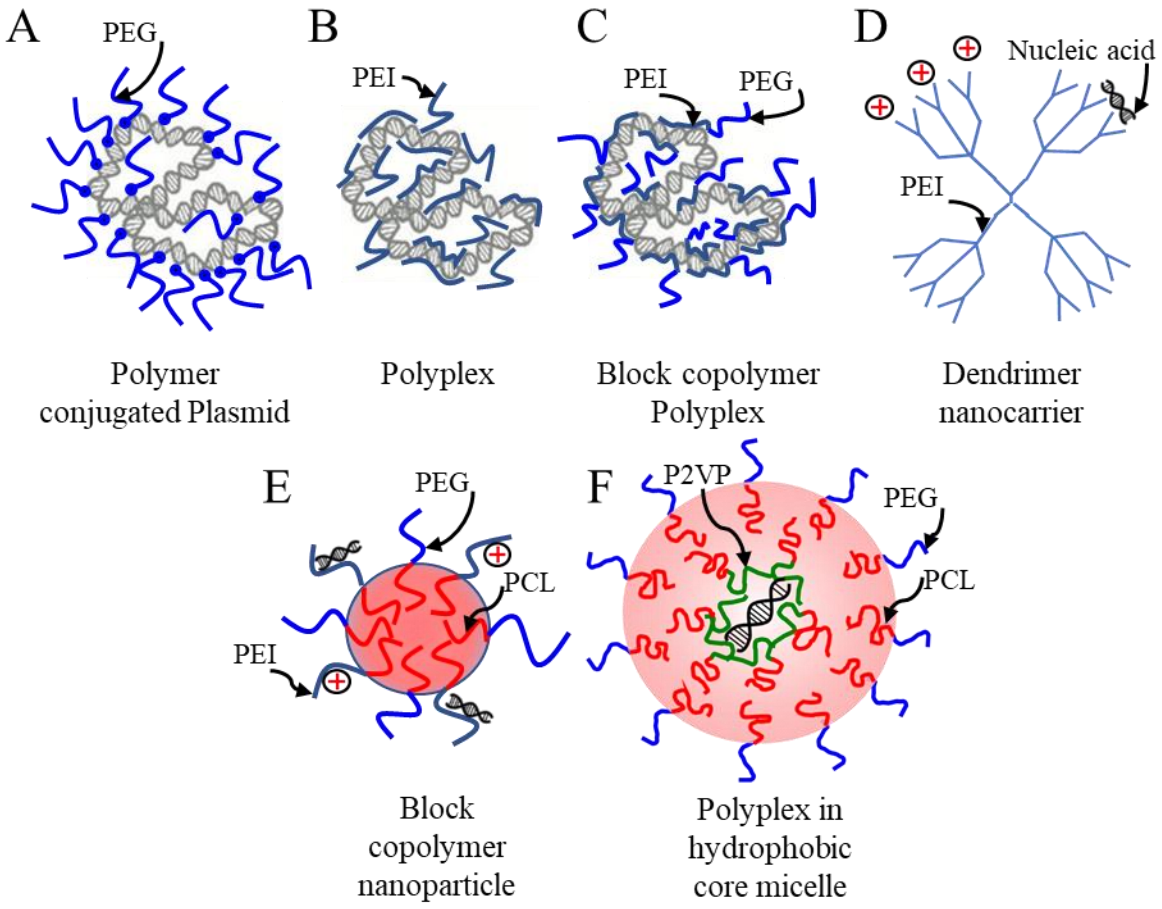

Figure 1.1: Different types of plasmid functionalization for delivery.

Further modification of polycations to make them more hydrophobic has been widely shown to improve protection of DNA-polymer conjugates and increase transfection efficiency.[33,37] One such study by Alshamsan et al. conjugated stearic acid and oleic acid to PEI, wherein it was

determined that the addition of hydrophobic moieties led to better complexation and condensation of siRNA compared with PEI.[38] The result was explained by the flexibility of the aliphatic chains providing hydrophobic interactions with the siRNA.[38] Alternatively, a study with lipids incorporated along the backbone of PEI actually reduced the association with plasmid DNA.[39] That study by Neamnark et al explained this observation as the reduced availability of amine groups to bind the DNA.[39] Importantly, adding hydrophobic groups to vector components was also shown to increase serum stability of gene vectors by the introduction of cohesive hydrophobic interactions. For example, a study by Avinash et al. showed that cholesterol conjugated PEI was able to prevent proteins in serum from dissociating the polyplexes.[40]

Further improvements to stability can be achieved by introducing phase segregation between hydrophobic and hydrophilic regions by using block copolymers containing at least one polycation block and one hydrophobic block. In such cases, self-assembly in water creates core-shell nanocarriers termed "polyplex micelles".[41] The hydrophobic cores also allow for codelivery of nucleic acids with small molecule drugs or other hydrophobic material wherein hydrophobic drug is loaded into the core. In most examples of polyplex micelles the nucleic acids surround the hydrophobic core bound to portions of the coronal layer.[42–46] For example, a study by Li et al. used a PEO-PEI-PCL triblock copolymer wherein after assembly, the PCL formed a hydrophobic core and a PEO-PEI corona. The charged PEI in the corona allows for siRNA binding in the corona and doxorubicin could be loaded into the PCL core. The particles were then used for codelivery of doxorubicin and siRNA.[47]

There are a few examples in the literature of gene delivery vectors in which polyplexes are surrounded by a thin layer of hydrophobic blocks with an external shell of PEG. For example, Ochietti et al. used Pluronic® which contains the hydrophobic poly(propylene oxide) PPO in a

triblock with PEO. The hydrophobic PPO blocks surround a core consisting of PEI-DNA complexes, while PEO provides the protective corona and a point of attachment for targeting groups.[48] In that study, they found that PEI-DNA complexes were not susceptible to dissociation by serum proteins when incorporated into Pluronic®.[48] However, to our knowledge, prior to this work, there were no previous examples in the literature of vectors in which nucleic acid-cationic polyplexes are embedded within *hydrophobic* cores such that they are surrounded by a contiguous protective matrix of hydrophobic chains. Such a "polyplex-in-hydrophobic-core" (PIHC) micelle gene vector should provide better separation between the biological environment and the nucleic acid cargo for ideal protection against nucleases and other serum proteins. It would also open up the possibility of selective release via light-triggered gold nanoparticle mediated melting of the hydrophobic phase. Incorporation of DNA into the hydrophobic cores of polyplex micelles would provide additional protection from serum proteins by providing a hydrophobic barrier between the biological environment and the nucleic acid. The literature couldn't provide any examples of these structures.

1.3 Gold nanoparticles for biomedical applications

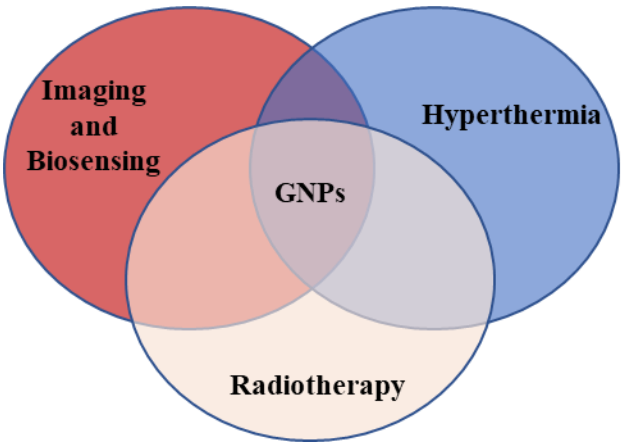

Figure 1.2. Venn diagram visualizing GNPs in the space of biomedical applications.

Gold Nanoparticles (GNPs) are nanoscale clusters of atoms ranging from 1 to 100 nm consequently containing hundreds of atoms.[49] GNPs are used for a wide range of biomedical applications. These applications can be generally distributed into four main categories:

imaging, biosensing, radiotherapy, and triggered release / hyperthermia.[12,49–52]

GNPs employed in biomedical applications are composed of both a gold crystal and an organic ligand bound to the surface of the gold crystal.[53–56] The gold core is the API and its properties are exploited for the above applications.[57–59] The organic ligand is present to stabilize the GNPs in the blood and repel serum proteins. GNPs are often chosen over other high electron density metals because of their lower cost and lower toxicity.[60]

The properties that make gold attractive for biomedical applications are its high atomic mass and surface plasmon resonance. Gold can attenuate x-rays better than lighter metals due to its high atomic mass. X-ray attenuation refers to the loss of intensity as x-rays travel through a sample that occurs through absorption and scattering of the beam. The intensity of x-ray scattering is related to an atom's electron density and increases with increasing electron density. Gold is heavier than light elements like iodine which increases its electron density and gives GNPs the ability to scatter x-rays at a higher intensity than lighter atoms.[58] As well, light impacting upon surface atoms of GNPs cause their conduction band electrons to collectively oscillate and subsequently produce an electric field of approximately 300 nm.[61] The maximum amplitude of the collective oscillation of those surface electrons is called the surface plasmon resonance (SPR). The spectral wavelength of a surface plasmon position is dependant on the type of environment it are in and its size and shape.[62–64] When a GNP surface plasmon is generated by an incident photon of the resonant frequency, one of the non radiative relaxation pathways for the plasmon is thermal radiation.[63,65] The heated electron gas transfers its thermal energy to the nanoparticle crystal which warms the crystal, and allows GNPs to provide local heating to tissues.[66]

GNPs have been used as contrast agents within computed tomography (CT) imaging to help identify potential tumours.[67–69] The imaging technique CT rosters high energy x-rays around

a patient to computationally generate anatomical images, and potentially locate tumours in a patient.[70] Biological materials like bones contain more heavy atoms like calcium, making them more electron dense than soft tissue, and subsequently those materials attenuate x-rays more than lighter tissues like skin. The detector receives x-rays that are transmitted from the source and through the patient as it rosters across the patient, and an image is produced wherein lighter regions are from tissues that attenuate x-rays more than the darker regions which attenuate x-rays to a lesser degree. This process manifests an anatomical image with more electron dense materials having a lighter shade. Tumours are usually more dense than the surrounding healthy tissue and can often be distinguished using CT imaging, which has made the technique a common non invasive method for the diagnosis of many cancers since the 1980s.[71] When tumours are not sufficiently dense to be distinguished by CT, contrast agents must be used.[58,67,72] Studies by Kim et al compare the use of ~30 nm GNPs functionalized with PEG as contrast agents to Ultravist, which is a commercially available iodine based contrast agent. Their in-vitro work showed that the GNPs attenuated x-rays 5.7 times more than Ultravist. Furthermore, their in-vivo work showed that intravenously injected pegylated GNPs were retained in the bloodstream for 2.5 times longer than Ultravist and a two fold contrast between tumors and surrounding tissue was achieved in hepatoma bearing mice.[73] Work by Khademi et al demonstrate that active targeting moiety can be leveraged to direct the GNPs to a certain area and further increase contrast. They functionalized the surface of their ~13 nm GNPs with cysteamine conjugated to folic acid. They ran CT imaging of the tumor baring mice before and after injection of contrast agents. In scans where no GNP contrast agents were used the small tumors weren't visible. When GNPs were injected, the GNPs created 2.03 times more contrast in the tumor area, making the tumors identifiable by CT imaging. When GNPs conjugated to folic acid were injected the tumor area had 4.3 times more contrast,

demonstrating the increased accumulation in the tumors as a result of folic acid targeting.[74] Deng et al created amphiphilic GNPs by grafting of both PCL-thiol and poly 2-(2-methoxyethoxy) ethyl methacrylate thiol to the gold surface.[75] The polymer functionalized GNPs were then self assembled into larger polymer structures incorporating the GNPs. They did this to modify the SPR frequency of the GNPs which was the main objective of their paper. However, out of all their structures it was the one containing the most GNPs that was most effective in both CT imaging and photothermal therapy.[75]

Hyperthermia, thermal ablation, or thermal therapy are all names for the same treatment where tissues in a patient are heated to damage cancer cells more than regular tissue.[76] Different techniques can be used to generate the heat for treatment including heated blankets and ultrasound, but when laser light is the heat source it is called photothermal therapy.[77] Hyperthermic treatment of cancer can be done locally or regionally. Regional hyperthermia involves treating the whole body or an entire portion of the body and is usually done at lower temperature. Lower temperature hyperthermic treatment usually results in increased circulation to the heated area.[76] Subsequently, it was shown increasing circulation in tumor areas can potentially stop hypoxia from developing by renormalizing the vasculature surrounding the tumor area.[76] Higher temperature treatment is usually used in local hyperthermic treatment to directly kill cancer cells in a small area. In these techniques keeping the heat localised is essential to not damaging surrounding tissue.[77] Localisation of the heat to the desired area is an application GNPs can fulfill.

Exposing GNPs to visible and near IR frequency light that is resonant with the GNP surface plasmon can generate heat. This process within a patient can provide local heating to an area when the GNPs have localised there, which is called hyperthermic treatment.[66,76,78] For in vivo photothermal treatment rod shaped gold nanoparticles are chosen because their aspect ratio allows

them to absorb light in the near infrared (NIR) region. Heat is generated with NIR light because it can penetrate through the body and remain nonharmful for long periods of time.[66,79] Zhang et al demonstrated that GNP hyperthermia could kill murine melanoma cells in vitro with exposure of light with a wavelength of 808 nm; however, the mechanism of death varied with temperature. At sufficient power the heat generated (~ 49 °C) from GNPS decorated with PEI and mercaptoundecanoic acid directly damaged surrounding tissues and cell death is primarily necrotic, whereas at lower temperature (43 °C) larger portions of cells die from apoptosis.[80] Chen, et al have shown that hyperthermic treatment with cetrimonium bromide (CTAB) GNRs inside of HepG2 cells and activated with 13.56 radio frequency are able to create an apoptotic response.[81]

The photothermal effects used in GNP hyperthermia can also be used for the triggered release of nano carriers. Liposomes carrying CRISPR CAS-9 along with GNPs as well as liposomes carrying dyes have been released using heating from GNPs.[82,83] Cavitation of liposomes occurs as a result of bubbles forming within the liposome from gas formation near the surface of the GNP as temperatures rise close to 600°C during the irradiation.[83,84] A paper about the use of of curcumin and bi metallic silver core gold shell nanoparticle loaded polystyrene-poly(ethylene oxide) nanocarrier created by Wu et al are an example of photothermal release from polymeric systems. They document a temperature induced volume transition that allows curcumin to burst release from the nanocarrier when swollen at elevated temperatures. They explain the swelling as a function of coronal chain (PEG) condensing and providing less of a diffusion distance for curcumin molecules to leave the nanocarrier.[85]

Radiotherapy is the application of high energy particles, usually x-rays, onto tumor areas to shrink tumor volumes by killing cancer cells. Seventy percent of the body is water and so x-rays passing through the body dominantly produce free radicals created from interacting with water.[70]

Radiation can interact directly with DNA to create damage or with water to create super oxides and peroxides within the cell which can attack the DNA of a cancer cell.[70] Healthy cells are also going to be exposed to the x-rays and have their DNA damaged as well. The method is feasible because cancer cells repair their DNA at a slower rate, and often die before the healthy cells do. Therefore progress has been made creating strategies that maximize the ratio of dead cancer cells to dead normal tissue from any given exposure.[70]

GNPs that have accumulated in the tumor area can be used to enhance the killing of cancerous tissue by radiation through absorbing radiation too weak to kill cancer cell DNA and re-emitting the radiation as charged particles capable of damaging DNA.[86] The ability of GNPs to interact with high energy photons is also applied in radiotherapy to create other high energy particles beyond the free radicals created from the interactions of the radiation with just water.[87,88] If the incoming x-ray radiation has sufficient energy one of the possible events is the emission of an Meitner-Auger electron. Meitner-Auger electrons result from the Meitner-Auger effect wherein surface atoms have a core electron removed by incident x-ray radiation, which causes a rearrangement of valence electrons to transition to lower energy orbitals. The transitions produce their own x-rays which can knock out a second electron which are called the Meitner-Auger electrons.[89] These free electrons can damage materials at a range of a hundred nanometers within tissues, subsequently increasing the toxicity of the radiation dose relative to areas containing no GNPs.[86,90,91] When the GNPs are within the cell, they are close enough to the nucleus that the free electrons generated from the radiation can create double stranded breaks in the DNA which cause cell death.[87] Studies by Chithrani et al treated HeLa cells with GNPs of multiple sizes and, they exposed them to 4 Gy of X-ray radiation, and they noticed that smaller GNPs (50 nm) created much more sensitization effect than that of the larger (74 nm) GNPs.[90] This result was further

backed by Morozov et al when they investigated radio sensitization with GNPs of different sizes.[92] Joh et al has shown GNPs' ability to enhance cellular damage from radiation when high power (20 Gy) exposure is used and how that can be applied to shrink tumor volumes. Moreover, they showed how the GNPs could accumulate and shrink xenografted brain tumors in mice while minimizing tissue damage to the surrounding brain.[93]

1.4 Thermodynamics of block copolymer self-assembly.

Amphiphilic diblock copolymers are polymers composed of chains of hydrophilic repeat units covalently linked to chains of hydrophobic repeat units. In polar organic solvents, amphiphilic diblock copolymers self-assemble into PNPs when above a critical water content (CWC) at a specific polymer concentration. The PNP structures visualized in Figure 1.3 include cores of insoluble blocks (red) and coronae of soluble blocks (blue). PNPs can have multiple morphologies: e.g. spheres, cylinders, vesicles, and bilayer structures are common and widely reported in the literature.[94–97] These structures result from the spontaneous aggregation (self-assembly) of many amphiphilic chains packing together and adjusting their confirmation in order to reduce the total free energy of the system.[98–100]

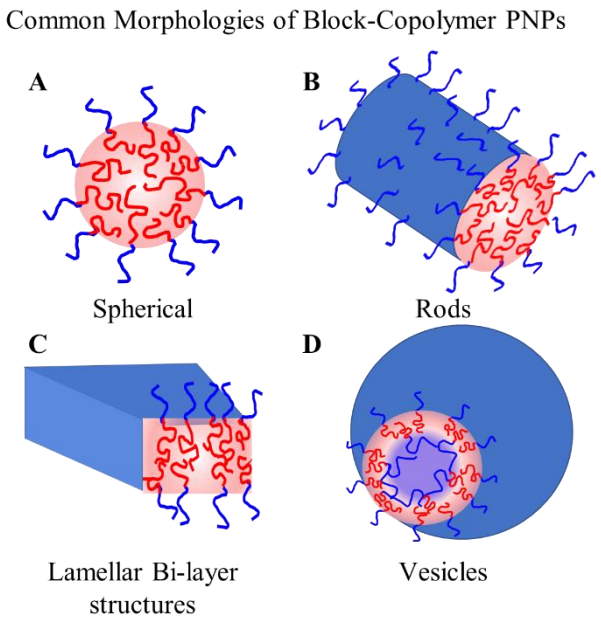

Figure 1.3. Common amphiphilic diblock copolymer nanoparticle morphologies.

The second law of thermodynamics is the basis for understanding self assembling systems in nature. A system at constant temperature (T) and pressure (P) will spontaneously transition to states of lower Gibbs energy, (G). The change in Gibbs energy is related to changes in the enthalpy (H) and entropy (S) of the system through Equation 1 below.

$$(1)\ \Delta G = \Delta H - T\Delta S$$

Equation 1 shows how the total change in Gibbs energy (ΔG) is comprised of enthalpic and entropic contributions which appear as ΔH and ΔS, respectively.[101]

The driving force for the self assembly, (ΔG_1 in equation 2), of block copolymers above the CWC arises from a combination of entropic and enthalpic factors and is dependant on the water content. The self assembly of block copolymer solutions from polar organic solvents was extensively studied by Eisenberg and his colleagues through aggregation of PS-*b*-PAA in DMF with varying amounts of water.[101] They found that at water contents a few wt % above the CWC, the self assembly was enthalpically driven. They reasoned that the movement of PS blocks from the solvent into the micelle core exchanged unfavourable PS/solvent for PS-PS and solvent-solvent interactions, resulting in an exothermic process. At higher water contents ($\geq$10 wt % above the CWC), entropy drives the assembly.[101] The change in entropy is positive and outweighs the enthalpic term because at higher water concentration there are sufficient hydrophobic interactions between PS chains and water to create ordered water. The order within the solvent molecules upon self assembly is lost, creating a positive ΔS term. Regardless of water content, the driving force for self assembly is a result of the change in the interactions of the core forming blocks as they move from the solvent to the core; this contribution to the change in Gibbs energy appears as ΔG_1 in Equation 2 below.[101]

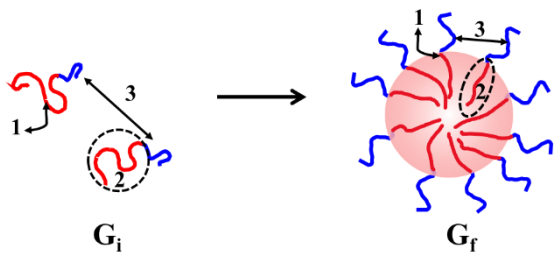

Figure 1.4. Schematic indicating first and final state of self assembly and highlighting the three main contributions to ΔG.

The next concept to introduce is the Gibbs free energy of self assembly, ΔG_{SA} in Equation 2. The difference in Gibbs energy of block copolymer chains freely dissolved in a mixture above the CWC (G_i) in Figure 1.4 and the Gibbs energy of those same chains existing in an aggregate with

other chains (G_f) is the total Gibbs energy change of self assembly and is composed of three thermodynamic terms.

$$(2)\ \Delta G_{sa} = \Delta G_1 + \Delta G_2 + \Delta G_3$$

The term ΔG_2 in Equation 2 refers to the change in Gibbs energy resulting from reduction in conformational entropy of the core-forming chains when confining polymer chains to an aggregate. Figure 1.4 shows the initial state (G_i) where core-forming blocks exist as random coils in the solvent, and the final state (G_f) where the core-forming block are stretched due to steric interactions with closely packed chains. This results in a decrease in the entropy of the core-forming blocks, which makes ΔG_2 positive. The ΔG_3 term originates from the change in repulsive interactions between corona-forming blocks before and after assembly. As illustrated in Figure 1.4 there is only weak interchain repulsion between coronal blocks in state G_i as they are far apart from one another, but after self-assembly in state G_f many coronal chains have aggregated to the same PNP and are now close enough to feel a significant amount of interchain repulsion. The increased interchain repulsion may be steric or electrostatic in nature (depending on whether the hydrophilic blocks carry a charge or not) and results in an increase in the enthalpy of the corona-forming blocks, which makes ΔG_3 positive. In summary, ΔG_{SA} consists of one negative term (ΔG_1) which drives self-assembly and two positive terms (ΔG_2 and ΔG_3) which regulate self-assembly.

Under equilibrium conditions, the block copolymer chains will aggregate in manner that minimizes the total Gibbs energy by minimizing the overall contribution of the ΔG_2 and ΔG_3 terms.

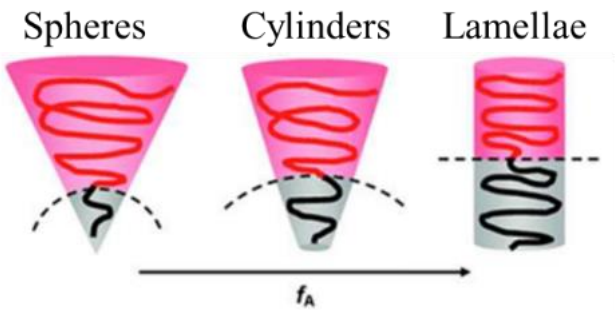

Figure 1.5. Schematic of cone column mechanism showing decrease in curvature with increasing fraction of core-forming block.[99]

Now let us consider how PNP morphological transitions occur via minimization of ΔG_2 and ΔG_3 terms, as expressed by the cone-column model. A schematic of the model is presented in Figure 1.5 adjacent. During self-assembly, microphase separation between incompatible blocks occurs, forming a defined interface between hydrophobic blocks in the core (black regions, Figure 1.5) and hydrophilic blocks in the corona (red regions, Figure 1.5). As shown in the figure, as the interfacial curvature changes from high curvature (spherical morphology) to intermediate curvature (cylindrical morphology) to low curvature (lamellar morphology or vesicles), the free volume of the coronal (red) blocks decreases while the free volume of the core blocks (black) increases. As a result, interactions between neighboring corona-forming blocks increase while interactions between neighboring core-forming blocks decrease, reducing the stress on the ΔG_2 term but raising the stress on the ΔG_3 term. Therefore, changes in curvature provide a means for the system to respond to chemical changes that put stress on either ΔG_2 or ΔG_3, giving rise to various morphological transitions. For example, as shown in Figure 1.5, as the composition of the block copolymer changes from less hydrophobic (short core-forming block) to more hydrophobic (long core-forming block), there is an increasing chemical stress on the core-forming block stretching term, ΔG_2. In response, the system reduces the stress on ΔG_2 by

decreasing the curvature, resulting in morphological transitions from spheres to cylinders to lamellae (or vesicles).

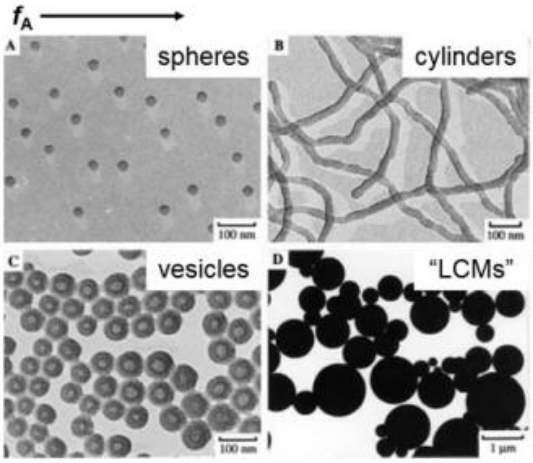

Figure 1.6. Morphologies acquired after self assembly when decreasing the PAA fraction of PS-*b*-PAA block copolymers. [98]

The effect of block copolymer composition on interfacial curvature is best exemplified by work from Zhang and Eisenberg in 1996 wherein they change the fraction of corona and core forming blocks in their PS-*b*-PAA assemblies.[98] As they reduce the fraction of corona forming block they noticed transition in the obtained morphology after self assembly starting from (A) spheres through (B) rods to (C) vesicles and finally (D) large compound micelles as shown in figure 1.6. Their findings show that decreasing the fraction of the corona forming block lowers interfacial curvature and leads to corresponding morphological transitions.[98,102] Eisenberg attributed this to the decreased importance of coronal chain repulsion (ΔG_3) as the relative length of the coronal chains decreased, which leads to a decrease in interfacial curvature in order to reduce stress on the ΔG_2 term.[102,103] It should be pointed out that in the case of systems where the corona forming block has a much longer degree of polymerization than the core forming block, the ΔG_3 term will always dominate over the ΔG_2 term, and so the aggregates will always be spherical (minimum curvature), whereas

aggregates with core forming blocks longer than the corona-forming blocks are said to be "crew-cut" aggregates and are thus capable of adopting multiple morphologies.[102]

Along with block copolymer composition, several other chemical variables can also affect the relative importance of ΔG_2 and ΔG_3 terms and can therefore be used as experimental handles to change PNP morphologies. These include: copolymer concentration, water content, solvent choice, and addition of ions.[10,102]

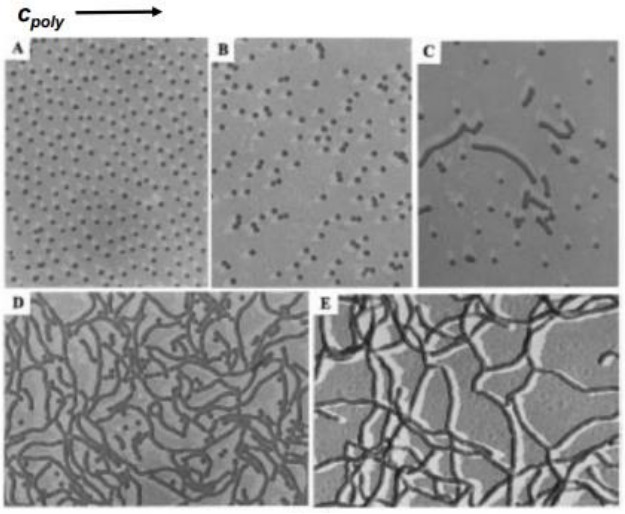

Figure 1.7. PS-*b*-PAA PNPs formed at 5.5 wt% H_2O in DMF and polymer concentrations of: 1.0 (A) 2.0 (B), 2.5(C), 3.0 (D), and 3.5 wt % (E).[102]

The effect of copolymer concentration on micelle morphologies is demonstrated in Figure 1.7. At sufficiently low concentrations below the critical micelle concentration (CMC), there is no self-assembly. Increasing the block copolymer concentration increases the driving force for self-assembly (ΔG_1) until self-assembly occurs above CMC. Further increases in block copolymer concentration further increase the driving force for self-assembly, which increases interfacial chain packing density.[102,104] More chains packing at the surface increases steric interactions, leading to greater stretching of core chains, increasing stress on ΔG_2.[100,102] To lower stress on ΔG_2 the system lowers interfacial curvature and as a result PNPs transition from spheres to cylinders to vesicles with increasing polymer concentration. For example, Eisenberg and Zhang demonstrated that increasing the concentration of PS_{410}-*b*-PAA_{25} block copolymer from 2.0 through 2.6 up until 4 wt % causes transition from spheres through rods to vesicles morphologies respectively.[100]

Another experimental variable affecting morphological transitions is the choice of initial solvent, which affects the nature of interactions between solvent and the core-forming blocks during self-assembly. Eisenberg and Zhang in a 1998 paper assembled PNPs from PS_{200}-*b*-PAA_{18} dissolved in tetrahydrofuran (THF) in dimethylformamide (DMF) at different concentrations.

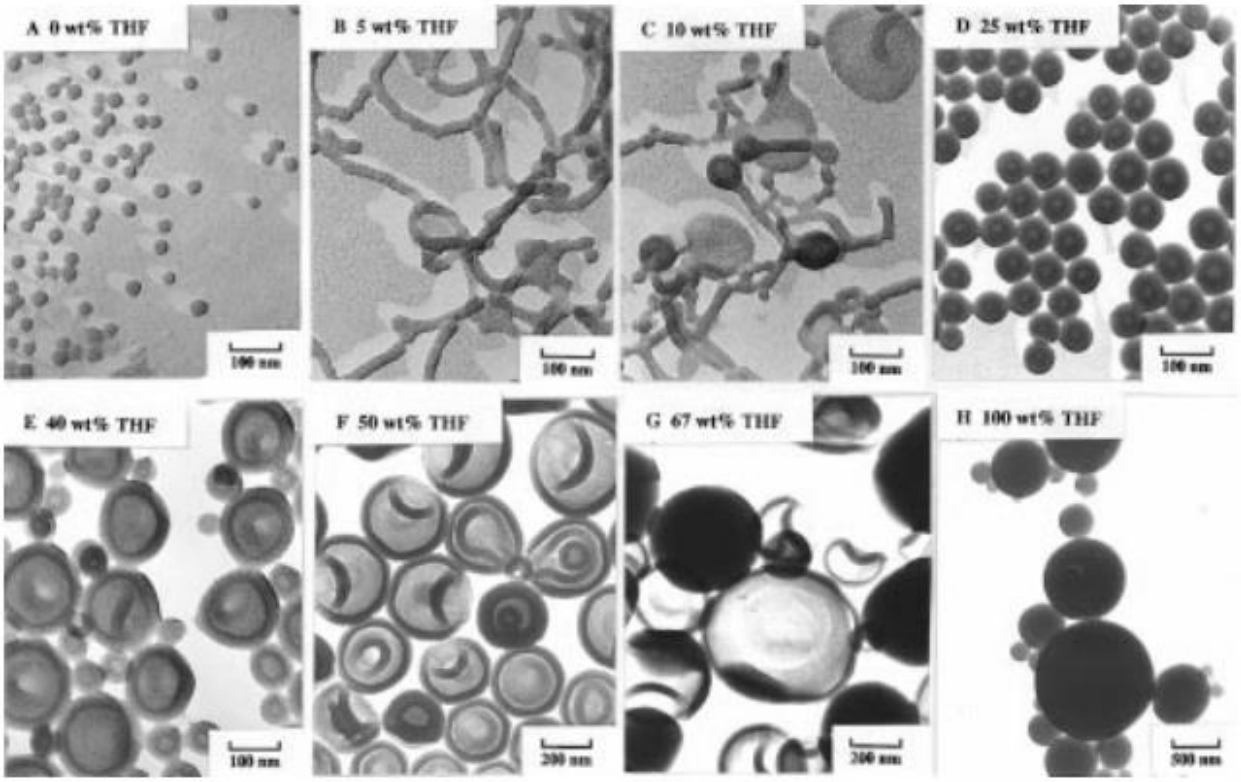

Figure 1.8. TEM images of PS_{200}-*b*-PAA_{18} aggregates self assembled at 0.5 wt% polymer and from increasing amount of THF in DMF: (A) 0 wt % THF; (B) 5 wt % THF; (C) 10 wt % THF; (D) 25 wt % THF; (E) 40 wt % THF; (F) 50 wt % THF; and (G) 67 wt % THF.[105]

THF has a solubility parameter closer to PS than DMF, therefore THF is a stronger solvent for PS.[102] Increased swelling of the core by the stronger solvent puts chemical stress on ΔG_2 due to swelling and stretching of core-forming blocks. In response, the system lowers interfacial curvature to relax ΔG_2.[105] Therefore, as the THF content of the initial solvent increases in Figure 1.8, morphologies transition from spheres to cylinders and then to vesicles.[102,105]

The addition of ions provides another handle on morphological transitions, due to their effect on interactions between the corona-forming blocks and therefore the ΔG_3 term. The PS-*b*-PAA aggregates prepared in solutions with higher sodium chloride content feel less coronal chain repulsion due to screening of the charges on the PAA chains. The resulting chemical reduction of stress on ΔG_3 provides access to lower curvature structures in order to reduce stress on ΔG_2. This results in transitions to lower curvature structures, from spheres to cylinders to vesicles, with increasing salt content.[106] They also added small amounts of hydrochloric acid (HCL) or $CaCl_2$ in increasing amounts. The results for the HCL are included in Figure 1.9 and are similar for NaCL and $CaCl_2$.[106] In each case at the lowest added ion content the PNPs are spherical (A), and as the added ion content increases the self-assembly results in rods (B), then vesicles (C), then large compound vesicles (LCV) (D) for each type of ion respectively.

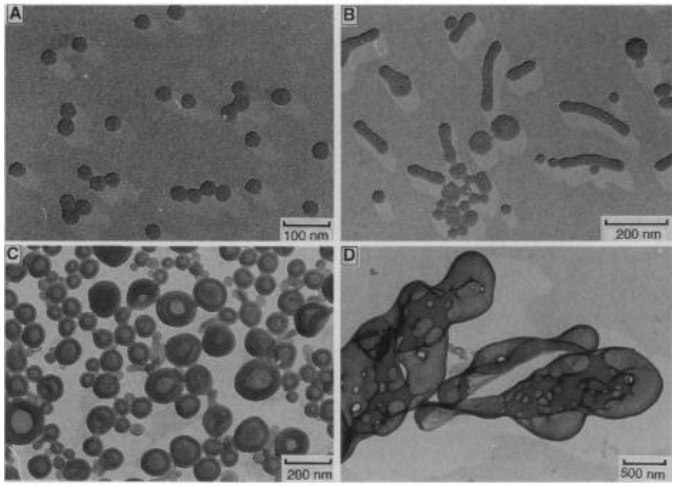

Figure 1.9. TEM images of PS_{410}-*b*-PAA25 micelles assembled at 1 wt % in DMF with different HCL concentrations. (A) 190 µM; (B) 210 µM; (C) 240 µM; and (D) 270 µM.[106]

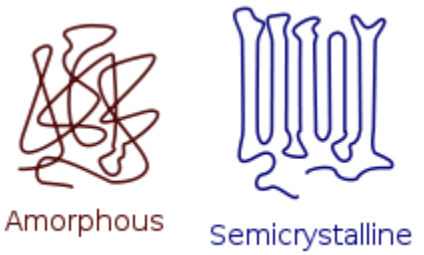

Figure 1.10. Schematic of chains in an amorphous polymer and a semi crystalline polymer.

Some core-forming blocks contain crystalline as well as amorphous regions under conditions of PNP formation. The formation of crystalline regions (or crystallites) within the PNP cores will affect the thermodynamics of self assembly. The term semicrystalline is used to describe polymers with crystalline regions in addition to amorphous portions in their overall structure. These crystalline regions exist only below their melting temperature (T_m). The melting (or freezing) temperature of crystallites is always higher than the glass transition temperature (T_g) since amorphous chains must have high mobility in order to adjust conformation and migrate into the ordered state. Chain crystallization is driven by strong attractive Van der Waals and/or H-bonding interactions between chain segments. Figure 1.10 illustrates how chains pack in a semicrystalline polymer relative to amorphous polymers. The ordered structure that results from chains packing together in their highly extended linear conformations creates a sizeable negative change in entropy. The driving force for the formation of these crystalline regions is then the negative enthalpic (exothermic) contribution.[99,107,108] The addition of chain crystallization to the free energy balance of self-assembly leads to an increased tendency for low-curvature structures, which provide more efficient packing of core-forming blocks for crystallite formation. For example, Eisenberg et al. have demonstrated transitions from spheres to rods and rods to lamellae driven by increased crystallization.[109]

1.5 Fundamentals of microfluidic platforms for the synthesis of polymer nanoparticles

Microfluidics is a discipline which manipulates liquids in small channels with diameters less than 1 mm. The attraction of microfluidics for mixing reactors stems from the small dimensions involved. Microfluidics reactors offer mixing of small reagent volumes, improved heat and mass transfer, increased control over mixing, additional experimental variable of flow rate, and control over flow dynamics.[10]

Microfluidic device dimensions create low Reynolds numbers by reducing the cross section through which fluids flow, subsequently changing turbulent to laminar flow. The expression for the Reynolds number is in equation 3 below:

(3) $$Re = \frac{Ul}{v}$$

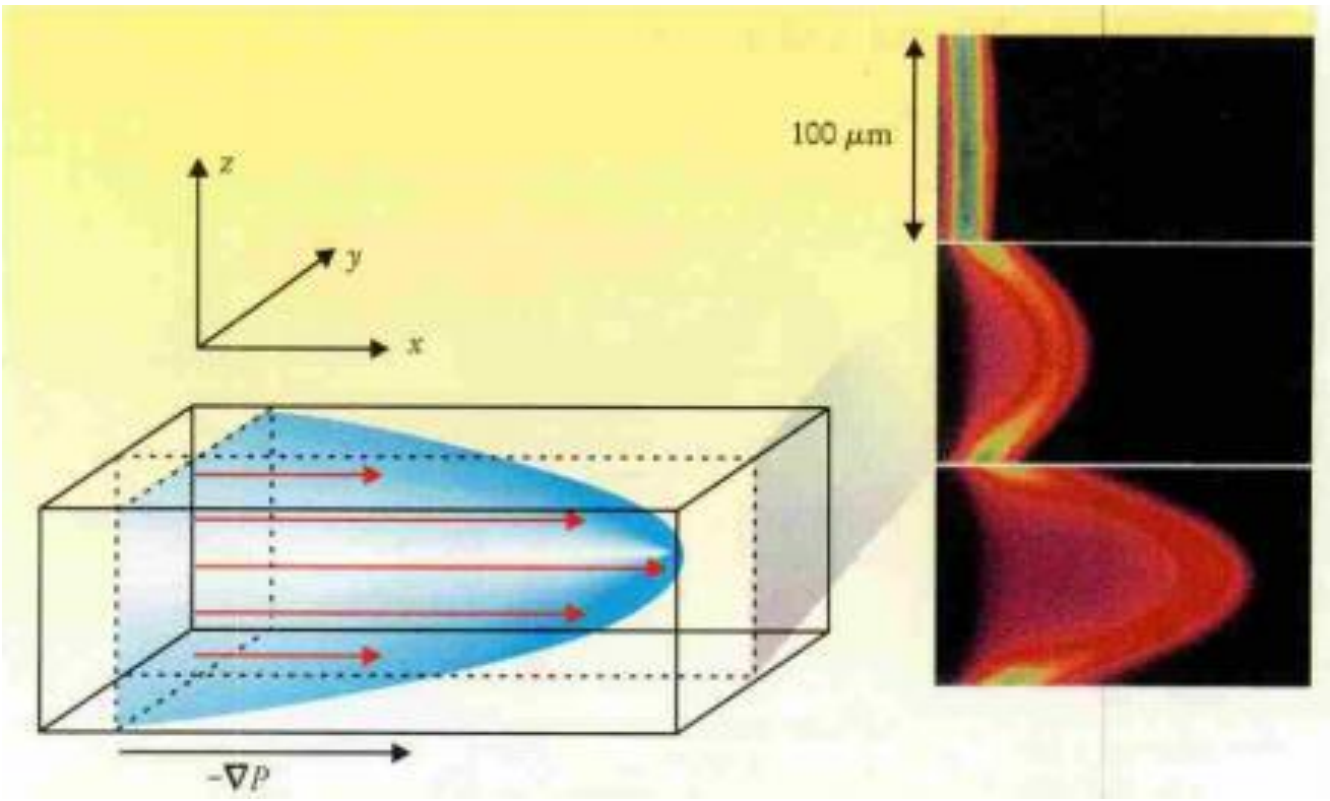

Figure 1.11. Flow profiles in microchannels. A pressure gradient -∇P along a channel generates a parabolic or Poiseuille flow profile in the channel. The velocity of the flow varies across the entire cross-sectional area of the channel. On the right is an experimental measurement of the distortion of a volume of fluid in a Poiseuille flow. The frames show the state of the volume of fluid 0, 66, and 165 mS after the creation of a fluorescent molecule.[117]

where *l* is the length of the channel diameter, *U* is characteristic velocity of a fluid and *v* is the kinematic viscosity.[110,111] For most microfluidic devices the Reynolds number is ~10^{-1}. At these low Reynolds numbers, the flow of the liquid transitions from turbulent flow to laminar flow as surfrface tensions and viscous forces dominate over inertial and gravitational forces. In laminar flow systems fluid elements travel parallel to the channel along concentric hollow cylinders with a parabolic velocity profile that increases from the outside to the center, which is visualized in Figure 1.11.[110,112] In laminar flow the only movement orthogonal to the flow is a result of

diffusional forces, whereas in turbulent flow fluid elements can be moving in any direction. This gives laminar flow the ability to better control mixing volumes in microfluidic reactors.

The parabolic velocity profile in Figure 1.11 manifests because of the no slip condition, wherein adhesive forces between the wall and the first layer of fluid are stronger than cohesive forces between particles in the solution. This makes the fluid flow near the wall stationary and creates the profile illustrated in Figure 1.11 and is called Poiseuille flow. This flow can be achieved by mechanical pumping of liquid through syringes into the microfluidic reactor. The flow is pressure driven and precisely controlled.

Single-phase microfluidic reactors offer faster mixing than traditional benchtop stir plates because each 10-fold reduction in volume corresponds to an increase in surface area to volume ratio and a 100-fold decrease in mixing time.[113] On-chip mixing can occur through two different mechanisms: diffusion and stirring. Diffusion results from the Brownian motion of particles near an interface of two solutions. Particles from either solution traverse the interface in a response to a chemical energy gradient derived from entropic forces. Eventually a homogenous solution arises when the chemical potential is exhausted. The second mechanism of mixing is stirring and refers to the movement of fluid elements from their laminar layers due to advection.[114,115] Chaotic advection is possible in laminar systems and results from the folding and stretching of fluid elements from vortices present in the flow path.[115] The aforementioned process produces thinner fluid elements from which molecules can diffuse more easily because they have a higher surface area to volume ratio. The most efficient mixing requires both mechanisms.

Many strategies have been employed to decrease the mixing times of microfluidic reactors. The most common method is hydrodynamic focussing. A schematic illustrating a typical hydrodynamic flow focusing apparatus is shown in Figure 1.12. The next common method is

addition of geometric features to the microfluidic reactor by adding a serpentine structure, or zig-zags, or grooves. The herring bone reactor is an example of this and is illustrated in Figure 1.13.[114,116,117] Another common strategy is the addition of a second phase (i.e. argon) into the flow path to create a two-phase reactor. The Moffitt lab uses a two-phase reactor that is illustrated in Figure 1.14. There are many more mixing strategies that will not be discussed ranging from electric field manipulation to the use of magnetic beads in the mixing chamber that intersects the flow path.[114]

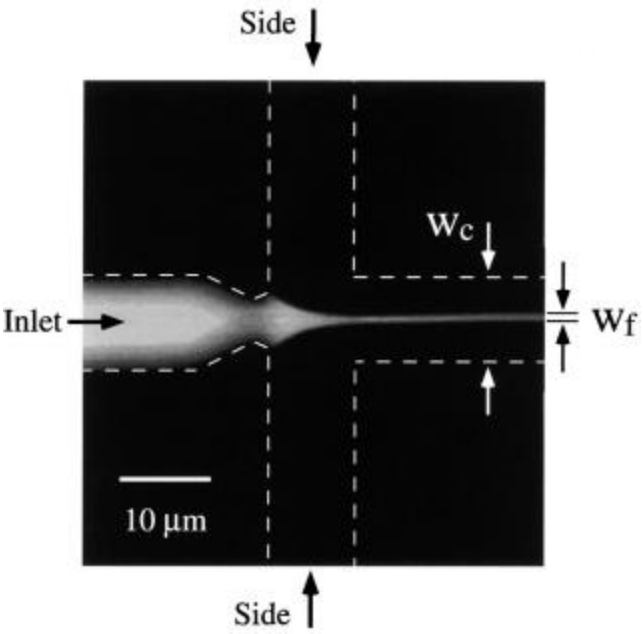

Figure 1.12. Fluorescent image of fluorescent dye being hydrodynamically focussed by two non fluorescent buffers. White dotted lines are channel walls. W_c and W_f show the width of the channel and focussed inlet stream.[118] respectively.[122]

In hydrodynamic focussing, mixing is increased by decreasing diffusional distances without introducing turbulence.[116–118] The reactor in Figure 1.12 is a hydrodynamic focussing mixing reactor capable of mixing samples in less than 10 µS.[118] The inlet stream usually contains the sample and is sandwiched by two sheath streams which compress the liquid from the inlet stream. The amount of compression is controlled by the pressure used to inject the sheath streams relative to the inlet stream. Compression of the inlet stream to 50 nm has been achieved.[118] Molecules travelling in inlet streams at length scales in the nanometer range can rapidly diffuse across the inlet stream and

mixing is therefore fast. This technique is also important for flow cytometry as macromolecules can be positioned in the center of a channel before being analyzed by downfield optical devices.[117]

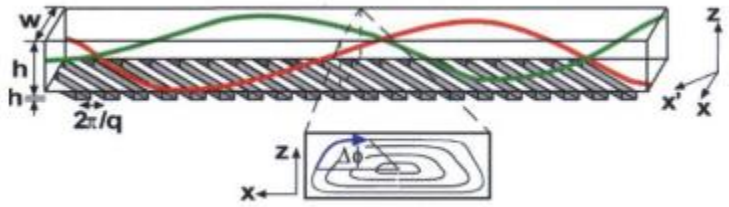

Figure 1.13. Schematic of a single-phase staggered herring bone mixer. Transverse flow paths are labelled in green and red.[120]

Changing the geometry of the microfluidic reactor can accelerate mixing by creating chaotic flow.[119] The introduction of slanted groove patterns in the herring bone mixers, shown in Figure 1.13, cause transverse flow across the horizontal plane of the chip (shown in the red and green flow paths) which creates rotating vortices in the x – z plane as shown in the inset in Figure 1.13 below the chip.[120] The authors don't call these vortices; instead they call them circular flows about an axis, which is the definition of a vortex in fluid mechanics.[115,120,121] There are many other examples of different shaped mixers with zigzags, and F shapes, and curved passages not discussed here that exist to decrease mixing times in these reactors.[114,116,121]

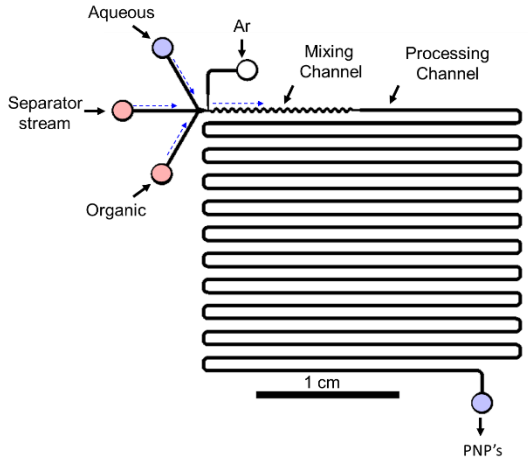

Figure 1.14. Schematic of the Moffit lab reactor.

The strategy employed by our group to decrease mixing time is to incorporate another phase into the reactor. The Moffit groups two-phase reactor has been used to decrease mixing times.[122] The chip has four inlets: a stream containing water in organic solvent, a stream containing pure polar organic solvent, a stream containing polymers dissolved in polar organic solvent, and a stream of

argon. Solvent systems are loaded by syringe pump and Teflon tubing into the inlets. A regulator controls the gas pressure of argon flowing through a Teflon tube into the gas inlet. A schematic of the chip is shown in Figure 1.14 above. The aqueous stream and stream containing the dissolved polymers are separated by a stream of organic solvent so that no mixing by diffusion can occur before gas is introduced to mix the channels.[123] The gas is introduced to compartmentalize liquid segments in the channel. Figure 1.15 A below shows the process by which gas is added to the reactor.

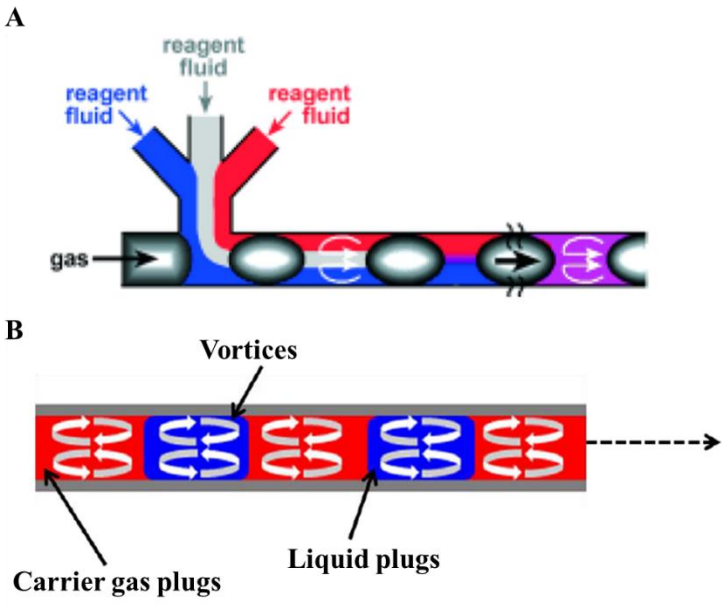

Figure 1.15. (A) Schematic of reactor inlet showing liquid plugs separated by gas segments and subsequent mixing of liquid plugs.[127] (B) Schematic showing mixing patterns inside liquid and gas plugs all moving downstream.

As the gas plugs are generated, they create counter rotating vortices causing chaotic advection and mixing the contents of the liquid plugs as shown in Figure 1.15 A.[122–124] The vortices occur throughout the liquid and air plugs and travel along the channel as shown in Figure 1.15 B. [10] Control of the flow rate is the handle by which the experimenter can adjust the mixing and shear forces on chip. This is achieved by setting the injection rate of mechanical pumps controlling the liquid and adjusting the pressure of the regulator controlling the gas. The shear rate and mixing rates increase with increasing flow rate.[12,125]

Shear generated in microfluidic channels of two-phase reactors is responsible for the flow-dependent morphologies.[19] Large amounts of shear, above that of traditional benchtop mixing, can be generated in microfluidic chips. The typical shear rate for benchtop mixing with a magnetic stir bar is ~ 1 s^{-1} whereas computational fluid dynamic calculations show shear rates on the Moffit lab chip are ~ 10^4 – 10^5 which are orders of magnitude larger.[13,125] Shear can affect particle morphology by providing enough energy for collision based coalescence and breakup of PNPs.[122] Comparative studies between a herringbone and the Moffit lab two phase mixers were done by Zhequi Zhu, a previous group member. She found that at low flow rates where shear was comparable between designs the same morphologies were formed on either mixer, but at high flow rates with considerable shear there were significantly different morphologies obtained from the Moffitt lab reactor while morphologies in the SHB reactor remained consistent.[18] This indicated that below a critical flow rate, the shear rate within the "hot spots" will not be sufficiently high to activate shear processing. This study also separated the mixing effects from shear effects on chip and demonstrated that the Moffitt lab reactor is much more capable of shear processing. Changing the flow rate on the Moffitt lab microfluidic reactor has changed the morphologies of polycaprolactone-*block*-poly(ethylene oxide) PCL-*b*-PEO aggregates in work done by Aman Bains et al.[126] Controlling the morphology and properties of PNPs by changing the flow rate is a theme of the Moffitt lab. Chih Wei Wang et al showed that it is possible to reduce the size of quantum dot compound micelles (QDCMs) by increasing the flow rates on our chips during assembly. The high shear rate reduces the size of the QDCMs through shear induced particle breakup.[13] Previous group members Aman Bains, Ruyao Chen and Yimeng Cao have each demonstrated how the morphology, sizes and drug delivery properties (loading, release, and cytotoxicity) of PNPs loaded with anticancer drugs, paclitaxel, curcumin, or SN-38 respectively,

can be controlled by changing the flow rate on the Moffitt microfluidic platform during self assembly.[15,16,127]

1.6 Focus of the Thesis

The main goal of this thesis is to build a toolbox of strategies and materials that allow for the transport of a nucleic acid into a single cell, and also allow for isolation of the nucleic acid from the intracellular environment until thermo-triggered release of the PNP by irradiation from an external light source. A hierarchical self-assembly strategy to produce a PNP platform for plasmid gene incorporation and co-incorporation of GNPs was applied. The structure of the final GNP-PIHC-PNPs is shown as a schematic in Figure 1.16.

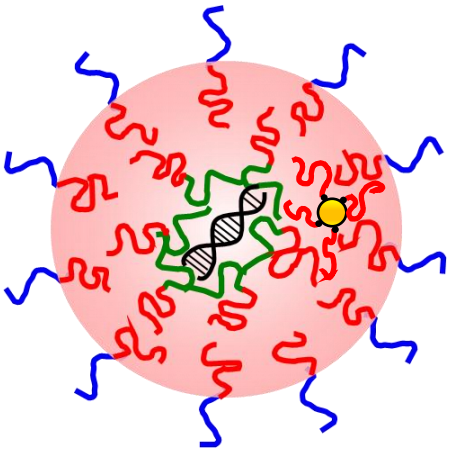

Figure 1.16. Schematic of a GNP-PIHC-PNP

Smaller goals consist of loading both the pDNA and the GNPs into PCL-*b*-PEO PNPs separately and allow for discerning which variables are important in maximizing the encapsulation efficiency of both pDNA and GNPs. Benefits of encapsulation of pDNA in PCL-*b*-PEO include high stability and increased protection of genetic material. That could translate into more temperate storage conditions and longer shelf life of products like DNA vaccines made with liposomes.

Finally, GNPs could enable light-triggered release of selected plasmids when multiple different GNP-PIHC-PNPs are located within a single cell. If the release of multiple particles containing different plasmid genes can be controlled, then this represents another layer of control over regulation of gene expression, moreover one the experimenter can control. This layer could be termed epi-synthetic biology.

1.7 Description of dissertation chapters

The content of the remaining chapters of this dissertation are described as follows. First, we developed a two-step, hierarchical self-assembly strategy to encapsulate nucleic acids within the PCL cores of PCL-*b*-PEO PNPs, this being deemed PIHC "Polyplex-in-Hydrophobic-Core" micelle. The PIHC micelles demonstrate protection of encapsulated pDNA from nuclease degradation and successful transformations of bacterial cells and uptake mammalian cells (Chapter 2).

Next, we developed a methodology for encapsulation of Gold GNPs within the PCL cores of PCL-*b*-PEO PNPs; we further showed that encapsulation of GNPs increases their uptake into cells relative to an appropriate control. Finally we demonstrate that the process can be applied to GNRs as well (Chapter 3).

The process developed in Chapter 2 showed improved results when microfluidic mixing was applied in the second self-assembly step. Therefore, we investigated the effect of microfluidic shear forces on the structural integrity of nucleic acids of various sizes, both with and without polymer functionalization. (Chapter 4).

Chapter 5 describes the main conclusions of this dissertation, along with perspectives and future work.

1.8 References

1. Tishkoff, S. A. & Verrelli, B. C. Patterns of human genetic diversity: Implications for human evolutionary history and disease. *Curr. Opin. Genet. Gov*. 4, 293–340 (2003).
2. Cystic Fibrosis Canada. **The Canadian Cystic Fibrosis Registry 2020 Annual Data Report**. Toronto, Canada: Cystic Fibrosis Canada. (2022) https://www.cysticfibrosis.ca/registry/2020AnnualDataReport.pdf last accessed January 15th 2023.
3. Jackson, M., Marks, L., May, G. H. W. & Wilson, J. B. The genetic basis of disease. *Essays Biochem*. **62(5),** 643–723 (2018).
4. De Smedt, S. C., Demeester, J. & Hennink, W. E. Cationic polymer based gene delivery systems. *Pharm. Res.* **17**, 113–126 (2000).
5. Owens, D. E. & Peppas, N. A. Opsonization, biodistribution, and pharmacokinetics of polymeric nanoparticles. *Int. J. Pharm.* **307**, 93–102 (2006).
6. Read, M. L., Logan, A. & Seymour, L. W. Barriers to gene delivery using synthetic vectors. *Adv. Genet.* **53**, 19–46 (2005).
7. Ginn, S. L., Amaya, A. K., Alexander, I. E., Edelstein, M. & Abedi, M. R. Gene therapy clinical trials worldwide to 2017: An update. *J. Gene Med.* **20**, 1–16 (2018).
8. Hardee, C., Arévalo-Soliz, L., Hornstein, B. & Zechiedrich, L. Advances in non-viral DNA vectors for gene therapy. *Genes (Basel).* **8**, 65 (2017).
9. Moffitt, M. G. Self-assembly of polymer brush-functionalized inorganic nanoparticles: from hairy balls to smart molecular mimics. *J. Phys. Chem. Lett.* **4**, 3654–3666 (2013).
10. Bains, A., Wulff, J. E. & Moffitt, M. G. Microfluidic synthesis of dye-loaded polycaprolactone-block-poly(ethylene oxide) nanoparticles: Insights into flow-directed

loading and in vitro release for drug delivery. *J. Colloid Interface Sci.* **475**, 136–148 (2016).

11. Yusuf, H. *et al.* Size control of mesoscale aqueous assemblies of quantum dots and block copolymers. *Langmuir.* **23**, 868–878 (2007).
12. Yusuf, H. *et al.* A hierarchical self-assembly route to three-dimensional polymer−quantum dot photonic arrays. *Langmuir.* **23**, 5251–5254 (2007).
13. Wang, C. W., Oskooei, A., Sinton, D. & Moffitt, M. G. Controlled self-assembly of quantum dot-block copolymer colloids in multiphase microfluidic reactors. *Langmuir.* **26**, 716–723 (2010).
14. Huang, Y., Moini Jazani, A., Howell, E. P., Oh, J. K. & Moffitt, M. G. Controlled microfluidic synthesis of biological stimuli-responsive polymer nanoparticles. *ACS Appl. Mater. Interfaces.* **12**, 177–190 (2020).
15. Chen, R., Wulff, J. E. & Moffitt, M. G. Microfluidic processing approach to controlling drug delivery properties of curcumin-loaded block copolymer nanoparticles. *Mol. Pharm.* **15**, 4517–4528 (2018).
16. Cao, Y. *et al.* Microfluidic manufacturing of SN-38-loaded polymer nanoparticles with shear processing control of drug delivery properties. *Mol. Pharm.* **16**, 96–107 (2019).
17. Jensen, D., Cao, Y., Lu, C., Wulff, J. E. & Moffitt, M. G. Microfluidic encapsulation of SN-38 in block copolymer nanoparticles: Effect of hydrophobic block composition on loading and release properties. *Can. J. Chem.* **97**, 337–343 (2019).
18. Xu, Z. *et al.* Synthesis, self-assembly, and drug delivery characteristics of poly(methyl caprolactone- co -caprolactone)- b -poly(ethylene oxide) copolymers with variable compositions of hydrophobic blocks: Combining chemistry and microfluidic processing

for polymeric. *ACS Omega* **2**, 5289–5303 (2017).

19. Xu, Z., Lu, C., Riordon, J., Sinton, D. & Moffitt, M. G. Microfluidic manufacturing of polymeric nanoparticles: Comparing flow control of multiscale structure in single-phase staggered herringbone and two-phase reactors. *Langmuir*. **32**, 12781–12789 (2016).
20. Bains, A., Cao, Y. & Moffitt, M. G. Multiscale control of hierarchical structure in crystalline block copolymer nanoparticles using microfluidics. *Macromol. Rapid Commun.* **36**, 2000–2005 (2015).
21. Corsi, K., Chellat, F., Yahia, L. & Fernandes, J. C. Mesenchymal stem cells, MG63 and HEK293 transfection using chitosan-DNA nanoparticles. *Biomaterials.* **24**, 1255–1264 (2003).
22. Dang, J. M. & Leong, K. W. Natural polymers for gene delivery and tissue engineering. *Adv. Drug Deliv. Rev.* **58**, 487–499 (2006).
23. Herriott, M. Nucleases and their inhibitors in the cellular components of human blood.. *Arch. Biochem. Biophys.* **101**, 88–95 (1963).
24. Vermeulen, L. M. P., Brans, T., De Smedt, S. C., Remaut, K. & Braeckmans, K. Methodologies to investigate intracellular barriers for nucleic acid delivery in non-viral gene therapy. *Nano Today* **21**, 74–90 (2018).
25. Wu, P. *et al.* Non-viral gene delivery systems for tissue repair and regeneration. *J. Transl. Med.* **16**, 1–20 (2018).
26. Rolland, A. Nuclear gene delivery: The Trojan horse approach. *Expert Opin. Drug Deliv.* **3**, 1–10 (2006).
27. Collins, E., Birchall, J. C., Williams, J. L. & Gumbleton, M. Nuclear localisation and pDNA condensation in non-viral gene delivery. *J. Gene Med.* **9**, 265–274 (2007).

28. Jeon, O., Lim, H., Lee, M., Song, S. J. & Kim, B. Poly(L -lactide-co-glycolide) nanospheres conjugated with a nuclear localization signal for delivery of plasmid DNA. *J. Drug Target.* **15**, 190–198 (2007).

29. Sturzu, A. & Heckl, S. The fluorinated and chlorinated nuclear localization sequence of the SV 40 T antigen. *Chem. Biol. Drug Des.* **73**, 127–131 (2009).

30. van der Aa, M. A. E. M. *et al.* An NLS peptide covalently linked to linear DNA does not enhance transfection efficiency of cationic polymer based gene delivery systems. *J. Gene Med.* **7**, 208–217 (2005).

31. Mao, H. *et al.* Chitosan-DNA nanoparticles as gene carriers: Synthesis, characterization and transfection efficiency. *J. Control. Release.* **70**, 399–421 (2001).

32. Mansouri, S. *et al.* Chitosan-DNA nanoparticles as non-viral vectors in gene therapy: strategies to improve transfection efficacy. *Eur. J. Pharm. Biopharm.* **57**, 1–8 (2004).

33. Liu, Z., Zhang, Z., Zhou, C. & Jiao, Y. Hydrophobic modifications of cationic polymers for gene delivery. *Prog. Polym. Sci.* **35**, 1144–1162 (2010).

34. Mendes, L. P., Pan, J. & Torchilin, V. P. Dendrimers as nanocarriers for nucleic acid and drug delivery in cancer therapy. *Molecules.* **22**, 1–21 (2017).

35. Duncan, R. & Izzo, L. Dendrimer biocompatibility and toxicity. *Adv. Drug Deliv. Rev.* **57**, 2215–2237 (2005).

36. Lv, H., Zhang, S., Wang, B., Cui, S. & Yan, J. Toxicity of cationic lipids and cationic polymers in gene delivery. *J. Control. Release.* **114**, 100–109 (2006).

37. Kulkarni, S. A. & Feng, S. S. Effects of particle size and surface modification on cellular uptake and biodistribution of polymeric nanoparticles for drug delivery. *Pharm. Res.* **30**, 2512–2522 (2013).

38. Alshamsan, A. *et al.* Formulation and delivery of siRNA by oleic acid and stearic acid modified polyethylenimine. *Mol. Pharm.* **6**, 121–133 (2009).

39. Neamnark, A. *et al.* Aliphatic lipid substitution on 2 kDa polyethylenimine improves plasmid delivery and transgene expression. *Mol. Pharm.* **6**, 1798–1815 (2009).

40. Bajaj, A., Kondaiah, P. & Bhattacharya, S. Synthesis and gene transfection efficacies of pei-cholesterol-based lipopolymers. *Bioconjug. Chem.* **19**, 1640–1651 (2008).

41. Li, Y. *et al.* Toroidal packaging of pDNA into block ionomer micelles exerting promoted in vivo gene expression. *Biomacromolecules.* **16**, 2664–2671 (2015).

42. Wang, Y., Gao, S., Ye, W. H., Yoon, H. S. & Yang, Y. Y. Co-delivery of drugs and DNA from cationic core-shell nanoparticles self-assembled from a biodegradable copolymer. *Nat. Mater.* **5**, 791–796 (2006).

43. Gao, Y. *et al.* PH/Redox dual-responsive polyplex with effective endosomal escape for codelivery of siRNA and doxorubicin against drug-resistant cancer cells. *ACS Appl. Mater. Interfaces.* **11**, 16296–16310 (2019).

44. Wang, K. *et al.* Structure-invertible nanoparticles for triggered co-delivery of nucleic acids and hydrophobic drugs for combination cancer therapy. *Adv. Funct. Mater.* **25**, 3380–3392 (2015).

45. Qian, J. *et al.* Folate-decorated hydrophilic three-arm star-block terpolymer as a novel nanovehicle for targeted co-delivery of doxorubicin and Bcl-2 siRNA in breast cancer therapy. *Acta Biomater.* **15**, 102–116 (2015).

46. Shen, Y. *et al.* Co-delivery of siRNA and paclitaxel into cancer cells by hyaluronic acid modified redox-sensitive disulfide-crosslinked PLGA-PEI nanoparticles. *RSC Adv.* **5**, 46464–46479 (2015).

47. Li, J. *et al.* Interfacial properties and micellization of triblock poly(ethylene glycol)-poly(ε-caprolactone)-polyethyleneimine copolymers. *Acta Pharm. Sin. B.* **10**, 1122–1133 (2020).

48. Ochietti, B. *et al.* Altered organ accumulation of oligonucleotides using polyethylenimine grafted with poly(ethylene oxide) or pluronic as carriers. *J. Drug Target.* **10**, 113–121 (2002).

49. Conde, J., Dias, J. T., Grazú, V., Moros, M. & Baptista, P. V. Revisiting 30 years of biofunctionalization and surface chemistry of inorganic nanoparticles for nanomedicine. *frontiersin.org*. **2**, 1–27 (2014).

50. Hasan, S. A review on nanoparticles : Their synthesis and types biosynthesis : mechanism. *Res. J. Recent Sci.* **4**, 1–3 (2015).

51. Hyon, B., Na, B., Song, I. C. & Hyeon, T. Inorganic nanoparticles for MRI contrast agents. *Adv. Mater.* **744**, 2133–2148 (2009).

52. Dhand, C. *et al.* Methods and strategies for the synthesis of diverse nanoparticles and their applications: A comprehensive overview. *RSC Adv.* **5**, 105003–105037 (2015).

53. Mansfield, E., Tyner, K. M., Poling, C. M. & Blacklock, J. L. Determination of nanoparticle surface coatings and nanoparticle purity using microscale thermogravimetric analysis. *Anal. Chem.* **86**, 1478–1484 (2014).

54. Wang, J., Li, W. & Zhu, J. Encapsulation of inorganic nanoparticles into block copolymer micellar aggregates: Strategies and precise localization of nanoparticles. *Polymer (Guildf).* **55**, 1079–1096 (2014).

55. Nath, S., Jana, S., Pradhan, M. & Pal, T. Ligand-stabilized metal nanoparticles in organic solvent. *J. Colloid Interface Sci.* **341**, 333–352 (2010).

56. Song, Y. & Murray, R. W. Dynamics and extent of ligand exchange depend on electronic charge of metal nanoparticles. *J. Am. Chem. Soc.* **124**, 7096–7102 (2002).

57. Jain, S., Hirst, D. G. & O'Sullivan, J. M. Gold nanoparticles as novel agents for cancer therapy. *Br. J. Radiol.* **85**, 101–113 (2012).

58. Cormode, D. P., Naha, P. C. & Fayad, Z. A. Nanoparticle contrast agents for computed tomography: A focus on micelles. *Contrast Media Mol. Imaging* **9**, 37–52 (2014).

59. Lin, G., Lisi, X. & Zhiyong, W. Efficacy of MRI visible iron oxide nanoparticles in delivering minicircle DNA into liver via. *Biomaterials.* **34(4)**, 3688–3696 (2013).

60. Ahmed, W., Bhatti, A. S. & van Ruitenbeek, J. M. Efficient seed-mediated method for the large-scale synthesis of Au nanorods. *J. Nanopart. Res.* **19**, (2017).

61. Nguyen, H., Park, J., Kang, S. & Kim, M. Surface Plasmon Resonance: A versatile technique for biosensor applications. *Sensors.* **15**, 10481–10510 (2015).

62. Burda, C., Chen, X., Narayanan, R. & El-Sayed, M. A. Chemistry and properties of nanocrystals of different shapes. *Chem. Rev.* **105(4)**, 1025-1102 (2005).

63. Huang, X. & El-Sayed, M. A. Gold nanoparticles: Optical properties and implementations in cancer diagnosis and photothermal therapy. *J. Adv. Res.* **1**, 13–28 (2010).

64. Link, S. & El-Sayed, M. A. Optical properties and ultrafast dynamics of metallic nanocrystals. *Annu. Rev. Phys. Chem.* **54**, 331–366 (2003).

65. Huang, X., Jain, P. K., El-Sayed, I. H. & El-Sayed, M. A. Plasmonic photothermal therapy (PPTT) using gold nanoparticles. *Lasers Med. Sci.* **23**, 217–228 (2008).

66. Gu, X., Li, D. D., Yeoh, G. H., Taylor, R. A. & Timchenko, V. Heat generation in irradiated gold nanoparticle solutions for hyperthermia applications. *Processes* **9**, 1–19 (2021).

67. Kosuge, H. *et al.* Potential of gold nanoparticles for noninvasive imaging and therapy for vascular inflammation: Gold nanoparticles for vascular imaging and therapy. *Mol. Imaging Biol.* **24**, 692–699 (2021).

68. Hara, D. *et al.* Prostate cancer targeted X-ray fluorescence imaging via gold Nanoparticles functionalized with prostate-specific membrane antigen (PSMA). *Int. J. Radiat. Oncol. Biol. Phys.* **111**, 220–232 (2021).

69. Terracciano, R. *et al.* Intratumoral gold nanoparticle-enhanced CT imaging: An in vivo investigation of biodistribution and retention. *Proc. IEEE Conf. Nanotechnol.* **2020-July**, 349–353 (2020).

70. Cervantes, G. A. *Technical fundamentals of radiology and CT*. (IOP Publishing, 2016).

71. Fletcher, J. G. *et al.* Abnormalities seen on CT and the clinical diagnosis of pancreatic cancer : Retrospective review of CT scans obtained before diagnosis. *Am. J. Roentgenol.* **182**, 897–903 (2004).

72. Al Zaki, A. *et al.* Gold-loaded polymeric micelles for computed tomography-guided radiation therapy treatment and radiosensitization. *ACS Nano.* **8**, 104–112 (2014).

73. Kim, D., Park, S., Lee, J. H., Jeong, Y. Y. & Jon, S. Antibiofouling polymer-coated gold nanoparticles as a contrast agent for in vivo X-ray computed tomography imaging. *J. Am. Chem. Soc.* **129**, 12585–12585 (2007).

74. Khademi, S. *et al.* Targeted gold nanoparticles enable molecular CT imaging of head and neck cancer: An in vivo study. *Int. J. Biochem. Cell Biol.* **114**, 105554 (2019).

75. Deng, H. *et al.* Theranostic self-assembly structure of gold nanoparticles for NIR photothermal therapy and X-Ray computed tomography imaging. *Theranostics.* **4**, 904–918 (2014).

76. Dunne, M., Regenold, M. & Allen, C. Hyperthermia can alter tumor physiology and improve chemo- and radio-therapy efficacy. *Adv. Drug Deliv. Rev.* (2020).

77. Hildebrandt, B. *et al.* The cellular and molecular basis of hyperthermia. *Crit. Rev. Oncol. Hematol.* **43**, 33–56 (2002).

78. Hainfeld, J. F. *et al.* Gold nanoparticle hyperthermia reduces radiotherapy dose. *Nanomedicine.* **10**, 1609–1617 (2014).

79. Huang, X., El-Sayed, I. H., Qian, W. & El-Sayed, M. A. Cancer cell imaging and photothermal therapy in the near-infrared region by using gold nanorods. *J. Am. Chem. Soc.* **128**, 2115–2120 (2006).

80. Zhang, Y. *et al.* Temperature-dependent cell death patterns induced by functionalized gold nanoparticle photothermal therapy in melanoma cells. *Sci. Rep.* **8**, 1–9 (2018).

81. Chen, C.-C. *et al.* Presence of gold nanoparticles in cells associated with the cell-killing effect of modulated electro-hyperthermia. *ACS Appl. Bio Mater.* **2**, 3573–3581 (2019).

82. Wang, P. *et al.* Thermo-triggered release of CRISPR-Cas9 system by lipid-encapsulated gold nanoparticles for tumor therapy. *Angew. Chem. Int. Ed.* **57**, 1491–1496 (2018).

83. Wu, G., Mikhailovsky, A., Khant, H., Chiu, W. & Zasadzinski, J. A. Remotely triggered liposome release by near infrared light absorption via hollow gold nanoshells. *AIChE Annu. Meet. Conf. Proc.* **130**, 8175–8177 (2008).

84. Annis, D. S., Mosher, D. F. & Roberts, D. D. Photochemical mechanisms of light-triggered release from nanocarriers. *Adv Drug Deliv Rev* **27**, 339–351 (2009).

85. Wu, W., Shen, J., Banerjee, P. & Zhou, S. Water-dispersible multifunctional hybrid nanogels for combined curcumin and photothermal therapy. *Biomaterials.* **32**, 598–609 (2011).

86. Ku, A., Facca, V. J., Cai, Z. & Reilly, R. M. Auger electrons for cancer therapy – a review. *EJNMMI Radiopharm. Chem.* **4(1)**, 1–36 (2019).

87. Kuncic, Z. & Lacombe, S. Nanoparticle radio-enhancement: Principles, progress and application to cancer treatment. *Phys. Med. Biol.* **63(2)**, (2018).

88. Mesbahi, A. A review on gold nanoparticles radiosensitization effect in radiation therapy of cancer. *Reports Pract. Oncol. Radiother.* **15**, 176–180 (2010).

89. Stabin, M. G. *Radiation Protection and Dosimetry*. (Springer New York, 2003).

90. Chithrani, D. B. *et al.* Gold nanoparticles as radiation sensitizers in cancer therapy. *Radiat. Res.* **173**, 719–728 (2010).

91. Rehman, M. U., Jawaid, P. & Kondo, T. Dual effects of nanoparticles on radiation therapy: as radiosensitizers and radioprotectors. *Radiat. Environ. Med.* **5**, 40–45 (2016).

92. Morozov KV., Kolyvanova MA, Kartseva ME, Shishmakova EM, Dement'eva OV, Isagulieva AK, Salpagarov MH, Belousov AV, Rudoy VM, Shtil AA, Samoylov AS, Morozov VN. Radiosensitization by Gold Nanoparticles: Impact of the Size, Dose Rate, and Photon Energy. *Nanomaterials (Basel)*. **10**, 952-968 (2020).

93. Joh DY, Sun L, Stangl M, Al Zaki A, Murty S. Selective targeting of brain tumors with gold nanoparticle-induced radiosensitization. *PLOS ONE.* **8**, (2013).

94. Cai, S., Vijayan, K., Cheng, D., Lima, E. M. & Discher, D. E. Micelles of different morphologies: Advantages of worm-like filomicelles of PEO-PCL in paclitaxel delivery. *Pharm. Res.* **24**, 2099–2109 (2007).

95. Rasappa, S. *et al.* Morphology evolution of PS- b -PDMS block copolymer and its hierarchical directed self-assembly on block copolymer templates. *Microelectron. Eng.* **192**, 1–7 (2018).

96. Kim, Y., Dalhaimer, P., Christian, D. A. & Discher, D. E. Polymeric worm micelles as nano-carriers for drug delivery. *Nanotechnology.* **16(7)**, (2005).

97. Oltra, N. S., Nair, P. & Discher, D. E. From stealthy polymersomes and filomicelles to "self" peptide-nanoparticles for cancer therapy. *Annu. Rev. Chem. Biomol. Eng.* **5**, 281–299 (2014).

98. Zhang, L. & Eisenberg, A. Multiple morphologies and characteristics of "crew-cut" micelle-like aggregates of polystyrene-b-poly (acrylic acid) diblock copolymers in aqueous solutions. *J. Am. Chem. Soc.* **118**, 3168–3181 (1996).

99. Zhang, L. & Eisenberg, A. Multiple morphologies of "crew-cut " aggregates of polystyrene-b-poly (acrylic acid) block copolymers. *Science.* **268**, 1728–1731 (1995).

100. Zhang, L., Shen, H. & Eisenberg, A. Phase separation behavior and crew-cut micelle formation of polystyrene-6-poly(acrylic acid) copolymers in solutions. *Macromolecules.* **30**, 1001–1011 (1997).

101. Shen, H., Zhang, L. & Eisenberg, A. Thermodynamics of crew-cut micelle formation of polystyrene-b-poly(acrylic acid) diblock copolymers in DMF/H 2 O mixtures. *J. Phys. Chem. B.* **101**, 4697–4708 (1997).

102. Mai, Y. & Eisenberg, A. Self-assembly of block copolymers. *Chem. Soc. Rev.* **41**, 5969–5985 (2012).

103. Discher, D. E. & Ahmed, F. Polymersomes. *Annu. Rev. Biomed. Eng.* **8**, 323–341 (2006).

104. Zhang, L. & Eisenberg, A. Thermodynamic vs kinetic aspects in the formation and morphological transitions of crew-cut aggregates produced by self-assembly of polystyrene-b-poly(acrylic acid) block copolymers in dilute solution. *Macromolecules.* **32**, 2239–2249 (1999).

105. Yu, Y., Zhang, L. & Eisenberg, A. Morphogenic effect of solvent on crew-cut aggregates of apmphiphilic diblock copolymers. *Macromolecules.* **31**, 1144–1154 (1998).

106. Zhang, L., Yu, K. & Eisenberg, A. Ion-induced morphological changes in "crew-cut" aggregates of amphiphilic block copolymers. *Science. (80-.).* **272**, 1777–1779 (1996).

107. Du, Z. X., Xu, J. T. & Fan, Z. Q. Regulation of micellar morphology of PCL-b-PEO block copolymers by crystallization temperature. *Macromol. Rapid Commun.* **29**, 467–471 (2008).

108. He, W.-N. & Xu, J.-T. Crystallization assisted self-assembly of semicrystalline block copolymers. *Prog. Polym. Sci.* **37**, 1350–1400 (2012).

109. Rizis, G., Van De Ven, T. G. M. & Eisenberg, A. Crystallinity-driven morphological ripening processes for poly(ethylene oxide)-block-polycaprolactone micelles in water. *Soft Matter.* **10**, 2825–2835 (2014).

110. Tabeling, P. *Introduction to Microfluidics*. (Oxford University Press, Incorporated, 2006).

111. Zhang, J. *et al.* Fundamentals and applications of inertial microfluidics: A review. *Lab Chip.* **16**, 10–34 (2016).

112. Whitesides, G. M. & Stroock, A. D. Flexible methods for microfluidics. *Phys. Today.* **54**, 42–48 (2001).

113. Tabeling, P. Physics at the micrometric scale. in *Introduction to Microfluidics.* (Oxford University Press, 2005).

114. Suh, Y. K. & Kang, S. A review on mixing in microfluidics. *Micromachines* **1**, 82–111 (2010).

115. Aref, H. Stirring by chaotic advection. *J. Fluid Mech.* **143**, 1–21 (1984).

116. Lee, C. Y., Chang, C. L., Wang, Y. N. & Fu, L. M. Microfluidic mixing: A review. *Int. J.*

Mol. Sci. **12**, 3263–3287 (2011).

117. Ward, K. & Fan, Z. H. Mixing in microfluidic devices and enhancement methods. **25**, 1–33 (2015).

118. Knight, J. B., Vishwanath, A., Brody, J. P. & Austin, R. H. Hydrodynamic focusing on a silicon chip: Mixing nanoliters in microseconds. *Phys. Rev. Lett.* **80**, 3863–3866 (1998).

119. Stroock, A. D. *et al.* Chaotic mixer for microchannels. *Science. (80-.).* **295**, 647–651 (2002).

120. Stroock, A. D. *et al.* Chaotic mixer for microchannels. *Science. (80-.).* **295**, 647–651 (2002).

121. Williams, M. S., Longmuir, K. J. & Yager, P. A practical guide to the staggered herringbone mixer. *Lab Chip* **8**, 1121–1129 (2008).

122. Wang, C., Sinton, D. & Moffitt, M. G. Flow-directed block copolymer micelle morphologies via microfluidic self-assembly. *J. Am. Chem. Soc.* **133**, 18853–18864 (2011).

123. Bains, A., Wulff, J. E. & Moffitt, M. G. Microfluidic synthesis of dye-loaded polycaprolactone-block-poly(ethylene oxide) nanoparticles: Insights into flow-directed loading and in vitro release for drug delivery. *J. Colloid Interface Sci.* **475**, 136–148 (2016).

124. Song, H., Chen, D. L. & Ismagilov, R. F. Reactions in droplets in microfluidic channels. *Angew. Chem. Int. Ed.* **45**, 7336–7356 (2006).

125. Schabas, G. *et al.* Formation and shear-induced processing of quantum dot colloidal assemblies in a multiphase microfluidic chip. *Langmuir.* **24**, 10596–10603 (2008).

126. Bains, A., Cao, Y. & Moffitt, M. G. Multiscale control of hierarchical Structure in

Crystalline block copolymer nanoparticles using microfluidics. *Macromol. Rapid Commun.* **36**, 2000–2005 (2015).

127. Bains, A. & Moffitt, M. G. Effects of chemical and processing variables on paclitaxel-loaded polymer nanoparticles prepared using microfluidics. *J. Colloid Interface Sci.* **508**, 203–213 (2017).

Chapter 2

Hierarchical Self-Assembly Route to "Polyplex-in-Hydrophobic Core" Micelles for Gene Delivery

Contributions: This chapter has been published as an article in *Chemistry of Materials*. Sundiata Kly and Matt Moffitt conceived the experiments; Sundiata Kly, Lucas Andrew, and Erin Moloney conducted the experiments; Sundiata Kly analyzed the data with input from Jeremy Wulff and Matt Moffitt; Yuhang Huang assisted with figure preparation; Matt Moffitt wrote the published article.

2.1 Introduction

Gene therapy opens up new routes for the treatment of chronic disease by modulating gene expression in targeted cells through the delivery of nucleic acids.[1] Although viral delivery vectors can lead to high transfection efficiencies in animal models, their clinical applications are limited by potential immunogenicity and mutagenesis.[2,3] In addition, the limited size capacity of viral particles precludes delivery of larger nucleic acids required for some gene therapies.[4] Therefore, the development of safe and effective non-viral gene delivery vectors has become an intense field of investigation at the interface of materials science and molecular biology.[2,3,5,6] In particular, polymer nanoparticles (or PNPs) offer a number of advantages for gene delivery compared to their lipid-based counterparts, including stability, ease of functionalization and variability of properties.[7-11]

In order to serve as effective gene delivery vehicles, PNP vectors should be designed with four main characteristics. First, they should provide stable encapsulation of the nucleic acids while protecting them from constituents in the extracellular environment; for example, both deoxyribonucleases (DNases) and ribonucleases (RNases) will bind and degrade exposed exogenic nucleic acids in the blood.[4,12,13] Second, PNP vectors should disperse in the bloodstream and deliver the nucleic acids to the target cells through passive or active targeting.[4,12,13] Third, they

should facilitate cellular uptake followed by release of nucleic acids to trigger the desired transfection events.[4,12,13] Finally, the vector material should be broken down and excreted by the patient with minimal toxicological effects.[4,12,13]

In order to address these diverse considerations, a wide range of polymeric systems have been developed, involving varying complexities of molecular design. The simplest polymeric systems for gene delivery are polycations capable of electrostatic binding with negatively-charged nucleic acids, forming polymer-nucleic acid complexes (polyplexes).[8] A large number of polymers with linear, branched, and dendritic architectures have been applied in this manner, including polyethylenimine (PEI), poly(L-lysine) (PLL), and poly(amido-amine) (PAMAM).[8,10] Chemical modification of the simple polycation motif provides various routes to improving the gene delivery properties. For example, attaching poly(ethylene glycol) (PEG) chains to polyplexes (PEGylation) forms a hydrophilic shell layer surrounding the polyplex which increases blood dispersibility and lowers cytotoxicity.[8] Moreover, there is evidence that PEGylation increases nucleic acid resistance to nuclease degradation, by sterically inhibiting penetration of nucleases to the polyplex core.[12]

The installation of hydrophobic groups onto the polycation framework is another important strategy for improving the properties of gene delivery PNPs.[12,14] When these hydrophobic moieties are relatively small (i.e. non-polymeric), such as alkyl chains or cholesterol groups, the resulting hydrophobic interactions in water give rise to increased polyplex stability and nuclease resistance through an increase in the driving force for polymer association around the nucleic acid cargo.[12,14] Even greater opportunities for enhanced gene delivery capabilities can be realized when the hydrophobic groups are polymeric chains covalently attached to polyplex-forming polycations within a block copolymer architecture.[4,9,12-23] Self-assembly of these block copolymers in aqueous environments gives rise to PNPs (termed “polyplex micelles”) in which the hydrophobic chains

compartmentalize into discrete hydrophobic domains segregated from the polycation-nucleic acid polyplex. In the vast majority of block copolymer-based gene delivery vehicles, the hydrophobic blocks (usually biodegradable polyesters, including polylactic acid, polylactic-*co*-glycolic acid and polycaprolactone (PCL)) form a hydrophobic micelle core, surrounded by a hydrophilic shell containing the polyplex along with PEG chains to increase dispersibility and provide steric shielding against nucleases.[4] Within these polyplex micelles, the role of the hydrophobic core is to increase polyplex stability through strong hydrophobic interactions[4,12,14] and chain crystallization,[24] while serving as a reservoir for hydrophobic drugs or other agents in combination therapy applications.[4,16,18,21,23]

Although PEG chains in the shell layer of polyplex micelles provide some steric shielding against nucleases, they do not preclude the penetration of nucleases to the nucleic acid cargo over long exposure times,[12] underlining the need for additional efforts to increase nuclease tolerance. One approach is to design polyplex micelles in which the hydrophobic domains act as physical barriers between the encapsulated nucleic acids and nucleases in the bloodstream.[12,14,22] A recent example includes the development of a triblock copolymer with a thermoswitchable poly-(2-*n*-propyl-2-oxazoline) middle block and end blocks of hydrophilic and cationic polymers.[22] Following polyplex formation with nucleic acids, raising the temperature above the LCST of poly-(2-*n*-propyl-2-oxazoline) formed a thin (~1.5 nm) hydrophobic barrier consisting of a single layer of hydrophobic chains surrounding the polyplex core. Although this layer was found to increase resistance to nuclease attack, the authors determined that the coverage of the thin hydrophobic barrier is incomplete (~38%), which suggests that other strategies may be required to fully block nuclease penetration.[22]

A promising route to generating a contiguous and multichain hydrophobic physical barrier is to embed the polyplex *within* the hydrophobic micelle core, such that each encapsulated nucleic acid is surrounded by a matrix of condensed hydrophobic chains. To our knowledge, no such examples of PNP vectors, which we term "polyplex-in-hydrophobic-core" (PIHC) micelles, have appeared in the literature. Notable challenges to this strategy include: 1) the "solubility problem" of driving charged nucleic acids into a matrix of hydrophobic chains, 2) the "release problem" of providing a mechanism for nucleic acid escape within the intracellular environment, and 3) the "integrity problem" of retaining the structure and functionality of nucleic acids during encapsulation and release. We were further motivated to develop a methodology for PIHC micelle formation that employed commercially available block copolymers, without the need for complicated synthetic methodologies.

In this chapter, we apply a hierarchical block copolymer self-assembly process to generate the first example of a PIHC micelle structure (Figure 2.1). The resulting PIHC micelles are formed in two distinct self-assembly steps: 1) in step 1 (SA1, Figure 2.1A), nucleic acids are complexed through electrostatic binding with the poly(2-vinylpyridine) chains of a polycaprolactone-*block*-poly(2-vinylpyridine) (PCL-*b*-P2VP) block copolymer, forming stable block ionomer micelles with a polyplex core and a PCL coronal layer (PCL-pDNA); 2) in step 2 (SA2, Figure 2.1B), the PCL chains of PCL-pDNA are condensed with the PCL chains of a polycaprolactone-*block*-poly(ethylene glycol) (PCL-*b*-PEG) block copolymer *via* water addition and dialysis, forming PIHC micelles. As a proof-of-concept, we apply this hierarchical approach to form PIHC micelles containing the plasmid DNA (pDNA) pUC18, which codes for antibiotic resistance to ampicillin in bacteria. We apply optimized solvent conditions for SA1 and microfluidic mixing for SA2 to produce mainly spherical PIHC micelles with ~30-nm cores. Gel electrophoresis following DNase

I exposure indicates protection of encapsulated nucleic acids from structural degradation within the hydrophobic core, while bacterial transformation experiments prove that the plasmid retains functionality following encapsulation and release. Moreover, PIHC micelles show a 10× enhancement in transformation efficiencies compared to “free” plasmid, along with a linear increase in activation over 8 h associated with slow release of plasmid from PCL cores. Finally, we show that PIHC micelles are readily taken up by eukaryotic MDA-MB-231 cells, suggesting feasibility of this approach for future mammalian cell transfection experiments.

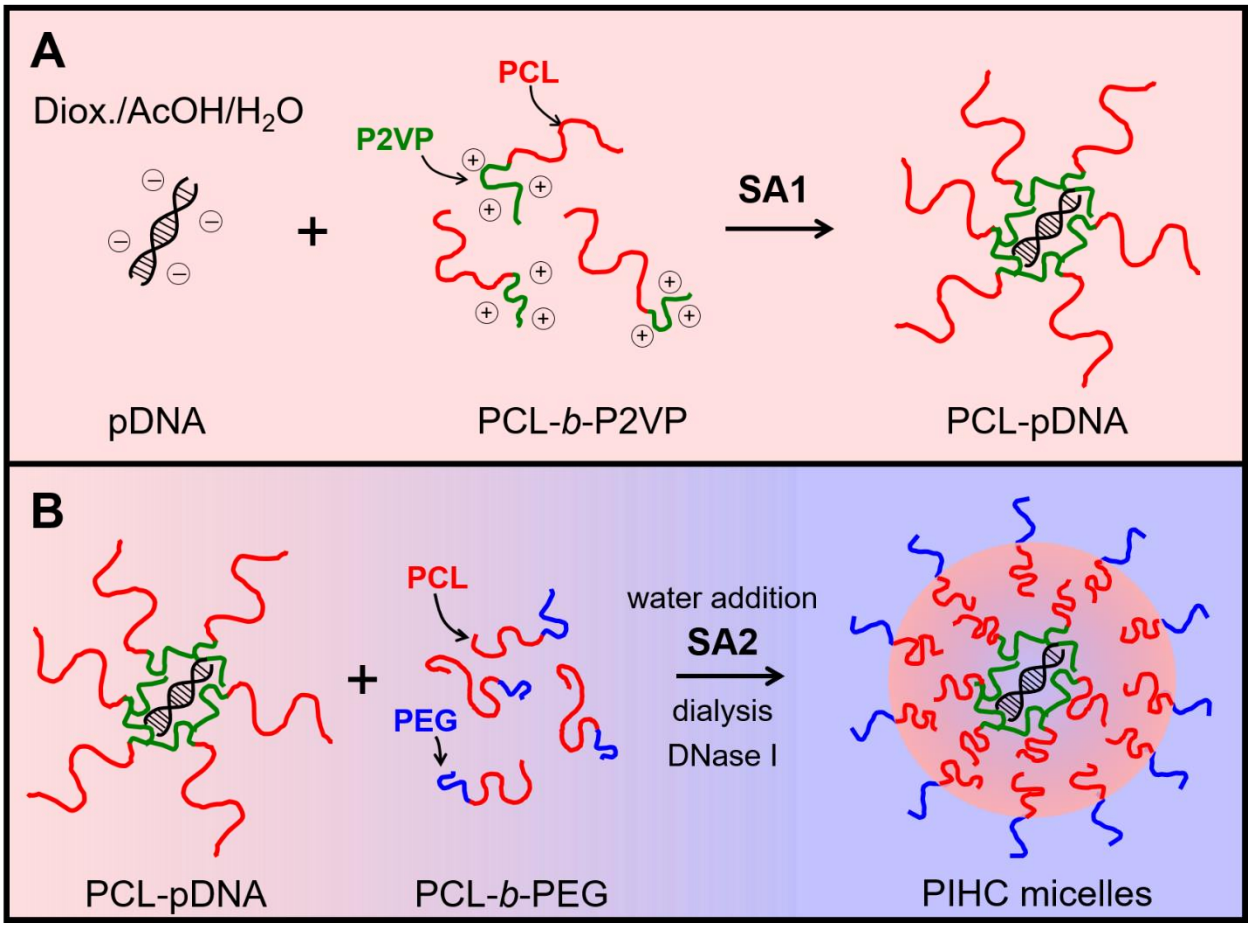

Figure 2.1. Schematics of two-step hierarchical self-assembly process to form PIHC micelles. (A) In the first step (SA1), pDNA and PCL-*b*-P2VP undergo electrostatic complexation in an dioxane/acetic acid/water mixture to form the block ionomer micelle intermediate PCL-pDNA. (B) In the second step (SA2), PCL-pDNA and PCL-*b*-PEG undergo microprecipitation *via* water addition to form PIHC micelles. The sizes of various components in these schematics are not representative of their natural sizes. Actual sizes of each constituent are described later in the text.

2.2 Experimental Methods

2.2.1 Materials.

Polycaprolactone-*block*-poly(ethylene glycol) (PCL(12k)-*b*-PEG(5k), $Đ$ = 1.11, Advanced Polymer Materials Inc), polycaprolactone-*block*-poly(2-vinylpyridine) (*b*-PCL(35.0k)-*b*-P2VP(20.5k), $Đ$ = 1.10, Polymer Source Inc.) and poly(2-vinylpyridine) (P2VP(35k), $Đ$ = 1.07, Sigma) were used without further purification. All block copolymer solutions were prepared by adding solvent to the solid polymer and stirring overnight before use. Lurai-Bertani (LB) broth (Fisher), glycerol (>99.0%, Sigma,), ampicillin (Sigma), trypticase soy agar (Sigma), hydrochloric acid (HCl, 36.5-38.0%, Sigma), sodium hydroxide solution (1N, Sigma), ethidium bromide (EtBr, 95%, Sigma), 1,4-dioxane (99.9%+ HPLC grade, Sigma), acetic acid (99.7%+, Sigma), sodium acetate (99%+, Sigma), pyridine (99.8%, Sigma), sulfuric acid (37% (v/v), Ricca), hydrogen peroxide (30% (w/w), Sigma), ascorbic acid (>99.0%, Sigma), ammonium molybdate tetrahydrate (>99.0%, Sigma), 8-anilino-1-napthalenesulfonic acid ammonium salt (ANSA, >97%, Sigma), sodium sulfite (>98%, Sigma), phosphate standard solution (0.65 mM, Sigma), agarose (Sigma), tris-acetate-ethylenediaminetetraacetic acid buffer (TAE, Sigma), DNA gel loading dye (Fisher), Dulbecco's modified eagles medium (DMEM, Sigma), fetal bolvine serum (FBS, Gibco), phosphate buffered saline pH 7.4 (Sigma), trypsin (0.25%, Gibco), phenol red (Fischer), 1′-dioctadecyl-3,3,3′,3′-tetramethylindocarbocyanine perchlorate (DiI, Sigma), 4′,6-diamidino-2-phenylindole (DAPI, Sigma), fluorescein diacetate (95%, Sigma), acetone (>99.5%, Sigma), and DNase I kit: DNase (1 U/µL), DNase I 10× reaction buffer with $MgCl_2$, and 50 mM EDTA (Fisher) were used as received. Super optimal broth with catabolite repression (SOC) medium and CCMB medium were made from the ingredients lists below (all purchased from Sigma) and autoclaved prior to use then stored at room temperature on the benchtop and at 4°C respectively. The SOC

media was composed of tryptone, yeast extract, NaCl (>99.0%) and D-(+)-glucose (>99.5%). The CCMB media was composed of potassium acetate (>99.0%,), glycerol (>99.0%), calcium chloride dihydrate (>99%), manganese chloride tetrahydrate (98%), magnesium chloride hexahydrate (>99.0%), and potassium hydroxide (>85 %).

2.2.2 pDNA Isolation and Characterization.

Bacterial pUC18 plasmid DNA (pDNA) contains 2686 basepairs and 5372 phosphate groups and has a molecular weight of 1.75×10^3 kDa. pDNA was isolated from a frozen stock of Escherichia coli (*E.coli*) W1130 stored at -80°C in a 20% (v/v) glycerol/water solution. In a typical isolation process, the frozen stock was streaked onto TSA agar plates containing 200 μg/mL ampicillin and allowed to grow overnight. 10 mL LB growth medium were inoculated from the TSA plates and allowed to grow overnight in an incubator at 37 °C with shaking (300 rpm) to produce an overnight culture. 2.0 mL of the overnight culture were used to inoculate 2.0 L of LB growth medium and allowed to grow overnight at 37 °C with shaking (300 rpm) to produce an isolation culture, which was divided into 4 × 500 mL aliquots. pDNA was then isolated from each aliquot into deionized (DI) water using a QIAGEN® Plasmid Maxiprep kit, resulting in ~1 mL pDNA samples which were further concentrated to 200-300 μL using centrifugal evaporation. All pDNA samples were characterized using a Thermo Fisher ND-1000 NanoDrop to determine purity and concentration. Since the experiments described in subsequent sections required higher pDNA concentrations than were accessible using a single Maxiprep kit, pDNA stock solutions consisted of multiple (3-6) isolated samples which were pooled and mixed by gentle vortexing. Only isolated samples with an absorbance ratio $A_{260:280} = 1.8 \pm 0.1$ were used for pooling. All pooled samples had absorbance ratios of $A_{260:280} = 1.8 \pm 0.1$ and $A_{260:230} = 2.00 \pm 0.03$ and pDNA concentrations in the range of 700-1000 ng/μL. Finally, all pooled samples were diluted using DI water to a final

pDNA concentration of 696 ng/μL and were stored at 4°C to be used as pDNA stock solutions in the experiments described below.

2.2.3 Fluorescence Characterization of Binding between pDNA and Poly(2-vinylpyridine).

The following fluorescence experiments were carried out to confirm binding between P2VP and pDNA. Inside a quartz fluorescence cuvette, 45 μg pDNA (64.5 μL of pDNA stock) were suspended in 3.0 mL DI water that had been previously acidified to pH 3 using HCl. Then, aqueous EtBr solution (10.0 mg / mL) was added to the cuvette at a molar ratio of 1:1 EtBr : phosphate (5.5 μL) and the contents of the cuvette were mixed on an orbital shaker at 300 rpm for 30 s, followed by a fluorescence measurement of the mixture. Next, P2VP homopolymer was dissolved in acidified DI water (pH 3, HCl) to a concentration of 17.0 mg/mL. The P2VP solution was then added to the cuvette at a molar ratio of 4:1 pyridinium : phosphate (3.4 μL) and the contents of the cuvette were mixed at 300 rpm for 12 h, followed by a second fluorescence measurement of the mixture. Finally, 60 μL of 1 N NaOH were added and the contents of the cuvette were mixed at 300 rpm for 1 h, followed by a final fluorescence measurement of the neutralized mixture (pH ~7). All fluorescence measurements were carried out on an Edinburgh Instruments FLS920 fluorimeter, with excitation at 285 nm from a Xe900 xenon arc lamp and emission measured by a R9289 photomultiplier tube. Fluorescence emission spectra were collected between 565 nm and 800 nm and corrected for instrument response.

2.2.4 Functionalization of pDNA with PCL-b-P2VP (SA1).

Functionalization of pDNA for all experiments discussed in this chapter refers to the electrostatic binding of negatively charged phosphodiester groups on the pDNA backbone with positively charged P2VP homopolymer or P2VP-*b*-PCL block copolymer. For each experiment, 45.0 μg of pDNA (64.5 μL of pDNA stock) were transferred to a 1.5 mL Eppendorf tube followed by dilution with variable quantities of DI water (0, 17, 57, 195, or 340 μL). The resulting pDNA solutions were added with stirring to 500-600 μL of a 70/30 (v/v) mixture of dioxane/acetic acid in a Teflon centrifuge tube. Next, more 70/30 (v/v) acetic/acid dioxane mixture was added to bring the volume of the tube to 1.0 mL, such that the pDNA concentration was 45 ng/μL. The solutions were weighed in order to determine the following variable water concentrations: 6.2, 7.8, 11.6, 24.9, and 39.1 wt %. For functionalization in the presence of salt, sodium acetate was dissolved in the 70/30 (v/v) mixture of dioxane/acetic acid such that the salt concentration after the addition of the aqueous pDNA solution was either 0.01 or 0.1 M. Finally, PCL-*b*-P2VP in dioxane (17.0 mg / mL) was added to the pDNA solution at a molar ratio of 4:1 pyridinium : phosphate (9.3 μL). The resulting SA1 mixture was stirred at 800 rpm overnight at 21 °C.

2.2.5 Determination of pDNA Functionalization Efficiency.

In order to quantify the efficiency of pDNA functionalization, the following procedure was applied after overnight stirring of the SA1 mixture. First, 2.0 mL of chilled isopropanol (stored at -4 °C) were added to the centrifuge tube containing the SA1 mixture followed by incubation at -4 °C for 4 h. Next, the mixture was centrifuged at 12000 × g for 30 min to yield a colorless opaque pellet containing a blend of functionalized and unfunctionalized pDNA. This pellet was isolated by decanting off the clear liquid and then dissolving in 3.0 mL chloroform, followed by three wash

steps using 3.0 mL acidified DI water (pH 3, acetic acid) for each step. After each wash step, the organic and aqueous layers were separated in a separatory funnel and the bottom organic layer was collected for the next wash. The chloroform solution was transferred to a test tube and the solvent was removed by gently passing air over the test tubes for 24 hours. After drying, the phosphate content in the chloroform solution was determined using a phosphate assay and compared to the phosphate content in the total amount of 45 μg of pDNA used in the SA1 experiment. Since only functionalized pDNA (PCL-pDNA) is soluble in chloroform, the following equation was used to determine the functionalization efficiency of pDNA (*FE*):

$$FE = \frac{[\text{phosphate}]_{\text{chloroform}}}{[\text{phosphate}]_{\text{total pDNA}}} \times 100\ \%$$

In the above equation, phosphate concentrations represent the number of moles of phosphate extracted into 200 μL DI water.

Reported *FE* values were determined by averaging the values from triplicate preparations under the same conditions (water and salt content). Standard errors ($\pm\sigma$) on *FE* values were calculated from the standard deviation (s) of triplicate values: $\sigma = \frac{s}{\sqrt{3}}$. Optimized functionalization (highest *FE* values) was found at 6.2 wt% water and no salt, such that these optimized conditions were used for all experiments described below. Unencapsulated pDNA was not quantified and assumed to be removed through centrifugal filtration after DNase treatment.

2.2.6 Release of pDNA from PCL-pDNA.

To rule out degradation of pDNA following the SA1 step, pDNA was released from the copolymer for gel electrophoresis analysis in the following manner. First, after overnight stirring of the SA1 mixture (6.2 wt % water and no salt added), a pellet containing functionalized and

unfunctionalized pDNA was isolated and dissolved in chloroform as described in the previous section. Then, after washing 3× with acidified water (pH 3, acetic acid) to remove unfunctionalized pDNA, the chloroform fraction containing PCL-pDNA was transferred from the separatory funnel to a new vial. Next, 3.0 mL of DI water was layered on top of the chloroform and 60 µL of pyridine was added to the chloroform layer. The two-phase mixture was stirred at 800 rpm for 3 hours at 21°C followed by separation of chloroform and aqueous layers in a separatory funnel. The aqueous fraction containing released pDNA was concentrated by centrifugal evaporation to a volume of < 100 µL and then analyzed by gel electrophoresis.

2.2.7 Bulk Encapsulation of PCL-pDNA in PIHC micelles (Bulk SA2).

After overnight stirring of the optimized SA1 mixture (6.2 wt% water and no salt), PCL-*b*-PEG in dioxane (10.4 mg / mL) was added at a mass ratio of 1:10 PCL-*b*-PEG : pDNA + PCL-*b*-P2VP (2.0 µL). The solution was allowed to stir at 800 rpm for 3 h and then transferred to a small clean vial. To initiate self-assembly, water was added to the solution at a constant injection rate of 120 µL/min using a syringe pump with stirring at 800 rpm until a water content of 33 wt % was reached. Then 10 mL of DI water was added followed by immediate vortex mixing. Finally, the dispersion was transferred to 6-8 kDa MWCO dialysis tubing and dialyzed against DI water for 18 h, changing the water every hour for the first 4 hours.

After dialysis, unencapsulated pDNA was removed from the aqueous dispersion before quantification of pDNA using a combination of enzymatic digestion and centrifuge filtration. First, the dialyzed sample was concentrated to 2.5 mL using a centrifuge filter (Macrosep, PALL) with MWCO = 100 kDA by centrifuging for 12 minutes at 5000 × g. The concentrated sample was then split equally into two 1.5 mL microcentrifuge tubes. To each tube, 150 µL of DNase I 10× reaction

buffer were added, followed by addition of water to the 1.5 mL mark and gentle vortexing. Then 12.5 μL of DNase I enzyme were added to each tube and the mixture was again vortexed gently, followed by 1 h incubation at 21 °C. After incubation, 22.5 μL EDTA solution (50 mM) were added to each tube and the mixture was vortexed gently. Finally, the sample was recombined and washed by adding 12.5 mL DI water then concentrating to 2.5 mL using a centrifuge filter (Macrosep, PALL) with MWCO = 100 kDA by centrifuging for 12 minutes at 5000 × g. The wash step was repeated two more times. The particles after removal of unencapsulated pDNA were designated PIHC micelles (bulk preparation).

2.2.8 Microfluidic Reactor Fabrication.

The microfabrication steps followed previously described procedures from our group.[36] Firstly, negative masters were fabricated on silicon wafers (Silicon Materials) using the negative photoresist SU-8 100 (Microchem). A 150 μm-thick SU-8 film was spin-coated at 2,000 rpm onto the silicon wafer and heated at 65 °C for 12 min and then at 95 °C for 50 min. After the wafer was cooled, a photomask was placed directly above, and the wafer was exposed to UV light for 100 s. Then, the UV-treated film was heated at 65 °C for 1 min and then 95 °C for 20 min. Finally, the silicon wafer was submerged in SU-8 developer (Microchem) and rinsed with isopropanol until all unexposed photoresist was removed.

Microfluidic chips were fabricated from polydimethylsiloxane (PDMS) using a SYLGARD 184 silicon elastomer kit (Dow Corning). For fabrication of all PDMS chips, the elastomer and curing agent were mixed at a 7:1 ratio and degassed under vacuum. The resulting mixture was poured over a clean negative master chip in a Petri dish and further degassed until all remaining air bubbles were removed. The PDMS was heated at 85 °C until cured (~20 min) and then peeled

from the negative master; holes were punched through the reservoirs of the resulting PDMS chip to allow for the insertion of tubing. A thin PDMS film (substrate layer) was also made on a glass slide by spin-coating a 20:1 elastomer/curing agent mixture followed by curing. The substrate layer was then permanently bonded to the base of the microfluidic reactor (channel layer) after both components were exposed to oxygen plasma for 90 s. The resulting reactor (Figure 2.6) has a set channel depth of 150 μm and consists of a sinusoidal mixing channel 100 μm wide and a straight processing channel 200 μm wide.

2.2.9 Flow Delivery and Control.

The steps of flow delivery and control followed previously described procedures.[36] Pressure-driven flow of liquids to the reactor inlet was provided using 1 mL gastight syringes (Hamilton) mounted on syringe pumps (Harvard Apparatus). The microfluidic chip was connected to the liquid syringes via 1/16th-inch (OD) Teflon tubing (Mandel Scientific). Argon (Ar) gas flow was introduced to the chip via an Ar tank regulator and a downstream regulator (Johnston Controls) for fine adjustments. The chip was connected to the downstream regulator through a 1/16th-inch (OD)/100-μm (ID) Teflon tube (Mandel Scientific). The liquid flow rate (Q_{liq}) was programmed via the syringe pumps, and the gas flow rate (Q_{gas}) was fine-tuned via the downstream pressure regulator in order to set a total nominal flow rate (Q) of 200 μL/min. Due to the compressible nature of the gas and the high gas/liquid interfacial tension, discrepancies arise between the nominal (programmed) and actual values of Q_{gas}, Q_{gas}/Q_{liq}, and the total flow rate (Q_{total}). Therefore, actual values of Q_{gas}, Q_{gas}/Q_{liq}, and $Q_{total} = Q_{gas} + Q_{liq}$ for each microfluidic experiment were calculated from the average volume of gas bubbles in the microchannels and are reported in *Supporting Information* (Table S1). Specifically, an image of the microchannels was captured using a Genie Nano-C1280 camera (1stVision) equipped with an On-Semi Python1300 sensor and

a C-Mount Manual Iris Varifocal lens (1/1.8", 4-13mm, *f*/1.5) (Tamron) at each of three different time periods at the beginning, middle, and end of the sample collection process. Analysis of the gas bubbles and liquid plugs within the microfluidic reactor was achieved using image analysis software (ImageJ), which gives the end-to-end distance of individual gas bubbles and liquid plugs, $L_{gas,i}$ and $L_{liq,i}$, respectively, under a given set of flow conditions. The gas-to-liquid flow ratio, Q_{gas}/Q_{liq}, was determined from each image as the ratio between measured $\sum_i L_{gas,i}$ and $\sum_i L_{liq,i}$ (i = 20-50). Actual gas-to-liquid flow ratios for all experimental runs are reported as average values determined from 3 images for each run. All actual Q_{total} values within Table S1 are within 10 % of nominal Q values.

2.2.10 Microfluidic Encapsulation of PCL-pDNA in PIHC micelles (Microfluidic SA2).

After overnight stirring of the optimized SA1 mixture (6.2 wt% water and no salt), PCL-*b*-PEG in dioxane (10.4 mg / mL) was added at a mass ratio of 1:10 PCL-*b*-PEG : pDNA + PCL-*b*-P2VP (2.0 µL). The solution was allowed to stir at 800 rpm for 3 h and was then used as the PCL-pDNA/PCL-*b*-PEG stream for microfluidic assembly. For microfluidic preparation of PIHC micelles, the following three liquid streams were combined to give stable gas-segmented liquid plugs within the reactor, (1) the PCL-pDNA/PCL-*b*-PEG stream (2) pure dioxane; and (3) pure DI water. The flow rates of the three liquid streams were equal for all runs, and the steady-state on-chip water concentration was 33 wt %. Due to dilution by the additional two liquid streams, PCL-pDNA and PCL-*b*-PEG were 3× more dilute during self-assembly in the microfluidic channels than during bulk self-assembly. For each microfluidic run, 3× 1 mL liquid portions were collected from the chip into vials containing 10 mL DI water and then combined. In order to remove residual dioxane and acetic acid, the resulting PNP dispersions were then immediately transferred into a 6−8 kDa MWCO dialysis membrane and dialyzed against DI water for 18 h, with changing of DI

water every hour for the first 4 h. After dialysis, unencapsulated pDNA was removed from the aqueous dispersion using a combination of enzymatic digestion and centrifuge filtration as described in the bulk SA2 section. The final particles after removal of unencapsulated pDNA were designated PIHC micelles (microfluidic preparation).

2.2.11 Preparation of Positive and Negative Control Samples.

The positive control sample was prepared using an equivalent amount of pDNA which was exposed to the same solvents, dialysis, and centrifugal filtration as PIHC micelle formation. However, no copolymers were added and no DNase I digestion step was applied to the positive control sample. Briefly, 45.0 μg of pDNA (64.5 μL of pDNA stock) were added to a 30 % (v/v) mixture of dioxane/acetic acid in a Teflon centrifuge tube such that the total volume was 1.0 mL. The solution was then injected into 10 mL DI water at 120 μL / min followed by overnight dialysis for 18 h, changing the water every hour for the first 4 hours. Following dialysis, the aqueous pDNA dispersion was concentrated to 2.5 mL by centrifugal filtration, then washed by adding 12.5 mL DI water and re-concentrating to 2.5 mL. The wash step was repeated two more times, resulting in a final aqueous dispersion of 2.5 mL, which was designated the positive control sample. The mass of pDNA in the positive control was determined to be 41 μg using the phosphate assay, indicating that <10% pDNA was lost in the various steps described above.

The negative control sample was prepared using equivalent amounts of pDNA and copolymers and with the same solvents, dialysis, and centrifugal filtration steps as PIHC micelle formation. However, the pDNA was added *after* the SA2 step in the preparation of the negative control sample such that it was not encapsulated during subsequent DNAase digestion. Briefly, 9.2 μL PCL-*b*-P2VP in dioxane (17.0 mg / mL) and 2.0 μL PCL-*b*-PEG in dioxane (10.4 mg / mL)

were added to a 30 % (v/v) mixture of dioxane/acetic acid such that the total volume was 1.0 mL. The solution was then injected into 10 mL DI water at 120 μL / min followed by overnight dialysis for 18 h, changing the water every hour for the first 4 hours. After dialysis, 45.0 μg of pDNA (64.5 μL of pDNA stock) were added to the resulting dispersion, followed by concentrating the dispersion to 2.5 mL using centrifugal filtration. The concentrated sample was then split equally into two 1.5 mL microcentrifuge tubes, and to each tube 150 μL of DNase I 10× reaction buffer were added. After the addition of water to 1.5 mL, the mixture was vortexed followed by addition of 12.5 μL of DNase I enzyme to each tube. The mixture was vortexed again, then incubated for 1 h at 21ºC. Next, 22.5 μL EDTA solution (50 mM) were added to each tube. After vortexing, the sample was recombined and washed by adding 12.5 mL DI water then concentrating to 2.5 mL using centrifuge filtration. The wash step was repeated two more times, resulting in a final aqueous dispersion of 2.5 mL, which was designated the negative control sample.

2.2.12 Determination of pDNA Encapsulation Efficiency.

To determine pDNA encapsulation efficiencies, the pDNA content in bulk and microfluidic PIHC micelle samples, and in the positive and negative controls, were analyzed. First, the aqueous dispersion (2.5 mL) was transferred to a test tube and water was removed by gently passing air over the test tube for 24 hours. After drying, the pDNA content was determined using a phosphate assay. For the PIHC micelles, all unencapsulated pDNA had been removed by digestion with DNase I and subsequent washing steps, such that the remaining pDNA was assumed to be encapsulated within the micelles. Therefore, the following equation was used to determine the encapsulation efficiency of pDNA (*EE*) :

$$EE = \frac{[\text{phosphate}]_{\text{sample}}}{[\text{phosphate}]_{\text{total pDNA}}} \times 100\ \%$$

In the above equation, $[\text{phosphate}]_{\text{sample}}$ represents the number of moles of phosphate extracted from the dried PIHC micelle sample or control into 200 μL DI water, and $[\text{phosphate}]_{\text{total pDNA}}$ represents the concentration of phosphate in the total starting mass of pDNA (45 μg) extracted into 200 μL DI water (0.69 mM). Reported *EE* values for bulk and microfluidic PIHC micelle preparations were determined by averaging the values from triplicate preparations under the same conditions. Standard errors ($\pm\sigma$) on *EE* values were calculated from the standard deviation (*s*) of triplicate values: $\sigma = \frac{s}{\sqrt{3}}$. For the positive control sample described in the previous section, the *EE* value was determined to be 91%, confirming that most of the initial pDNA could be recovered and measured without DNase I exposure, with <10% lost in the centrifugal filtration and washing process.

2.2.13 Release of pDNA from PIHC micelles.

To rule out degradation of encapsulated pDNA following SA1, SA2, and DNase I digestion of unencapsulated pDNA, encapsulated pDNA was released from microfluidic PIHC micelles for gel electrophoresis analysis. First, the aqueous micelle dispersion (2.5 mL) was concentrated by centrifuge evaporation to a volume of < 200 μL. The resulting concentrated dispersion was then added to 100× excess (v/v) of acetonitrile in order to dissociate the PIHC micelles. A white precipitate was observed, attributed to salts from the DNase I buffers. The acetonitrile was carefully decanted from the vial containing the salts and transferred to a centrifuge tube. The acetonitrile solution containing free PCL-*b*-PEG chains and PCL-pDNA was chilled for 4 h at -4°C in the freezer and then centrifuged at 12,000 × g for 30 minutes to pellet the PCL-pDNA fraction. The supernatant was discarded, and the pellet was dissolved in 3 mL chloroform. Next, 3.0 mL of DI water was layered on top of the chloroform and 60 μL of pyridine was added to the

chloroform layer. The two-phase mixture was stirred at 800 rpm for 3 hours at 21°C followed by separation of chloroform and aqueous layers in a separatory funnel. The aqueous fraction containing released pDNA was concentrated by centrifugal evaporation to a volume of < 20 μL and then analyzed by gel electrophoresis.

2.2.14 Bacterial Cell Transformation Experiments.

To prepare competent Escherichia coli K12 (E.coli K12) cells for PIHC micelle and control transformation experiments, 10 mL of sterile LB broth was inoculated with E.coli K12 and allowed to grow overnight at 37 °C with shaking to produce an overnight culture. Then 50.0 mL of sterile LB broth was inoculated with 200 μL of the overnight culture and allowed to grow to OD600 = 0.5. Cells were collected by centrifugation at 1,000 × g for 14 minutes, re-suspended in 17.0 mL of CCMB (calcium chloride manganese buffer), then collected again by centrifugation at 1,000 × g for 10 minutes. Finally, the cells were re-suspended in 4.16 mL of CCMB buffer and stored overnight at -80 °C.

Transformation experiments were carried out in triplicate using a single sample of PIHC micelles prepared using microfluidic encapsulation along with the positive and negative control samples described above. First, three empty 13 mL culture tubes (for PIHC micelles, positive control, and negative control) were chilled on ice for at least 30 minutes while the competent cells were thawed on ice. Then, 5.0 μL of the PIHC micelle sample, positive control sample, and negative control sample were added to each of the culture tubes, followed by addition of 200 μL of competent cells to each tube. All tubes were incubated on ice for 25 min then transferred to 42 °C water for 70 s then back to ice for 2 min. Next, 1 mL of SOC medium was added to each tube and the tubes were incubated at 37 °C with 300 rpm shaking. At incubation times of 1, 3, and 8 h,

100 μL from each tube was plated on agar petri dishes containing 200 μg / mL ampicillin and allowed to grow overnight at 37 °C.

To determine transformation efficiencies (CFU per μg pDNA), the number of colonies on each plate were counted and divided by the pDNA masses (in μg) used in the transformation based on pDNA masses in the sample and controls. Reported transformation efficiency values were determined by averaging the values from triplicate transformation experiments. Standard errors (±σ) on transformation efficiency values were calculated from the standard deviation (s) of triplicate values: $\sigma = s/\sqrt{3}$. The masses of pDNA in the negative and positive control samples were determined to be 0 μg and 41 μg using the phosphate assay. The mass of pDNA in the PIHC micelle sample was determined to be 2.9 μg based on the initial mass of 45 μg and the average *EE* value for microfluidic encapsulation (6.5 ± 1.1%).

2.2.15 Fluorescence Imaging of PIHC Micelle Uptake in MDA-MB-231 Cells.

In order to confirm uptake of PIHC micelles into cells using fluorescence microscopy, microfluidic PIHC micelles were prepared as previously described, but with the following two additional steps for labelling pDNA and PCL components with different fluorescent dyes. First, before the SA1 step, 45 μg (64.5 μL of pDNA stock) were transferred to a 1.5 mL Eppendorf tube and 2.0 μL of DAPI solution (1.0 mg / mL in DI water) were added followed by overnight incubation in the dark at 4 °C. The SA1 experiment was then conducted as described previously. Second, before the microfluidic SA2 step, 4.0 μL of a DiI solution (0.1 mg / mL in dioxane) was added immediately after the addition of PCL-*b*-PEG to the SA1 mixture. The SA2 experiment was then conducted as described previously to produce DAPI/DiI-labelled PIHC micelles.

Human breast cancer cells were used as a model system to determine cell uptake of PIHC micelles. MDA-MB-231 cells were grown to ~70% confluence in 75 cm^2 tissue culture flasks, then trypsinized, collected, and pelleted by centrifugation (5 min at 313 × g). The cell pellet was then suspended in DMEM, and the cell concentration was determined using a hemocytometer. After the initial cell concentration was determined, the suspension was diluted to 1.0×10^5 cells/mL. Next, a pipette was used to seed the cells at a density of 3.0×10^5 cells per well in a 6-well plate (Costar) and the plate was then incubated for 24 h at 37 °C with 5% CO_2 for cell adhesion. Within each well, aqueous dispersions of DAPI/DiI-labelled PIHC micelles were mixed 1:5 (v/v) with the cell media for a final PIHC micelle concentration of 0.014 mg/mL. After 4 h incubation at 37 °C, the cells were washed 3× with 1 mL of PBS buffer. Fluorescein diacetate was dissolved to a concentration 0.05 mg/mL in a solution of 1.0 wt % acetone in DI water. Then 1 mL of the fluorescein diacetate solution was added to each well, and the cells were incubated in the dark for 5 min then washed 3× with 1 mL of PBS and immediately imaged. Fluorescence images were captured using a Cytation5 microplate reader equipped with fluorescent microscope (BioTek), with three fluorescent filter cubes of emission (nm)/excitation (nm) = 377/447, 469/525, and 586/647. Images were taken using a 20× objective.

2.2.16 Gel Electrophoresis.

Samples were mixed in a 1:6 (v/v) ratio with DNA gel loading dye, then 18.0 µL of each solution were subjected to electrophoresis (100 mV for 1 h) in a 1% agarose gel in 1× TAE buffer. Gels were stained by immersion in an aqueous EtBr bath (0.5 µg/mL) for 15 min and then imaged in an AlphaImager™ Gel Imaging System (Alpha Innotech). All gel runs were compared against a 1kb DNA ladder (Fisher).

2.2.17 Phosphate Assays.

Phosphate assays enabled quantitative determination of pDNA content in multicomponent samples. To prepare a sample for a phosphate assay, the liquid sample was transferred to a test tube then solvent was removed by passing air over the test tube for 24 h. Next, 200 µL of DI water was added to the dried sample. In separate test tubes, 200 µL of phosphate standard solutions were prepared with known concentrations of 0, 0.15, 0.30, 0.45, and 0.65 mM phosphate. Next, 400 µL of sulfuric acid were added to each test tube followed by vortex mixing. Then, 200 µL of hydrogen peroxide were added to each test tube followed by immediate vortexing and capping each test tube with a glass marble (***Warning: piranha solution is a powerful oxidizer and must be handled with extreme care!!***). The tubes were heated to between 205-215 °C and maintained within this temperature range for 90 min, then cooled at room temperature for 5 min. Next, 100 µL of aqueous ascorbic acid solution (10 wt %), 4.6 mL of ammonium molybdonate tetrahydrate solution (0.890 mM) in 0.25 N sulfuric acid, and 200 µL of 0.209 mM ANSA solution in 14.3 wt % aqueous sodium sulfite were added sequentially to each test tube, vortexing immediately after addition of each solution. Finally, the test tubes were heated at 100 °C for 15 min followed by colorimetric measurements. A standard calibration curve was generated from absorbance values at 830 nm on an Agilent 8453 UV−vis spectrophotometer and unknown phosphate concentrations were determined by comparison with the calibration curve.[45]

2.2.18 Critical Water Content Determination.

Static light scattering measurements were carried out to determine the CWC of PCL-*b*-P2VP under conditions of pDNA functionalization. Light scattering experiments were performed on a Brookhaven Instruments photocorrelation spectrometer equipped with a BI-200SM goniometer

and a BI-Mini-L30 30 mW red (636 nm) compact diode laser, at a scattering angle of 90° and a temperature of 25 °C. To prepare the sample solution, a 1.0 mL mixture of 45 μg pDNA and 158 μg PCL-*b*-P2VP in 70/30 (v/v) dioxane/acetic acid was prepared (6.2 wt % water and no salt) as described previously (SA1 step), except that the dioxane/acetic acid mixture was pre-filtered to remove dust (2 × 0.20 μm nominal pore size Teflon syringe filters, VWR). After overnight stirring of the SA1 mixture, pre-filtered DI water (2 × 0.20 μm nominal pore size nylon syringe filters, National Scientific) was added in successive 0.03−0.06 g quantities using a micropipette. After each addition of water the sample was allowed to equilibrate for 20 min before the scattered light intensity was measured. The resulting scattered light intensity was plotted vs. water concentration. In an attempt to obtain light scattering measurements for water contents below 6.2 wt %, an equivalent amount of pDNA was also added from a more concentrated stock (790 ng/mL), such that the initial water content was 5.7 wt %; at that water content, pDNA was observed by eye to precipitate in the dioxane/acetic acid mixture before the P2VP-*b*-PEG copolymer was added.

2.2.19 Dynamic Light Scattering.

DLS measurements were carried out for determination of hydrodynamic sizes and size distributions following SA1 and SA2 self-assembly steps on a Brookhaven Instruments ZetaPALS Analyzer equipped with a solid state Laser (660 nm) with a maximum power output of 35 mW. All DLS measurements were performed at an experimental temperature of 25 °C and at a scattering angle of 90°. Solvents used for DLS sample preparation were pre-filtered using 2 × 0.20 μm nominal pore size nylon syringe filters (National Scientific) for DI water and 2 × 0.20 μm nominal pore size Teflon syringe filters (VWR) for dioxane/acetic acid.

For DLS of PCL-pDNA following the SA1 step, the following sample preparation steps were carried out after overnight stirring of the SA1 mixture. First, 2.0 mL of chilled isopropanol (stored at -4 °C) were added to the mixture followed by incubation at -4 °C for 4 h. Next, the mixture was centrifuged at 12000 × g for 30 min to yield a colorless opaque pellet which was isolated by decanting off the clear liquid. The pellet was then re-suspended in 1.0 mL of pre-filtered SA1 solvent mixture (30% (v/v) dioxane/acetic acid with 6.2 wt % water) by gentle vortexing and transferred to a dust-free cuvette for DLS measurements. For DLS of PIHC micelles following the SA2 step and DNase I digestion and washing, 200 μL of the micelle dispersion were added to 3.0 mL pre-filtered water is a dust-free cuvette for DLS measurements.

The determination of PCL-pDNA hydrodynamic size in the SA1 solvent mixture required calculations of the viscosity (η = 1.18 cP) and refractive index (n = 1.39) of the SA1 solvent mixture at 25 °C. The viscosity of the mixture was calculated using the Refutas equation:[46]

$$\eta = \exp\left(\exp\left(\frac{\left(\sum_{i=0}^{N} w_i \times (14.534 \times \left(\ln\left(\eta_i + 0.8\right)\right) + 10.975)\right) - 10.975}{14.534}\right)\right) - 0.8$$

where η_D = 1.22 cP, η_A = 1.15 cP, and η_W = 0.91 cP are the viscosities of dioxane, acetic acid and water components, respectively. In the SA1 mixture, the mass fractions of the components are w_D = 0.63, w_A = 0.31, and w_W = 0.07. The refractive index of the mixture was calculated using a weighted sum (by volume fractions) of refractive index values for the liquid components:[47]

$$n = \sum_{i=0}^{N} (\phi_i \times n_i)$$

where n_D = 1.42, n_A = 1.37, and n_W = 1.33 are the refractive indexes of dioxane, acetic acid and water components, respectively. In the SA1 mixture, the volume fractions of the components are ϕ_D = 0.65, ϕ_A = 0.28, and ϕ_W = 0.06.

Reported $d_{h,eff}$ values were determined using the method of cumulants by averaging values from triplicate preparations under the same conditions. Standard errors ($\pm\sigma$) on $d_{h,eff}$ values were calculated from the standard deviation (s) of triplicate values: $\sigma = \frac{s}{\sqrt{3}}$.

2.2.20 Transmission Electron Microscopy.

Negatively stained samples for TEM imaging were prepared by depositing a drop of ~0.1 mg/mL PIHC micelle dispersion on a Formvar/carbon-coated 200-mesh copper TEM grid (Ted Pella Inc.) followed by a drop of 1 wt % uranyl acetate aqueous solution as a negative staining agent. Excess liquid was immediately removed using lens paper, followed by drying of the remaining liquid under ambient conditions. Imaging was performed on a JEOL JEM-1400 transmission electron microscope, operating at an accelerating voltage of 80 kV and equipped with a Gatan Orius SC1000 CCD camera.

2.3 Results and Discussion

2.3.1 Reversible Binding of pDNA with P2VP Homopolymer.

We chose PCL-*b*-P2VP as the polycation-containing block copolymer component for pUC18 complex formation due to its commercial availability, solubility in polar organic solvent mixtures, and pH-sensitive charging of the P2VP block. The plasmid pUC 18 was chosen for this proof-of-concept study based on its relatively small size and extensive study in the literature.[25-28]

However, since the use of P2VP as a nucleic acid-binding polycation has not been widely explored,[29] we were interested in confirming reversible polyplex binding in a model system of pUC18 and P2VP homopolymer in acidic aqueous media. For this experiment, ethidium bromide (EtBr) was used as a fluorescent probe in a competitive binding assay. EtBr is known to intercalate between base pairs in the DNA double helix, which significantly increases its fluorescence intensity; therefore, binding of DNA with polycations can be monitored via displacement of EtBr and concomitant decrease in EtBr fluorescence.[30] As shown in Figure 2.2, following an initial fluorescence measurement of the EtBr-pDNA complex at pH = 3 (black curve), the EtBr emission intensity decreased significantly after addition of P2VP at a ratio of 4 : 1 pyridinium : phosphate (blue curve), indicating displacement of EtBr as negatively charged pDNA formed a polyplex with positively charged P2VP. Then, when the pH was increased to pH 7 by NaOH addition, deprotonation of pyridinium groups led to release of pDNA from the polymer, allowing the EtBr-pDNA complex to reform with an increase in EtBr fluorescence (red curve). These results suggested that P2VP blocks of PCL-*b*-P2VP should form reversible polyplexes with pDNA under suitable conditions of solvent and pH.

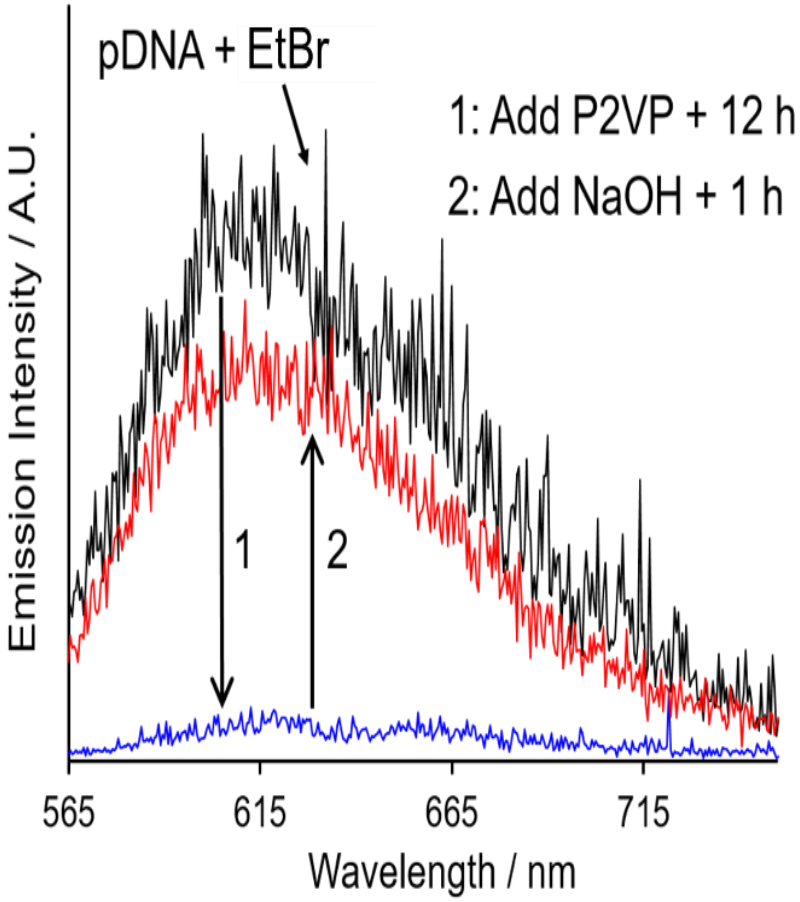

Figure 2.2. EtBr fluorescence emission showing reversible pH-dependent complexation of P2VP and pDNA. Black data correspond to the emission spectrum of a mixture of pDNA and ethidium bromide. Blue data correspond to the emission spectrum of the same mixture, after addition of poly(2-vinylpyridine). Red data correspond to the emission spectrum of the same mixture treated with poly(2-vinylpyridine), in which sodium hydroxide has been added to deprotonate the pyridine residues, freeing bound pDNA back into solution.

2.3.2 Optimization of Solvent Conditions for PCL-pDNA Formation (SA1 Step).

The formation of a polyplex between pDNA and the P2VP blocks of PCL-*b*-P2VP (SA1, Figure 2.1A) requires a fine balance of solvent properties. First, the solvent should be sufficiently polar to support charging of the P2VP blocks. Second, the solvent should be sufficiently nonpolar to support solubilisation of the PCL blocks. Third, the pH of the medium must be low enough to lead to protonation of 2VP groups. Finally, the pDNA should retain its remain non degraded in the solvent medium. To optimize polyplex formation based on these criteria, we evaluated the SA1 process at a constant ratio of 4 : 1 P2VP pyridinium : pDNA phosphate in various mixtures of dioxane, acetic acid, water, and salt.

Upon formation of the desired block ionomer micelle polyplexes (SA1, Figure 2.1), the complexed pDNA becomes functionalized by the surrounding coronal layer of PCL chains, rendering it soluble in nonpolar organic solvents such as chloroform. Therefore, we were able to characterize the efficiency of pDNA functionalization in the following manner. First, the various SA1 mixtures were pelleted down by addition of chilled isopropanol followed by centrifugation; the resulting pellet was then extracted into chloroform and the chloroform solution was washed several times with acidified water (pH = 3) to remove any unfunctionalized pDNA. Finally, the amount of pDNA in the chloroform layer was determined using a phosphate assay and compared to the total initial pDNA amount (45 μg). The resulting percentage was taken to be the functionalization efficiency (*FE*).

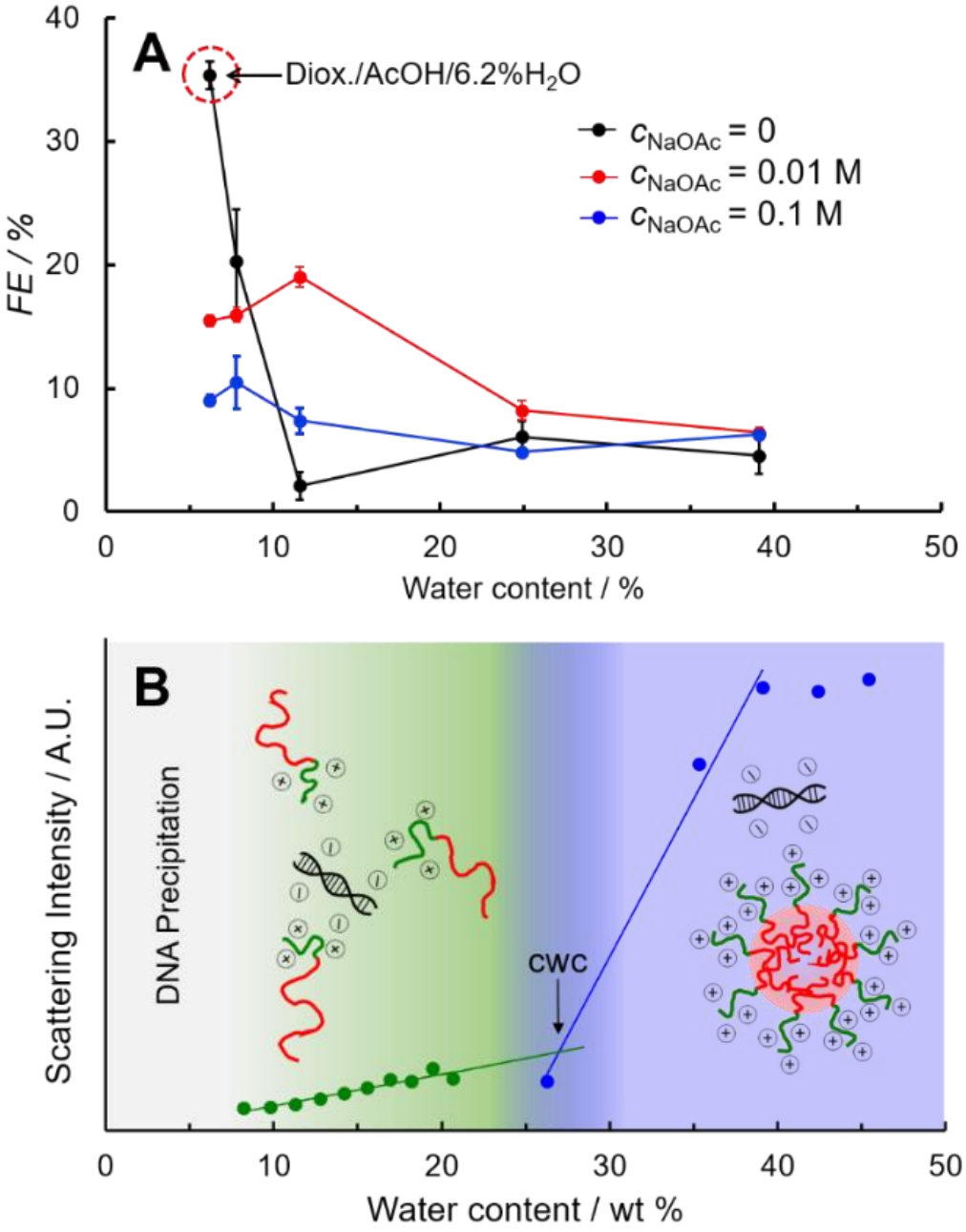

Figure 2.3. (A) Functionalization efficiencies (*FE*) of PCL-pDNA formed in 70/30 dioxane/acetic acid (v/v) at different water and salt contents. Error bars were determined from triplicate preparations. (B) Static light scattering intensities of SA1 mixture at different water contents showing critical water content (CWC) associated with micellization of PCL-*b*-P2VP chains.

In preliminary experiments, we carried out the SA1 process at extreme dioxane/acetic acid ratios of 0/100 and 99/1 (v/v). We found that *FE* was higher in the 0/100 (no dioxane) case (38%) than in the 99/1 (high dioxane) case (25%). However, gel electrophoresis (not shown) indicated degradation of pDNA in the "no dioxane" mixture, whereas pDNA remained non degraded following SA1 in the high dioxane mixture. These results suggested that while high acetic acid contents promote polyplex formation, they also significantly degrade the pDNA structure. Finally, we settled on a 70/30 dioxane/acetic acid (v/v) mixture for all experiments described below, which gave *FE* values comparable to those in the "no dioxane" case but without concomitant pDNA degradation or loss of functionality (*vida infra*).

While holding the dioxane/acetic acid ratio constant at 70/30 (v/v), we next investigated the effects of water content and salt addition (sodium acetate) on *FE* (Figure 2.3A). In the absence of salt, we found that the SA1 mixtures required a minimum water content of ~6 wt %, below which pDNA was found to precipitate. As the water content was increased from 6.2 wt % to 11.6 wt %t (black data points, Figure 2.3A), the *FE* values drop sharply (from 35% to less than 5%). We considered the possibility that this drop in *FE* was associated with the formation of regular micelles with PCL cores and P2VP coronae above the critical water content (CWC) of the PCL blocks. To investigate this, we carried out a CWC determination of the copolymer/pDNA solution using static light scattering (SLS) (Figure 2.3B); these results reveal the CWC to be ~25 wt %—well above the water contents associated with the sharp drop in *FE* (Figure 2.3A)— such that PCL-*b*-P2VP micellization cannot explain the observed trend. One possible explanation is that the increase in water content gradually converts the PCL blocks to a more globular conformation, which increases attractive interactions between the PCL blocks as covalently attached P2VP

blocks surround the pDNA; these attractive interactions between proximal PCL globules could disrupt pDNA-P2VP polyplex formation, thus lowering *FE*.

When salt is added to the SA1 mixture, we found a general decrease in *FE* values, especially at low water contents. For the lowest water content (6.2 wt %), *FE* values are found to decrease sharply from 35 % with no salt (black data points, Figure 2.3A), to 15 % (c_{NaOAc} = 0.01 M, red data points, Figure 2.3A) to 9 % (c_{NaOAc} = 0.1 M, blue data points, Figure 2.3A). This effect can be attributed to the screening of electrostatic attractive interactions between negative phosphate groups on the pDNA and positive pyridinium groups on the P2VP blocks, which increases with the ionic strength of the mixture. Based on the maximum *FE* value shown in Figure 2.3A (38 %, red dashed circle), we chose the optimized SA1 conditions of 70/30 dioxane/acetic acid (v/v), 6.2 wt % water and no salt added for the remaining experiments described below.

2.3.3 Characterization of PCL-pDNA Intermediate.

Following the optimized SA1 step, the block ionomer micelles consisting of a PCL shell layer and a pDNA-P2VP polyplex core are designated PCL-pDNA. Before proceeding with the SA2 step, the size and pDNA backbone integrity of the PCL-pDNA intermediate were characterized (Figure 2.4). First, the effective hydrodynamic size distribution in the SA1 solvent mixture was determined by dynamic light scattering (DLS, Figure 2.4A). The resulting CONTIN size distribution reveals a single particle population; the corresponding cumulant analysis gives a mean effective hydrodynamic diameter of $d_{h,eff}$ = 120 ± 8 nm, which includes both the condensed pDNA-P2VP polyplex core and the expanded PCL shell (Figure 2.4A).

We next investigated the degradation of pDNA following the optimized SA1 process. Before structural analysis by gel electrophoresis, pDNA was released from the block ionomer

micelles. To do this, functionalized pDNA was first isolated from the SA1 mixture by centrifugation then dispersed in chloroform, following the same procedure used for *FE* determination. Next, as shown in Figure 2.4B, a DI water layer was placed on top of the chloroform dispersion, followed by addition of pyridine to the chloroform layer. The two-phase mixture was then stirred for 3 hours, leading to deprotonation of P2VP pyridinium groups by the added pyridine; as a result, pDNA was released from the block ionomer micelles and extracted into the aqueous phase.

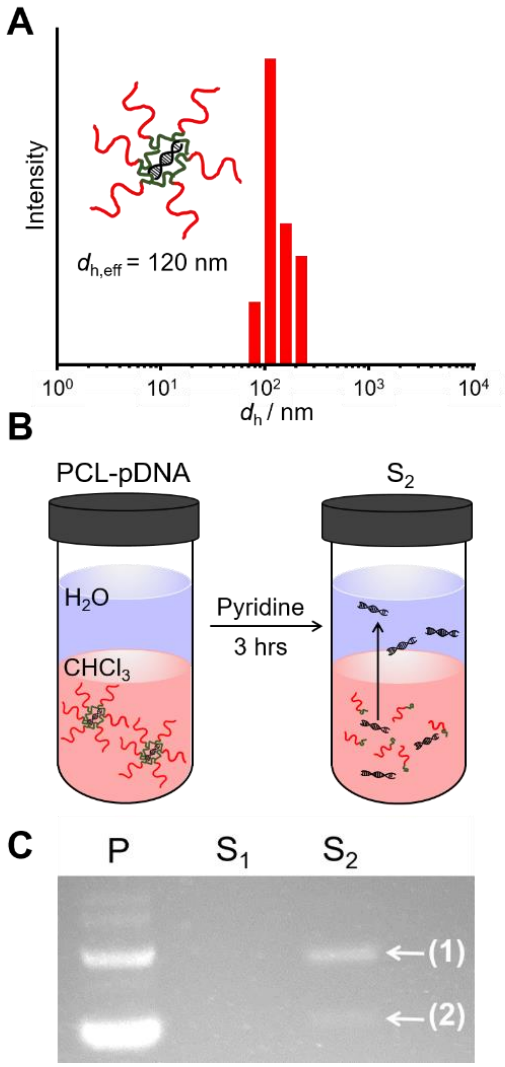

Figure 2.4. Characterization of PCL-pDNA block ionomer micelle intermediate. (A) DLS intensity distributions (CONTIN analysis) and mean effective hydrodynamic diameters, $d_{h,eff}$ (cumulant analysis) of PCL-pDNA in 70/30 dioxane/acetic acid (v/v) + 6.2 wt % water (SA1 solvent mixture). (B) Schematic describing method of release of pDNA from PCL-pDNA for gel electrophoresis characterization. (C) Gel electrophoresis of untreated pDNA standard (lane P), control sample (lane S_1), and pDNA released from PCL-pDNA (lane S_2). Both lanes P and S_2 show bands associated with open circular (1) and supercoiled (2) forms, confirming that no major degradation of pDNA occurs during SA1. However, the ratio of isoforms has changed.

The pDNA that had been released from PCL-pDNA (lane S_2, Figure 2.4C) was run on the gel alongside an untreated pDNA standard (lane P, Figure 2.4C) and a control sample (lane S_1) produced by stirring the two-phase mixture for only 30 min following pyridine addition. The presence of pDNA bands in lane S_2 but not in lane S_1 suggests that 30 min stirring with pyridine was not sufficient to release pDNA from the block ionomer micelles although 3 h stirring was sufficient. The two main bands of the pDNA standard (lane P), attributed to open circular (1) and supercoiled (2) forms, are also observed for pDNA released from PCL-pDNA (lane S_2). This indicates that the SA1 step did not degrade the functionalized pDNA such that the pDNA backbone remains intact. It does however appear that supercoiled isoform is lost to open circular.

2.3.4 Formation of PIHC Micelles from Self-Assembly of PCL-pDNA with PCL-b-PEG (SA2 Step).

Having confirmed the incorporation and integrity of the pDNA backbone and double helix within the intermediate PCL-pDNA (Figure 2.1A), we proceeded with the second self-assembly step. First, a dioxane solution containing PCL-*b*-PEG chains was added to the SA1 mixture. Then, water was added to above the critical water content using either the bulk or microfluidic method (Figure 2.5A) to initiate SA2 *via* co-condensation of PCL chains on PCL-pDNA and PCL-*b*-PEG components (Figure 2.1B). This microprecipitation process formed the desired structures, with cores containing the pDNA polyplex surrounded by a protecting matrix of condensed hydrophobic PCL chains. The resulting dispersions were dialyzed against DI water to remove organic solvents. Finally, unencapsulated pDNA was removed from the sample by a process of DNase I digestion, followed by several cycles of centrifugal filtration and washing (Figure 2.5B). The final particles following removal of unencapsulated pDNA are designated PIHC micelles. Recent work from our group has demonstrated significant effects of on-chip shear forces in two-phase microfluidic

reactors such as the one applied here (Figure 2.6) on the structure and function of polymer-based materials for nanomedicine materials.[31-37] Therefore, we were interested in comparing PIHC micelle samples prepared by the bulk and microfluidic SA2 processes in terms of their encapsulation efficiencies (*EE*), size distributions, and morphologies.

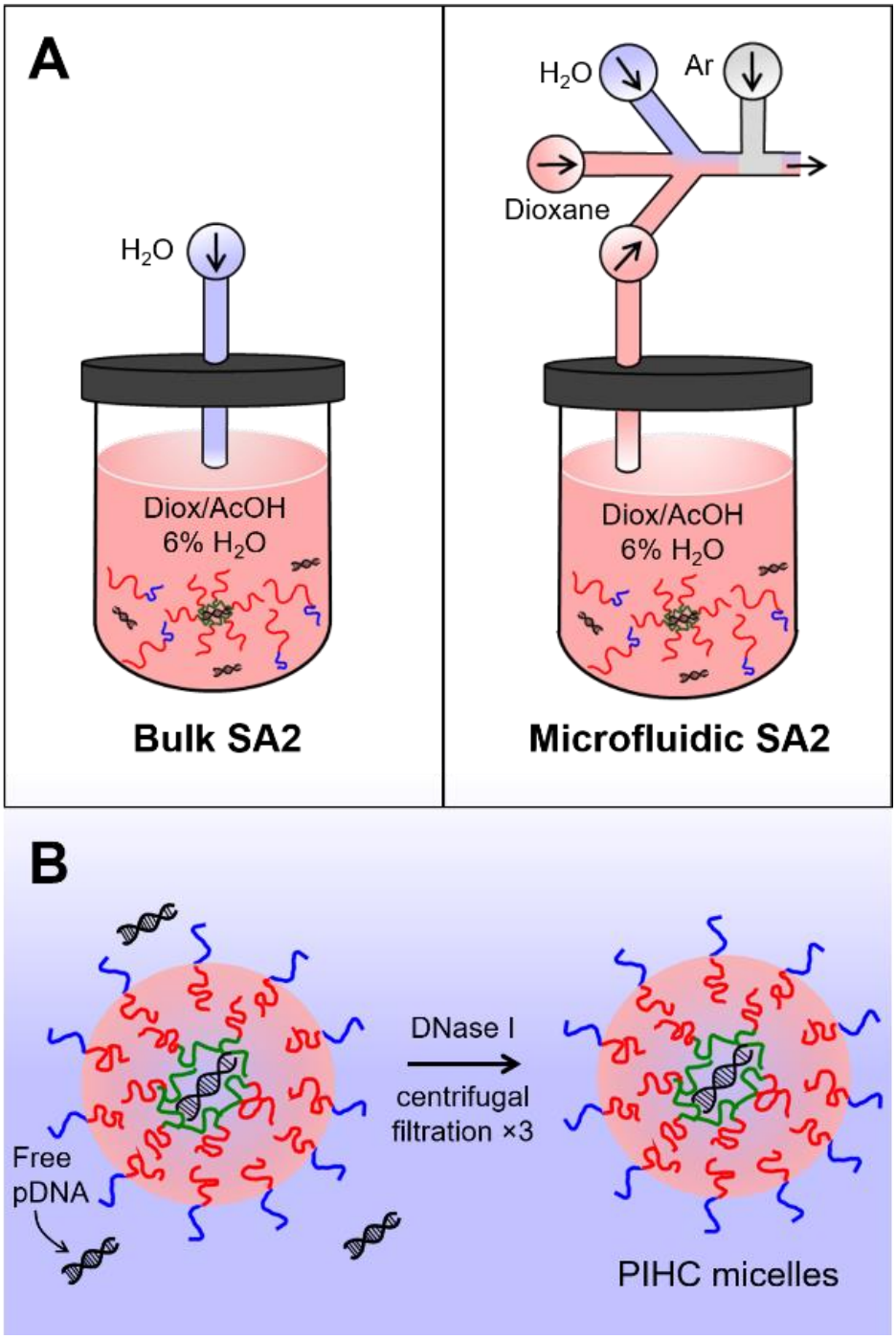

Figure 2.5. Schematics describing second self-assembly step (SA2) and subsequent workup to produce PIHC micelles. (A) Bulk (left) and microfluidic (right) methods for mixing copolymer/pDNA components with water to initiate SA2. (B) Removal of free pDNA from dialyzed suspensions by DNase I digestion and centrifugal filtration.

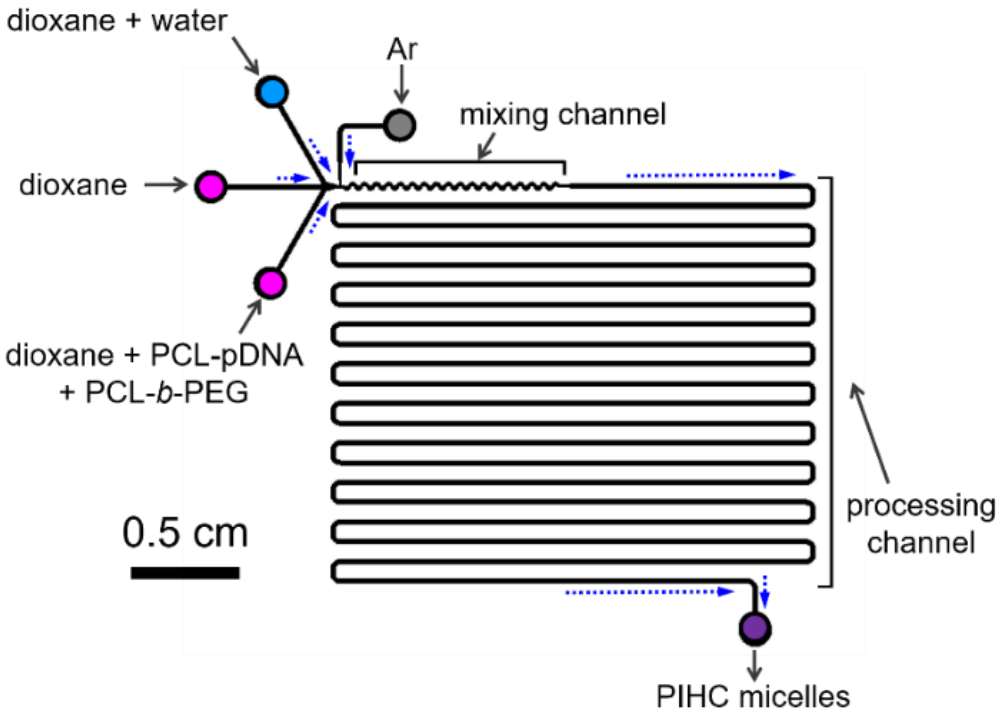

Figure 2.6. Schematic of two-phase microfluidic chip used for SA2 (microfluidic method).

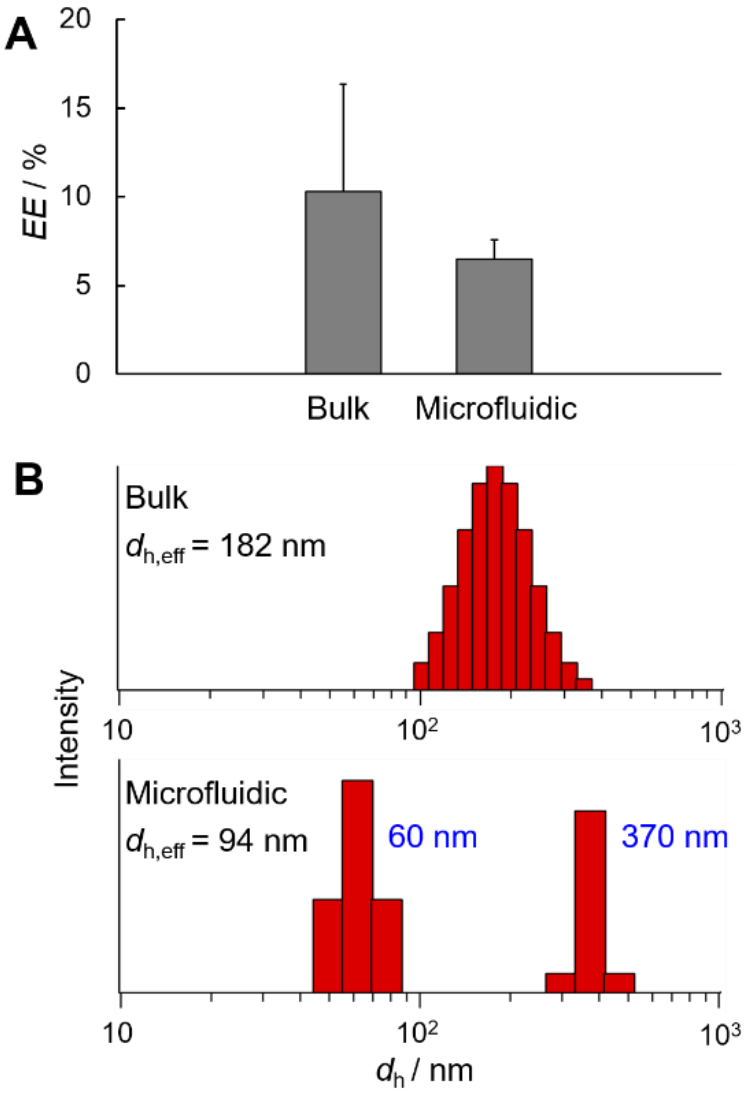

Figure 2.7. (A) Encapsulation efficiencies (*EE*) of PIHC micelles formed using bulk and microfluidic methods. Error bars were determined from triplicate preparations. (B) DLS intensity distributions (CONTIN analysis) and mean effective hydrodynamic diameters, $d_{h,eff}$ (cumulant analysis) of bulk (top) and microfluidic (bottom) PIHC micelles in deionized water. For PIHC micelles formed using the microfluidic method, the peak diameters of the small and large particle populations in the intensity distribution are 60 nm and 370 nm, respectively.

Encapsulation efficiencies (*EE*), determined from phosphate analysis of the PIHC micelles, describe the percentage of total initial pDNA (45 μg) that was encapsulated in the hydrophobic cores following both SA1 and SA2 steps. The mean *EE* values shown for bulk (10.7%) and microfluidic (6.5%) methods in Figure 2.7A were determined from triplicate preparations; despite the slightly higher mean *EE* value obtained using the bulk method, the variability of the method was significantly higher compared to the microfluidic approach, giving rise to a much larger experimental uncertainty. We attribute the greater reproducibility in *EE* values using the microfluidic method to improved control over mixing in the microfluidic channels.[38] In our determination of *EE*, we make the assumption that all pDNA that was not encapsulated in the hydrophobic cores was removed in the process of DNase I digestion, centrifugal filtration, and washing. To test this assumption, we carried out a phosphate assay of the negative control sample, which was prepared using the same steps, copolymers, and reagents as the PIHC micelle samples, except with the pDNA added *after* the SA2 step, such that the pDNA would remain outside the hydrophobic cores during DNase I digestion. No detectable phosphate was measured in the negative control, confirming that pDNA in both PIHC micelle samples was protected from DNase I digestion by its location *within* the hydrophobic cores of the micelles.

In Figure 2.7B, CONTIN size distributions and mean effective hydrodynamic diameters, $d_{h,eff}$, from DLS data are compared for bulk and microfluidic PIHC micelle preparations. In both cases, measured $d_{h,eff}$ values ($d_{h,eff}$ = 182 ± 2 nm for bulk and $d_{h,eff}$ = 94 ± 3 nm for microfluidic preparations) include the condensed PCL cores of PIHC micelles along with the solubilized PEG shells. Along with the larger mean size of the bulk sample, CONTIN analysis reveals that bulk PIHC micelle formation gives rise to a single broad size distribution (Figure 2.7B, *top*), compared to microfluidic formation which results in two separate populations of smaller (~60 nm) and larger

(~370 nm) particles (Figure 2.7B, *bottom*). The two populations in the microfluidic CONTIN size distribution (Figure 2.7B, *bottom*) are similar in intensity; however, these distributions are weighted according to scattered light intensity which strongly emphasizes larger particles in the distribution, suggesting that the number of ~60 nm particles strongly dominates over the number of ~370 nm particles. In fact, when the microfluidic CONTIN result in Figure 2.7B is converted to a number-weighted distribution (Figure S2.2, *Supporting Information*), the larger particle population disappears and only a single population of smaller particles is observed.

TEM images of the corresponding bulk and microfluidic samples (Figure 2.8) support the DLS analysis. Within the images, the uranyl acetate staining agent is selectively bonded to the PEG coronae such that the PCL cores appear bright. In the bulk sample, a broad distribution of irregularly shaped aggregates are observed (Figure 2.8A). In contrast, the microfluidic sample is comprised mainly of low-polydispersity spherical PIHC micelles with ~30-nm cores, along with a small number of large irregular aggregates (Figure 2.8B). The smaller size of the spherical PCL cores determined by TEM (~30 nm) compared to the hydrodynamic diameters determined by DLS (~60 nm) is consistent with a hydrated PEG layer of ~15 nm surrounding the PIHC micelles; this is about half the contour length of the 5k PEG chains (31.8 nm), suggesting that the coronal chains are ~50% extended.

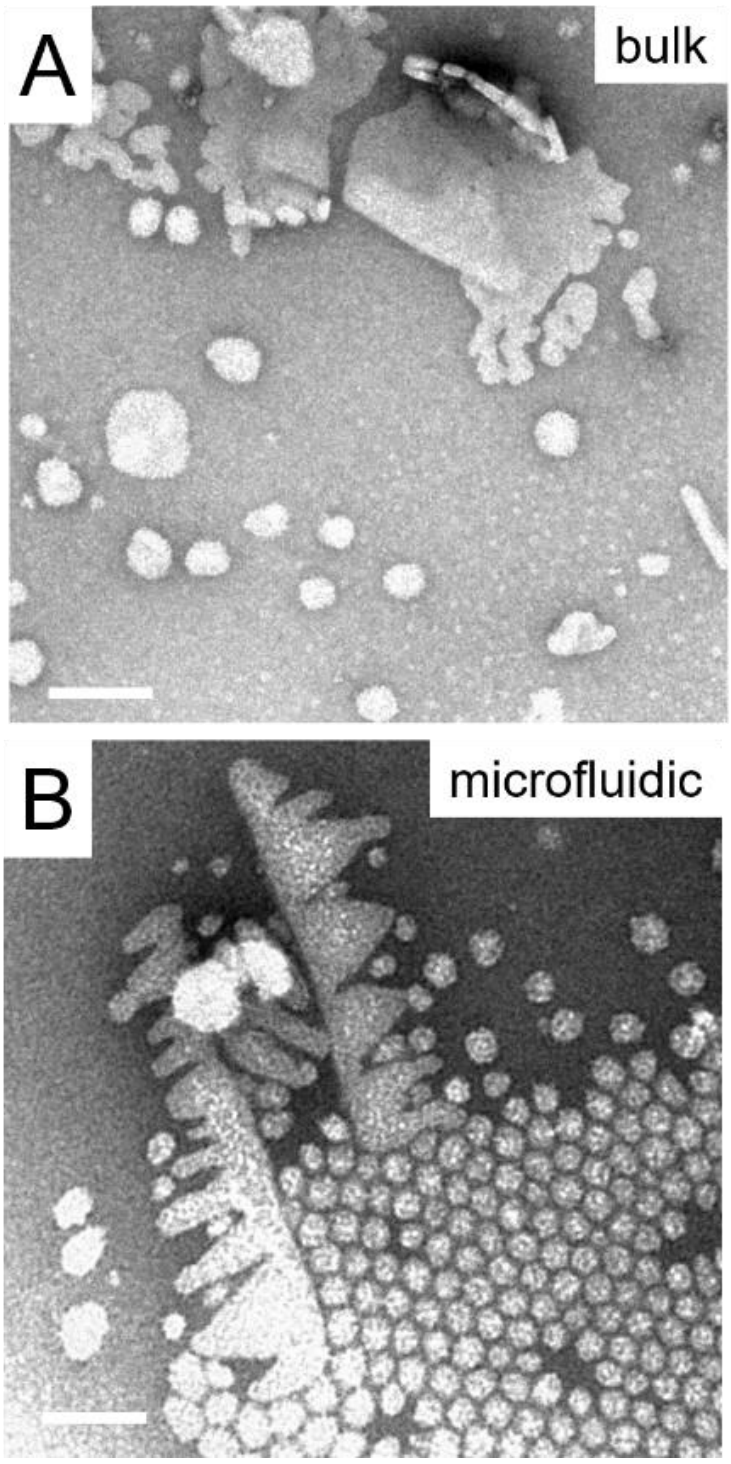

Figure 2.8. Transmission electron microscopy (TEM) images of PIHC micelles formed using the (A) bulk and (B) microfluidic methods. Scale bars are 100 nm.

We explain the contrasting size distributions and morphologies of the bulk and microfluidic PIHC micelle populations by considering the different SA2 self-assembly environments in the two cases. In the bulk SA2 case, water is added dropwise to the copolymer/pDNA mixture, with slow diffusional mixing leading to chemical heterogeneity throughout the sample as self-assembly occurs; this forms a broad distribution of aggregates which become kinetically trapped by slow chain dynamics as the water content increases. In contrast, the fast mixing[38] between water and the copolymer/pDNA stream in the microfluidic mixing channel (Figure 2.6) results in a homogenous chemical environment during the SA2 process, leading to a uniform population of spherical PIHC micelles. The subsequent exposure to high shear "hot spots"[39] in the processing channel (Figure 2.6) gives rise to an interplay of shear-induced coalescence and shear-induced breakup,[40] which could explain the presence of some larger non-spherical aggregates within the microfluidic sample. Another possibility is that the minor population of larger aggregates forms from excess individual PCL-*b*-PEG chains that do not co-assemble with PCL-pDNA in the SA2 process (Figure 2.1B). Based on the predominance of small, low-polydispersity spheres, which are favourable for cell uptake[37] and targeting,[7] in addition to the greater reproducibility of pDNA encapsulation, we selected the microfluidic preparation method for further analysis, including *in vitro* cell experiments.

We can estimate the pDNA occupancy of the micelles in the microfluidic PIHC micelle sample by making a few simplifying assumptions. First, based on the dominant spherical micelle population in the TEM images (Figure 2.8B), we assume that all of the PCL from both copolymer components assembles into 30-nm spherical cores; we calculate the core volume ($V = \frac{4}{3}\pi r^3$) to be V_{core} = 1.4 × 10^{-17} mL. Then, using a density value of 1.14 g/mL for the PCL cores,[41] we calculate the mass of the cores to m_{core} = 1.6 × 10^{-17} g. We next assume that no copolymer is lost

in the self-assembly, dialysis, and centrifugal filtration steps; this assumption, together with the total PCL mass added in both SA1 (0.100 mg) and SA2 (0.015 mg) steps (m_{PCL} = 0.115 × 10^{-3} g), allows us to estimate the number of spherical micelles in the sample: $N_{mic} = m_{PCL} / m_{core} = 7 \times 10^{12}$. Next, based on the initial mass of pDNA (45 μg) and the mean *EE* value for the microfluidic sample (6.5 %), we determine the total pDNA mass in the PIHC micelles to be $m_{pDNA} = 2.92 \times 10^{-6}$ g. Then, using this value and the molecular weight of pUC18 (M_{pDNA} = 1.75 × 10^6 g/mol), we estimate the number of encapsulated plasmids in the sample using: $N_{pDNA} = \frac{m_{pDNA}}{M_{pDNA}} \times N_A$, where $N_A = 6.02 \times 10^{23}$. This calculation gives $N_{pDNA} = 1 \times 10^{12}$, which, together with $N_{mic} = 7 \times 10^{12}$, yields a pDNA occupancy of 0.14, or about 1 plasmid per 7 micelles. This value should only be taken as a rough estimate; the pDNA occupancy may be much higher, considering possible polymer losses and/or partitioning of single copolymer chains into larger non-spherical aggregates.

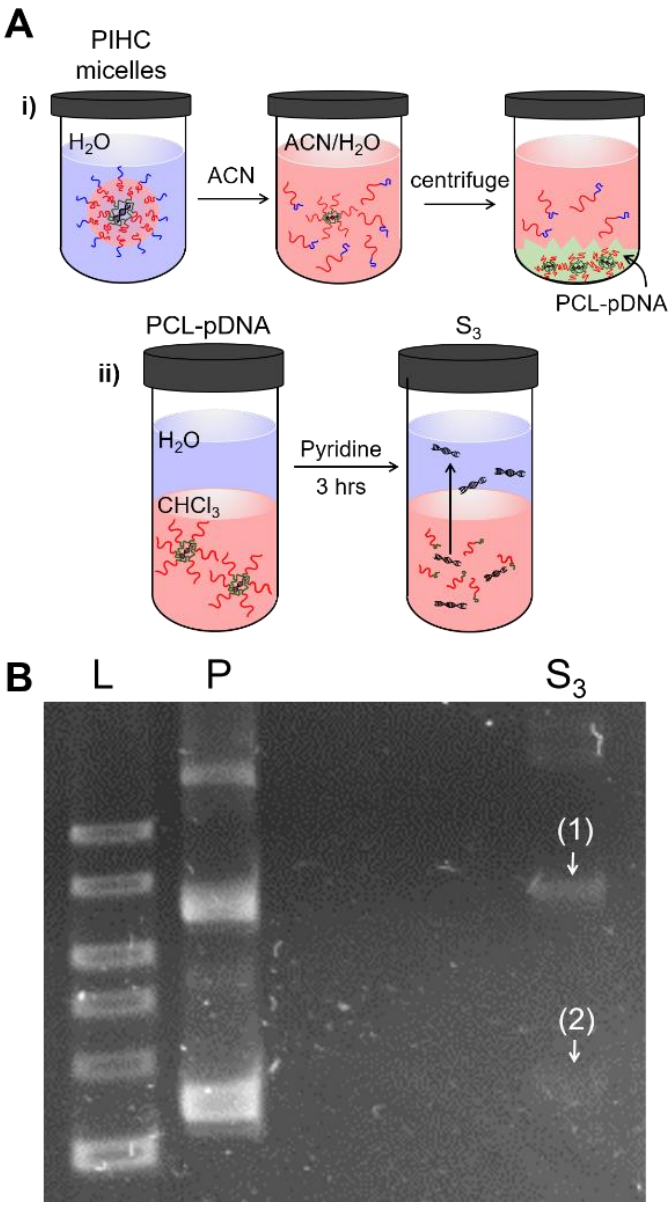

Figure 2.9. (A) Schematic describing the two-step method of release of pDNA from PIHC micelles: (i) PIHC micelle breakup and (ii) dissociation of block ionomer polyplex and extraction of free pDNA. (B) Gel electrophoresis of a 1kb DNA ladder (lane L), untreated pDNA standard (lane P), and pDNA released from PIHC micelles (lane S_3). Both lanes P and S_3 show bands associated open circular (1) and supercoiled (2) forms, confirming that little degradation of pDNA occurs during SA1 and SA2.

In order to confirm the structural integrity of the pDNA backbone and double helix following SA2 self-assembly, we released encapsulated pDNA in a two-step process. First, acetonitrile was added to the microfluidic dispersion, leading to PCL dissolution and concomitant PIHC micelle breakup (Figure 2.9A, i). Next, the constituent block ionomer polyplexes were recovered by centrifugation, dispersed in chloroform, then disassembled by addition of pyridine and extraction of free pDNA into an aqueous layer (Figure 2.9A, ii). The resulting pDNA (lane S_3, Figure 2.9B) was run on a gel with the untreated pDNA standard (lane P) and a 1kb DNA ladder (lane L). Similar to pDNA release following the SA1 step, we find that the two main bands of the pDNA standard (lane P), attributed to open circular (1) and supercoiled (2) forms, are present following SA2 self-assembly (lane S_3). This confirms that neither SA1 nor SA2 steps resulted in degradation of encapsulated pDNA.

2.3.5 Bacterial Cell Transformation.

To investigate the functionality and timed release of pDNA from PIHC micelles, we carried out transformation experiments on competent *E.coli* K12 cells. Figure 2.10 shows transformation efficiencies as functions of incubation time for the microfluidic PIHC micelle sample along with the negative and positive controls. The negative control consisted of nanoparticles produced in the same manner as PIHC micelle formation except with pDNA added *after* SA2 assembly, such that pDNA was not encapsulated during DNase I exposure. The positive control consisted of free pDNA that was exposed to the same solvents, dialysis and centrifugal filtration as encapsulated pDNA except without the addition of copolymers and without DNase I exposure.

As shown in Figure 2.10, no transformants were observed for the negative control at any incubation time up to 8 h (red data points). This indicates that DNase I exposure precluded

subsequent transformation when pDNA was not encapsulated *within* the hydrophobic cores of the accompanying copolymer nanoparticles; we attribute this result to complete degradation of unencapsulated pDNA by DNase I, as supported by phosphate assay results for the negative control (discussed previously). On the other hand, significant bacterial transformation was found for the positive control (blue data points), which increased between 1 h and 3 h of incubation but then leveled off with no further increase measured after 8 h of incubation. This result confirms the functionality of free pDNA without DNAase I exposure; it also indicates some time dependence of bacterial transformation by free pDNA in the first 3 h of incubation but negligible time dependence in the subsequent 5 h of incubation. Compared to the positive control, the PIHC micelle sample (black data points, with dashed linear trendline) showed dramatically higher transformation efficiencies at all time points (up to 12× higher after 8 h of incubation). It also showed a much stronger positive time dependence over the entire 8 h incubation period.

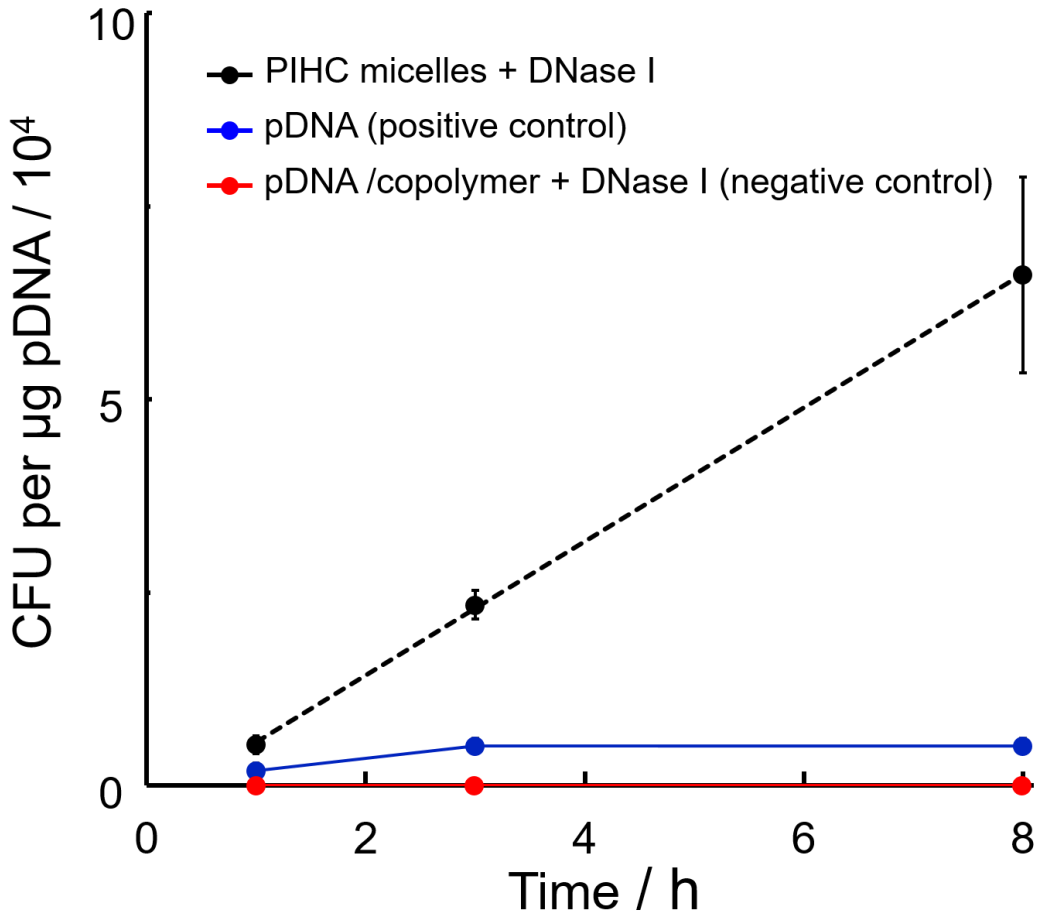

Figure 2.10. Transformation efficiencies versus incubation time for competent *E. coli* K12 treated with PIHC micelles (black data points and dashed linear trendline), positive control (blue data

points), and negative control (red data points). Positive and negative controls are described in the text. Blue and red lines are guides for the eye.

The higher transformation efficiencies of PIHC micelles compared to the free plasmid may be related to a lowering of energy barriers for uptake by the competent cells, due to a combination of lower charge and smaller hydrodynamic diameter (~60 nm) of the spherical micelles compared to uncondensed pUC18 (140-160 nm).[42] A similar ~10-fold increase in transformation efficiencies of competent *E. coli* was previously found for pDNA complexed to Fe_3O_4 nanoparticles, although the authors did not propose a mechanism in that study.[43] Since the primary goals of the bacterial transformation experiments were to investigate functionality and timed release of encapsulated pDNA following DNase I exposure, further investigation of the mechanism of transformation enhancement was beyond the scope of this study. Of particular interest for future use of PIHC micelles as vectors for mammalian cell transfection is the slow and controlled activation of pDNA in the cellular environment, characterized by the observed increase in transformation over 8 h, in contrast to free pDNA which showed no increase in activity after 3 h. We attribute this time dependence to the location of the pDNA-P2VP polyplex within the micellar PCL cores, such that pDNA release within the cell requires hydrolytic degradation of the surrounding matrix of PCL chains.[31,44] We note that the transformation efficiency should level off once all of the plasmids within the PIHC micelles have been released, suggesting that pDNA release was not completed after 8 h of incubation. Such slow release of pDNA from PICH micelles could open up novel pathways to controlled cell transfection triggered by external chemical and physical stimuli that increase rates of degradation or melting of the semicrystalline PCL core.

2.3.6 Uptake of PIHC Micelles into MDA-MB-231 Cells.

Finally, we investigated uptake of PIHC micelles by MDA-MB-231 (human breast cancer) cells using fluorescence microscopy (Figure 2.11). The PIHC micelles used for these experiments were labelled with two different fluorescent dyes during synthesis: 1. DAPI is a DNA-intercalating dye that was used to selectively label the pDNA and 2. DiI is a hydrophobic dye that was used to label the PCL cores. The cytosolic regions of the MDA-MB-231 cells were also labelled with fluorescein diacetate. A comparison of data in Figure 2.11B (blue fluorescence from DAPI-labeled pDNA) and Figure 2.11C (red fluorescence from DiI-labeled micelles) confirmed that plasmid DNA was successfully delivered to many of the target cells. We also note that all cells that were positive for pDNA (blue florescence) also showed the presence of lipophilic polymer (red fluorescence)— consistent with the proposed PIHC-based delivery mechanism.

Figure 2.11E shows an overlay of blue fluorescence from DAPI-labeled pDNA with red fluorescence from DiI-labeled micelles. The overlaid data reveals a lack of co-localization between the two species, which suggests that at least some of the pDNA has escaped the delivery vehicle during the 4 hour incubation period. Taken together, the data in Figure 2.11 strongly support the potential for PIHC micelles to deliver genetic cargo to mammalian cells. The incubation temperature for the growth of these cells corresponds to the temperature where PCL begins fast hydrolytic degradation. So, it is likely that particles are breaking down and releasing their contents in the cell. [44]

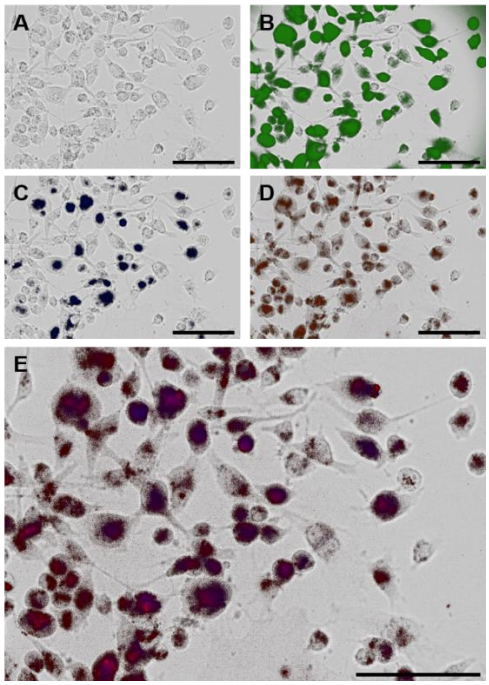

Figure 2.11. Fluorescence imaging data showing penetration of DAPI/DiI-labeled PIHC micelles into MDA-MB-231 cells. Encapsulated pDNA was labelled with DAPI (blue) and PCL cores of the micelles were labelled with DiI (red). The cells were counterstained with fluorescein diacetate (green) to identify the cytosolic compartment. (A) Bright-field image of MDA-MB-231 cells used for the experiment. (B) Overlay of background-subtracted green channel fluorescence

(fluorescein) with bright-field image, confirming cellular integrity. (C) Overlay of background-subtracted blue fluorescence (DAPI) with bright-field image, confirming the presence of pDNA in many, but not all of the target cells. (D) Overlay of background-subtracted red fluorescence (DiI) with bright-field image, confirming the presence of micelles within cytosolic regions of the cells. The greater cellular occupancy of DiI-labeled micelles compared with DAPI-labeled pDNA is consistent with the calculated 1:7 occupancy of plasmids within polymer micelles. (E) Overlay of DAPI and DiI fluorescence with bright-field image, indicating that DAPI-labeled pDNA does not co-localize with DiI-labeled micelles following 4 hours of incubation time in which plasmid DNA can escape from internalized polymer micelles. Unfortunately the release time is on the order of PCL-b-PEO micelle degradation and thus there may be leakage of dyes from micelles resulting in uncharacteristic DAPI / DiI staining.Scale bars are 100 μm.

2.4 Conclusions

We have applied a hierarchical block copolymer self-assembly approach to produce for the first time “polyplex in hydrophobic core” (PIHC) micelles as non-viral vectors for gene delivery. The PIHC micelle structure is generated through a simple, two-step self-assembly process starting with electrostatic binding between the nucleic acid cargo and a PCL-*b*-P2VP block copolymer (SA1), followed by microprecipitation with a PCL-*b*-PEG block copolymer (SA2) to form micelles with PEG coronae and nucleic acid-P2VP polyplexes embedded within condensed PCL hydrophobic cores. As a proof-of-concept, we produced PIHC micelles containing the plasmid pUC18 following optimization of SA1 and SA2 steps; using microfluidic mixing for the SA2 step, we generated mainly spherical PIHC micelles with ~30-nm PCL cores and ~60-nm hydrodynamic diameters. Encapsulated plasmids showed resistance to DNase I degradation compared to a negative control in which plasmids were located outside the micelle cores. In bacterial

transformation experiments, PIHC micelles showed enhanced activity compared to unencapsulated plasmids along with a linear time dependence over 8 h of incubation time, associated with slow release *via* hydrolytic degradation of PCL cores. PIHC micelles were also readily taken up by MDA-MB-231 (human breast cancer) cells, suggesting feasibility for mammalian cell transfection experiments. These results demonstrate that the PIHC micelle structure provides excellent nuclease protection and controlled release by embedding nucleic acids in a surrounding matrix of condense hydrophobic polymer chains. Moreover, the hierarchical self-assembly approach demonstrated here produces structural and functional complexity in non-viral gene delivery vectors using commercially available block copolymers, without the need for complicated synthetic methodologies.

2.5 References

1. Dunbar, C. E.; High, K. A.; Joung, J. K.; Kohn, D. B.; Ozawa, K.; Sadelain, M. Gene therapy comes of age. *Science.* **359**, eaan4672 (2018).

2. Hardee, C. L.; Arevalo-Soliz, L. M.; Hornstein, B. D.; Zechiedrich, L. Advances in non-viral DNA vectors for gene therapy. *Genes* **8**, 65 (2017).

3. Xiang, Y. G.; Oo, N. N. L.; Lee, J. P.; Li, Z. B.; Loh, X. J. Recent development of synthetic nonviral systems for sustained gene delivery. *Drug Discov. Today* **22**, 1318-1335 (2017).

4. Pereira-Silva, M.; Jarak, I.; Alvarez-Lorenzo, C.; Concheiro, A.; Santos, A. C.; Veiga, F.; Figueiras, A. Micelleplexes as nucleic acid delivery systems for cancer-targeted therapies. *J. Controlled Release.* **323,** 442-462 (2020).

5. Li, S.; Huang, L. Nonviral gene therapy: Promises and challenges. *Gene Ther.* **7**, 31-34 (2000).

6. Li, L.; He, Z.-Y.; Wei, X.-W.; Gao, G.-P.; Wei, Y.-Q. Challenges in CRISPR/CAS9 delivery: Potential roles of nonviral vectors. *Hum. Gene Ther.* **26**, 452-462 (2015).

7. Elsabahy, M.; Wooley, K. L. Design of polymeric nanoparticles for biomedical delivery applications. *Chem. Soc. Rev.* **41**, 2545-2561 (2012).

8. Fliervoet, L. A. L.; Engbersen, J. F. J.; Schiffelers, R. M.; Hennink, W. E.; Vermonden, T. Polymers and hydrogels for local nucleic acid delivery. *J. Mater. Chem. B.* ***6,*** 5651-5670 (2018).

9. Cabral, H.; Miyata, K.; Osada, K.; Kataoka, K. Block Copolymer micelles in nanomedicine applications. *Chem. Rev.* **118**, 6844-6892 (2018).

10. Chen, C. K.; Huang, P. K.; Law, W. C.; Chu, C. H.; Chen, N. T.; Lo, L. W. Biodegradable polymers for gene-delivery applications. *Int. J. Nanomed.* **15**, 2131-2150 (2020).

11. Salameh, J. W.; Zhou, L.; Ward, S. M.; Santa Chalarca, C. F.; Emrick, T.; Figueiredo, M. L. Polymer-mediated gene therapy: Recent advances and merging of delivery techniques. *Wires Nanomed. Nanobi.* **12**, e1598 (2020).

12. Uchida, S.; Kataoka, K. Design concepts of polyplex micelles for in vivo therapeutic delivery of plasmid DNA and messenger RNA. *J. Biomed. Mater. Res. A.* **107**, 978-990 (2019).

13.. Kargaard, A.; Sluijter, J. P. G.; Klumperman, B. Polymeric siRNA gene delivery: transfection efficiency versus cytotoxicity. *J. Controlled Release*. **316**, 263-291 (2019).

14. Kim, H. J.; Kim, A.; Miyata, K.; Kataoka, K. Recent progress in development of siRNA delivery vehicles for cancer therapy. *Adv. Drug Deliver. Rev.* **104**, 61-77 (2016),

15. Endres, T. K.; Beck-Broichsitter, M.; Samsonova, O.; Renette, T.; Kissel, T. H. Self-assembled biodegradable amphiphilic PEG-PCL-lPEI triblock copolymers at the borderline between micelles and nanoparticles designed for drug and gene delivery. *Biomaterials*. **32**, 7721-7731 (2011).

16. Cao, N.; Cheng, D.; Zou, S. Y.; Ai, H.; Gao, J. M.; Shuai, X. T. The synergistic effect of hierarchical assemblies of siRNA and chemotherapeutic drugs co-delivered into hepatic cancer cells. *Biomaterials*. **32**, 2222-2232 (2011).

17. Cheng, D.; Cao, N.; Chen, J. F.; Yu, X. S.; Shuai, X. T. Multifunctional nanocarrier mediated co-delivery of doxorubicin and siRNA for synergistic enhancement of glioma apoptosis in rat. *Biomaterials*. **33,** 1170-1179 (2012).

18. Endres, T.; Zheng, M. Y.; Kilic, A.; Turowska, A.; Beck-Broichsitter, M.; Renz, H.; Merkel, O. M.; Kissel, T. Amphiphilic biodegradable PEG-PCL-PEI triblock copolymers for FRET-capable in vitro and in vivo delivery of siRNA and quantum dots. *Mol. Pharm.* **11,** 1273-1281 (2014).

19. Wu, Y.; Zhang, Y.; Zhang, W.; Sun, C. L.; Wu, J. Z.; Tang, J. H. Reversing of multidrug resistance breast cancer by co-delivery of P-gp siRNA and doxorubicin via folic acid-modified core-shell nanomicelles. *Colloid Surface B.* **138,** 60-69 (2016).

20. Lin, D. S.; Jiang, Q.; Cheng, Q.; Huang, Y. Y.; Huang, P. S.; Han, S. C.; Guo, S. T.; Liang, Z. C.; Dong, A. J. Polycation-detachable nanoparticles self-assembled from mPEG-PCL-*g*-SS-PDMAEMA for in vitro and in vivo siRNA delivery. *Acta Biomater.* **9**, 7746-7757 (2013).

21. Lee, S. Y.; Yang, C. Y.; Peng, C. L.; Wei, M. F.; Chen, K. C.; Yao, C. J.; Shieh, M. J. A Theranostic micelleplex co-delivering SN-38 and VEGF siRNA for colorectal cancer therapy. *Biomaterials*. **86**, 92-105 (2016).

22. Osawa, S.; Osada, K.; Hiki, S.; Dirisala, A.; Ishii, T.; Kataoka, K. Polyplex micelles with double-protective compartments of hydrophilic shell and thermoswitchable palisade of poly(oxazoline)-based block copolymers for promoted gene transfection. *Biomacromolecules*. **17**, 354-361 (2016).

23. Chen, M. H.; Zhang, Y.; Chen, Z. J.; Xie, S. Z.; Luo, X. M.; Li, X. H. Synergistic antitumor efficacy of redox and pH dually responsive micelleplexes for co-delivery of camptothecin and genes. *Acta Biomater.* **49**, 444-455 (2017).

24. Grossen, P.; Witzigmann, D.; Sieber, S.; Huwyler, J. PEG-PCL-based nanomedicines: A biodegradable drug delivery system and its application. *J. Controlled Release*. **260**, 46-60 (2017).

25. Huff, J.; Grant, B.; Penning, C.; Sullivan, K. Optimization of routine transformation of escherichia coli with plasmid DNA. *BioTechniques*. **9**, 570-572, 574, 576 (1990).

26. West, S.; Schweizer, H.; Dall, C.; Sample, A.; Runyen-Janecky, L. Construction of improved escherichia-pseudomonas shuttle vectors derived from pUC18/19 and sequence of the region required for their replication in pseudomonas aeruginosa. *Gene*. **148**, 81-86 (1994).

27. Yokoya, A.; Shikazono, N.; Fujii, K.; Urushibara, A.; Akamatsu, K.; Watanabe, R. DNA damage induced by the direct effect of radiation. *Radiat. Phys. Chem.* **77**, 1280-1285 (2008).

28. Yoshida, N.; Sato, M. Plasmid uptake by bacteria: A comparison of methods and efficiencies. *Appl. Microbiol. Biotechnol.* **83**, 791-798 (2009).

29. Nazemi, A.; Boott, C. E.; Lunn, D. J.; Gwyther, J.; Hayward, D. W.; Richardson, R. M.; Winnik, M. A.; Manners, I. Monodisperse cylindrical micelles and block comicelles of controlled length in aqueous media. *J. Am. Chem. Soc.* **138**, 4484-4493 (2016).

30. Danielsen, S.; Maurstad, G.; Stokke, B. T. DNA–polycation complexation and polyplex stability in the presence of competing polyanions. *Biopolymers*. **77**, 86-97 (2005).

31. Bains, A.; Wulff, J. E.; Moffitt, M. G. Microfluidic synthesis of dye-loaded polycaprolactone-*block*-poly (ethylene oxide) nanoparticles: Insights into flow-directed loading and in vitro release for drug delivery. *J. Colloid Interf. Sci.* **475**, 136-148 (2016).

32. Bains, A.; Cao, Y. M.; Kly, S.; Wulff, J. E.; Moffitt, M. G. Controlling structure and function of polymeric drug delivery nanoparticles using microfluidics. *Mol. Pharm.* **14**, 2595–2606 (2017).

33. Cao, Y.; Silverman, L.; Lu, C.; Hof, R.; Wulff, J. E.; Moffitt, M. G. Microfluidic manufacturing of SN-38-loaded polymer nanoparticles with shear processing control of drug delivery properties. *Mol. Pharm.* **16**, 96-107 (2018).

34. Chen, R.; Wulff, J. E.; Moffitt, M. G. Microfluidic processing approach to controlling drug delivery properties of curcumin-loaded block copolymer nanoparticles. *Mol. Pharm.* **15**, 4517-4528. (2018).

35. Jensen, D.; Cao, Y.; Lu, C.; Wulff, J. E.; Moffitt, M. G. Microfluidic encapsulation of SN-38 in Block copolymer nanoparticles: Effect of hydrophobic block composition on loading and release properties. *Can. J. Chem.* **97**, 337-343 (2019).

36. Huang, Y.; Moini Jazani, A.; Howell, E. P.; Oh, J. K.; Moffitt, M. G. Controlled microfluidic synthesis of biological stimuli-responsive polymer nanoparticles. *ACS Appl. Mater. Interfaces*. **12**, 177-190 (2019).

37. Huang, Y.; Jazani, A. M.; Howell, E. P.; Reynolds, L. A.; Oh, J. K.; Moffitt, M. G. Microfluidic shear processing control of biological reduction stimuli-responsive polymer nanoparticles for drug delivery. *ACS Biomater. Sci. Eng.* **6**, 5069-5083 (2020).

38. Schabas, G.; Wang, C. W.; Oskooei, A.; Yusuf, H.; Moffitt, M. G.; Sinton, D. Formation and shear-induced processing of quantum dot colloidal assemblies in a multiphase microfluidic chip. *Langmuir*. **24**, 10596-10603 (2008).

39. Wang, C. W.; Oskooei, A.; Sinton, D.; Moffitt, M. G. Controlled self-assembly of quantum dot-block copolymer colloids in multiphase microfluidic reactors. *Langmuir*. **26**, 716-723 (2010).

40. Wang, C. W.; Sinton, D.; Moffitt, M. G. Morphological control via chemical and shear forces in block copolymer self-assembly in the lab-on-chip. *ACS Nano*. **7**, 1424-1436 (2013).

41. Rosa, D.; Neto, I. C.; Calil, M.; Pedroso, A.; Fonseca, C.; Neves, S. Evaluation of the thermal and mechanical properties of poly(ε-caprolactone), low-density polyethylene, and their blends. *J. Appl. Polym. Sci.* **91**, 3909-3914 (2004).

42. Tsoi, M.; Do, T. T.; Tang, V.; Aguilera, J. A.; Perry, C. C.; Milligan, J. R. Characterization of condensed plasmid DNA models for studying the direct effect of ionizing radiation. *Biophys. Chem.* **147**, 104-110 (2010).

43. Saei, A. A.; Barzegari, A.; Majd, M. H.; Asgari, D.; Omidi, Y. Fe_3O_4 Nanoparticles engineered for plasmid DNA delivery to Escherichia coli. *J. Nanopart. Res.* **16**, 1-11 (2014).

44. Geng, Y.; Discher, D. E. Hydrolytic Degradation of poly(ethylene oxide)-block-polycaprolactone worm micelles. *J. Am. Chem. Soc.* **127**, 12780-12781 (2005).

45. Bartlett, G. R. Phosphorus assay in column chromatography. *J. Biol. Chem.* **234**, 466-468 (1959).

46. Maples, R. E.: *Petroleum Refinery Process Economics*. (Pennwell books, 2000).

47. Reis, J. C. R.; Lampreia, I. M.; Santos, Â. F.; Moita, M. L. C.; Douhéret, G. Refractive index of liquid mixtures: Theory and experiment. *ChemPhysChem*. **11**, 3722-3733 (2010).

Chapter 3

Polymer Brush-Directed Encapsulation of Gold Nanoparticles within Polycaprolactone-*block*-Poly(ethylene glycol) Micelles and Enhanced of Cellular Uptake

Contributions: This chapter has been modified from the submitted version of a paper to include experiments undertaken at the suggestion of reviewers. Sundiata Kly and Matt Moffitt conceived the experiments; Sundiata Kly and Zach Snow conducted the experiments; Sundiata Kly and Matt Moffitt analyzed the data; Yuhang Huang assisted with figure preparation; Matt Moffitt and Sundiata Kly wrote the chapter.

3.1 Introduction

Gold nanoparticles (GNPs) have generated wide spread interest to be included in the nanomedicine toolbox for both imaging and treatment of cancer, due to their range of interesting optical and physicochemical properties, well-established synthetic methods, and low toxicities.[1-6] For example, surface plasmons generated when GNPs interact with light can produce intense localized heating for the photothermal treatment of cancers.[1,2,4,7] In addition, GNPs have been applied as effective sensitizers for radiotherapy; the interaction of radiation with GNPs generates secondary electrons that can cause direct and indirect damage (via free radical formation) to cancer cells.[8,9] For diagnostic applications, the various properties of GNPs make them effective contrast agents for a number of different imaging modalities.[3] For example, the high electron attenuation coefficient of GNPs provide the required contrast for CT imaging within soft tissues.[1,3,6]

The encapsulation of GNPs (1-50 nm) within larger, block copolymer-based micellar polymer nanoparticles (PNPs, 50-200 nm) offers a number of advantages for biomedical applications, including improved stability, reduced toxicity, and ease of functionalization for active targeting.[2,10] Moreover, by controlling the sizes of PNP carriers, a number of size-dependent biological barriers that limit the utility of small, unencapsulated GNPs can be overcome, improving circulation times, biodistributions, and cell uptake.[11] For instance, carriers with sizes in the range

of 50-200 nm can avoid the rapid clearance pathways experienced by much smaller particles, eventually localizing in cancerous tumours by EPR effects.[11] In addition, it has been demonstrated that GNP cell uptake is optimized in the size regime of ~50 nm,[12] such that encapsulation within PNPs could enhance the uptake of smaller GNPs. Moreover, there is some evidence that smaller GNPs are excreted more efficiently than larger GNPs;[11,13] therefore, PNPs containing many small GNPs could deliver effective gold quantities for the desired application, while allowing for subsequent fast clearance by the patient.[11] Finally, the hydrophobic cores of PNP carriers provide opportunities for co-encapsulating GNPs with anticancer drugs or other inorganic nanoparticles for combined therapy or theranostic applications.[14,15]

In addition to the advantages described above, encapsulation of GNPs within polymeric carriers may also provide more efficient routes to cellular uptake. In different studies, it has been demonstrated that GNP cell uptake is optimized in the size regime of 20-50 nm,[15,16] such that encapsulation within PNPs could enhance the uptake of smaller GNPs by increasing their effective size. It has further been shown that the elasticity of nanoparticles is an important factor in cell uptake via macrophage phagocytosis and receptor-mediated endocytosis;[17] this effect could positively or negatively affect the uptake of encapsulated GNPs, depending on the material properties of the encapsulating vector. Encapsulation also provides ease of functionalization through an outer polymer layer, which could be used to enhance uptake through addition of peptides and small molecules that trigger endocytosis.[18,19] Finally, the ability to encapsulate multiple GNPs within a single PNP vector could provide an inherent advantage for increasing the efficiency of cell uptake; however, to our knowledge, the effect of GNP occupancy (number of GNPs per PNP vector) on the cellular uptake of GNPs has not been previously studied.

Polycaprolactone (PCL)-based amphiphilic block copolymers are widely applied as excipients in drug delivery and other biomedical applications,[20,21] including the encapsulation of GNPs.[11,13,22-35] PCL is a hydrophobic aliphatic polyester which undergoes hydrolytic degradation under physiological conditions, making it an excellent *in vivo* host for nanoparticles and therapeutic molecules.[20,21,36-38] To date, two general strategies have been applied for encapsulating GNPs within the hydrophobic cores of PCL-based amphiphilic block copolymers. In the first strategy, block copolymers with thiol-terminated PCL blocks are conjugated to GNPs through S-Au bonds, leading to PNPs consisting of a single GNP surrounded by a condensed layer of PCL with an outer shell of solubilized poly(ethylene glycol) (PEG) or other hydrophilic blocks or multiblocks.[13,23-34] Since the block copolymers act as ligands attached to individual GNPs, this strategy lowers the probability for the encapsulation of multiple small GNPs within a single PNP carrier at the low concentrations of GNPs typically used in synthesis. The second strategy involves encapsulation of GNPs stabilized by dodecanethiol ligands within the hydrophobic cores of PCL-*b*-PEG block copolymers.[11,35] Unlike the previous strategy, this approach produces PNPs containing multiple GNPs, although the limited intrinsic solubility of dodecanethiol-capped GNPs within the PCL cores necessitates special mixing or purification steps to obtain size-controlled PNPs. For example, Prud'homme and coworkers utilized flash nanoprecipitation in a multi-inlet vortex mixer, in order to kinetically trap dodecanethiol-capped GNPs within the cores of PCL-*b*-PEG PNPs.[35] In another example, the Tsourkas group used a similar PCL-*b*-PEG copolymer but applied a microemulsion method to encapsulate multiple dodecanethiol-capped, 1.9-nm GNPs within hydrophobic PNP cores; this method required subsequent size purification using differential centrifugation in order to obtain size-controlled samples of low polydispersity.[11] In addition, the

dodecanethiol ligands employed in both of these studies may contribute to cytotoxicity in some applications.[39]

In this work, we combine a two-step assembly strategy with flow-variable microfluidic mixing to produce hierarchical PNPs containing multiple GNPs encapsulated within PCL cores and surrounded by a PEG shell. The step-wise process generates structural hierarchy using commercially available polymer materials, without the need for complex synthetic methodologies. In the first step, GNPs are functionalized with a brush layer of PCL chains by reaction with thiol-terminated PCL ligands to produce PCL-GNPs (Figure 3.1A). In the second step, PCL-GNPs are co-dissolved with PCL-*b*-PEG in dimethylformamide (DMF), followed by water addition and nanoprecipitation to yield GNP-PNPs (Figure 3.1B). The PCL brush layers formed in the first step increase the compatibility of GNPs with the PCL blocks of PCL-*b*-PEG, directing their encapsulation within the PCL cores of micellar PNPs under both bulk and microfluidic mixing conditions. Moreover, flow-tunable shear provides variability of PNP size and encapsulation state when the second step is carried out in a two-phase microfluidic mixer, allowing a unique series of samples with different distributions of GNPs throughout the PNP populations to be produced. By comparing uptake of these various GNP vectors by MDA-MB-231 cancer cells with statistical analysis of TEM data, we show for the first time that encapsulation of multiple GNPs per PNP vector enhances gold uptake compared to vectors containing an average of 1 or fewer GNPs.

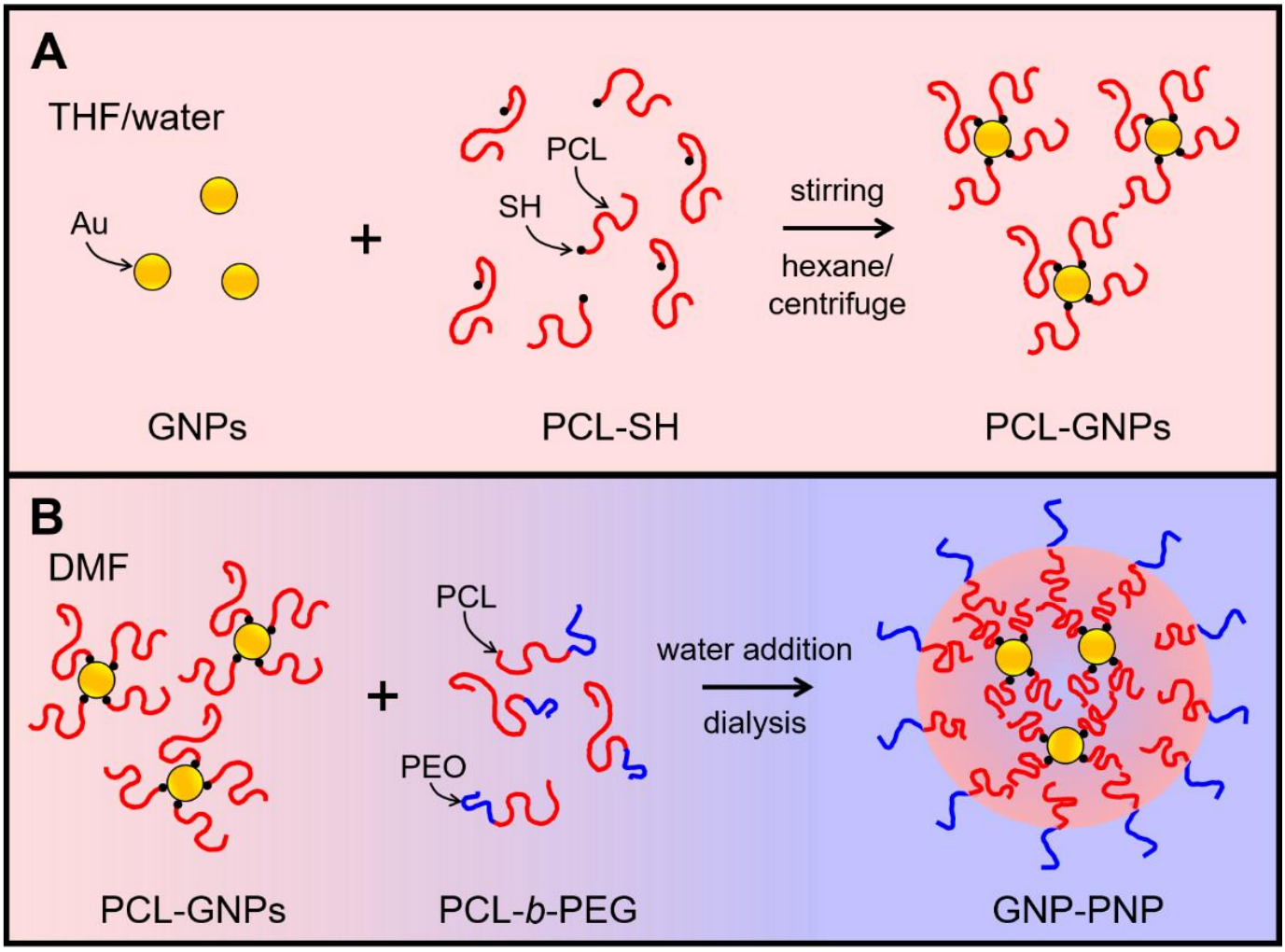

Figure 3.1. Schematic of the two-step brush-directed encapsulation strategy, showing (A) functionalization of GNPs with PCL-SH to form PCL-brush functionalized PCL-GNPs and (B) encapsulation of PCL-GNPs in GNP-PNPs by self-assembly with PCL-*b*-PEG copolymer chains.

3.2 Experimental

3.2.1. Materials.

Gold nanoparticles (GNPs) and gold nanorods (GNRs) were synthesized using chloroauric acid trihydrate (>99.95 %, Sigma), sodium borohydride (≥ 98 %, Sigma), L-ascorbic acid (99 %, Sigma), cetyltrimethylammonium bromide (CTAB, ≥ 99%, Sigma), and silver nitrate (≥ 99%, Sigma), which were used as received. GNPs and GNRs were surface-functionalized using (α-thiol, w-hydroxy)-terminated polycaprolactone (PCL-SH, M_n = 2.1k, $Đ$ = 1.2, SH-functionality ≥ 95 %) purchased from Polymer Source Inc. For control experiments, GNPs were also surface-functionalized using (α-thiol, w-hydroxy)-terminated poly(ethylene oxide) (PEG-SH, M_n = 5.0k, $Đ$ = 1.1, SH-functionality ≥ 95 %) purchased from Nanocs. Encapsulation of PCL-GNPs and PCL-GNRs occurred *via* self-assembly of polycaprolactone(6.0k)-*block*-poly(ethylene oxide)(5.0k) (PCL-*b*-PEG, $Đ$ = 1.1, Advanced Polymer Materials), where numbers in brackets indicate number-average molecular weights of the respective blocks. The following solvents were used in the experiments: HPLC-grade tetrahydrofuran (THF, ≥ 99.9 %, Sigma), dimethylformamide (DMF, ≥ 99.8 %, Sigma), reagent-grade chloroform ($CHCl_3$, ≥ 98 %, Fischer), and hexane (≥ 95 %, Sigma). Sodium hydroxide (NaOH, 10 N, Sigma), paraformaldehyde (95 %, Sigma), hydrochloric acid (HCl, 37 %, Sigma), sulfuric acid (37 % (v/v), Ricca), hydrogen peroxide (30 % (w/w), Sigma), and ACS reagent nitric acid (70 %, Sigma) were used as received. Argon gas (> 99.998 %) was purchased from Praxair. Gold standard solution for GFAA analysis (TraceCERT®, 1000 mg/L Au in HCl) was purchased from Sigma and 0.25 % Trypsin-EDTA was purchased from Gibco. Dulbecco's Modified Eagle's Medium (DMEM) was purchased from Gibco and fetal bovine serum (FBS) was purchased from Thomas Fischer.

3.2.2 Gold Nanoparticle (GNP) Synthesis.

Gold nanoparticles were synthesized by the reduction of chloroauric acid with sodium borohydride ($NaBH_4$) as described by Martin et al.[36] First, a solution of chloroauric acid trihydrate (0.03 M) in DI water was prepared; the resulting gold stock solution was stored at 4 °C in a polyethylene bottle prior to use. Next, the reducing solution was prepared immediately before use in the following manner. First, a solution of $NaBH_4$ (1×10^{-4} M) in DI water was prepared; then, 10 N NaOH was added to the $NaBH_4$ solution until the NaOH concentration was 0.1 N. To prepare a batch of GNPs, 166.7 μL of gold stock solution were diluted with 10 mL of DI water in an 8-dram glass vial. The solution was then vortexed at 1800 rpm as 350 μL of the reducing solution were injected all at once into the vortex, resulting in a sudden color change from yellow to dark red. After injection of the reducing solution, the GNP dispersion was vortexed for another 3 s then immersed in an oil bath at 80 °C for 5 min, resulting in a gradual colour change from dark red to bright red. In the same manner, 10 batches were prepared in tandem and then immediately pooled to produce ~105 mL of GNP dispersion.

3.2.3 Gold Nanorod (GNR) Synthesis.

The synthesis of GNRs was adapted from previous work of Sau at el.[37] The synthesis began with the formation of gold seeds as follows. First, a solution chloroauric acid trihydrate (0.01 M) in DI water was prepared; the resulting gold stock solution was stored at 4 °C in a polyethylene bottle prior to use. Then, a solution of cetyltrimethylammonium bromide (CTAB) (0.1 M) in DI water was prepared by sonication and heating to 25 ºC. Within a glass test tube, 250 μL of the gold stock solution was added to 7.5 mL of the CTAB solution at 25 ºC followed by mixing by inversion. Next, a solution of $NaBH_4$ (0.01 M) in DI water was prepared and chilled on ice (reducing solution). 60 μL of the chilled reducing solution was added to the test tube containing

gold and CTAB and the solution was mixed by inversion for 2 min resulting in a gradual color change from yellow to red. Finally, the gold seed dispersion was incubated at 25 °C for at least 3 h and used before 24 h.

To prepare a batch of GNRs, a growth solution was prepared at 25 ºC in a clean glass test tube. First, 4.75 mL of CTAB solution was added to the test tube, followed by 200 μL of gold stock solution, and finally 30 μL of silver nitrate solution (0.01 M) in DI water. The growth solution was mixed by inversion 3 times. Next, 32 μL of an L-ascorbic acid (0.1 M) solution in DI water were added to the growth solution, followed by addition of 25 μL of the nascent gold seed dispersion. The resulting dispersion was mixed by inversion for 10 s and then incubated at 25 °C for 24 h, resulting in a gradual color change from orange to purple. The purple color arises from a combination of GNRs (blue) and small GNPs (red) in the dispersion. Therefore, the dispersion was centrifuged at 17500 × g for 30 minutes. The red supernatant containing GNPs and CTAB flocculent was discarded and the pellet was re-suspended in 1.5 mL of DI water. This centrifugation/re-suspension process was repeated two more times, yielding a clear blue dispersion of GNRs. In the same manner, multiple batches of GNRs were prepared in tandem and then immediately pooled to produce the final GNR dispersion.

3.2.4 Functionalization of GNPs and GNRs with Thiol-terminated Polycaprolactone (PCL-SH).

In order to promote their encapsulation within PNPs, both GNPs and GNRs were functionalized with a brush layer of PCL chains in the following manner. First, a solution of PCL-SH (1.7 mg mL^{-1}) was prepared by adding THF to the solid polymer and stirring for at least 3 h. Next, the PCL-SH solution was added dropwise to the aqueous GNP or GNR dispersion under constant stirring (800 rpm) to a volume ratio of 2:1 (e.g. 200 mL of PCL-SH solution added to 100

mL of GNP dispersion). This volume ratio corresponds to a thiol:Au molar ratio of 3.4:1 for the GNP dispersion; the molar ratio was higher but unknown for the GNR dispersion due to removal of spherical gold seeds during GNR synthesis as described above. The resulting dispersions were left to stir overnight.

After overnight stirring, a red or blue flocculent was observed in the GNP or GNR dispersion, respectively. Water and solvent were removed from the dispersion by rotary evaporation. The resulting solid was re-suspended in 3 mL of $CHCl_3$ to yield a slightly cloudy dark red (GNPs) or dark blue (GNRs) dispersion, which was transferred to a 25 mL Teflon centrifuge tube. Next, hexane was slowly added dropwise with vortexing until a cloudy precipitate was observed. At this point, the dispersion was centrifuged at 4000 × g for 30 minutes, then the colorless supernatant was removed from the pellet. The supernatant was air-dried, resulting in a cloudy white film which was attributed to excess PCL-SH chains. Next, the pellet was re-suspended in 3 mL $CHCl_3$ and filtered through a Kimwipe packed into a Pasteur pipette, into a clean 25 mL Teflon centrifuge tube, resulting in a clear dark red (GNPs) or dark blue (GNRs) dispersion. The centrifugation/re-suspension process was repeated two more times (but without Kimwipe filtering), after which no PCL-SH was observed by eye in the dried supernatant. The pellet resulting from the final centrifugation step was dried overnight under an argon flow, then re-suspended in DMF and stirred overnight to form a dispersion of 0.33 wt % PCL-GNPs or PCL-GNRs for bulk encapsulation experiments. For microfluidic encapsulation experiments, dispersions of 1.0 wt % PCL-GNPs in DMF were prepared in the same manner.

3.2.5 Functionalization of GNPs with Thiol-terminated Poly(ethylene glycol) (PEG-SH).

A sample of poly(ethylene glycol)-functionalized GNPs was prepared as a control for cell uptake experiments. First, a solution of PEG-SH (17 mg mL^{-1}) was prepared by adding DI water to the solid polymer and stirring overnight. Next, the PEG-SH solution was added dropwise to the GNP dispersion under constant stirring (800 rpm) to a volume ratio of 1:5 (i.e. 4 mL of PEG-SH solution added to 20 mL of GNP dispersion). This volume ratio corresponds to a thiol:Au molar ratio of 1.4:1. The resulting dispersion was left to stir overnight.

After overnight stirring, the GNP dispersion was a clear orange-red color. The dispersion was transferred to multiple 1.5 mL centrifuge tubes and centrifuged at 16000 × g for 30 minutes, then the colorless supernatant was removed from the pellet. The supernatant was air-dried, resulting in a cloudy white film which was attributed to excess PEG-SH chains. Next, the pellet was re-suspended in 3 mL DI water. The centrifugation/re-suspension process was repeated two more times, after which no PEG-SH was observed by eye in the dried supernatant. The pellet resulting from the final centrifugation step was re-suspended in DI water and stored at 4 ºC until use.

3.2.6 Bulk Encapsulation of PCL-GNPs (or PCL-GNRs) in GNP-PNPs (or GNR-PNPs).

First, a 0.33 wt % solution of PCL-*b*-PEG was prepared by dissolving the solid polymer in DMF and stirring overnight to equilibrate. Next, for encapsulation of PCL-GNPs, the PCL-*b*-PEG solution was blended with the 0.33 wt % PCL-GNP dispersion in DMF (described previously) in various mass ratios, $r_{PCL\text{-}GNP}$ = 2, 10, 50, 75, 100, where $r_{PCL\text{-}GNP} = m_{PCL\text{-}GNP} / m_{PCL\text{-}b\text{-}PEG}$. Similarly, for encapsulation of PCL-GNRs, the PCL-*b*-PEG solution was blended with the 0.33 wt % PCL-GNR dispersion in DMF (described previously), using a single mass ratio of $r_{PCL\text{-}GNR}$ = 10, where $r_{PCL\text{-}GNR} = m_{PCL\text{-}GNR} / m_{PCL\text{-}b\text{-}PEG}$. Here $m_{PCL\text{-}GNP}$ and $m_{PCL\text{-}GNR}$ are the mass of PCL and gold in PCL

functionalized GNPs and GNRs respectively. To initiate self-assembly and GNP-PNP or GNR-PNP formation, 1.0 mL of each blend solution was injected *via* syringe pump at a constant rate (120 μL/min) with stirring (800 rpm) into 10 mL of DI water. Finally, the resulting GNP-PNP or GNR-PNP dispersions were transferred to 6-8 kDa MWCO dialysis tubing and dialyzed against DI water for 18 h, changing the water every hour for the first 4 hours.

3.2.7 Microfluidic Reactor Fabrication.

The microfabrication steps followed previously described procedures from our group.[21,41-43] Firstly, negative masters were fabricated on silicon wafers (Silicon Materials) using the negative photoresist SU-8 100 (Microchem). A 150 μm-thick SU-8 film was spin-coated at 2,000 rpm onto the silicon wafer and heated at 65 °C for 12 min and then at 95 °C for 50 min. After the wafer was cooled, a photomask was placed directly above, and the wafer was exposed to UV light for 100 s. Then, the UV-treated film was heated at 65 °C for 1 min and then 95 °C for 20 min. Finally, the silicon wafer was submerged in SU-8 developer (Microchem) and rinsed with isopropanol until all unexposed photoresist was removed.

Microfluidic chips were fabricated from polydimethylsiloxane (PDMS) using a SYLGARD 184 silicon elastomer kit (Dow Corning). For fabrication of all PDMS chips, the elastomer and curing agent were mixed at a 7:1 ratio and degassed under vacuum. The resulting mixture was poured over a clean negative master chip in a Petri dish and further degassed until all remaining air bubbles were removed. The PDMS was heated at 85 °C until cured (~20 min) and then peeled from the negative master; holes were punched through the reservoirs of the resulting PDMS chip to allow for the insertion of tubing. A thin PDMS film (substrate layer) was also made on a glass slide by spin-coating a 20:1 elastomer/curing agent mixture followed by curing. The substrate layer was then permanently bonded to the base of the microfluidic reactor (channel layer) after both

components were exposed to oxygen plasma for 90 s. The resulting reactor (Figure S3.1, *Supporting Information*) has a set channel depth of 150 μm and consists of a sinusoidal mixing channel 100 μm wide and sinusoidal processing channel 200 μm wide.

3.2.8 Flow Delivery and Control.

The steps of flow delivery and control followed previously described procedures. Pressure-driven flow of liquids to the reactor inlet was provided using 1 mL gastight syringes (Hamilton) mounted on syringe pumps (Harvard Apparatus). The microfluidic chip was connected to the liquid syringes via 1/16th-inch (OD) Teflon tubing (Mandel Scientific). Argon (Ar) gas flow was introduced to the chip via an Ar tank regulator and a downstream regulator (Johnston Controls) for fine adjustments. The chip was connected to the downstream regulator through a 1/16th-inch (OD)/100-μm (ID) Teflon tube (Mandel Scientific). The liquid flow rate (Q_{liq}) was programmed via the syringe pumps, and the gas flow rate (Q_{gas}) was fine-tuned via the downstream pressure regulator in order to set a total nominal flow rate (Q) of 50, 100, 200, or 400 μL/min. Due to the compressible nature of the gas and the high gas/liquid interfacial tension, discrepancies arise between the nominal (programmed) and actual values of Q_{gas}, Q_{gas}/Q_{liq}, and the total flow rate (Q_{total}). Therefore, actual values of Q_{gas}, Q_{gas}/Q_{liq}, and $Q_{total} = Q_{gas} + Q_{liq}$ for each microfluidic experiment were calculated from the average volume of gas bubbles in the microchannels and are reported in (Table S1, *Supporting Information*). Specifically, an image of the microchannels was captured using a Genie Nano-C1280 camera (1stVision) equipped with an On-Semi Python1300 sensor and a C-Mount Manual Iris Varifocal lens (1/1.8", 4-13mm, *f*/1.5) (Tamron) at each of three different time periods at the beginning, middle, and end of the sample collection process. Analysis of the gas bubbles and liquid plugs within the microfluidic reactor was achieved using image analysis software (ImageJ), which gives the end-to-end distance of individual gas bubbles and

liquid plugs, $L_{gas,i}$ and $L_{liq,i}$, respectively, under a given set of flow conditions. The gas-to-liquid flow ratio, Q_{gas}/Q_{liq}, was determined from each image as the ratio between measured $\sum_i L_{gas,i}$ and $\sum_i L_{liq,i}$ (i = 20-50). Actual gas-to-liquid flow ratios for all experimental runs are reported as average values determined from 3 images for each run. All actual Q_{total} values within Table S1 are within 10 % of nominal Q values.

3.2.9 Microfluidic Encapsulation of PCL-GNPs in GNP-PNPs.

First, a 1.0 wt % solution of PCL-*b*-PEG was prepared by dissolving the solid polymer in DMF and stirring overnight to equilibrate. Next, the PCL-*b*-PEG solution was blended with the 1.0 wt % PCL-GNP dispersion in DMF (described previously) in a mass ratio of either $r_{PCL\text{-}GNP}$ = 75 or $r_{PCL\text{-}GNP}$ = 100, where $r_{PCL\text{-}GNP} = m_{PCL\text{-}GNP} / m_{PCL\text{-}b\text{-}PEG}$. The solution was allowed to stir at 800 rpm for 3 h and was then used as the PCL-GNP/PCL-*b*-PEG stream for microfluidic assembly. For microfluidic preparation of GNP-PNPs, the following three liquid streams were combined to give stable gas-segmented liquid plugs within the reactor, (1) the PCL-GNP/PCL-*b*-PEG (solids) stream (2) pure DMF; and (3) 30 wt % DI water in DMF. The flow rates of the three liquid streams were equal for all runs, such that the steady-state on-chip water concentration was 10 wt % and the steady-state on-chip solids concentration (PCL-GNP + PCL-*b*-PEG) was 0.33 wt %. After microfluidic mixing, GNP-PNPs were collected from the chip into vials containing 10× excess by volume of deionized water. In order to remove residual dioxane and acetic acid, the resulting PNP dispersions were then immediately transferred into a 6−8 kDa MWCO dialysis membrane and dialyzed against DI water for 18 h, with changing of DI water every hour for the first 4 h.

3.2.10 Cell Uptake Experiments.

Human breast cancer cells were used as a model system to determine cell uptake of GNP-PNPs and PEG-GNPs, the latter serving as a control sample. MDA-MB-231 cells were grown to ~70% confluence in 75 cm^2 tissue culture flasks, then trypsinized, collected, and pelleted by centrifugation (5 min at 313 × g). The cell pellet was then suspended in DMEM, and the cell concentration was determined using a hemocytometer. After the initial cell concentration was determined, the suspension was diluted to 1.0×10^5 cells/mL. Next, the cells were seeded at a density of 3.0×10^5 cells per well in a 6-well plate. The plate was then incubated for 24 h at 37 °C with 5% CO_2 for cell adhesion. The gold concentration of each sample and control were determined using GFAA. To produce the dosing medium, each gold dispersion was diluted using cell medium to a common gold concentration of 500 nM. From each well, cell medium was first removed by pipette followed by the addition of 3.0 mL of dosing medium. After 4 h incubation at 37 °C, the cells were washed 3× with 1 mL of PBS buffer. Following the final wash step, the cells were trypsinized by adding 1 mL of trypsin-EDTA solution and 4 mL cell medium to each well. Two wells containing the same sample were combined and the resulting suspension was centrifuged at 1250 × g for 15 minutes at 4 °C. The supernatant was discarded from the pelleted cells and 5 mL of PBS were added to the cell pellet for re-suspension. Cell concentrations were determined using a hemocytometer. Finally, each cell suspension was transferred to a test tube and dried under compressed air flow for 24 hours.

Cytotoxicity Experiments. MDA-MB-231 cells were grown to ~80% confluence in cell medium (DMEM supplemented with 10% FBS) in a 75 cm^2 tissue culture flask, then trypsinized, collected, and pelleted by centrifugation (5 min at 313 × g). The cell pellet was then suspended in cell medium, and the cell concentration was determined using a hemocytometer. After the initial

cell concentration was determined, the suspension was diluted to 1.0×10^5 cells/mL. Next, a multichannel pipet was used to fill a 96-well plate with 100 μL / well of the diluted cell suspension. The cell-loaded plates were then incubated for 24 h at 37 °C under an atmosphere of 5% CO_2. After a 24 h cell incubation, each gold dispersion was diluted using cell medium to a gold concentration of 1 μM. Then, 100 μL diluted gold dispersion was added to the appropriate well of the 96-well plate, in order to generate a dosing concentration of 500 nM (identical to cell uptake experiments). The treated cells were incubated for 48 h at 37 °C under a 5% CO_2 atmosphere, then 20 μL of CellTiter-Blue was added to each well. The cells were incubated for 4 h at 37 °C under a 5% CO_2 atmosphere, and then fluorescence readings were recorded on a 96-well plate reader (λ_{ex} = 560 nm; λ_{em} = 590 nm emission). Cell viability was calculated for each well based upon the following formula:

$$Cell\ viability\ \% = \left[\frac{B - S_0}{B}\right] \times 100$$

Where S_0 is the sample reading (cells + gold + medium) and B is the average reading for the untreated population of cells (cells + medium).

3.2.11 Thermogravimetric Analysis (TGA).

TGA was used to analyze the copolymer content in PCL-GNPs before and after removal of excess PCL-SH by multiple centrifugation/re-suspension steps. In both cases, 5 mg of solid PCL-GNPs were placed in alumina crucibles for analysis. TGA experiments were conducted on a TA Instruments Q600 SDT simultaneous thermal analyzer with samples being placed in an aluminum oxide crucible, referenced against an empty aluminum oxide crucible. Data was collected with a ramp rate of 5 °C/min following temperature equalization at 50 °C under a nitrogen atmosphere flowing at 100 mL/min by scanning to 600 ºC.

3.2.12 Transmission Electron Microscopy.

Negatively stained samples for TEM imaging were prepared by depositing a drop of ~0.1 mg/mL GNP-PNP and GNR-PNP dispersions on a Formvar/carbon-coated 200-mesh copper TEM grid (Ted Pella Inc.) followed by a drop of 1 wt % uranyl acetate aqueous solution as a negative staining agent. Excess liquid was immediately removed using lens paper, followed by drying of the remaining liquid under ambient conditions. PCL-GNP and PCL-GNR samples were prepared by depositing 1 wt % dispersions in DMF onto a carbon-coated 200-mesh copper grid (Ted Pella Inc.). Excess liquid was immediately removed using lens paper, followed by drying of the remaining liquid under ambient conditions. Naked charged GNPs and CTAB-functionalized GNRs were deposited from dilute aqueous dispersions onto Formvar/carbon-coated 200-mesh copper TEM grids (Ted Pella Inc.). In both cases, a single drop was allowed to stand on the grid for 30 s before removing excess liquid using lens paper, followed by drying of the remaining liquid under ambient conditions. Imaging was performed on a JEOL JEM-1400 transmission electron microscope, operating at an accelerating voltage of 80 kV and equipped with a Gatan Orius SC1000 CCD camera. To obtain particle size distributions from TEM data, at least 300 GNPs in total were measured from three images taken in different regions of the grid. Reported uncertainties (σ) on particle dimensions were calculated from the standard deviation (s) of average dimensions determined from three images: $= \frac{s}{\sqrt{3}}$. To obtain scatter plots of GNP occupancy (Z) vs. GNP-PNP core diameters (d_c), at least 300 GNP-PNPs were measured from six images taken in different regions of the grid and the number of GNPs in each GNP-PNP was counted. For each sample, average GNP occupancies were then determined for the entire population (Z_{ave}) and for all GNP-PNPs below various maximum sizes: $Z_{ave,\ d<150\ nm}$, $Z_{ave,\ d<100\ nm}$, $Z_{ave,\ d<75\ nm}$, and $Z_{ave,\ d<50\ nm}$.

3.2.13 Dynamic Light Scattering.

DLS experiments were performed on a Brookhaven Instruments ZataPALS Analyzer equipped with a solid state laser (660 nm) with a maximum power output of 35 mW. DLS measurements of GNPs and GNP-PNPs were performed in DI water, with an experimental temperature of 25 °C and at a scattering angle of 90°. DLS measurements of PCL-GNPs were performed in DMF, with an experimental temperature of 25 °C and at a scattering angle of 90°. DI water used for DLS sample preparation was pre-filtered using 2 × 0.20 μm nominal pore size nylon syringe filters (National Scientific). DMF used for DLS sample preparation was pre-filtered using 2 × 0.20 μm nominal pore size Teflon syringe filters (VWR). Sample concentrations for DLS measurements were 0.17 mg/mL for GNPs, 0.07 mg/mL for PCL-GNPs and 0.007 mg/mL for GNP-PNPs. For each sample dispersion, mean effective hydrodynamic sizes were determined from three measurements of the autocorrelation function using cumulant analysis. Reported mean effective hydrodynamic sizes were determined by averaging values from triplicate preparations. Reported uncertainties (σ) on mean hydrodynamic sizes were calculated from the standard deviation (s) of values from triplicate preparations: $\sigma = \frac{s}{\sqrt{3}}$. To obtain scatter plots of GNP occupancy (Z) vs. GNP-PNP core diameters (d_c), at least 300 GNP-PNPs were measured from six images taken in different regions of the grid and the number of GNPs in each GNP-PNP was counted. For each sample, average GNP occupancies were then determined for the entire population (Z_{ave}) and for all GNP-PNPs below various maximum sizes: $Z_{ave,\ d<150\ nm}$, $Z_{ave,\ d<100\ nm}$, $Z_{ave,\ d<75\ nm}$, and $Z_{ave,\ d<50\ nm}$.

3.2.14 Graphite Furnace Atomic Absorption (GFAA) Analysis of Gold Content.

To each sample of dried cells produced from cell uptake experiments, 200 µL of DI water were added followed by 400 µL of 10 N sulfuric acid with vortex mixing. Finally, 200 µL of 30

wt % hydrogen peroxide were added to each test tube followed by immediate vortexing and capping with a glass marble (***Warning: piranha solution is a powerful oxidizer and must be handled with extreme care!!***). The tubes were heated to between 205-215 °C and maintained within this temperature range for 90 min. After 90 min heating, most of the water in the tubes had evaporated; the tubes were allowed to cool for 5 min until they could be safely handled. Then, 1.5 mL of 37 % HCl were added followed by 0.5 mL of 70 % nitric acid. The test tubes were again capped with glass marbles and heated at 120 °C for 30 min; next, ~2.5 mL of 10 % HCl were used to wash the dried contents of each test tube (with vortexing) into 10-mL volumetric flasks followed by dilution to 10.0 mL with 10 % HCl. Standards were prepared by diluting the gold standard solution to known concentrations of 0.0200, 0.0400, 0.0600, 0.0800, and 0.100 µg / mL in 10 % HCl.

Samples and standards were then analyzed using a Agilent 240 AA atomic absorption spectrometer with a GTA 120 graphite tube atomizer, a PSD 120 programmable sample dispensor, and a 25 mA Ne hollow-cathode lamp (Atomic Spectral Lamps). For all measurements, the injection volume was 15 µL. The absorbance peak area was determined at 242.8 nm with a 1 nm slit width. Table 3.1 shows the graphite tube heating program used for all samples and standards under a 0.3 L/min argon flow. Gold concentrations were determined by comparing sample measurements against a calibration curve obtained using measured standard solutions.

Table 3.1. Graphite Tube Heating Program Optimized for Gold Analysis

Step	Temperature / °C	Time / s	Argon Flow	Data Acquisition
1	85	5.0	On	No
2	95	40.0	On	No
3	120	10.0	On	No
4	500	5.0	On	No
5	500	1.0	On	No
6	500	2.0	Off	No
7	2600	1.1	Off	Yes
8	2600	2.0	Off	Yes
9	2600	2.0	On	No

3.3 Results and Discussion

3.3.1 Functionalization of GNPs with PCL-SH and Characterization of PCL-GNPs.

Following reaction of GNPs with PCL-SH in a THF/water mixture (Figure 3.1A), the resulting product was suspended in chloroform and subjected to repeated wash cycles to remove unattached polymer chains, each involving dropwise addition of hexane to the cloud point, centrifugation, removal of supernatant, and re-suspension in chloroform (Figure 3.2A). The resulting GNP particles functionalized with PCL-SH are designated PCL-GNPs. TGA of the PCL-GNP sample before washing (Figure 3.2B, red trace) is virtually indistinguishable from the PCL-SH chains alone (black trace), indicating an extremely low relative gold content before removal of excess, unattached PCL-SH. However, after repeated washing cycles, the TGA of PCL-GNP (blue trace) reaches a high-temperature plateau of 15% of the initial mass, corresponding to the gold content of the sample, from which a polymer content of 85% is determined.

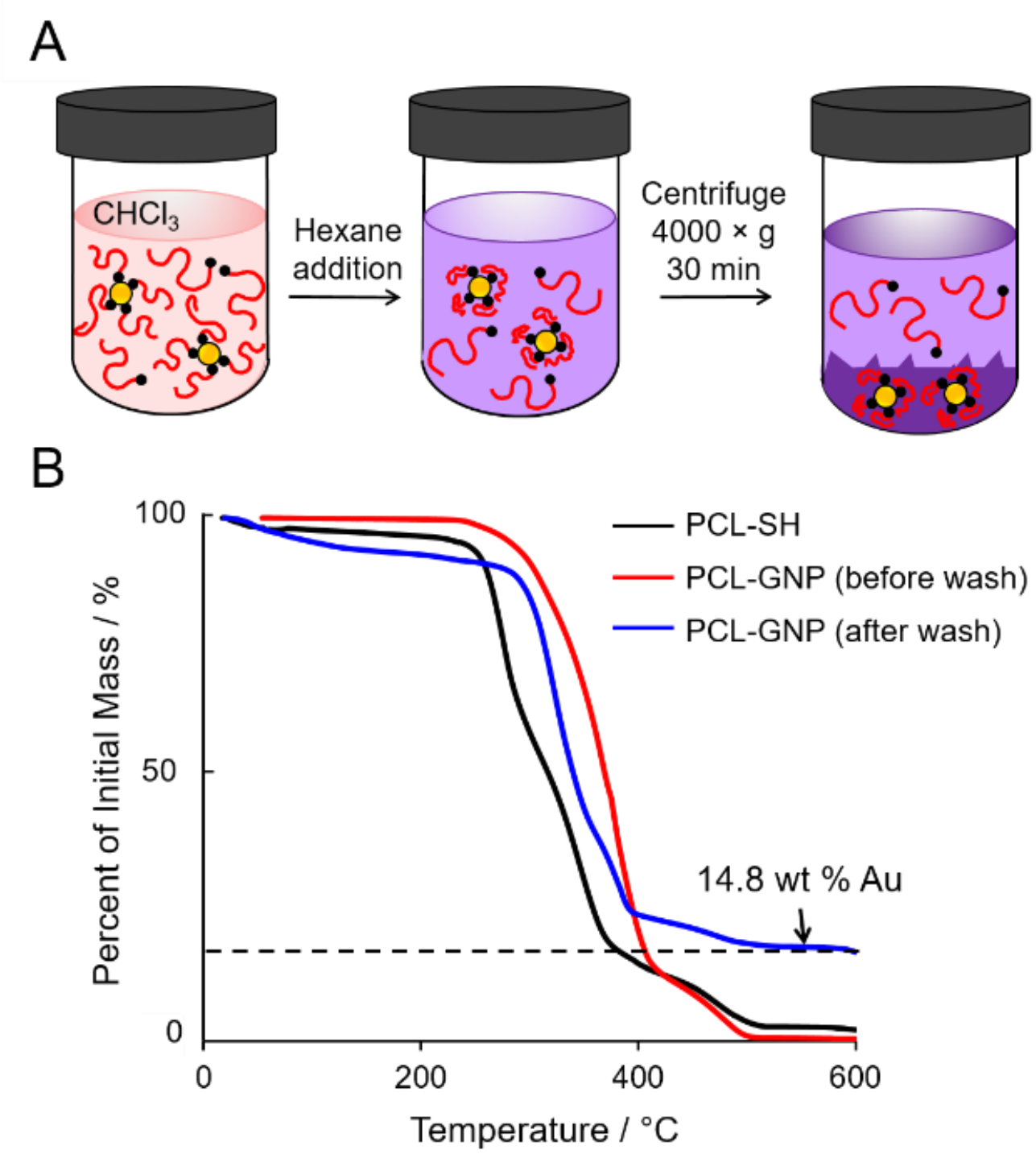

Figure 3.2. (A) Schematic of the wash cycle applied to remove excess PCL-SH chains following functionalization of PCL-GNPs. (B) TGA scans of PCL-GNPs before (red trace) and after (blue trace) wash cycles and comparison with pure PCL-SH (black trace).

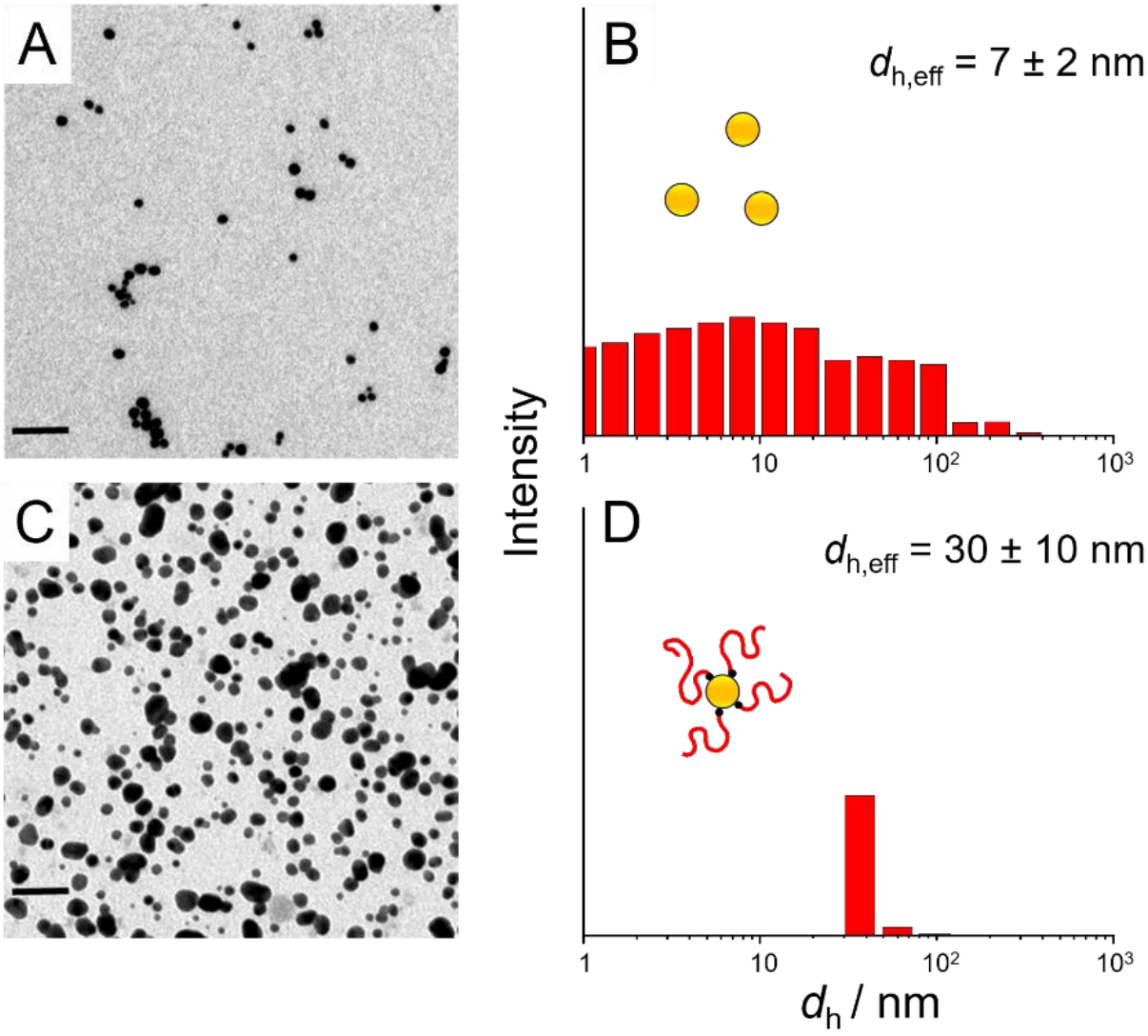

Figure 3.3. TEM images (A, C) and DLS analysis (B, D) for GNPs before (A, B) and after (C, D) PCL-SH functionalization. DLS analysis includes CONTIN hydrodynamic size distributions and mean effective hydrodynamic diameters, $d_{h,eff}$, from cumulant analysis for naked GNPs in water (B) and PCL-GNPs in DMF (D). Scale bars in TEM images are 50 nm.

TEM images of naked GNPs (before functionalization) deposited from aqueous dispersion and PCL-GNPs (after functionalization) deposited from DMF dispersion are shown in Figure 3.3, A and C, respectively; the corresponding TEM size distributions are provided in *Supporting Information* (Figure S3.2). TEM of the original GNPs and subsequent statistical analysis reveal a narrow size distribution peaked at a mean diameter of 7.2 ± 0.3 nm. Following functionalization with PCL-SH, the GNP cores have experienced some ripening, as evidenced by a broadening of the size distribution and an increase in the mean diameter to 12.1 ± 0.8 nm. It should be noted that only the GNP cores, and not the PCL brush layers, are visible in the TEM image in Figure 3.3C, due to the collapsed state of the polymer chains in the dried state and the low electron density of PCL compared to gold.

Information on the size distributions of dispersed particles corresponding to the TEM images in Figure 3.3, A and C is provided by the DLS CONTIN histograms in Figure 3.3, B and D. Also shown are corresponding mean hydrodynamic sizes from cumulant analysis for GNPs in water (before functionalization, Figure 3.3B) and PCL-GNPs in DMF (after functionalization, Figure 3.3D). Before functionalization, the GNP mean effective hydrodynamic diameter ($d_{h,eff}$ = 7 ± 2 nm) matches well with the mean core size from TEM (7.2 nm), consistent with the absence of a solubilized ligand layer in the sample. The broadness of the CONTIN histogram may reflect the formation of a small number of aggregates in the unfunctionalized aqueous sample. After functionalization, cumulant analysis reveals a mean effective hydrodynamic diameter of $d_{h,eff}$ = 30 ± 10 nm for PCL-GNPs in DMF, significantly larger than the corresponding mean core size from TEM (12.1 nm), confirming the presence of a solubilized brush layer of PCL chains surrounding the GNP cores. In addition to their larger mean hydrodynamic size, the PCL-GNPs in DMF (Figure

3.3D) show a much narrower DLS size distribution than unfunctionalized GNPs in water (Figure 3.3B), suggesting that the PCL brush layer promotes good dispersion and suppresses aggregation.

Based on the combination of TGA, TEM and DLS data discussed above, quantitative structural features of polymer brush-functionalized PCL-GNPs can be elucidated. First, by subtracting the functionalized GNP core radius (6 nm) from the hydrodynamic radius (15 nm), we determine a brush layer thickness of t_b = 9 nm. Based on the estimated fully-extended dimension of a single PCL repeat unit (~1 nm) and the average of number of repeat units in the attached PCL-SH chains (~18 CL repeat units), we calculate a fully-extended chain dimension of ~18 nm. Therefore, from the determined brush thickness of 9 nm, we estimate that PCL chains within the solubilized brush layer of PCL-GNPs are ~50 % extended.

Next, we can estimate the chain packing density of the brush layer, using several simplifying assumptions. First, assuming a spherical GNP shape and using the mean radius of functionalized GNP cores (6 nm), we determine the average GNP volume ($V = \frac{4}{3}\pi r^3$) to be V_{GNP} = 9.05 × 10^{-19} cm^3. Then, the density of gold (19.3 g cm^{-3}) is used to determine the average GNP mass, m_{GNP} = 1.75 × 10^{-17} g. Next, since we know from TGA that the GNP core is 15% of the entire mass of a PCL-GNP particle, we can determine the average PCL-GNP mass to be 1.16 × 10^{-16} g, from which the mass of PCL-SH chains per particle is m_{PCL} = 1.16 × 10^{-16} g - 1.75 × 10^{-17} g = 9.89 × 10^{-17} g. Therefore, based on the mean molar mass of PCL-SH (2100 g mol^{-1}), the number of PCL chains per particle is N_{PCL} = (m_{PCL} /MW_{PCL}) × N_A = 2.8 × 10^4. Finally, we calculate the surface area per GNP ($A = 4\pi r^2$) to be A = 452 nm^2, in order to arrive at a chain packing density ($\sigma_{PCL} = N_{PCL}/A$) of σ_{PCL} = 62 nm^{-2}, assuming all PCL-SH chains are connected to the GNP surface. This value is about an order of magnitude higher than typical reported thiol ligand densities.[38,39] This result suggests that some unattached PCL-SH chains persist in the sample

following the washing cycles; this may be due to co-crystallization of unattached PCL-SH with the PCL brush layer of PCL-GNPs during the wash cycle described in Figure 3.2A.

3.3.2 Bulk Encapsulation of PCL-GNPs and Effect of PCL-GNP/PCL-b-PEG Ratio on GNP-PNPs.

Polymer brush-functionalized PCL-GNPs were encapsulated within the hydrophobic cores of the block copolymer PCL-*b*-PEG using different nanoprecipitation methods. First, the PCL-GNP and PCL-*b*-PEO components were co-dissolved in DMF, followed by water addition and dialysis to produce GNP-PNPs (Figure 3.1B). Water addition and concomitant PNP formation were achieved either by direct injection of the DMF solution into an excess of water (bulk methed, Figure 3.4A), or by mixing the DMF solution with water in a two-phase, gas-liquid microfluidic reactor at various flow rates (microfluidic method, Figure 3.4B).

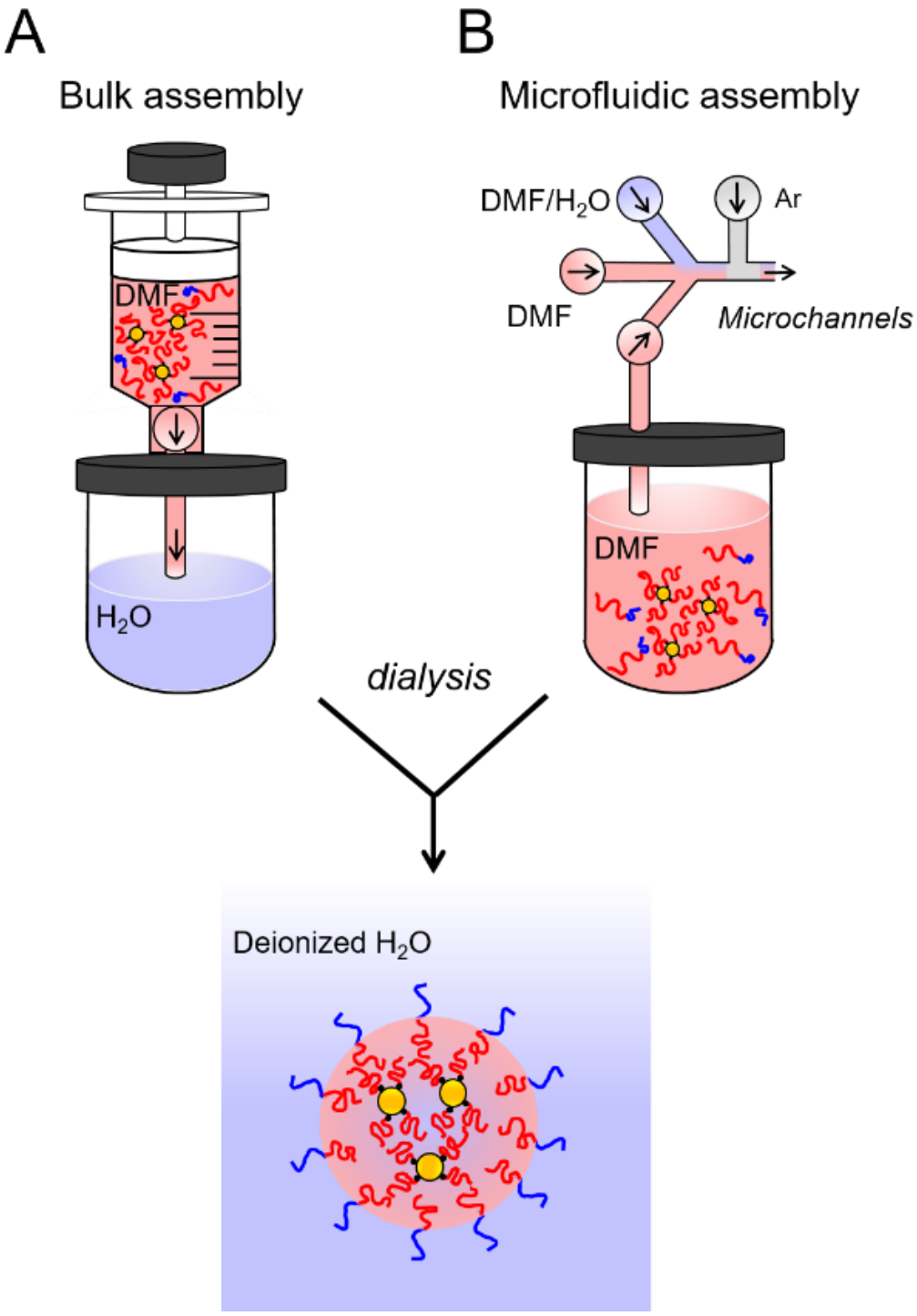

Figure 3.4. Schematics describing (A) bulk (left) and (B) microfluidic (right) methods for mixing copolymer/PCL-GNP components with water to form GNP-PNPs.

We first investigated the effect of the PCL-GNP/PCL-*b*-PEG ratio (w/w) in the initial DMF solution, $r_{PCL\text{-}GNP}$, on GNP-PNPs formed by the bulk method (Figure 3.5). In the TEM images in Figure 3.5, A-D, the PCL micelle cores appear light due to reverse staining, while the GNPs are distinct dark dots due to the high electron density of gold. In the various images, GNPs are clearly encapsulated within the PCL cores; the number of GNPs compared to the number of PNPs increases, and the number of empty PNPs decreases, as $r_{PCL\text{-}GNP}$ increases (Figure 3.5, A-D). In Figure 3.5A ($r_{PCL\text{-}GNP}$ = 2), most of the PNPs are empty, with only a few PNPs in the image containing a maximum of one GNP. As the relative amount of PCL-GNPs increases to $r_{PCL\text{-}GNP}$ = 10 (Figure 3.5B), a greater number of PNPs contain GNPs, with GNP encapsulation apparently favored by larger PNPs in the sample; several larger PNPs in the image contain multiple GNPs. The trend continues for $r_{PCL\text{-}GNP}$ = 50 (Figure 3.5C), with most PNPs containing GNPs and an increased number containing multiple GNPs. In Figure 3.5 D the trend ceases ($r_{PCL\text{-}GNP}$ = 75) as the smaller GNP-PNP particles have grown and are incorporating more GNPs per PNP. Finally, Figure 3.5E shows the maximum investigated PCL-GNP content (for $r_{PCL\text{-}GNP}$ = 100), at which many empty PNPs are present but the average size of the small PNPs has decreased whereas the average size of the larger PNPs has increased, with the smallest PNPs containing one GNP and the largest PNPs containing up to ~50 GNPs. We note that even in GNP-PNPs with the greatest number of GNPs, individual GNPs remain distinct and well-spaced, with a minimum distance of ~1 nm between neighboring GNPs. To fully understand the TEM data the DLS needs to be interpreted.

Mean effective hydrodynamic diameters, $d_{h,eff}$, determined from cumulant analysis of DLS data are plotted against $r_{PCL\text{-}GNP}$ in Figure 5E (black data points). As $r_{PCL\text{-}GNP}$ increases from 2 to 10, GNP-PNP $d_{h,eff}$ increases from 100 nm to 200 nm, and then increases further to 230 nm as $r_{PCL\text{-}}$

$_{GNP}$ increases to 50; further increase of $r_{PCL\text{-}GNP}$ to 75 decreases $d_{h,eff}$ to 100 nm, finally, a further increase in $r_{PCL\text{-}GNP}$ to 100 results in a increase in mean hydrodynamic size to $d_{h,eff}$ = 120 nm. The increase in size between $r_{PCL\text{-}GNP}$ = 2 and $r_{PCL\text{-}GNP}$ = 50 is attributed to the decrease in PEG chain density within the coronal layer as PNP cores increase in volume due to PCL-GNP encapsulation; this will lower the colloidal stability, resulting in some particle coalescence and formation of a small number of larger aggregates stabilized by PCL crystallization. The increased importance of large GNP-PNP aggregates (d_h = ~1000 nm) in the $r_{PCL\text{-}GNP}$ = 10 and $r_{PCL\text{-}GNP}$ = 50 samples is evidenced by the corresponding CONTIN distributions (Figure S3.3, S*upporting Information*). The sharp drop in $d_{h,eff}$ as $r_{PCL\text{-}GNP}$ further increases to 75 is not well understood, but is found to correspond to the disappearance of large aggregates in the d_h = ~1000 nm regime (Figure S3.3, *Supporting Information*). A possible explanation is that large aggregate formation is precluded by suppressed crystallization of PCL at the core-corona interface, caused by the disruption of chain packing by the large number of PCL-GNP particles in the core. PDI values from cumulant analysis of DLS data (Figure 5E, red data points) reveal that all GNP-PNP compositions form particle populations of relatively low polydispersity (PDI ≤ 0.3); PDI increases from 0.2 to 0.3 with the initial increase in $r_{PCL\text{-}GNP}$ from 2 to 10 then remains relatively constant to $r_{PCL\text{-}GNP}$ = 50, followed by a large decrease of PDI to 0.15 and a disappearance of the large aggregates and small aggregate (<30 nm). The further increase of $r_{PCL\text{-}GNP}$ to 100 sees the reappearance of small and large aggregates as the PDI climbs to just under 0.3 where many GNPs are included in the large aggregates and there are mostly small aggregates many of which are empty. This is not well understood but likely the result PCL-GNPS clustering into larger aggregates to reduce surface area that PCL-*b*-PEO would cover. The appearance of the empty small PNPs and large aggregates

suggests that at $r_{PCL\text{-}GNP}$ = 100 there might be PCL-GNP aggregates in the dispersion before water addition.

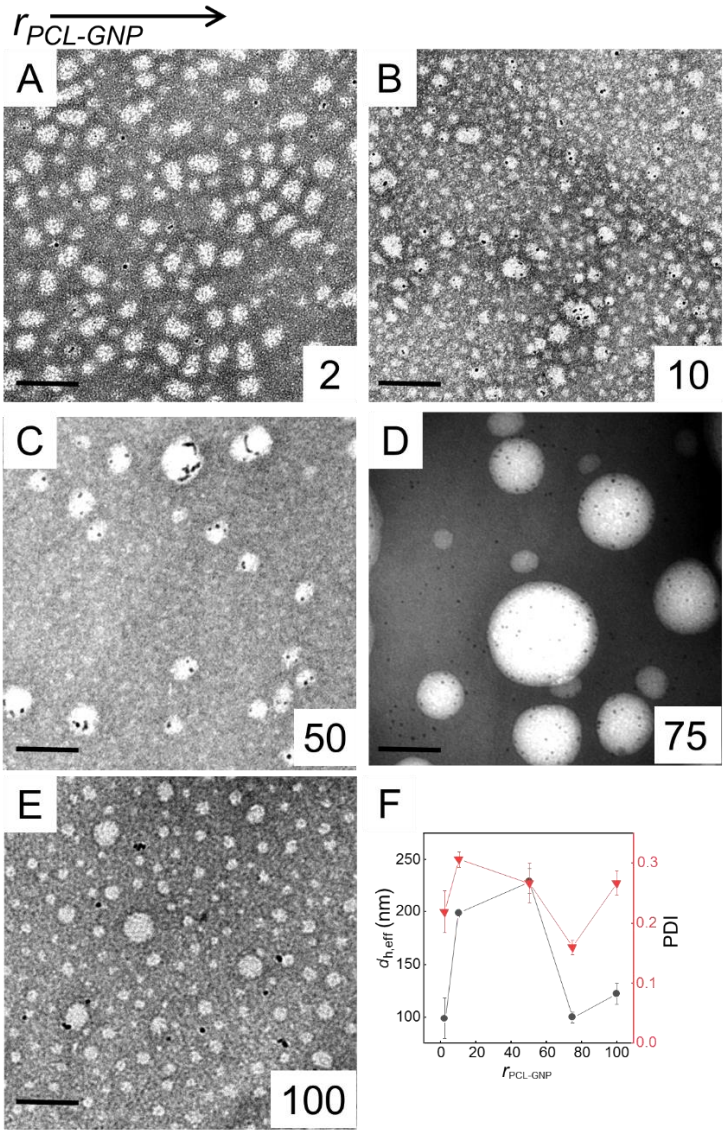

Figure 3.5. (A-E) TEM images of GNP-PNPs prepared using the bulk method at different PCL-GNP/PCL-*b*-PEG (w/w) ratios labelled in bottom right hand of each image, $r_{PCL-GNP}$. (F) Corresponding $d_{h,eff}$ (black data points) and PDI (red data points) values from cumulant analysis of DLS data plotted versus $r_{PCL-GNP}$. Reported values and error bars were determined from triplicate preparations Scale bars on TEM images are 100 nm.

3.3.3 Microfluidic Encapsulation of PCL-GNPs and Effect of Flow Rate on GNP-PNPs.

We next investigated the effect of microfluidic flow rate on the internal structure of GNP-PNPs formed at a constant PCL-GNP/PCL-*b*-PEG ratio of $r_{PCL\text{-}GNP}$ = 75 and $r_{PCL\text{-}GNP}$ = 100. The bulk experiment at $r_{PCL\text{-}GNP}$ = 75 and $r_{PCL\text{-}GNP}$ = 100, described in the previous section (Figure 3.5D), is used as a control in the microfluidic flow rate series, and is designated by zero flow rate, Q = 0 µL/min. The microfluidic samples were prepared at four different flow rates: Q = 50, 100, 200, and 400 µL/min. In the TEM image in Figure 3.6, C, GNP-PNPs formed at the fastest microfluidic flow rate appears to contain few GNPs, and large GNP aggregates much larger than those that appear in the TEM image of the PCL-GNPS (Figure 3.3C), therefore we assume that at this flow rate the PCL-GNPS are being amalgamated and so this flow rate was not studied further.

The GNP-PNPs prepared in bulk were 105 and 145 nm for $r_{PCL\text{-}GNP}$ = 75 and $r_{PCL\text{-}GNP}$ = 100 respectively. Increase in flow rate to Q = 50 µL/min leads to an increase in $d_{h,eff}$ up to 188 for the $r_{PCL\text{-}GNP}$ = 75 series while increased flow rate leads to a decrease to a decrease to 135 nm in the $r_{PCL\text{-}GNP}$ = 100 series. Increases in microfluidic flow rate to Q = 100 µL/min and then Q = 200 µL/min result in consecutive decreases in $d_{h,eff}$ to 176 nm and 66 nm, and then to $d_{h,eff}$ = 75 nm and 56 nm, for $r_{PCL\text{-}GNP}$ = 75 and $r_{PCL\text{-}GNP}$ = 100 series respectively. The observed decrease in the mean size of GNP-PNPs is consistent with the observed changes in the corresponding CONTIN distributions (Figure S3.4, *Supporting Information*), which show a sharp relative increase in the intensity of particles with d_h < 100 nm compared to particles with d_h > 100 nm between the bulk and microfluidic preparations. PDI values (Figure 3.6A and B, red data points) show an increase from microfluidic mixing at all flow rates relative to the bulk.

The decrease in size and change in internal structure between bulk and microfluidic preparations at Q = 200 µL/min of GNP-PNPs (Figure 3.6A and B) is a result of on-chip exposure

of nascent micelles to high-shear hot spots within the microfluidic channels. The maximum shear rate within these hot spots increases linearly with flow rate and can be used as a processing handle to tune the sizes, morphologies, internal structure, and properties of functional PNPs. In the $r_{PCL\text{-}GNP}$ = 100 system, the primary effect of the hot spots is to trigger shear-induced breakup of larger GNP-PNPs formed early in the mixing channel (Figure S3.1, *Supporting Information*), resulting in microfluidic GNP-PNPs that are smaller and more polydisperse than those formed in the bulk. Further increases in the shear rate within the hot spots *via* increases in flow rate have only a marginal effect on the resulting GNP-PNP sizes, and do not significantly effect on their internal organization. This suggests that the shear energy provided by the hot spots at the minimum flow rate allow kinetically trapped particles observed in the bulk sample to reach a state close to thermodynamic equilibrium. We note that the internal structure of the microfluidic GNP-PNPs is also suggestive of a free energy minimum, with GNPs migrated to the outer layer of the core driven by the associated interfacial tension. Finally, it appears that the shear energy provided at the highest flow rate, Q = 400 μL/min, is sufficient to mechanically rupture a small number of equilibrium GNP-PNPs, as evidenced by the gold clusters found in this sample alone. In the $r_{PCL\text{-}GNP}$ = 75 system there is first an increase in $d_{h,eff}$ going from Q = 0 to 100 μL/min likely as a result of shear induced chain stretching and crystallization from cores that are more solid than the $r_{PCL\text{-}GNP}$ = 100 system. Increasing Q to 200 μL/min the threshold for the stretching appears to be surpassed and shear energy is transferred into break up and a similar reduction in size to the $r_{PCL\text{-}GNP}$ = 100 system occurs.

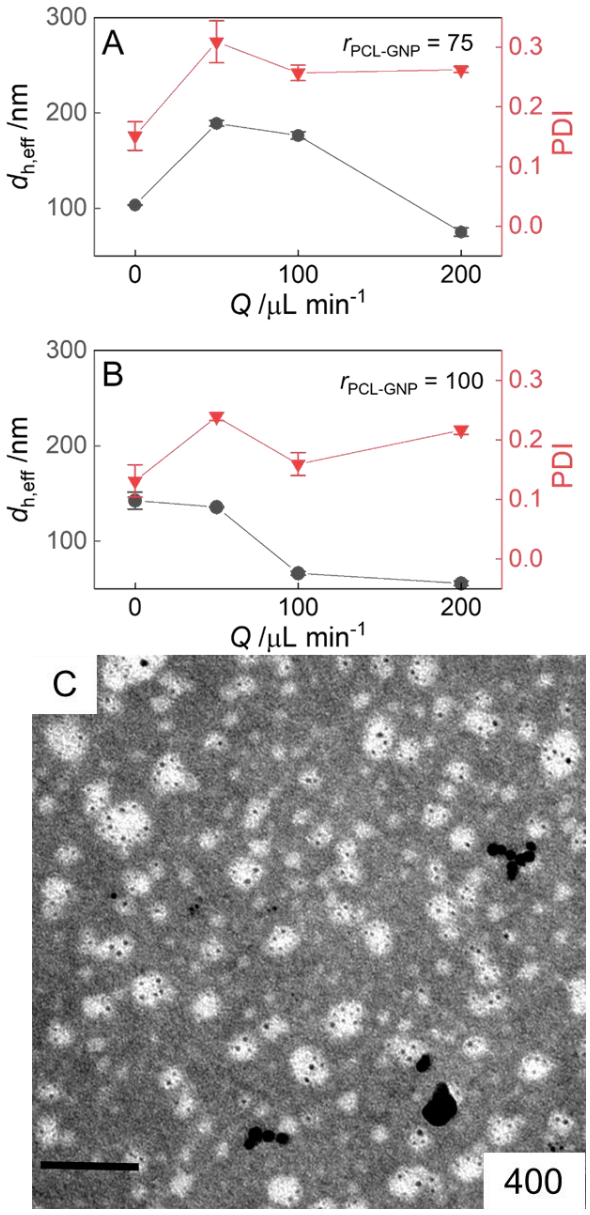

Figure 3.6. (A-B) Cumulant values from DLS measurements, $d_{h,eff}$ (black data points) and PDI (red data points), plotted versus Q for (A) $r_{PCL-GNP}$ = 75 (B) and $r_{PCL-GNP}$ = 100. Reported values and error bars were determined from triplicate GNP-PNP preparations. (C) TEM image of GNP-PNPs prepared at a PCL-GNP/PCL-*b*-PEG (w/w) ratio of $r_{PCL-GNP}$ = 100 using microfluidic mixing at Q = 400 μL • min^{-1}. Scale bar on TEM image is 200 nm.

3.3.4 Optical Properties of GNP, PCL-GNP, and GNP-PNP Dispersions.

One advantage of brush-directed GNP encapsulation is that the GNPs remain well-spaced by the surrounding brush layers within the PCL cores and therefore should retain the optical properties of individual GNPs. Photographs of dispersions at the three stages of GNP encapsulation (Figure 3.7A) and the corresponding UV-vis spectra (Figure 3.7B) support this feature of the current strategy. Transformation of GNPs to PCL-GNPs results in a change in the dispersion color from dark red to purple (Figure 3.7A), which is explained by the particle ripening observed by TEM, in addition to changes in solvent and surface chemistry. However, the self-assembly/encapsulation step does not give rise to any further color change; the purple color of the PCL-GNP dispersion persists in the GNP-PNP dispersion, although it becomes lighter due to dilution.

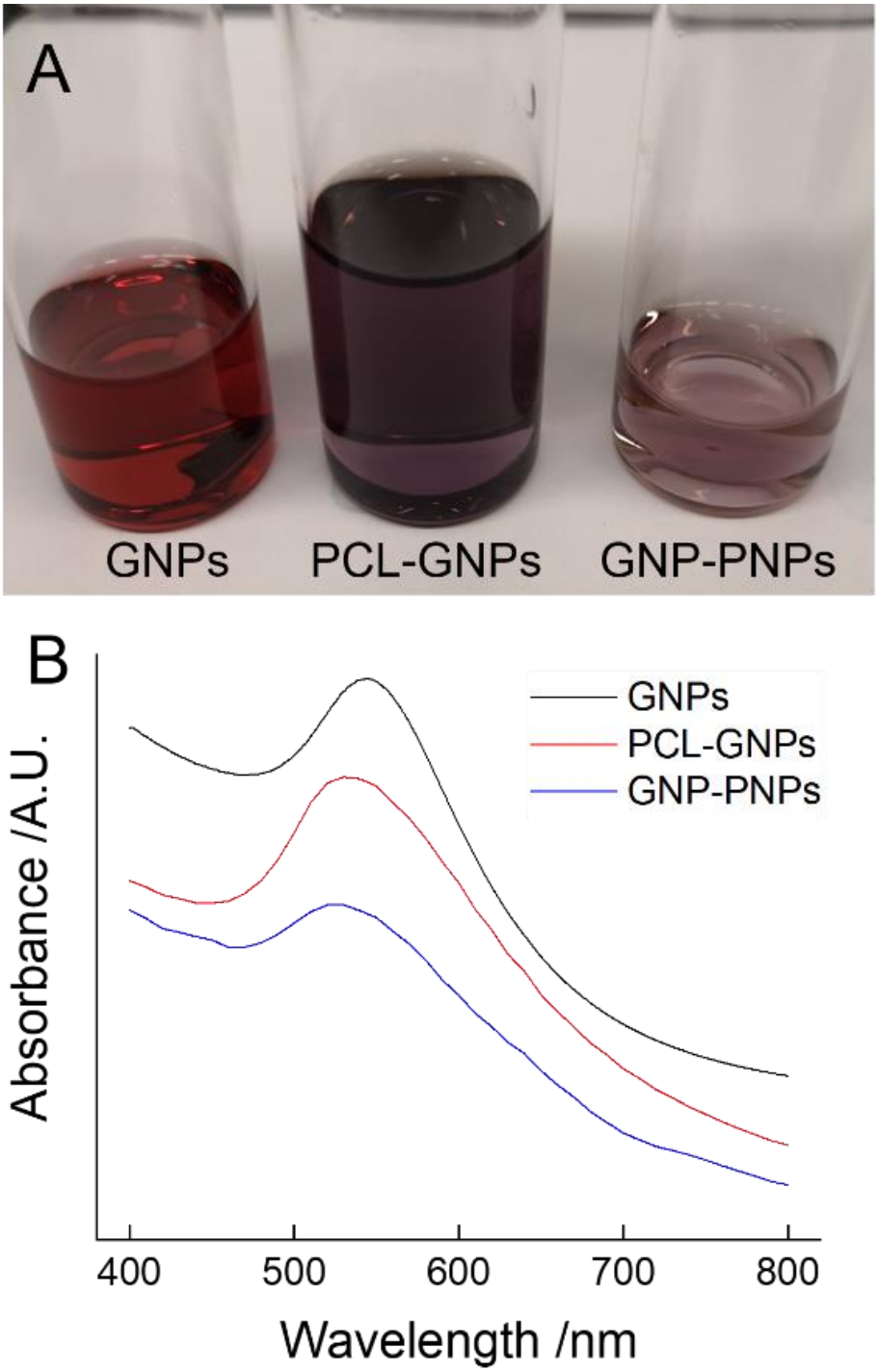

Figure 3.7. (A) Photographs of dispersions of GNPs (in water), PCL-GNPs (in DMF), and GNP-PNPs (in water) and (B) corresponding UV-vis spectra, which have been normalized and shifted along the *y*-axis for clarity.

Consistent with the observed color change between GNP and PCL-GNP dispersions (Figure 3.7A), the GNP surface plasmon peak at 545 nm (black trace, Figure 3.7B) shows broadening and a slight blue shift to 530 nm in the PCL-GNP dispersion (red trace, Figure 3.7B). On the other hand, consistent with the persistence of color upon PCL-GNP encapsulation (Figure 3.7A), the surface plasmon peaks of both PCL-GNP and GNP-PNP dispersions show 530 nm maxima (red and blue traces, respectively, Figure 3.7B), although the latter spectrum exhibits increased broadening from the overlapping scattering contribution of the larger GNP-PNP particles.

3.3.5 Functionalization and Encapsulation of GNRs.

In order to demonstrate the applicability of the present encapsulation strategy to other gold nanostructures, we carried out PCL-SH functionalization and PNP encapsulation of gold nanorods (GNRs). TEM images of synthesized GNRs before and after functionalization with PCL-SH are shown in Figure 3.8, A and C, respectively; corresponding distributions of the lengths and widths of GNRs from TEM images are provided in *Supporting Information* (Figure S3.5). Functionalization does not have a marked effect on the measured dimensions, with only very small changes to the mean length (44.9 ± 0.6 nm to 43 ± 1 nm) and mean width (25.9 ± 0.4 nm to 27 ± 1 nm) of GNR cores after adding the PCL brush layer. DLS analysis of mean effective hydrodynamic sizes before and after functionalization (Figure 3.8, B and D, respectively) support the addition of a soluble brush layer after reaction of GNRs with PCL-SH. Both CONTIN distributions show at least two diffusion modes associated with the non-centrosymmetric shape of GNRs, and all modes are found to shift to larger associated sizes after functionalization. In addition, the effective hydrodynamic diameter determined from cumulant analysis, which is the

dimension of an equivalent sphere, increases from 16 to 90 nm, strongly suggesting the presence of an additional polymer layer in the PCL-GNR dispersion.

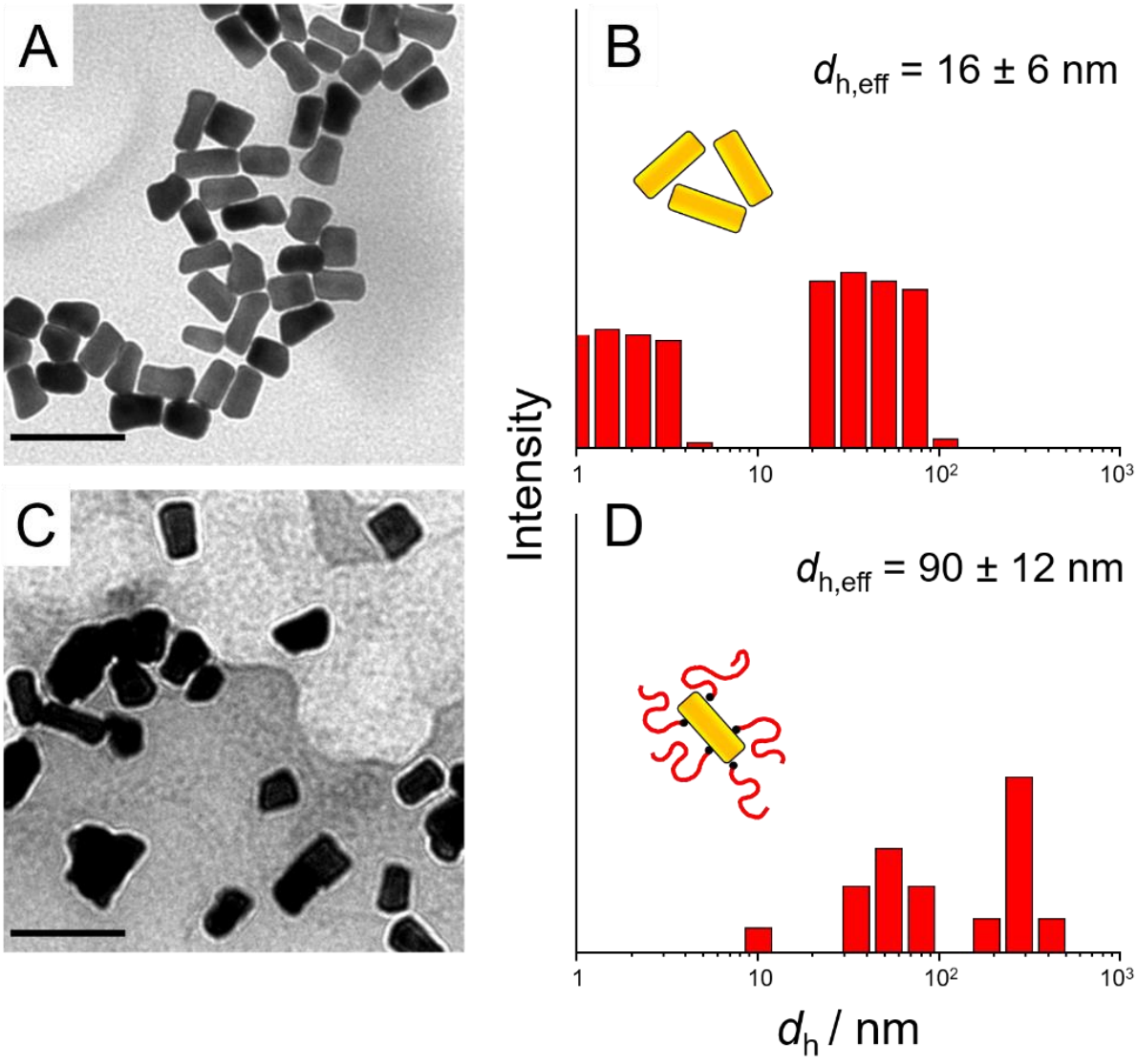

Figure 3.8. TEM images (A, C) and DLS analysis (B, D) for GNRs before (A, B) and after (C, D) PCL-SH functionalization. DLS analysis includes CONTIN hydrodynamic size distributions and mean effective hydrodynamic diameters, $d_{h,eff}$, from cumulant analysis for CTAB-functionalized GNRs in water (B) and PCL-GNRs in DMF (D). Scale bars in TEM images are 50 nm.

Finally, bulk encapsulation of PCL-GNRs was carried out at a single PCL-GNR / PCL-*b*-PEG (w/w) ratio of $r_{PCL\text{-}GNR} = 10$. Figure 3.9 shows TEM images of different grid regions for the resulting GNR-PNP sample. Many empty PNPs are present at this ratio, although all observed GNRs are found to be encapsulated within PCL cores. This confirms that different gold nanostructures can be encapsulated within biocompatible polymeric micelles using the present two-step strategy.

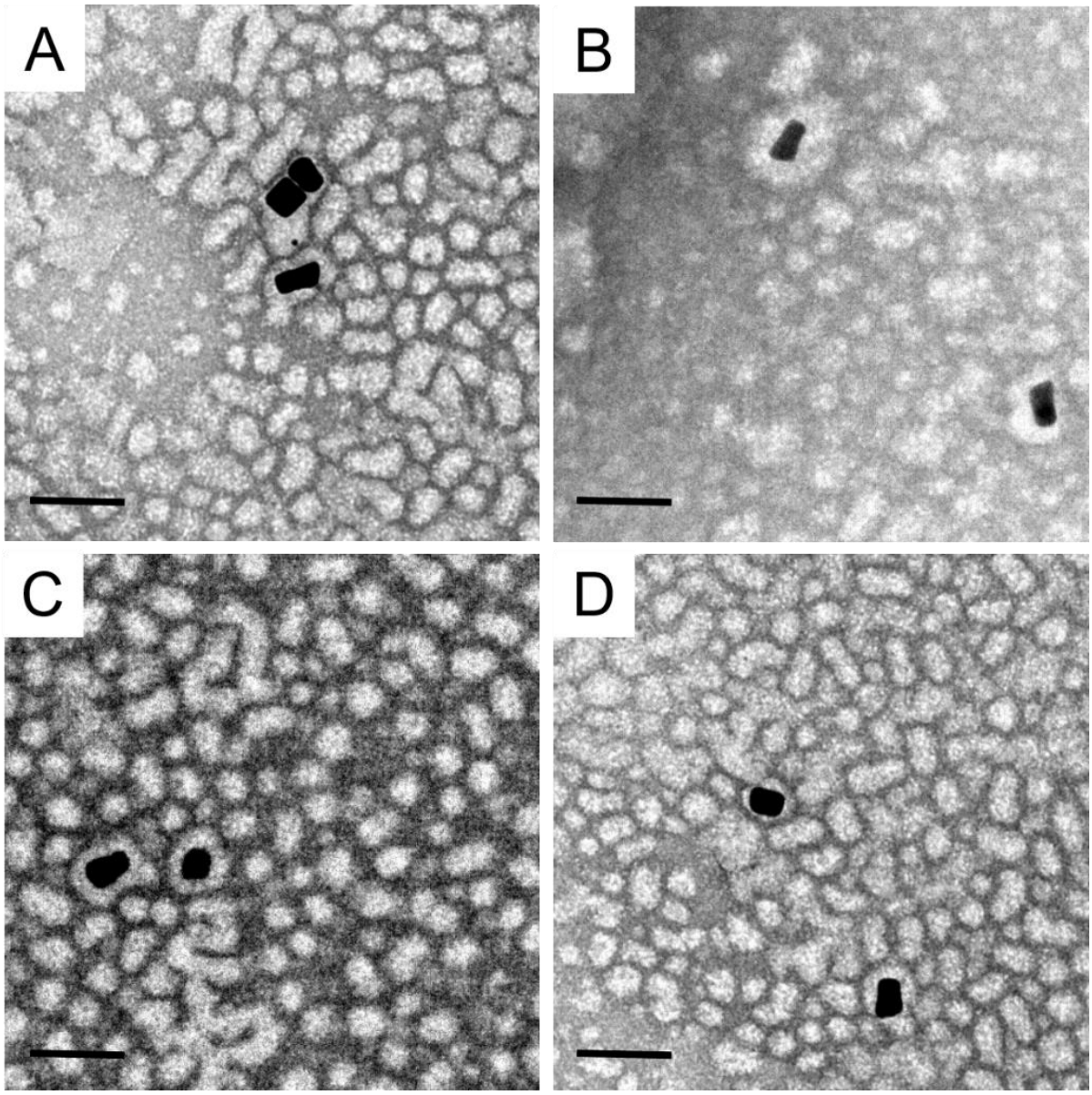

Figure 3.9. (A-D) TEM images taken in different regions of the grid for a sample of GNR-PNPs prepared at a PCL-GNR/PCL-*b*-PEG (w/w) ratio of $r_{PCL\text{-}GNP}$ = 10 using bulk mixing. Scale bars on TEM images are 200 nm.

3.3.6 Uptake of GNP-PNPs by MDA-MB-231 Cells.

Finally, we compared cell uptake of encapsulated GNPs (GNP-PNPs) prepared at $r_{PCL\text{-}GNP}$ = 75 system and $r_{PCL\text{-}GNP}$ = 100 and at Q = 0 , 50 , 100, and 200 μL/min with individual PEG-functionalized GNPs (PEG-GNPs). This study was performed in triplicate with new samples made from assembling stock solutions of PCL-GNPs and PCL-*b*-PEO for each replicate. The TEM and DLS data for the PEG-GNP control (Figure S3.6, *Supporting Information*) indicate that GNP diameters for the sample and control are similar (12 and 7 nm, respectively) whereas mean effective hydrodynamic diameters are very different (124 and 18 nm, respectively) due to encapsulation of multiple GNPs within a larger PNP in the sample dispersion. After incubating MDA-MB-231 cells with equal gold concentrations of either sample or control dispersions for 4 h at 37°C, the cells were washed 3× with PBS buffer before quantitative analysis of the amount of gold taken up by the cells.

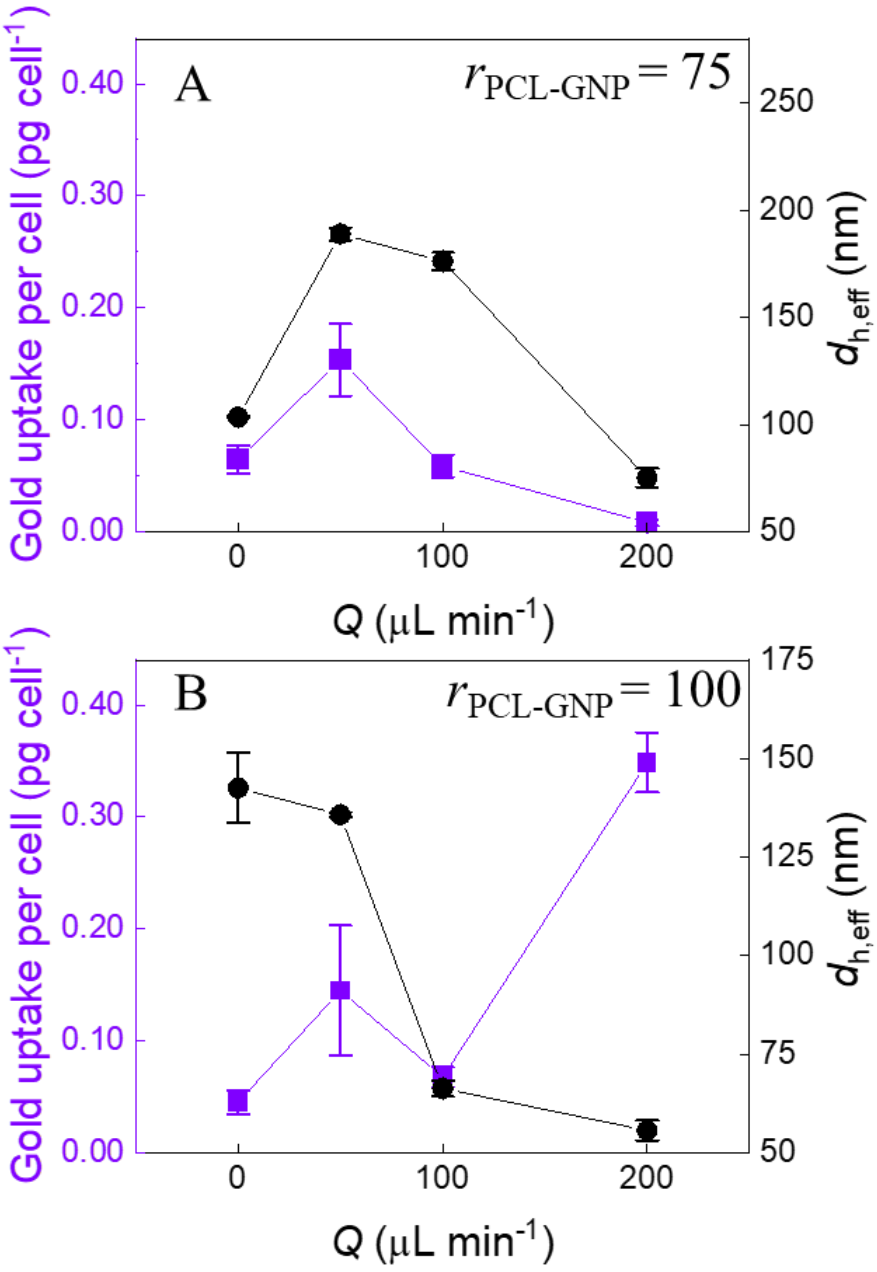

Figure 3.10. Results of cell uptake from GFAA analysis showing GNPs per cell from dosing cells with equal gold concentrations of GNP-PNPs formed at different flow rates (*Q*) on the microfluidic chip. (A) The $r_{PCL-GNP}$ = 75 system and (B) The $r_{PCL-GNP}$ = 100 system. Mean values and error bars were determined from triplicate incubation experiments using the same sample. Cell numbers were determined using a hemocytometer.

The method of converting MDA-MB-231 cells containing GNPs to solutions of Au^{3+} ions for GFAA analysis is described in the experimental; the associated GFAA calibration curve is provided in *Supporting Information* (Figure S3.7). Determined gold concentrations for cells treated with sample and control dispersions were converted to picograms (pg) of gold per cell. Mean values and associated errors (Figure 3.10) were determined from triplicate incubation experiments for the same samples and controls. The results show significantly higher uptake for GNP-PNPs prepared at $r_{PCL\text{-}GNP}$ = 100 system at Q = 200 µL/ min compared to PEG-GNPs and GNP-PNPS prepared at other conditions, confirming that encapsulation of GNPs by the current strategy is a viable route for improving cell uptake for therapeutic or diagnostic applications. The uptake for PEG-GNPS was found to be 0.05 ± 0.06 pg gold / cell while the cellular uptake for the at $r_{PCL\text{-}GNP}$ = 100 system at Q = 200 µL/ min was 0.35 ± .03 pg gold / cell. Statistical analysis show that the only sample to be statistically different than the PEG-GNP control at the 95% confidence level is the $r_{PCL\text{-}GNP}$ = 100 system at Q = 200 µL/ min. Since both sample and control particles are coated with a similar PEG surface layer, the enhanced encapsulation of GNP-PNPs is attributed to hydrodynamic size differences in addition to the packaging of multiple GNPs per GNP-PNP. Further enhancements of cell uptake can be expected from further GNP-PNP size optimization along with the addition of activating RGD peptides to the surface of GNP-PNPs,[40] A survey to analyze the TEM data was performed to investigate the effects of packaging, wherein GNP-PNPs were sized from TEM images for each condition and the number of GNPs within each PNP is counted. The data is presented in Figure 3.11 A - H as scatter plots.

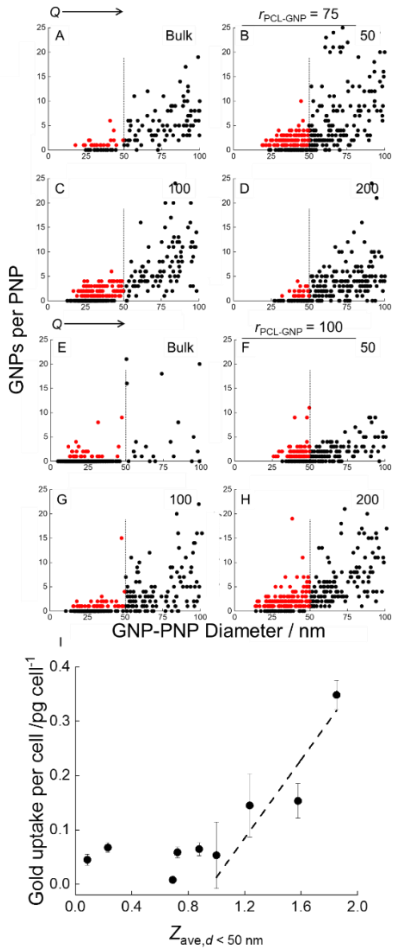

Figure 3.11. (A-D) Scatter plots demonstrating the occupancy of the GNP-PNPs (GNP per PNP) for GNP-PNPs of growing diameter for the $r_{PCL-GNP}$ = 75 condition at flow rates of 0, 50, 100, and 200 µL / min respectively. (E-H) Scatter plots demonstrating the occupancy of the GNP-PNPs (GNP per PNP) for GNP-PNPs of growing diameter for the $r_{PCL-GNP}$ = 100 condition at flow rates of 0, 50, 100, and 200 µL / min respectively. GNP-PNPs less than 50 nm that contain gold are red, while empty PNPs and GNP with diameter larger than 50nm are black. For counting n ≥ 300 PNPs for each sample. (I) Gold uptake per cell in picograms plotted against the average number of GNPs per PNPs less than 50 nm. PEG-GNP is the point at $Z_{ave,d<50\ nm} = 1$. Where $Z_{ave,d<50\ nm}$ is the average number of GNPS within a PNP with diameter less than 50 nm in a given sample.

The results in Figure 3.11 A-H demonstrate how changing the flow rate alters the distribution of GNPs within the GNP PNPs. Empty PNPs or GNP-PNPs with diameter larger than 50nm are indicated as black dots. GNP-PNPs less than 50 nm in diameter are indicated by red dots. Graphs A to D represent the $r_{PCL\text{-}GNP}$ = 75 conditions at flow rates of 0, 50, 100, and 200 µL / min respectively. The number of gold containing PNPs less than 50 nm is very low in the bulk and increases going to 50 µL/ min then decreases through 100µL /min to the final flow rate of 200 µL/ min. A similar pattern in graphs E to H emerge for the $r_{PCL\text{-}GNP}$ = 100 conditions, where there are few gold containing PNPs in the bulk, then there is an increase at 50µL/min followed by a decrease at 100 µL/min and then a large increase at the 200 µL/min conditions. The increase in cellular uptake of certain flow rates shown in Figure 3.10 correspond to larger fractions of GNP-PNPs being less than 50 nm.

There seem to be three factors that play a role in the uptake. The first factor is the number of GNP-PNPs less than 50nm, the second factor is the number of empty PNPs less than 50 nm, and the final factor is the number of GNPs per PNP in the GNP-PNPs less than 50 nm. To further investigate this, we plotted the gold uptake per cell in picograms against the average number of GNPs per PNP in GNP-PNPs less than 50 nm ($Z_{ave,d<50\ nm}$). The control of PEG-GNP which is just simply PEG decorated GNPs naturally has a $Z_{ave,d<50\ nm}$ = 1 because each particle is less than 50nm and contains only one gold particle. For samples with a $Z_{ave,d<50\ nm}$ < 1 there seems to be little difference in the gold uptake per cell as shown in Figure 3.11 I. Once the samples pass the $Z_{ave,d<50\ nm}$ = 1 there seems to be almost a linear increase in the gold uptake per cell with the $Z_{ave,d<50\ nm}$ value approaching $Z_{ave,d<50\ nm}$ = 2 which is the maximum for this series. Although further study is required to discern a detailed mechanism for the observed enhancement effect, we speculate that the uptake of multiple GNPs within a carrier of favorable size in a single endocytosis or

macropinocytosis event provides reduced-energy pathways allowing an increased number of GNPs to enter the cell.[50] Along with probing the effect of GNP occupancy for the first time, our results are also consistent with previous studies indicating preferential cellular uptake of nanoparticles in the 20-50 nm size regime.[15,16] Combining the two PCL-GNPs by condensing their PCL corona into the core of a GNP-PNP that is only 50 nm reduces the amount of stretching the cell would have to do to uptake the GNP-PNP relative to both PEG-GNPs. Example TEM images used in the statistical analysis of the GNP-PNPs for both $r_{\text{PCL-GNP}} = 75$ and 100 conditions at each flow rate is listed in *Supporting Information* (Figures S.39 to S3.16).

3.4 Conclusions

We demonstrate a PCL brush-directed encapsulation strategy to produce PNPs consisting of multiple 12-nm GNPs encapsulated within PCL cores and surrounded by a PEG shell. Specifically, GNPs are first functionalized with a brush layer of PCL chains followed by nanoprecipitation with PCL-*b*-PEGs and dialysis to produce PCL-GNPs. We investigate the effects of PCL-GNP/PCL-*b*-PEG (w/w) ratio and nanoprecipitation conditions on the mean sizes, polydispersities, and internal organization of GNP-PNPs. We show that the strategy can be successfully applied using simple bulk nanoprecipitation. We further demonstrate that additional size control can be obtained using microfluidic mixing in a two-phase, gas-liquid reactor for the second step. We demonstrate that the optical properties of individual GNPs are maintained upon encapsulation as a result of spacing between GNPs provided by the surrounding brush layers within PCL cores containing many GNPs. Furthermore, we demonstrate that encapsulation of GNPs by the current method enhances GNP uptake in MDA-MB-231 cancer cells compared to individual GNPs with similar PEG surface chemistry. In summary, PCL brush-directed encapsulation provides a versatile platform for packaging GNPs in biocompatible polymeric carriers for a wide range of therapeutic and diagnostic applications.

3.5 References

1. Dykman, L.; Khlebtsov, N. Biomedical applications of multifunctional gold-based nanocomposites. *Biochem. (Mosc.)* **81**, 1771-1789 (2016).

2. Luo, Z.; Xu, Y.; Ye, E.; Li, Z.; Wu, Y.-L. Recent progress in macromolecule-anchored hybrid gold nanomaterials for biomedical applications. *Macromol. Rapid Comm.* **40**, 1800029 (2019).

3. Luo, D.; Wang, X.; Burda, C.; Basilion, J. P. Recent development of gold nanoparticles as contrast agents for cancer diagnosis. *Cancers*. **13**, 1825 (2021).

4. D'Acunto, M.; Cioni, P.; Gabellieri, E.; Presciuttini, G. Exploiting gold nanoparticles for diagnosis and cancer treatments. *Nanotechnology*. **32**, 192001 (2021).

5. Si, P.; Razmi, N.; Nur, O.; Solanki, S.; Pandey, C. M.; Gupta, R. K.; Malhotra, B. D.; Willander, M.; de la Zerda, A. Gold nanomaterials for optical biosensing and bioimaging. *Nanoscale Adv.* **3**, 2679-2698 (2021).

6. Nejati, K.; Dadashpour, M.; Gharibi, T.; Mellatyar, H.; Akbarzadeh, A. Biomedical applications of functionalized gold nanoparticles: A review. *J. Clust. Sci.* **33,** 1-16 (2021).

7. Song, J.; Niu, G.; Chen, X. Amphiphilic polymer-guided plasmonic assemblies and their biomedical applications. *Bioconjug. Chem.* **28**, 105-114 (2016).

8. Butterworth, K. T.; McMahon, S. J.; Currell, F. J.; Prise, K. M. Physical basis and biological mechanisms of gold nanoparticle radiosensitization. *Nanoscale.* **4**, 4830-4838 (2012).

9. Cooper, D. R.; Bekah, D.; Nadeau, J. L. Gold nanoparticles and their alternatives for radiation therapy enhancement. *Front. Chem.* **2**. (2014)

10. Wang, J.; Li, W.; Zhu, J. Encapsulation of Inorganic Nanoparticles into Block Copolymer Micellar Aggregates: Strategies and Precise Localization of Nanoparticles. *Polymer*. **55,** 1079-1096 (2014).

11. Al Zaki, A.; Joh, D.; Cheng, Z.; De Barros, A. L. B.; Kao, G.; Dorsey, J.; Tsourkas, A. gold-loaded polymeric micelles for computed tomography-guided radiation therapy treatment and radiosensitization. *ACS Nano*. **8**, 104-112 (2014).

12. Chithrani, B. D.; Ghazani, A. A.; Chan, W. C. Determining the size and shape dependence of gold nanoparticle uptake into mammalian cells. *Nano Lett.* **6**, 662-668 (2006).

13. Sadauskas, E.; Danscher, G.; Stoltenberg, M.; Vogel, U.; Larsen, A.; Wallin, H. Protracted elimination of gold nanoparticles from mouse liver. *Nanomed.: Nanotechnol. Biol. Med.* **5,** 162-169 (2009).

14. Zhong, Y.; Wang, C.; Cheng, L.; Meng, F.; Zhong, Z.; Liu, Z. Gold nanorod-cored biodegradable micelles as a robust and remotely controllable doxorubicin release system for potent inhibition of drug-sensitive and resistant cancer cells. *Biomacromolecules*. **14**, 2411-2419 (2013).

15. Nguyen, C. T.; Tran, T. H.; Lu, X.; Kasi, R. M. Self-assembled nanoparticles from thiol functionalized liquid crystalline brush block copolymers for dual encapsulation of doxorubicin and gold nanoparticles. *Polym. Chem.* **5**, 2774-2783 (2014).

16. Bains, A.; Cao, Y. M.; Moffitt, M. G. Multiscale control of hierarchical structure in crystalline block copolymer nanoparticles using microfluidics. *Macromol. Rapid Comm.* **36,** 2000-2005 (2015).

17. Bains, A.; Cao, Y. M.; Kly, S.; Wulff, J. E.; Moffitt, M. G. Controlling structure and function of polymeric drug delivery nanoparticles using microfluidics. *Mol. Pharm.* **14,** 2595–2606 (2017).

18. Deng, H.; Zhong, Y.; Du, M.; Liu, Q.; Fan, Z.; Dai, F.; Zhang, X. Theranostic self-assembly structure of gold nanoparticles for NIR photothermal therapy and x-ray computed tomography imaging. *Theranostics.* **4**, 904 (2014).

19. Azzam, T.; Eisenberg, A. Monolayer-protected gold nanoparticles by the self-assembly of micellar poly(ethylene oxide)-*b*-poly(ε-caprolactone) block copolymer. *Langmuir*. **23**, 2126-2132 (2007).

20. Javakhishvili, I.; Hvilsted, S. Gold nanoparticles protected with thiol-derivatized amphiphilic poly(ϵ-caprolactone)-*b*-poly (acrylic acid). *Biomacromolecules*. **10**, 74-81 (2009).

21. Zhao, S.; Zhou, F.; Liu, R. Hybrid supramolecular hydrogels induced by au nanoparticles protected with MPEG-*b*-PCL copolymers with *α*-cyclodextrin. *Supramol. Chem.* **25**, 767-776 (2013).

22. Zhong, Y.; Wang, C.; Cheng, R.; Cheng, L.; Meng, F.; Liu, Z.; Zhong, Z. cRGD-directed, NIR-responsive and robust auNR/PEG–PCL hybrid nanoparticles for targeted chemotherapy of glioblastoma *in vivo*. *J. Control. Release*. **195**, 63-71 (2014).

23. Abbasian, M.; Mahmoodzadeh, F.; Salehi, R.; Amirshaghaghi, A. Chemo-photothermal therapy of cancer cells using gold nanorod-cored stimuli-responsive triblock copolymer. *New J. Chem.* **41**, 12777-12788 (2017).

24. Xu, F.; Zhang, P.; Zhang, J.; Yu, C.; Yan, D.; Mai, Y. Crystallization-driven two-dimensional self-assembly of amphiphilic PCL-*b*-PEO coated gold nanoparticles in aqueous solution. *ACS Macro Lett.* **7**, 1062-1067 (2018).

25. Li, Y.; Si, J.; Fan, H.; Yang, J.; Ye, X. Reduction-responsive diblock copolymer-modified gold nanorods for enhanced cellular uptake. *RSC Adv.* **8**, 27546-27555 (2018).

26. Abbasian, M.; Judi, M.; Mahmoodzadeh, F.; Jaymand, M. Synthesis and characterization of a pH-and glucose-responsive triblock copolymer via RAFT technique and its conjugation with gold nanoparticles for biomedical applications. *Polym. Advan. Technol.* **29**, 3097-3105 (2018).

27 Liu, M.; Huang, P.; Wang, W.; Feng, Z.; Zhang, J.; Deng, L.; Dong, A. An Injectable nanocomposite hydrogel co-constructed with gold nanorods and paclitaxel-loaded nanoparticles for local chemo-photothermal synergetic cancer therapy. *J. Mater. Chem.* **7**, 2667-2677 (2019).

28. Fallah iri sofla, S.; Abbasian, M.; Mirzaei, M. A novel gold nanorods-based pH-sensitive thiol-ended triblock copolymer for chemo-photothermo therapy of cancer cells. *J. Biomater. Sci. Polym. Ed.* **30**, 12-33 (2019).

29. Mahmoodzadeh, F.; Hosseinzadeh, M.; Jannat, B.; Ghorbani, M. Fabrication and characterization of gold nanospheres-cored pH-Sensitive thiol-ended triblock copolymer: A smart drug delivery system for cancer therapy. *Polym. Advan. Technol.* **30**, 1344-1355 (2019).

30. Zeng, L.; Su, Z.; Li, X.; Shi, S. Construction of triblock copolymer-gold nanorod composites for fluorescence resonance energy transfer via pH-sensitive allosteric. *Chin. Chem. Lett.* **31**, 3131-3134 (2020).

31. Gindy, M. E.; Panagiotopoulos, A. Z.; Prud'homme, R. K. Composite block copolymer stabilized nanoparticles: Simultaneous encapsulation of organic actives and inorganic nanostructures. *Langmuir*. **24**, 83-90 (2008).

32. Ahmed, F.; Discher, D. E. Self-porating polymersomes of PEG-PLA and PEG-PCL: Hydrolysis-triggered controlled release vesicles. *J. Control. Release*. **96,** 37-53 (2004).

33. Geng, Y.; Discher, D. E. Hydrolytic degradation of poly(ethylene oxide)-*block*-polycaprolactone worm micelles. *J. Am. Chem. Soc.* **127**, 12780-12781 (2005).

34. Cai, S.; Vijayan, K.; Cheng, D.; Lima, E. M.; Discher, D. E. Micelles of different morphologies: Advantages of worm-like filomicelles of PEO-PCL in paclitaxel delivery. *Pharm. Res.* **24**, 2099-2109 (2007).

35. Zhang, Y.; Newton, B.; Lewis, E.; Fu, P. P.; Kafoury, R.; Ray, P. C.; Yu, H. Cytotoxicity of organic surface coating agents used for nanoparticles synthesis and stability. *Toxicol. In Vitro.* **29**, 762-768 (2015).

36. Martin, M. N.; Basham, J. I.; Chando, P.; Eah, S.-K. Charged gold nanoparticles in non-polar solvents: 10-min synthesis and 2D self-assembly. *Langmuir*. **26**, 7410-7417 (2010).

37. Sau, T. K.; Murphy, C. J. Room temperature, high-yield synthesis of multiple shapes of gold nanoparticles in aqueous solution. *J. Am. Chem. Soc.* **126**, 8648-8649 (2004).

38. Hinterwirth, H.; Kappel, S.; Waitz, T.; Prohaska, T.; Lindner, W.; Lämmerhofer, M. Quantifying thiol ligand density of self-assembled monolayers on gold nanoparticles by inductively coupled plasma–mass spectrometry. *ACS Nano*. **7**, 1129-1136 (2013).

39. Smith, A. M.; Johnston, K. A.; Crawford, S. E.; Marbella, L. E.; Millstone, J. E. Ligand density quantification on colloidal inorganic nanoparticles. *Analyst*. **142**, 11-29 (2017).

49. Chithrani, B. D.; Chan, W. C. Elucidating the mechanism of cellular uptake and removal of protein-coated gold nanoparticles of different sizes and shapes. *Nano Lett.* **7,** 1542-1550 (2007).

50. Kettler, K.; Veltman, K.; van De Meent, D.; van Wezel, A.; Hendriks, A. J. Cellular uptake of nanoparticles as determined by particle properties, experimental conditions, and cell type. *Environmental Toxicology and Cchemistry*, *33*, 481-492 (2014)

Chapter 4

Effects of Microfluidic Shear on Plasmid DNA Structure: Implications for Polymeric Gene Delivery Vectors.

Contributions: This chapter is the submitted version of a paper. Sundiata Kly and Lucas Andrew conceived the experiments; Lucas Andrew and Erin Moloney conducted the experiments; Lucas Andrew and Sundiata Kly analyzed the data; Lucas Andrew and Matt Moffitt wrote the submitted manuscript.

4.1 Introduction

The application of nucleic acids (NAs) to disease treatment is increasingly at the forefront of medical research. NAs have the potential to address persistent problems associated with traditional drugs, including high cost, low specificity, and potentially serious side effects.[1] Techniques allowing delivery of NAs into affected cells to alter gene expression offer a versatile approach to disease treatment and prevention;[2-4] recent notable examples include the Pfizer-BioNTech and Moderna vaccines for COVID-19, which employ mRNA payloads encoding for the SARS-Cov-2 spike protein to stimulate antibody production in the body.[5,6]

The design of NA delivery systems requires consideration of NA stability under shear stress during both manufacturing and delivery to ensure the genetic payload remains intact. Of particular interest is plasmid DNA (pDNA), which is regularly employed in gene therapy trials yet is prone to shear-induced degradation.[7] In the bloodstream, nanoparticles encounter shear stress in the range of 200 - 1500 s^{-1}, which can lead to pDNA degradation and reduced effectiveness of treatment, necessitating formulation of gene delivery vehicles designed to protect the pDNA payload.[8-11] Furthermore, pDNA is susceptible to shear-based degradation at the various steps of a typical gene therapy manufacturing workflow. For example, pDNA can be unintentionally degraded by excessive shear forces during mechanical pDNA isolation[12] or due to mixing during

larger-scale alkaline lysis preparations,[13] even before any further processing is carried out. After collection from bacterial cells via alkaline lysis, circular pDNA can exist in both open circular (OC) and linear (LN) isoforms, in addition to the native and most bioactive supercoiled circular (SC) conformation.[14,15] Further processing can then result in relaxation of the SC pDNA to the OC or L isoforms through localized damage to the pDNA backbone, or complete degradation of the pDNA into even smaller inactive segments.[16]

Using a rotating disk shear device, Levy et al. demonstrated that degradation of moderate-to-large-sized pDNA (pQR186, 13 kb; pQR150, 20 kb; pMT103, 29 kb) began to occur at shear rates of ~10^5 s^{-1} and increased as shear rate increased.[14] Shear degradation was shown to be more pronounced with higher MW plasmids, with pQR186, pQR150, and pMT103 pDNA samples showing SC isoform contents of 80 %, 40 %, and 8 %, respectively, following exposure to a shear rate of 4.8 x 10^5 s^{-1}.[14] Furthermore, it was shown that pDNA was more susceptible to shear-induced degradation in low ionic strength solvents, such as ultrapure pDNA lysates, or mixed solvents with a fractional water content.[14] Despite these important insights, the rotating shear disc device used to generate shear in those experiments[14] did not accurately reproduce the numerous interfaces and spatially-dependent shear fields encountered more frequently in pDNA formulations.[17-22]

Microfluidic techniques are increasingly employed for continuous, highly controllable synthesis of nanoparticle-based therapeutics.[23-26] For example, using a hydrodynamic flow focusing microfluidic reactor,[27] Wilson and coworkers achieved fast mixing of poly(beta-amino ester) and DNA/sucrose solutions to achieve low-dispersity poly(beta-amino ester)-DNA polyplexes.[19] That study further showed that no shear-induced DNA degradation had occurred during microfluidic manufacturing,[19] although shear rates were relatively low in the single-phase reactor of that study.[27] Our group has applied tunable high shear forces generated within “hot

spots" of a two-phase (gas-liquid) microfluidic reactor as a useful experimental handle on structure-properties of polymer delivery systems,[17,28-37] including those for pDNA,[22] during formulation development and optimization. Compared to a typical single-phase reactor used for nanomedicine formulation, we have shown that maximum shear rates within the hot spots of two-phase (gas-liquid) reactors are about 2 orders of magnitude higher, ranging from ~10^5-10^6 s^{-1} and increasing linearly with flow rate.[38]

In addition to reactor design and shear environment,[17,38] the effects of shear on pDNA during microfluidic manufacturing of gene therapy agents are expected to depend on chemical aspects of the formulation.[14] For instance, during microfluidic self-assembly and processing of polymer delivery systems, shear is generally applied in the presence of polymer excipients,[33-35,37] which can be free in solution or bonded to the pDNA payload.[22] In addition, the formulation of nanomedicine delivery systems commonly requires non-aqueous solvent environments, including various mixtures of polar organic solvents.[17,29,30,33,36,39] For example, in our recent synthesis of "polyplex-in-hydrophobic-core" (PIHC) micelles for NA delivery, a mixture of dioxane, acetic acid and water was employed in the microfluidic channels to balance the requirements of polymer solubility, polymer charging, and NA backbone and double helix integrity.[22] These considerations point to a clear need to better understand the effects of variable high shear rate during microfluidic manufacturing on the structural integrity of pDNA backbone and helix of different molecular weights in different solvent environments and under different conditions of polymer binding.

In this article, we describe a systematic study of the effects of flow-variable, high shear rates (10^5 s^{-1} - 10^6 s^{-1}) in a two-phase, gas-liquid microfluidic reactor on the structural integrity of the pDNA backbone and helix of varying molecular weights and under various solvent and polymer binding conditions. Following microfluidic shear exposure, the structural integrity of

pDNA backbone and helix is determined based on evaluation of identified bands in agarose gels. Specifically, we show that in polar organic solvent mixtures (containing dioxane, water, and acetic acid), similar to those employed during PIHC assembly,[25] low-molecular weight pDNA (pUC18) experienced shear degradation at the highest maximum microfluidic shear rate (1.6×10^6 s^{-1}) but remained relatively intact at the lowest maximum shear rate (4×10^5 s^{-1}). However, in a pure, deionized water environment, we show that pUC18 did not undergo shear degradation at any investigated shear rate, indicating the importance of solvent environment on shear sensitivity of pDNA in microfluidic channels. Moreover, we demonstrate that a functionalized block copolymer-pUC18 polyplex, formed from binding polycaprolactone-*block*-poly(2-vinylpyridine) (PCL-*b*-P2VP) with pUC18 pDNA, significantly mitigated shear degradation in the mixed solvent environment, illustrating that block copolymer functionalization can protect pDNA from the negative effects of microfluidic processing. Finally, we show that higher-molecular weight pDNA (pDSK519 and pRK290) exhibited greater sensitivity to shear degradation within microfluidic hot spots than lower-molecular weight pDNA (pUC18), supporting earlier rotating disk experiments.[14] This study lays the foundation for better understanding and mitigation of negative shear effects during microfluidic self-assembly and processing of polymeric nanoparticles for NA delivery. It should thus expand the toolkit of researchers seeking to incorporate the numerous advantages of microfluidic manufacturing into their design of new gene therapy formulations.

4.2 Experimental

4.2.1 Materials.

Polycaprolactone(35.0k)-*block*-poly(2-vinylpyridine)(20.5k) (PCL-*b*-P2VP, $Đ$ = 1.10, Polymer Source Inc.) was used without further purification. Lysogeny Broth (LB) medium

(Fisher), glycerol (>99.0%, Sigma), ampicillin (Sigma), kanamycin A (Sigma), tetracycline (Sigma), trypticase soy agar (TSA, Sigma), hydrochloric acid (HCl, 36.5%-38.0%, Sigma), ethidium bromide (EtBr, 95%, Sigma), 1,4-dioxane (>99.9% HPLC grade, Sigma), glacial acetic acid (>99.7%, Sigma), agarose (Sigma), tris-acetate-ethylenediaminetetraacetic acid buffer (TAE, Sigma), DNA gel loading dye (Fisher), were used as received.

4.2.2 Plasmid DNA Isolation and Characterization.

Three different bacterial plasmid DNA (pDNA) strains were used: pUC18 (low molecular weight) contains 2686 basepairs (2.7 kb) and 5372 phosphate groups and has a molecular weight of 1.75 x 10^3 kDa;[22] pDSK519 (medium molecular weight) contains 8100 basepairs (8.1 kb) and 16200 phosphate groups and has a molecular weight of ~5.3 x 10^3 kDa;[40] pRK290 (high molecular weight) contains ~20000 basepairs (~20 kb) and ~40000 phosphate groups and has a molecular weight of ~1.3 x 10^4 kDa.[41] pDNA was isolated from a frozen stock of Escherichia coli (*E.coli*) W1130 stored at -80°C in a 20% (v/v) glycerol/water solution. In a typical isolation process, the frozen stock was streaked onto TSA agar plates containing either 200 μg/mL ampicillin, 50 μg/mL kanamycin A, or 10 μg/mL tetracycline for the pUC18, pDSK519, and pRK290 plasmids respectively and allowed to grow overnight. 10 mL LB growth medium were inoculated from the TSA plates and allowed to grow overnight in an incubator at 37 °C with shaking (300 rpm) to produce an overnight culture. 2.0 mL of the overnight culture were used to inoculate 2.0 L of LB growth medium and allowed to grow overnight at 37 °C with shaking (300 rpm) to produce an isolation culture, which was divided into 4 × 500 mL aliquots. pDNA was then isolated from each aliquot into deionized (DI) water using a QIAGEN® Plasmid Maxiprep kit, resulting in ~1 mL pDNA samples which were further concentrated to 200-300 μL using centrifugal evaporation. All pDNA samples were characterized using a Thermo Fisher ND-1000 NanoDrop to determine purity and concentration. Since the experiments described in subsequent sections required higher pDNA concentrations than were accessible using a single Maxiprep kit, pDNA stock solutions consisted of multiple (3-6) isolated samples which were pooled and mixed by gentle vortexing. Only isolated samples with an absorbance ratio $A_{260:280} = 1.8 \pm 0.1$ were used for pooling. All pooled samples had absorbance ratios of $A_{260:280} = 1.8 \pm 0.1$ and $A_{260:230} = 2.00 \pm 0.03$ and pDNA concentrations in

the range of 700-1000 ng/μL. Finally, all pooled samples were diluted using DI water to a final pDNA concentration of 696 ng/μL and were stored at 4°C to be used as pDNA stock solutions in the experiments described below.

4.2.3 Preparation of pDNA Dispersions for Microfluidics.

From pDNA stock solutions, pDNA dispersions in various solvents with and without block copolymer functionalization were prepared for microfluidic shear experiments. For shear experiments on naked pDNA in mixed organic solvents, 45 μg of pDNA (64.5 μL of pDNA stock) were added with stirring to 500-600 μL of dioxane in a 1.5 mL Teflon centrifuge tube. Next, more dioxane was added to bring the volume of the tube to 1.0 mL, such that the pDNA concentration was 45 ng/μL and the solvent composition was 94/6 (w/w) dioxane/water.

For shear experiments on naked pDNA in deionized (DI) water (pUC18 only), 45 μg of pDNA (64.5 μL of pDNA stock) were added with stirring to 500-600 μL of DI water in a 1.5 mL Teflon centrifuge tube. Next, more DI water was added to bring the volume of the tube to 1.0 mL, such that the pDNA concentration was 45 ng/μL and the solvent composition was pure water.

Finally, for shear experiments on block copolymer-functionalized pDNA in mixed organic solvents (pUC18 only), 45.0 μg of pDNA (64.5 μL of pDNA stock) were added with stirring to 500-600 μL of a 70/30 (v/v) mixture of dioxane/acetic acid in a 1.5 mL Teflon centrifuge tube. Next, more 70/30 (v/v) dioxane/acetic acid mixture was added to bring the volume of the tube to 1.0 mL. Finally, PCL-*b*-P2VP in tetrahydrofuran (THF, 17.0 mg / mL) was added to the pUC18 solution at a molar ratio of 40:1 pyridinium: phosphate (93 μL). The resulting mixture was stirred at 800 rpm overnight at 21 °C. In the final dispersion, the pDNA concentration was 45 ng/μL, the

copolymer concentration was 1.5 mg/mL, and the solvent composition was 60/26/8/6 (w/w/w/w) dioxane/acetic acid/THF/water. The block copolymer-functionalized pDNA particles were designated PCL-pDNA.

4.2.4 Microfluidic Reactor Fabrication.

The microfabrication steps followed previously described procedures from our group.[36] Firstly, negative masters were fabricated on silicon wafers (Silicon Materials) using the negative photoresist SU-8 100 (Microchem). A 150 μm-thick SU-8 film was spin-coated at 2,000 rpm onto the silicon wafer and heated at 65 °C for 12 min and then at 95 °C for 50 min. After the wafer was cooled, a photomask was placed directly above, and the wafer was exposed to UV light for 100 s. Then, the UV-treated film was heated at 65 °C for 1 min and then 95 °C for 20 min. Finally, the silicon wafer was submerged in SU-8 developer (Microchem) and rinsed with isopropanol until all unexposed photoresist was removed.

Microfluidic chips were fabricated from polydimethylsiloxane (PDMS) using a SYLGARD 184 silicon elastomer kit (Dow Corning). For fabrication of all PDMS chips, the elastomer and curing agent were mixed at a 7:1 ratio and degassed under vacuum. The resulting mixture was poured over a clean negative master chip in a Petri dish and further degassed until all remaining air bubbles were removed. The PDMS was heated at 85 °C until cured (~20 min) and then peeled from the negative master; holes were punched through the reservoirs of the resulting PDMS chip to allow for the insertion of tubing. A thin PDMS film (substrate layer) was also made on a glass slide by spin-coating a 20:1 elastomer/curing agent mixture followed by curing. The substrate layer was then permanently bonded to the base of the microfluidic reactor (channel layer) after both components were exposed to oxygen plasma for 90 s. The resulting reactor (Figure 1) has a set

channel depth of 150 μm and consists of a sinusoidal mixing channel 100 μm wide and a sinusoidal processing channel 200 μm wide.

4.2.5 Flow Delivery and Control.

The steps of flow delivery and control followed previously described procedures.[36] Pressure-driven flow of liquids to the reactor inlet was provided using 1 mL gastight syringes (Hamilton) mounted on syringe pumps (Harvard Apparatus). The microfluidic chip was connected to the liquid syringes via 1/16th-inch (OD) Teflon tubing (Mandel Scientific). Argon (Ar) gas flow was introduced to the chip via an Ar tank regulator and a downstream regulator (Johnston Controls) for fine adjustments. The chip was connected to the downstream regulator through a 1/16th-inch (OD)/100-μm (ID) Teflon tube (Mandel Scientific). The liquid flow rate (Q_{liq}) was programmed via the syringe pumps, and the gas flow rate (Q_{gas}) was fine-tuned via the downstream pressure regulator in order to set a total nominal flow rate (Q) of 200 μL/min. Due to the compressible nature of the gas and the high gas/liquid interfacial tension, discrepancies arise between the nominal (programmed) and actual values of Q_{gas}, Q_{gas}/Q_{liq}, and the total flow rate (Q_{total}). Therefore, actual values of Q_{gas}, Q_{gas}/Q_{liq}, and $Q_{total} = Q_{gas} + Q_{liq}$ for each microfluidic experiment were calculated from the average volume of gas bubbles in the microchannels and are reported in *Supporting Information* (Table S1). Specifically, an image of the microchannels was captured using a Dalsa Genie Nano-C1280 camera mounted on a Nikon Ti2-U microscope at each of three different time periods at the beginning, middle, and end of the sample collection process. Analysis of the gas bubbles and liquid plugs within the microfluidic reactor was achieved using image analysis software (ImageJ), which gives the end-to-end distance of individual gas bubbles and liquid plugs, $L_{gas,i}$ and $L_{liq,i}$, respectively, under a given set of flow conditions. The gas-to-liquid flow ratio, Q_{gas}/Q_{liq}, was determined from each image as the ratio between measured $\sum_i L_{gas,i}$ and

$\sum_i L_{\mathrm{liq},i}$ (i = 20-50). Actual gas-to-liquid flow ratios for all experimental runs are reported as average values determined from 3 images for each run. All actual Q_{total} values within Table S1 are within 10 % of nominal Q values.

4.2.6 Microfluidic Shear Experiments.

Microfluidic shear experiments were carried out by combining one of the pDNA dispersions described in the previous section "Preparation of pDNA Dispersions for Microfluidics" (the pDNA stream) with two additional liquid streams in the two-phase microfluidic reactor (Figure 4.1) at a specified flow rate to generate stable gas-segmented liquid plugs with concomitant high shear hot spots. For all experiments, the flow rates of the three liquid streams were equal. Targeted gas-to-liquid flow ratios, $Q_{\mathrm{gas}}/Q_{\mathrm{liq}}$, were ~1 for all experiments and nominal total flow rates were Q = 100, 200, or 400 µL/min, yielding maximum shear rates of 4×10^5, 8×10^5, 1.6×10^6 s^{-1}.[38]

For shear experiments on naked pDNA in mixed organic solvents, the following three liquid streams were combined: (1) the pDNA stream, (2) pure dioxane, and (3) 25% (v/v) acidified DI water (pH 3, 0.3% (w/w) acetic acid) in dioxane, to yield a steady-state on-chip pDNA concentration of 15 µg/mL and a steady-state on-chip solvent composition of 90/10/< 0.1 (w/w/w) dioxane/water/acetic acid. Following on-chip shear exposure, samples were collected from the chip into empty vials, then transferred into a 6−8 kDa MWCO dialysis membrane (Spectrum Laboratories) and dialyzed against DI water for at least 12 h to remove dioxane and acetic acid, with changing of deionized water every hour for the first 4h, prior to analysis by gel electrophoresis.

For shear experiments on naked pDNA in deionized (DI) water (pUC18 only), the following three liquid streams were combined: (1) the pDNA stream, (2) pure DI water, and (3) pure DI

water, to yield a steady-state on-chip pDNA concentration of 15 μg/mL and a steady-state on-chip solvent composition of pure DI water. Following on-chip shear exposure, samples were collected from the chip into empty vials, then analyzed by gel electrophoresis.

Finally, for shear experiments on block copolymer-functionalized pDNA (PCL-pDNA) in mixed organic solvents (pUC18 only), the following three liquid streams were combined: (1) the pDNA stream, (2) pure dioxane, and (3) pure dioxane, to yield a steady-state on-chip pDNA concentration of 15 μg/mL, a steady-state on-chip copolymer concentration of 0.5 mg/mL, and a steady-state on-chip solvent composition of 86/9/3/2 (w/w/w/w) dioxane/acetic acid/THF/water. Following on-chip shear exposure, samples were collected from the chip into empty vials, then PCL-pDNA particles were treated to remove copolymer chains as described in the section below, prior to analysis by gel electrophoresis.

4.2.7 Release of pDNA from PCL-pDNA.

Following on-chip shear exposure of PCL-pDNA, pDNA was released from the copolymer for gel electrophoresis analysis in the following manner. First, ice-cold isopropanol was added to the collected PCL-pDNA particles at a 1:1 (v/v) ratio and the resulting mixture was incubated for 4 h at 21°C to precipitate the PCL-pDNA, followed by centrifugation at 12000 × g for 30 min to yield a colorless opaque pellet. The supernatant was decanted, and the PCL-pDNA pellet was suspended in 1 mL 100 mM TAE buffer (pH 8) to deprotonate the P2VP blocks and release the electrostatically bound pDNA into the buffer. The suspension was centrifuged again at 12000 × g for 30 min to pellet the residual insoluble polymer. The supernatant comprised of pDNA in TAE buffer was collected and washed with chloroform to remove residual copolymer.

4.2.8 Zero-Shear Control Experiments.

In order to determine the effect of the mixed organic solvent environment on naked pDNA in the absence of shear (pUC18 only), pDNA dispersions were prepared in both glass and Teflon vials at a pDNA concentration of 15 μg/mL and a solvent composition of 90/10/< 0.1 (w/w/w) dioxane/water/acetic acid, identical to the steady-state on-chip solvent conditions of microfluidic shear experiments. Both glass and Teflon vials were used to assess the extent of adhesion of pUC18 pDNA to the walls of the glass collection vial following microfluidic experiments. The control dispersions were incubated for 90 min, then transferred into a 6−8 kDa MWCO dialysis membrane (Spectrum Laboratories) and dialyzed against DI water for at least 12 h to remove dioxane and acetic acid, with changing of deionized water every hour for the first 4h, prior to analysis by gel electrophoresis.

4.2.9 Agarose Gel Electrophoresis.

Aqueous pDNA samples for agarose gel electrophoresis analysis were concentrated by centrifugal evaporation to a volume of < 20 μL, then mixed in a 1:6 (v/v) ratio with DNA gel loading dye. 18.0 μL of each resulting solution were subjected to electrophoresis in 1× TAE buffer. Gel concentrations and running conditions varied depending on plasmid size. For pUC18 pDNA, samples were run in a 0.9% agarose gel at 5.8 V/cm for 1 h; for pDSK519 pDNA, samples were run in a 0.7% agarose gel at 5.0 V/cm for 90 min; for pRK290 pDNA, samples were run in a 0.5% agarose gel at 2.0 V/cm for 3 h. Gels were stained by immersion in an aqueous EtBr bath (0.5 μg/mL) for 15 min and then imaged in an AlphaImager™ Gel Imaging System (Alpha Innotech). All gel runs were compared against a 1kb DNA ladder (Fisher).

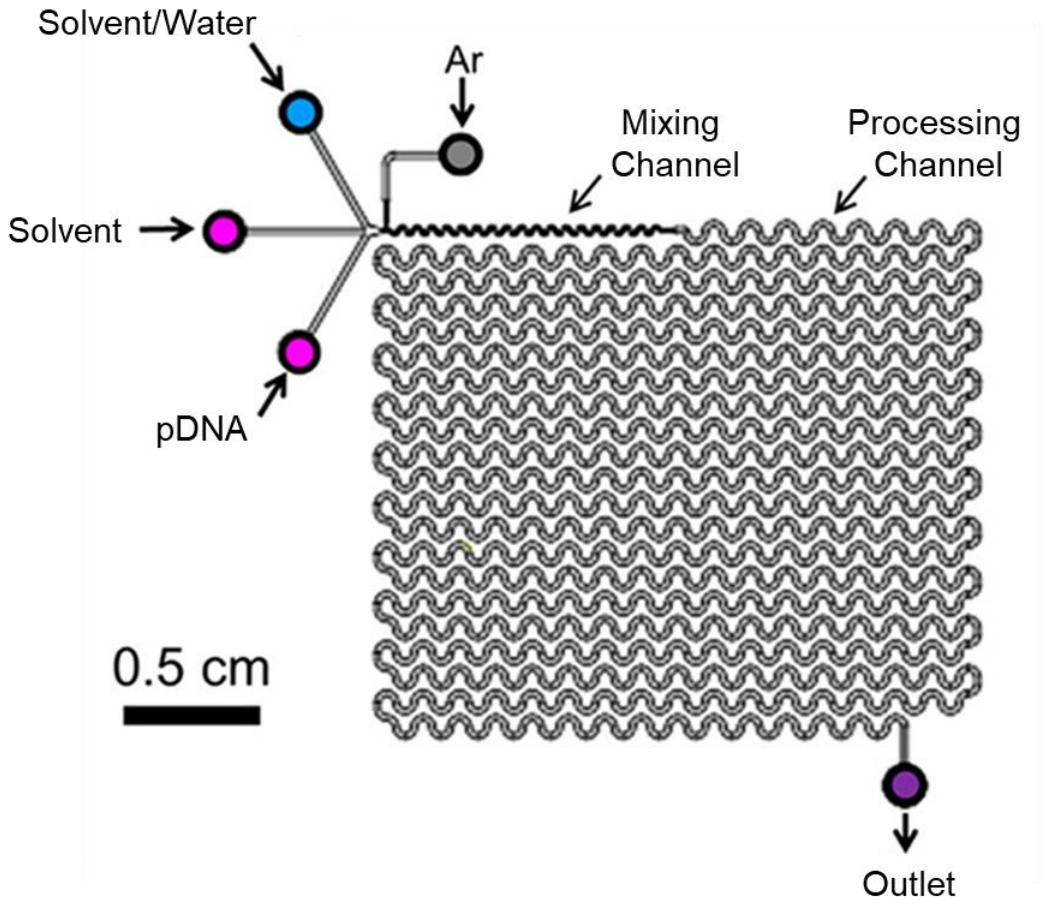

Figure 4.1. Diagram of the two-phase (gas-liquid) microfluidic reactor.

4.3 Results and Discussion

4.3.1 Effect of Microfluidic Shear on Naked pUC18 pDNA in Aqueous and Mixed Organic Solvent Environments.

We first investigated the effect of variable high-shear hot spots in a two-phase, gas-liquid microfluidic reactor on naked pUC18 pDNA under two different solvent conditions (aqueous and mixed organic) and different flow rates of Q = 100, 200, or 400 μL/min, corresponding to maximum shear rates of 4×10^5, 8×10^5, and 1.6×10^6 s^{-1}, respectively.[38] For the aqueous condition, the on-chip solvent composition was pure DI water and for the mixed organic solvent condition, the on-chip solvent composition was 90/10/< 0.1 (w/w/w) dioxane/water/acetic acid. The on-chip pDNA concentration for all experiments was 15 μg/mL. The mixed organic solvent composition approximates the dioxane/water mixtures applied in our previous paper for the hierarchical self-assembly of PIHC delivery vectors, including the presence of acetic acid to promote protonation of the copolymer.[22] Recognizing that similar mixed organic solvents could be used for future microfluidic processing of pDNA, we were motivated to determine the role of such mixed solvents in affecting the shear stability of pDNA in the microfluidic channels.

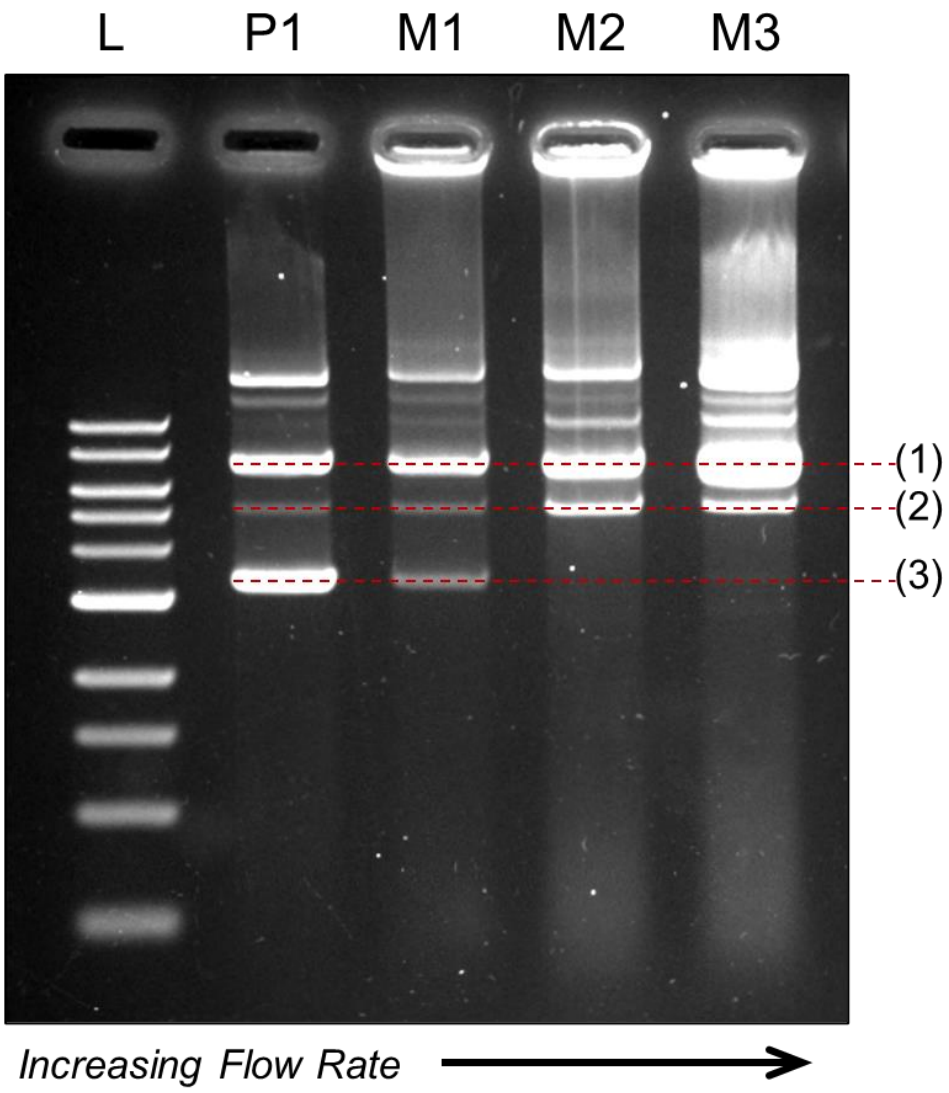

Figure 4.2. Effect of microfluidic flow rate on shear-induced degradation of naked low-molecular weight pDNA (pUC18, 2.7 kb) in a mixed organic solvent (90/10/< 0.1 (w/w/w) dioxane/water/acetic acid). Agarose gel electrophoresis image of a 1kb DNA ladder (lane L), untreated pDNA control (lane P1), and naked pDNA after passing through the microfluidic chip at flow rates of Q = 100 µL/min (lane M1), 200 µL/min (lane M2), and 400 µL/min (lane M3). Bands associated with OC (1), LN (2) and SC (3) isoforms are indicated.

We observed flow-rate dependent shear degradation of naked pUC18 in the microfluidic channels in mixed organic solvents. Figure 4.2 shows gels of naked pUC18 samples following microfluidic shear experiments in the mixed organic solvent environment at three different flow rates, Q = 100, 200, or 400 µL/min, corresponding to lanes M1, M2, and M3. Lanes L and P1 correspond to a 1kb DNA ladder and a naked pUC18 control sample that had not been run through the microfluidic chip. Bands corresponding to the three main pDNA isoforms, (1) OC, (2) LN, and (3) SC are identified.[14,15] In comparison with lane P1 (control), lane M1 (Q = 100 µL/min) shows a decrease in intensity of the SC band (3) relative to the OC (1) and LN (2) bands. Furthermore, lanes M2 Q = 200 µL/min (8×10^5 s^{-1}) and M3 Q = 400 µL/min (1.6×10^6 s^{-1}) show complete disappearance of the SC band (3), along with marked increases in the intensity of both OC (1) and LN (2) bands compared to lane P1 (control) and lane M1 (Q = 100 µL/min). Additionally, a progressive increase in streaking is observed at the bottom of the image between lanes M1 and M3, suggesting an increase in the concentration of small, fast-running fragments originating from multiple double stranded breaks.[14] Based on these observations, it appears that the maximum shear rate within the microfluidic channel at the lowest investigated flow rate, Q = 100 µL/min (4×10^5 s^{-1}), was sufficient to partially damage pUC18, leading to some relaxation of the SC isoform via localized nicks or double-strand breaks into OC and LN isoforms .[16] In the future we would like to compare these gels to ones where the plasmid has been cut with topoisomerase and an endonuclease to confirm the level of backbone degradation.

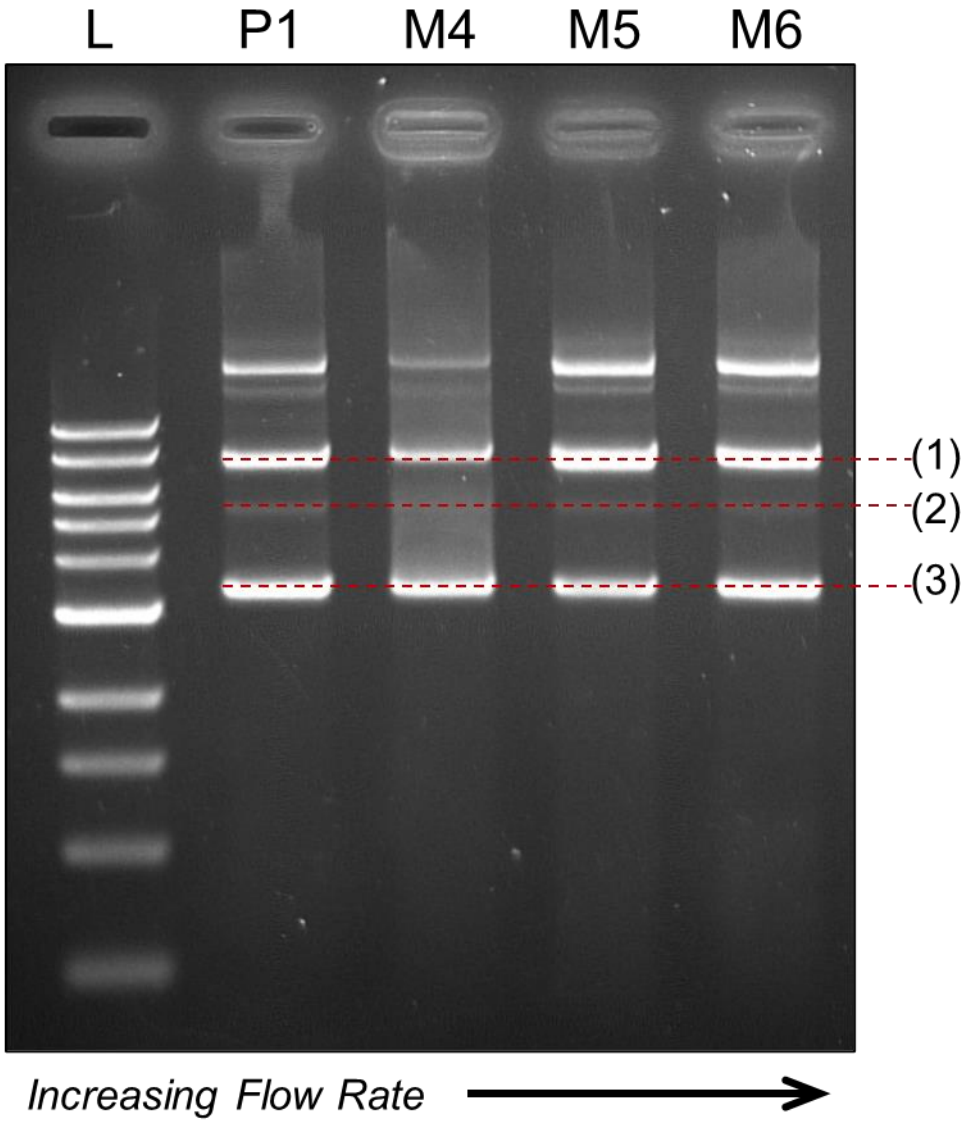

Figure 4.3. Effect of microfluidic flow rate on shear-induced degradation of naked low-molecular weight pDNA (pUC18, 2.7 kb) in an aqueous environment (pure DI water). Agarose gel electrophoresis image of a 1kb DNA ladder (lane L), untreated pDNA control (lane P1), and naked pDNA after passing through the microfluidic chip at flow rates of Q = 100 µL/min (lane M1), 200 µL/min (lane M2), and 400 µL/min (lane M3). Bands associated with OC (1), LN (2) and SC (3) isoforms are indicated.

In contrast, we did not observe flow-rate dependent shear degradation of naked pUC18 in the microfluidic channels in a purely aqueous environment. Figure 4.3 shows gels of naked pUC18 samples following microfluidic shear experiments in the aqueous (pure DI water) environment at three different flow rates, Q = 100, 200, or 400 μL/min, corresponding to lanes M4, M5, and M6, with lanes L and P1 corresponding to a 1kb DNA ladder and the naked pUC18 control sample respectively. Unlike the microfluidic shear experiments in mixed organic solvent, the intensity of the SC (3) band relative to the OC (1) and LN (2) bands in all three microfluidic lanes, M4, M5, and M6, remains similar compared to lane P1 (control). This indicates that shear-induced relaxation of the SC isoform of pUC18 into OC and LN isoforms was negligible in the microfluidic channels under aqueous conditions. Furthermore, unlike the series of experiments in mixed organic solvents, we see no streaking at the bottom of the gels in lanes M4, M5, or M6, suggesting an absence of complete degradation into small fragments at any experimental flow rate.

To confirm that the observed microfluidic degradation of pUC18 in mixed organic solvent (Figure 4.2) was shear-induced and not simply a solvent effect, we carried out control experiments in which pUC18 was incubated in the mixed solvent environment (90/10/< 0.1 (w/w/w) dioxane/water/acetic acid) under quiescent conditions for 90 min in both glass and Teflon vials. Figure 4.4 shows gels of naked pUC18 untreated (lane P1), incubated in mixed organic solvent in a glass vial (lane I1), and incubated in mixed organic solvent in a Teflon tube (lane I2). We observe a slight decrease in the intensity of the SC (3) band in both incubation experiments (lanes I1 and I2) compared to the control (land P1), indicating a possible solvent degradation effect under quiescent conditions. However, unlike the medium- and high-flow microfluidic experiments in the same solvent environment (Figure 4.2), the SC (3) band in both incubation experiments remains

intact, and the relative increase in the intensity of the OC (1) and LN (2) bands compared to the control is much less marked. This confirms that a combination of shear and the mixed organic solvent environment led to the flow-dependent degradation of naked pUC18 in the microfluidic channels. Moreover, we note that the ratios of band intensities are very similar in lanes I1 and I2, indicating that there was no significant loss of pDNA due to adhesion to the walls of the glass vials.

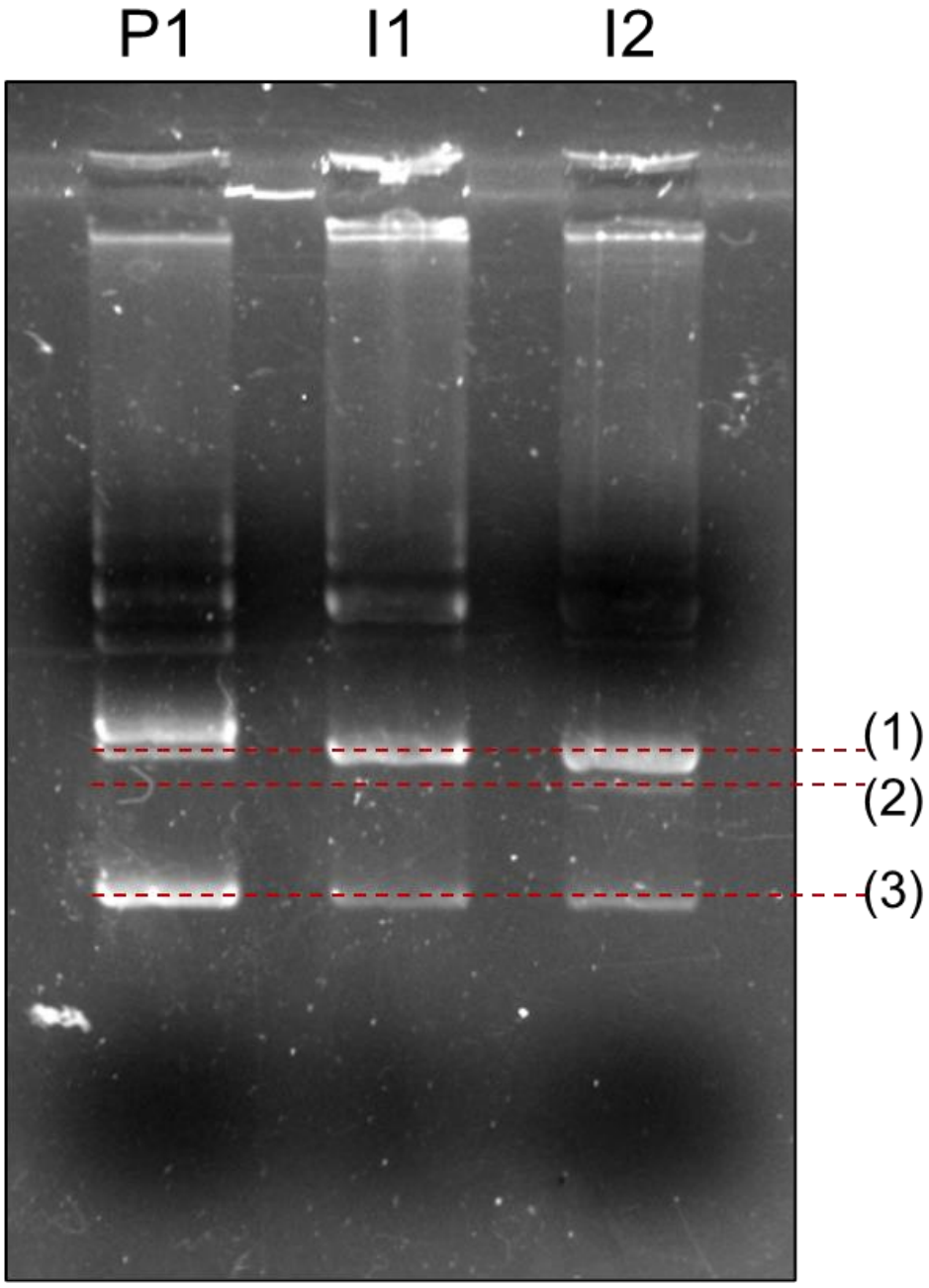

Figure 4.4. Zero-shear control incubation experiments on naked low-molecular weight pDNA (pUC18, 2.7 kb) in a mixed organic solvent (90/10/< 0.1 (w/w/w) dioxane/water/acetic acid). Agarose gel electrophoresis image of an untreated pDNA control (lane P1), and naked pDNA after incubation in the mixed solvent for 90 min in a glass vial (lane I1) and a Teflon tube (lane I2). Bands associated with OC (1), LN (2) and SC (3) isoforms are indicated.

4.3.2 Effect of Microfluidic Shear on Block Copolymer-Functionalized pUC18 pDNA in Mixed Organic Solvent.

Having demonstrated the flow-dependent microfluidic shear degradation of naked pUC18 in a mixed organic solvent environment, we were interested to determine whether complexation with a block copolymer containing one charged block and one hydrophobic block would provide some protection to the plasmid against microfluidic shear. For this experiment, the micellar polyplex PCL-pDNA was first formed as described in detail in the Experimental section and shown in brief in Figure 4.5. We then investigated the effect of variable high-shear hot spots in the two-phase, gas-liquid microfluidic reactor on the copolymer-functionalized pUC18 pDNA in a mixed organic solvent environment and the same flow rates applied to shear experiments on naked pUC18 (Q = 100, 200, or 400 µL/min, corresponding to maximum shear rates of 4×10^5, 8×10^5, and 1.6×10^6 s^{-1}, respectively). The on-chip solvent composition was 86/9/3/2 (w/w/w/w) dioxane/acetic acid/THF/water. The on-chip pDNA concentration for all experiments was 15 µg/mL, equivalent the microfluidic shear experiments on naked pUC18. We note that the on-chip mixed organic solvent composition for microfluidic shear experiments on the PCL-pDNA polyplex was somewhat different than the composition used in experiments on naked pDNA (90/10/< 0.1 (w/w/w) dioxane/water/acetic acid), including a higher acetic acid content, a lower water content, and the presence of some THF. These differences in on-chip solvent composition were necessitated by the solvent conditions required for the off-chip complexation reaction (Figure 4.5). However, the slightly different solvent compositions do not preclude direct comparison of shear effects on bare and functionalized pDNA. The mixed solvent conditions for the PCL-pDNA experiments have a lower on-chip water concentration; thus, due to the destabilizing effect of low dielectric constant organic solvent environments on the structural integrity of the pDNA double helix, we

expect that these conditions should be more severe on pDNA than the solvent conditions for the naked pDNA experiments.

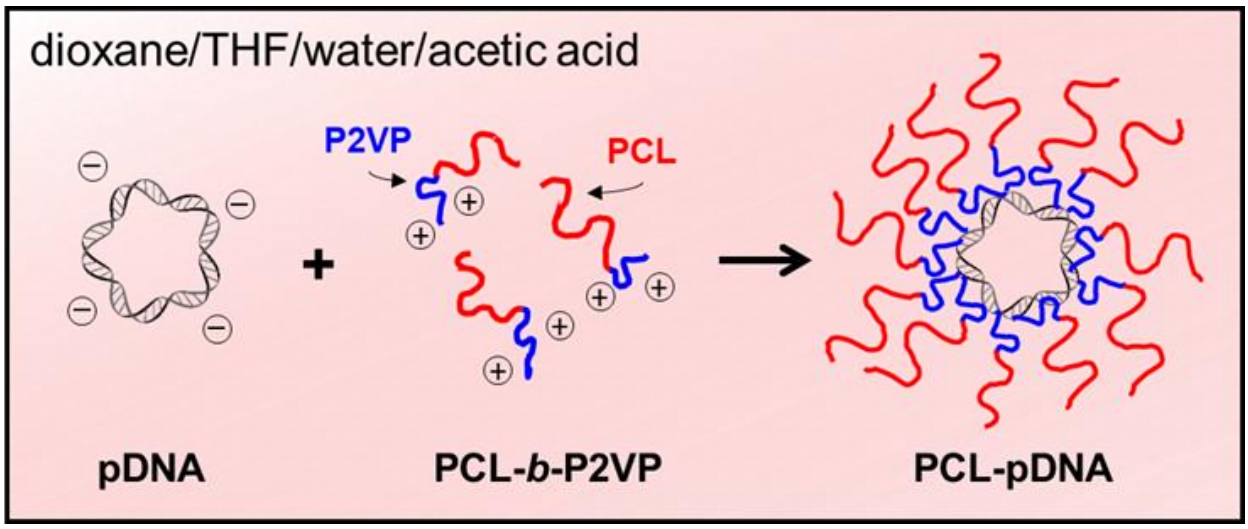

Figure 4.5. Schematic of pDNA functionalization reaction with PCL-*b*-P2VP to form PCL-pDNA micellar polyplex.

Following on-chip shear exposure, PCL-pDNA samples were collected from the chip into empty vials, then treated to remove copolymer chains followed by gel electrophoresis. The resulting analysis revealed that, in comparison with naked pUC18 (Figure 4.2), block copolymer complexation protected pUC18 from flow-rate dependent shear degradation in the microfluidic channels in mixed organic solvents. Figure 4.6 shows gels of pUC18 samples following microfluidic shear experiments on the PCL-pDNA polyplex at three different flow rates, Q = 100, 200, or 400 µL/min, corresponding to lanes M7, M8, and M9. Lanes L and P1 correspond to a 1kb DNA ladder and a naked pUC18 control sample that had not been run through the microfluidic chip. Bands corresponding to the three main pDNA isoforms, (1) OC, (2) LN, and (3) SC are

identified.[14,15] Similar to naked pUC18 (Figure 4.2), block copolymer-functionalized pUC18 shows a marked decrease in the intensity of the SC band (3) after being run through the chip at *Q* = 100 μL/min (lane M7) compared to the control (lane P1). This may be due to some shear-induced relaxation of the SC isoform within the PCL-pDNA polyplex at the lowest microfluidic flow rate, as was observed for naked pUC18 in similar mixed organic solvent at the same flow rate. However, unlike naked pUC18, microfluidic shear experiments on the PCL-pDNA polyplex led to persistence of the SC band at the two higher flow rates (lanes M8 and M9), without a corresponding increase in the relative intensity of LN and OC bands. This indicates that block copolymer complexation provides a viable route for protecting the SC isoform of pDNA against shear-induced relaxation during microfluidic processing in mixed organic solvents.

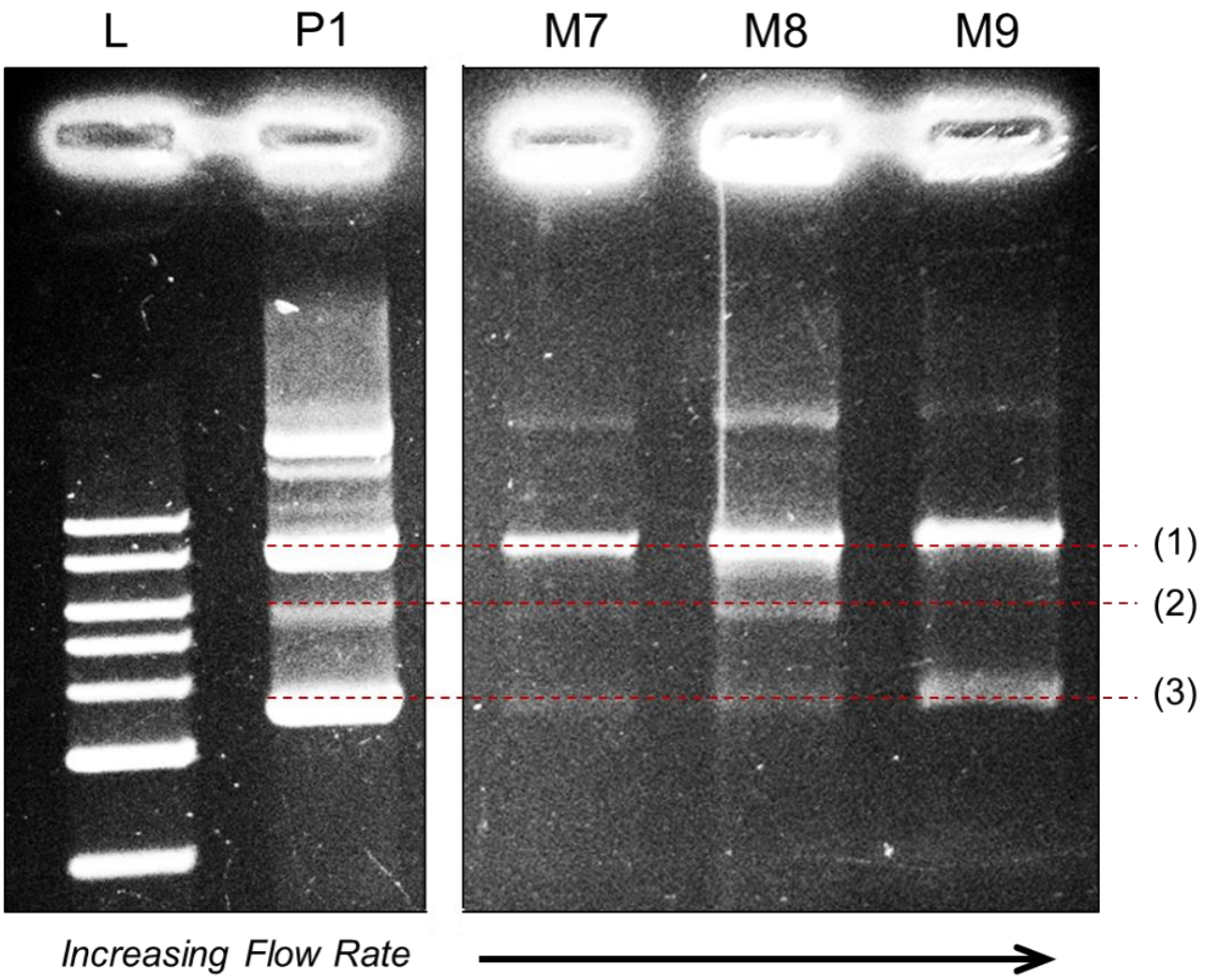

Figure 4.6. Effect of microfluidic flow rate on shear-induced degradation of block copolymer functionalized low-molecular weight pDNA (pUC18, 2.7 kb) in a mixed organic solvent 86/9/3/2 (w/w/w/w) dioxane/acetic acid/THF/water. Agarose gel electrophoresis image of a 1kb DNA ladder (lane L), untreated pDNA control (lane P1), and pDNA after passing through the microfluidic chip in the polyplex form PCL-pDNA at flow rates of Q = 100 µL/min (lane M7), 200 µL/min (lane M8), and 400 µL/min (lane M9). Bands associated with OC (1), LN (2) and SC (3) isoforms are indicated.

4.3.3 Effect of Microfluidic Shear on Higher-Molecular Weight pDNA in Mixed Organic Solvent.

As a follow-up to our findings on the effects of microfluidic shear on naked pUC18 pDNA in a mixed solvent environment (Figure 4.2), we also investigated in the effects of microfluidic shear on larger pDNA particles, naked pDSK519 (8.7 kb) and naked pRK290 (20 kb), under the same flow rates and mixed organic solvent conditions as those described earlier for naked pUC18 (2.7 kb) experiments. Agarose gel electrophoresis images of pDSK519 (Figure 4.7A) and pRK290 (Figure 4.7B) following microfluidic shear experiments at three different flow rates, Q = 100, 200, or 400 μL/min, corresponding to lanes M10, M11, and M12 (pDSK519) and lanes M13, M14, and M15 (pRK290) show the absence of any discernable pDNA bands for both plasmids at all investigated flow rates. This is in contrast to the untreated control plasmids pDSK519 (Figure 4.7A, lane P2) and pRK290 (Figure 4.7B, lane P3), which both show distinct bands corresponding to the indicated isoforms.[15]

The absence of discernable pDNA bands indicates that both pDSK519 and pRK290 plasmids were completely degraded into small fragments by microfluidic shear in the mixed organic solvent environment (Figure 4.7), in contrast to the pUC18 plasmid, which showed some degradation to small fragments at higher flow rates but also showed evidence of less severe damage, namely shear-induced relaxation to OC and LN isoforms, including at the highest flow rate (Figure 4.2). These results indicate that sensitivity to shear degradation in the microfluidic channels increases sharply with plasmid size. This further underlines the importance of considering multiple molecular and experimental factors when seeking to maintain the structural integrity of pDNA backbones and helices in a microfluidic context.

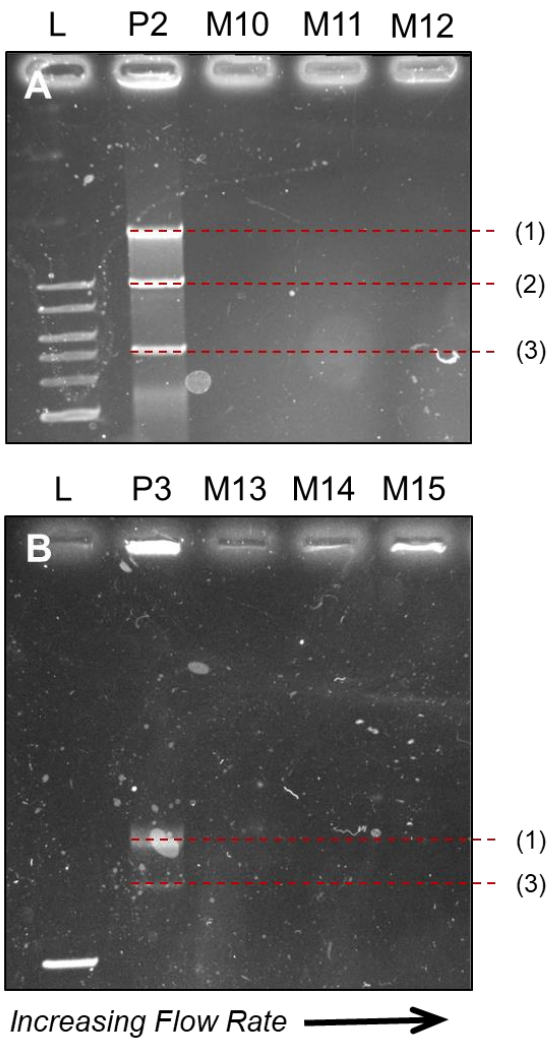

Figure 4.7. Effect of microfluidic flow rate on shear-induced degradation of (A) naked medium-molecular weight pDNA (pDSK519, 8.1 kb) and (B) naked high-molecular weight pDNA (pRK290, 20 kb) in a mixed organic solvent (90/10/< 0.1 (w/w/w) dioxane/water/acetic acid). Agarose gel electrophoresis images of a 1kb DNA ladder (lane L, A and B), untreated pDNA control (lane P2, A; land P3, B), and naked pDNA after passing through the microfluidic chip at flow rates of Q = 100 µL/min (lane M10, A; lane M13, B), 200 µL/min (lane M11, A; lane M14, B), and 400 µL/min (lane M12, A; lane M15, B). Bands associated with OC (1), LN (2) and SC (3) isoforms are indicated.

4.3.4 Discussion of Microfluidic Shear Results and Comparison with the Literature.

Our experiments showed a dramatic difference between microfluidic shear effects on plasmids in pure water and in mixed organic solvents, with pDNA showing higher sensitivity to both shear-induced fragmentation and shear induced-relaxation into less biologically active OC and LN isoforms in the latter solvent system. Previous works have demonstrated that shear-induced degradation of pDNA in aqueous environments decreases with increased ionic strength of the medium, perhaps due to decreasing pDNA hydrodynamic diameter or suppression of secondary shear-associated effects such as thermal reactions activated by viscous friction-generated heat.[7,14] Similar to increased ionic strength, decreased dielectric constant of the solvent environment has also been shown to decrease the hydrodynamic diameter of DNA.[42-44] Thus it may at first appear contradictory that the mixed organic solvent environment in this study enhanced rather than suppressed microfluidic shear effects compared to those found in pure water. However, the mechanism of condensation differs in each of these cases; for aqueous solutions with varying ion content, condensation is electrostatically driven through charge inversion leading to condensate nucleation.[45] On the other hand, in organic solvent systems with low dielectric constants, condensation is driven by hydrophobic effects, which also destabilize the DNA double helix.[42-44] Therefore, the destabilization of the double helix structure of pDNA in an organic solvent such as the dioxane-dominant mixture described in this work likely renders it more susceptible to shear-based degradation.

Our results are broadly consistent with the earlier experiments of Levy et al. in a rotating disk device although with important differences.[14] As mentioned previously, Levy et al. have shown that applying comparably lower shear rates ranging from 1.4×10^5 to 4.8×10^5 s^{-1} using a rotating shear device can cause complete degradation of large pDNA (pQR186, 13 kb; pQR150, 20 kb;

pMT103, 29 kb) from the SC isoform into small fragments.[14] However, in contrast to our experiments on pUC18, they did not observe incomplete degradation in the form of shear-induced relaxation from SC to OC and LN isoforms. It is important to note that all plasmids employed in ref. 14 were larger than pUC18 (2.7 kb), such that this difference may be attributed in part to the ability of pUC18 to evade complete degradation due to its smaller size, as supported by our observation of complete shear-induced fragmentation of the larger pDSK519 (8.1 kb) and pRK290 (20 kb) in the microfluidic channels. However, the different shear environments of the two studies must also be taken into account; in the two-phase microfluidic channels of the current work, plasmids are in constant circulation within relatively low shear regions with only periodic exposure to high-shear "hot spots",[17] in contrast to the more uniform shear of the rotating disk device in the experiments of Levy et al.[14]

Coordination of nucleic acids with amphiphilic block copolymers to form polyplexes has long been employed as a strategy for protection from mechanical stress and enzymatic degradation.[46,47] Among the most common block copolymer for this purpose is poly(ethylene glycol)-*block*-poly(L-lysine) (PEG-*b*-PLL). For example, Katayose and Kataoka showed that polyplexes of ColE1 pDNA and PEG-*b*-PLL are water soluble in a large concentration range, and that complexation pushes the T_m of the pDNA towards higher temperatures.[48] Additionally, the polyplexes exhibited dramatically increased resistance to enzymatic degradation by DNAse I.[48] More recently, Agarwal *et al.* similarly reported the use of PEG-*b*-PLL to form DNA origami polymeric micelles (DOPMs). When encapsulated in DOPMs, DNA was protected from degradation by nucleases and from condensation at high ionic strength.[49] While these examples explored the protection of DNA in aqueous solutions with PEG coronal blocks in contrast to the organic-soluble PCL coronal blocks we report here, the mechanism of protection is largely comparable, with complexation of

DNA with positively-charged PLL or P2VP blocks allowing DNA to resist condensation and maintain its native conformation. As mentioned earlier, we attribute the increased sensitivity of naked pDNA to microfluidic shear in organic solvent to hydrophobic interaction-driven condensation and denaturation increasing susceptibility of the pDNA degradation. Since complexation by block copolymers has been shown to mitigate this condensation effect, we expect that the pDNA is able to maintain a more native-like conformation while complexed, resulting in a lower degree of shear-based degradation.

4.4 Conclusions

As the application of microfluidic platforms for developing novel polymeric gene delivery vectors increases, thorough examination of the integrity of encapsulated payloads under shear is necessary. Our group has previously shown that two-phase, segmented gas-liquid microfluidic reactors provide excellent top-down control over particle size and morphology but exposes the components to high shear rates (10^5-10^6 s^{-1}), which could have detrimental effects on the pDNA payload. Therefore, in this work we exposed pDNA particles of varying size to variable shear forces in a two-phase, gas-liquid microfluidic reactor and analyzed the products of on-chip shear-induced degradation. We showed that small naked pDNA (pUC18, 2.7 kb) exhibited shear-rate dependent shear degradation in a mixed organic solvent (dioxane/water/acetic acid; 90/10/<0.1 w/w/w), with supercoil isoform relaxation and complete fragmentation increasing as maximum shear rates in the microfluidic "hot spots" increases from 4×10^5 to 2×10^6 s^{-1}. However, over the same range of shear rates, pUC18 showed no evidence of microfluidic shear-induced degradation in a pure aqueous environment. We also demonstrated that shear degradation effects in mixed organic solvents were significantly attenuated by complexation of pDNA with the block copolymer polycaprolactone-*block*-poly(2-vinylpyridine) prior to exposure to microfluidic shear. Finally, we showed that medium (pDSK519, 8.1 kb) and large (pRK290, 20 kb) naked pDNA were significantly more sensitive to shear-induced microfluidic degradation than pUC18. The ability to use variable shear forces as a processing tool to fine-tune the structure and properties of polymer nanoparticles, while at the same time minimizing detrimental shear effects on the genetic payload, should empower further research into novel gene delivery vectors through microfluidic methods.

4.5 References

1. Dunbar, C. E.; High, K. A.; Joung, J. K.; Kohn, D. B.; Ozawa, K.; Sadelain, M. Gene therapy comes of age. *Science*. **359**, 175-+ (2018).

2. Hardee, C. L.; Arevalo-Soliz, L. M.; Hornstein, B. D.; Zechiedrich, L. Advances in non-viral DNA vectors for gene therapy. *Genes-Basel*, **8**, (2017).

3. Xiang, Y. G.; Oo, N. N. L.; Lee, J. P.; Li, Z. B.; Loh, X. J. Recent development of synthetic nonviral systems for sustained gene delivery. *Drug Discov. Today*. **22**, 1318-1335.(2017).

4. Pereira-Silva, M.; Jarak, I.; Alvarez-Lorenzo, C.; Concheiro, A.; Santos, A. C.; Veiga, F.; Figueiras, A. Micelleplexes as nucleic acid delivery systems for cancer -targeted therapies. J. Control. Release. **323**, 442-462 (2020).

5. Wang, Z.; Schmidt, F.; Weisblum, Y.; Muecksch, F.; Barnes, C. O.; Finkin, S.; Schaefer-Babajew, D.; Cipolla, M.; Gaebler, C.; Lieberman, J. A. mRNA vaccine-elicited antibodies to SARS-CoV-2 and circulating variants. *Nature*. **592**, 616-622 (2021).

6. Mallapaty, S. COVID vaccines slash viral spread–but Delta is an unknown. *Nature*. **596**, 17-18 (2021).

7. Lengsfeld, C.; Anchordoquy, T. Shear-induced degradation of plasmid DNA. J. Pharm. Sci. **91**, 1581-1589 (2002).

8. Charoenphol, P.; Huang, R. B.; Eniola-Adefeso, O. Potential role of size and hemodynamics in the efficacy of vascular-targeted spherical drug carriers. *Biomaterials*. **31**, 1392-1402 (2010).

9. Gomez-Garcia, M. J.; Doiron, A. L.; Steele, R. R.; Labouta, H. I.; Vafadar, B.; Shepherd, R. D.; Gates, I. D.; Cramb, D. T.; Childs, S. J.; Rinker, K. D. Nanoparticle localization in blood vessels: Dependence on fluid shear stress, flow disturbances, and flow-induced changes in endothelial physiology. *Nanoscale*. **10**, 15249-15261 (2018).

10. Klingberg, H.; Loft, S.; Oddershede, L. B.; Møller, P. The influence of flow, shear stress and adhesion molecule targeting on gold nanoparticle uptake in human endothelial cells. *Nanoscale*. **7**, 11409-11419 (2015).

11. Thompson, A. J.; Eniola-Adefeso, O. Dense nanoparticles exhibit enhanced vascular wall targeting over neutrally buoyant nanoparticles in human blood flow. *Acta biomater*. **21**, 99-108 (2015).

12. Carlson, A.; Signs, M.; Liermann, L.; Boor, R.; Jem, K. J. Mechanical disruption of Escherichia coli for plasmid recovery. *Biotechnol. Bioeng.* **48**, 303-315 (1995).

13. Chamsart, S.; Patel, H.; Hanak, J.; Hitchcock, A.; Nienow, A. The impact of fluid-dynamic-generated stresses on chDNA and pDNA stability during alkaline cell lysis for gene therapy products. *Biotechnol. Bioeng*. **75**, 387-392 (2001).

14, Levy, M.; Collins, I.; Yim, S.; Ward, J.; Titchener-Hooker, N.; Ayazi Shamlou, P.; Dunnill, P. Effect of shear on plasmid DNA in solution. *Bioprocess Eng*. **20**, 7-13 (1999).

15. Molloy, M. J.; Hall, V. S.; Bailey, S. I.; Griffin, K. J.; Faulkner, J.; Uden, M. Effective and robust plasmid topology analysis and the subsequent characterization of the plasmid isoforms thereby observed. *Nucleic Acids Res*. **32**, e129-e129 (2004).

16. Levy, M. S.; D O'Kennedy, R.; Ayazi-Shamlou, P.; Dunnill, P. Biochemical engineering approaches to the challenges of producing pure plasmid DNA. ***Trends*** *Biotechnol*.**18**, 296-305 (2000).

17. Schabas, G.; Wang, C. W.; Oskooei, A.; Yusuf, H.; Moffitt, M. G.; Sinton, D. Formation and shear-induced processing of quantum dot colloidal assemblies in a multiphase microfluidic chip. *Langmuir*. **24,** 10596-10603 (2008).

18. Nesterova, I. V.; Hupert, M. L.; Witek, M. A.; Soper, S. A. Hydrodynamic shearing of DNA in a polymeric microfluidic device. *Lab Chip*. **12**, 1044-1047 (2012).

19. Wilson, D. R.; Mosenia, A.; Suprenant, M. P.; Upadhya, R.; Routkevitch, D.; Meyer, R. A.; Quinones-Hinojosa, A.; Green, J. J. Continuous microfluidic assembly of

biodegradable poly (beta-amino ester)/DNA nanoparticles for enhanced gene delivery. *J. Biomed. Mater. Res. Part A.* **105**, 1813-1825 (2017).

20. Meacle, F.; Zhang, H.; Papantoniou, I.; Ward, J.; Titchener-Hooker, N.; Hoare, M. Degradation of supercoiled plasmid DNA within a capillary device. *Biotechnol. Bioeng.* **97**, 1148-1157 (2007).

21. Wu, S.; Li, C.; Zheng, Q.; Xu, L. Modelling DNA extension and fragmentation in contractive microfluidic devices: A Brownian dynamics and computational fluid dynamics approach. *Soft Matter*. **14**, 8780-8791 (2018).

22. Kly, S.; Andrew, L. J.; Moloney, E. G.; Huang, Y.; Wulff, J. E.; Moffitt, M. G. Hierarchical self-assembly route to "polyplex-in-hydrophobic-core" micelles for gene delivery. *Chem Mater*. **33**, 6860-6875 (2021).

23. Valencia, P. M.; Farokhzad, O. C.; Karnik, R.; Langer, R. Microfluidic technologies for accelerating the clinical translation of nanoparticles. *Nat Nanotechnol*. **7**, 623-629 (2012).

24. Capretto, L.; Carugo, D.; Mazzitelli, S.; Nastruzzi, C.; Zhang, X. L. Microfluidic and lab-on-a-chip preparation routes for organic nanoparticles and vesicular systems for nanomedicine applications. *Adv Drug Deliver Rev*. **65**, 1496-1532 (2013).

25. Liu, D.; Zhang, H.; Fontana, F.; Hirvonen, J. T.; Santos, H. A. Current developments and applications of microfluidic technology toward clinical translation of nanomedicines. *Adv Drug Deliver Rev*. **128**, 54-83 (2018).

26. Liu, Y.; Yang, G.; Hui, Y.; Ranaweera, S.; Zhao, C. X. Microfluidic nanoparticles for drug delivery. *Small* **2022**. 2106580 (2022).

27. Lu, M.; Ho, Y.-P.; Grigsby, C. L.; Nawaz, A. A.; Leong, K. W.; Huang, T. J. Three-dimensional hydrodynamic focusing method for polyplex synthesis. *ACS Nano*. **8**, 332-339 (2014).

28. Wang, C. W.; Sinton, D.; Moffitt, M. G. Flow-directed block copolymer micelle morphologies via microfluidic self-assembly. *J. Am. Chem. Soc*. **133**, 18853-18864 (2011).

29. Wang, C. W.; Bains, A.; Sinton, D.; Moffitt, M. G. Flow-directed loading of block copolymer micelles with hydrophobic probes in a gas-liquid microreactor. *Langmuir*. **29**, 8385-8394 (2013).

30. Xu, Z. Q.; Yan, B.; Riordon, J.; Zhao, Y.; Sinton, D.; Moffitt, M. G. Microfluidic synthesis of photoresponsive spool-like block copolymer nanoparticles: flow-directed formation and light-triggered dissociation. *Chem Mater*. **27**, 8094-8104 (2015).

31. Bains, A.; Cao, Y. M.; Moffitt, M. G. Multiscale control of hierarchical structure in crystalline block copolymer nanoparticles using microfluidics. *Macromol. Rapid Commun*. **36**, 2000-2005 (2005).

32. Bains, A.; Wulff, J. E.; Moffitt, M. G. Microfluidic synthesis of dye-loaded polycaprolactone-block-poly (ethylene oxide) nanoparticles: Insights into flow-directed loading and in vitro release for drug delivery. *J. Colloid. Interf. Sci*. **475**, 136-148 (2016).

33. Bains, A.; Cao, Y. M.; Kly, S.; Wulff, J. E.; Moffitt, M. G. Controlling structure and function of polymeric drug delivery nanoparticles using microfluidics. *Molecular pharmaceutics*. **14**, 2595–2606 (2017).

34. Chen, R.; Wulff, J. E.; Moffitt, M. G. Microfluidic processing approach to controlling drug delivery properties of curcumin-loaded block copolymer nanoparticles. *Mol. Pharm*.**15**, 4517-4528 (2018).

35. Cao, Y.; Silverman, L.; Lu, C.; Hof, R.; Wulff, J. E.; Moffitt, M. G. Microfluidic manufacturing of SN-38-loaded polymer nanoparticles with shear processing control of drug delivery properties. *Mol. Pharm*.. **16**, 96-107 (2018).

36. Huang, Y.; Moini Jazani, A.; Howell, E. P.; Oh, J. K.; Moffitt, M. G. Controlled microfluidic synthesis of biological stimuli-responsive polymer nanoparticles. ***ACS Appl. Mater.*** **12**, 177-190 (2019).

37. Huang, Y.; Jazani, A. M.; Howell, E. P.; Reynolds, L. A.; Oh, J. K.; Moffitt, M. G. Microfluidic shear processing control of biological reduction stimuli-responsive polymer nanoparticles for drug delivery. ***ACS*** *Biomater. Sci. Eng.* **6**, 5069-5083 (2020).

38. Xu, Z. Q.; Lu, C. H.; Riordon, J.; Sinton, D.; Moffitt, M. G. Microfluidic manufacturing of polymeric nanoparticles: Comparing flow control of multiscale structure in single-phase staggered herringbone and two-phase reactors. *Langmuir*. **32**, 12781-12789 (2016).

39. Wang, C. W.; Sinton, D.; Moffitt, M. G. Morphological control via chemical and shear forces in block copolymer self-assembly in the lab-on-chip. *ACS Nano*. **7**, 1424-1436 (2013).

40. Keen, N.; Tamaki, S.; Kobayashi, D.; Trollinger, D. Improved broad-host-range plasmids for DNA cloning in gram-negative bacteria. *Gene*. **70**, 191-197 (1988).

41. Ditta, G.; Stanfield, S.; Corbin, D.; Helinski, D. R. Broad host range DNA cloning system for gram-negative bacteria: construction of a gene bank of Rhizobium meliloti. *Proc. Natl. Acad. Sci. U.S.A.* **77**, 7347-7351 (1980).

42. Arscott, P. G.; Ma, C.; Wenner, J. R.; Bloomfield, V. A. DNA condensation by cobalt hexaammine (III) in alcohol–water mixtures: Dielectric constant and other solvent effects. *Biopolymers*. **36**, 345-364 (1995).

43. Mel'nikov, S. M.; Khan, M. O.; Lindman, B.; Jönsson, B. Phase behavior of single DNA in mixed solvents. *J. Am. Chem. Soc*. **121**, 1130-1136 (1999).

44. Ke, F.; Luu, Y. K.; Hadjiargyrou, M.; Liang, D. Characterizing DNA condensation and conformational changes in organic solvents. *PLOS ONE*. **5**, e13308 (2010).

45. Besteman, K.; Van Eijk, K.; Lemay, S. Charge inversion accompanies DNA condensation by multivalent ions. *Nat. Phys*. **3**, 641-644. (2007).

46. Yin, H.; Kanasty, R. L.; Eltoukhy, A. A.; Vegas, A. J.; Dorkin, J. R.; Anderson, D. G. Non-viral vectors for gene-based therapy. *Nat. Rev. Genet*. **15**, 541-555 (2014).

47. Osada, K. Development of functional polyplex micelles for systemic gene therapy. *Polym. J*. **46**, 469-475 (2014).

48. Katayose, S.; Kataoka, K. Water-soluble polyion complex associates of DNA and poly (ethylene glycol)−poly (l-lysine) block copolymer. *Bioconjugate Chem.* .**8**, 702-707 (1997).

49. Agarwal, N. P.; Matthies, M.; Gür, F. N.; Osada, K.; Schmidt, T. L. Block copolymer micellization as a protection strategy for DNA origami. *Angew. Chem.* **56**, 5460-5464 (2017).

Chapter 5

Conclusions and Future Directions

5.1 Most significant contributions to original knowledge

This thesis has introduced many novel particles, strategies, and processes; this concluding section highlights the author's foremost accomplishments. In retrospect, the assembly of the PIHC-PNP (Chapter 2) is clearly the highlight of this thesis. An article on this chapter's finding published in *Chemistry of Materials* in August 2021 has already had 500 views. The "polyplex-in-hydrophobic-core" PIHC-PNP represents the first polyplex to shield pDNA behind a contiguous layer of hydrophobic polymer.

Applications of GNPs in radiotherapy and CT imaging require large threshold levels of gold in sensitive areas to be effective. The work in this thesis addressed that issue by showing that the cellular uptake of GNPs could be increased by packaging them into GNP-PNPs (Chapter 3). This should be recognized as the second greatest achievement in this thesis. Understanding how the shape, size, and texture of GNPs contribute to the cellular uptake of GNP has yielded many publications, and now the knowledge that smaller GNPS of different shapes can be incorporated into larger polymeric carriers for increased uptake has been provided. This chapter has a separate written manuscript that is currently under review for publication.

Microfluidic processing has been widely utilized in manufacture of drug delivery systems because flow rate, temperature, and residence time can easily be controlled. More specifically, two-phase gas-liquid reactors increase mixing as a result of chaotic advection due to compartmentalization of liquid plugs; however, high shear rates develop at phase interfaces in the chip and the shear effects on nucleic acid on these chips hasn't been investigated. To date, the application of flow-tunable shear forces to the manufacture of nucleic acid DDS in a two-phase reactor has not been reported in the literature. The work in Chapter 4 demonstrated how microfluidic shear processing effects the fidelity of different sizes of pDNA in organic solvents.

5.2 Additional contributions to original knowledge

5.2.1 The study of pDNA and pDNA polyplexes in organic solvent

Incorporation of nucleic acids including plasmids into delivery systems begins with binding the nucleic acids through electrostatic interaction with their negatively charged backbone. The conditions under which this happens in aqueous systems is well known at this point, with optimal conditions for binding nucleic acids widely reported for a plethora of drug delivery systems with and without polymers. To our knowledge, the first paper evaluating plasmids in organic solvents was published in 1995 twenty years before this project had started.[1] Arscot et al studied pUC18 pDNA in mixtures of water and alcohols that are commonly used in the pDNA extraction process. Their study did not propose construction of any sort of drug delivery system, nor did it explore low water concentrations or low dielectric constants. Since then and up until 2014 there have been many studies that investigate the use of nucleic acid oligomers in organic solvents, but none using DNA lengths anywhere near plasmids plasmids.[2,3] Since then, there have been many studies binding pDNA in the aqueous phase and moving it into the organic phase but none binding pDNA when the PDNA is in the organic phase. Nor are there studies of pDNA stability in low dielectric solutions with very low water content (< 10 %). The undertakings in this thesis represent the beginnings of an understanding of how nucleic acid functionalization is different in low dielectric constant organic solvents.

In Chapter 2 we investigated the effects of salt, water, and acid concentration on the binding of P2VP-*b*-PCL to plasmid DNA in a mixture of acetic acid and dioxane. Successful phase transfer of pDNA polyplexes into chloroform acetic acid and dioxane occurred best (38 % phase transfer efficiency) when functionalization occurred at a water content of 6.2 wt % in pure acetic acid, which represents slightly more than the minimum amount of water needed to solubilize the pDNA

in the organic solvent mixture. It was also found that polyplex formation was more complete at higher acid concentrations; however, at the highest acid concentration the plasmids were damaged, highlighting the complexity of the problem and the importance of optimizing solvent conditions. Phase transfer efficiency of polyplexes with no salt and the lowest water content were: 38 % at 100 wt % acetic acid, 35% at 30 wt % acetic acid in dioxane, and 25 % at 1% acetic acid in dioxane. Keeping the acetic acid at 30 wt % in dioxane and increasing the water content at 7.8, 11.6, 24.9, and 39.1 wt % produced fewer functionalized polyplexes. The presence of salt was shown to decrease polyplex formation at most water contents, and at 6.2 wt % water addition of salt decreased phase transfer efficiency from 35% to 15% and to 9% with increasing salt concentrations of 0, 0.01, and 0.1 M sodium acetate respectively.

In Chapter 3 we investigated how the length of plasmids effect their stability in organic solvents. It was found that PUC18, the smallest plasmid studied here (2686 bp), could be dissolved in dioxane and water and be retrieved from either solvent without severe damage while not in a polyplex with polymer. The larger plasmid pRK290 (~20,000 bp) could not be retrieved from dioxane, indicating that it had broken down. This represents the first time the length dependent stability of plasmids in dioxane had been investigated.

5.2.2 The effect of solvent and polymer functionalization of microfluidic shear processing on the self-assembly of plasmids into block copolymer aggregates.

The synthesis of new cation-containing block copolymers, as well as the modification of existing cationic block copolymers, along with addition of ions and the varying of solvent conditions, are all examples of "bottom up" approaches to increasing the success of nucleic acid vehicles.[4–10] The advancement of microfluidic reactors has allowed for the manufacture of these types of aggregates on chip. On chip manufacture of nucleic acid containing block copolymer aggregates gives the experimenter the extra variable of flow rate.[11] The flow rate controls the shear stress on chip and can alter the morphology of the aggregate obtained post processing. The Moffitt group has previously demonstrated this "top-down" approach to obtaining a high degree of morphological control of self-assembling amphiphilic block copolymers on a two-phase gas-liquid segmented microfluidic reactor.[12–16] For example, the work of Aman Bains et al has shown the flow control over morphology of paclitaxel loaded PCL-*b*-PEO nanoparticles.[12]

Microfluidic mixing and has been recognized as a more controlled form of manufacture for polymer based nucleic acid delivery vehicles.[17–19] Previously, the Green group has shown faster mixing on chip produces smaller polyplexes.[20] The work by Wilson et al in 2017 demonstrated the assembly of polyplexes from pDNA and poly(beta-amino esters) via microfluidic hydrodynamic focusing.[20] They found that microfluidic processing on their chip had no effect on the morphology of their PNPs. The work of Grigsby et al showed microfluidic manufacture of poly(amido-amine) pDNA polyplexes on chip at different flow rates.[21] They saw a slight decrease in the size of their polyplexes with increasing flow rate and attribute this to increased mixing time having reduced their polyplex size. Debus and coworkers manufactured polyplexes of PEI / pDNA and showed no variation in morphology as a function of flow rate.[22] All of the above-mentioned work was done

in single phase microfluidic reactors. Comparative studies between the staggered herring bone mixer and the Moffitt lab chip by Xu et al demonstrated that the single-phase chips lack the shear needed to overcome the energetic barriers of shear induced coalescence and breakup of particles.[23] Like the examples using polyplexes above, the morphology of the PNPs obtained did not alter with increasing the flow rate in single phase chips. Many companies in the field have interest in microfluidic reactor technology and here we expand this interest to two phase reactors capable of shear processing.

Moreover, plasmids that can integrate into mammalian chromosomes would be necessary to recreate the transformation carried out in Chapter 2 as a transfection in mammalian cells. The simplest of these plasmids, (which contain no therapeutic genes), must be larger than pUC18 (2758 kb) by design, because it must code for replication and identification in both prokaryotic and eukaryotic organisms.[24] The most basic of these plasmids are 5 kbp in size.[24] The larger dimensions and extra charge of larger plasmids proved to be more complicated to work with than pUC18.

In Chapter 3 we investigated the conditions that effect microfluidic processing of nucleic acids and polymer drug delivery systems. This type of knowledge is relevant to the design of three bacterial plasmids, pUC 18, pDSK519 and pRK290, which have lengths of 2686, 8699 and ~20,000 base pairs respectively. We discovered that processing pDNA on chip in water does not affect plasmids stability under any shear conditions for plasmids of any size: the pUC18 maintained its fidelity after processing at 100, 200 and 400 µL/ min and the largest plasmid pRK290 retained its fidelity at all flow rates as well. We also investigated the same shear effects in an organic solvent system (1,4-dioxane). The pUC18 plasmid was recoverable at all flow rates, but there was a noticeable loss of the supercoiled isoform. The larger plasmids were not recoverable at any flow rate, indicating that the shear effects are much more prominent in organic

solvents. Moreover, upon functionalization of pUC18 with P2VP-b-PCL, it was possible to recover the supercoiled band at 200 and 400 µL / min, which illustrated the ability of cationic block copolymers to stabilize plasmids under shear forces present in microfluidic reactors run with organic solvents. This is important knowledge to consider for future designs of genetic therapies because it explores the limits of what is possible on chip.

5.2.3 The self-assembly of GNPs into larger GNP-containing block copolymer aggregates

In order to maximize the effectiveness of GNP formulations, the following considerations should be addressed. First, the GNPs must remain stable in plasma and the extracellular environment while travelling to their destination insofar as, for example, interactions with fibrinogen and thrombin in the blood can cause coagulation of human blood.[25] This means that proper GNP dimensions and stabilizing ligands should be selected to avoid coagulation with blood proteins, salt induced aggregation of GNPs, or toxicity from accumulation in undesired locations.[53,133] Secondly, GNPs must be taken up into the tumor environment prior to photothermal release of the drug delivery system (DDS) and CT imaging, or into cells to be effective for radio sensitization and hyperthermic treatment. [29–31] Finally the GNPs must be broken down and cleared from the body while remaining nontoxic.

To address the above concerns the literature is replete with polymeric, lipid, and ceramic delivery systems.[32–34] The complexity of the systems fluctuates, and the selection of materials is critical to function. Simplistic polymeric assemblies are traditionally homopolymers linked to GNPs through thiol groups and manifest from ligand exchange or GNP synthesis resulting in polymer gold conjugates (PGCs).[35–37] Complexity arises with the desire for additional functions like codelivery or active targeting.[38] Many homopolymers, diblocks, triblocks, linear and branched

bloc copolymers have been employed in these assemblies, including polyethylene glycol, PCL-*b*-PEO, and polyion polyethyleneimine-*block*-polyethyleneglycol-*block*-polycaprolactone (PEI-*b*-PEG-*b*-PCL), [39–41] modifying the surface of the GNP with hydrophilic non charged homopolymer supplies routes to enhance biodistribution properties and reduce immunogenicity. For example, PEG chains are frequently attached to GNPs in PGCs to form a hydrophilic shell layer that increases blood dispersibility.[42] Functionalization with amphiphilic block copolymers containing hydrophobic blocks like PCL add stability by creating a hydrophobic layer separating the gold surface from the bulk solution. This also provides a reservoir for incorporation of hydrophobic drugs; however, the hydrophobic layer may be incomplete, and the dimensions of these particles are controlled solely by the dimensions of the chemical constituents.[40] Recently other groups have attempted to improve this hydrophobic layer by assembling micelles of β-cyclodextrin-{poly(lactide)-poly(2-(dimethylamino) ethyl methacrylate)-poly[oligo(2-ethyl-2-oxazoline)methacrylate] with chloroauric acid in their core, and then reducing the gold in situ to generate GNPs within micelle cores without functionalizing gold first.[43]

The decoration of the surface of GNPs with hydrophobic ligands and subsequent self assembly with amphiphilic block co-polymers has been employed to incorporate GNPs into larger nano carriers.[34,44] Originally the ligands are small molecules (i.e., non-polymeric) like dodecane thiol or stearyl amine, which have been used to load GNPs into the core of PCL-*b*-PEO PNPs by Zaki et al or into the vesicle wall of liposomes by Amgoth et al, respectively.[34,44] However, the ease with which small molecules can functionalize GNPs does not outweigh the toxicity associated with their clearance. Both dodecane thiol and stearyl amine ligands are toxic for ingestion and injection.[45,46] More recently hydrophobic polymer functionalization has been used to achieve the same ends. So far, few authors in the literature assemble hydrophobically functionalized GNPs

into block copolymer PNPs. These include GNPs decorated with PGLA and PS for biomedical and analytical purposes, respectively.[47,48]

Our GNPs assembled with a hydrophobic polymer brush into larger block co-polymer PNPs provide several benefits beyond what is achievable with functionalizing GNPs directly with polymers. The first benefit is providing a full contiguous hydrophobic layer around the GNPs to further increase the stability.[49] This expanded layer can provide additional space to retain small molecule drugs for codelivery of APIs.[50] The second is the clustering of multiple GNPs into a PNP to increase the amount of gold per particle without having to increase the size of the GNPs, which complicates the final PNP synthesis.[44] In theory having more gold particles per PNP should increase cellular uptake efficiency as fewer PNPs need to be endocytosed for more gold to enter, or fewer endocytic events are needed to capture the same amount of gold. The smaller GNPs of 4 nm were shown by Rich et al to be more effective than larger GNP sizes in attenuating x-rays.[51] However, other studies by Kettler show that GNPs with a diameter of ~ 50 nm have the optimum cellular uptake.[52] This allows the PNPs to bring GNPs more optimized for attenuating in a larger quantity. The final advantage is the ability to finely tune the morphology of the PNPs without modifying the existing components. All the factors typically at work in BCP assembly demonstrated in our group's previous papers are at play here with the additional handle of PCL-GNP to BCP ratios.[15,53] Once the loading level is chosen the morphology can also be altered through varying flow rate during microfluidic processing, which gives top-down control over GNP-PNP morphologies.[54]

In Chapter 4 we determined the PCL-GNP to PCL-*b*-PEO ratio of 2, 10, 50, and 100 created particles with hydrodynamic diameters of 110 ± 10, 232 ± 4, 240 ± 12, and 123 ± 2 nm respectively. The ratio of 100 – 1 was chosen because it produced GNP-PNPs with the most GNPs per PNP

while retaining a sufficiently low hydrodynamic diameter for intravenous delivery. The cellular uptake of GNP-PNPs were compared to the PEG-GNPs with a slightly smaller hydrodynamic diameter. The uptake of the GNP-PNPs were determined to be 49.9 ± 0.4 thousand GNPs per cell while the uptake of the PEG-GNPs was determined to be 36 ± 1 thousand GNPs per cell. The difference in cellular uptake was found to be extremely significant between PEG-GNPs and GNP-PNPs. Naturally we investigated the effect of flow tunable shear microfluidic processing on the self-assembly of PCL-GNPs and PCL-b-PEO. The bulk preparation was compared to samples assembled on two-phase gas-liquid microfluidic chip at 0, 100, 200, and 400 μL / min yielding particles of 123 ± 2, 53 ± 2, 50 ± 4 and 47 ± 4 nm respectively. The morphology at each flow rate was large and small spheres containing GNPs, spheres with GNPs on surface, small spheres containing GNPs and small spheres with aggregated GNPs respectively. It was notable that at the highest flow rate, the GNPs were being destroyed and forming large non spherical aggregates.

5.3 Suggestions for future work

The suggested work section contains three paragraphs, each one offering different directions for future research aligned with the three focus points of the thesis. The first paragraph addresses the possibilities of new mRNA and pDNA PIHC-PNPs that can be manufactured. The second paragraph addresses the ongoing research incorporating GNPs into GNP-PNPs and their use in CT imaging, and radiotherapy. Ultimately the goal discussed in the focus of this thesis in the Introduction was not fully achieved, so the final paragraph concerns future work toward readdressing it.

5.3.1 The future directions of incorporating nucleic acids in PNPs.

The most obvious expansion of this thesis work is to apply the strategy developed in Chapter 2 to transfecting human cells. Naturally this process is more difficult because it contains two additional barriers. The first barrier is escape from the endosome and the second is transport across the nuclear membrane. Accordingly, there is work to be done to optimize this process. This might include incorporation of GNPs for photothermal release from the endosomes to linking of nuclear localisation sequences onto the PIHC-PNPs to increase nuclear transport. We have already designed an experiment to incorporate mammalian pZsGreen1-N1 plasmids into PIHC-PNPs and introduce it to HELA cells. The pZsGreen1-N1 plasmid contains genre for green fluorescent proteins and thus the success of transfection can be monitored by optically.

There are many avenues for future research incorporating nucleic acids into PNPS, but with the SARS-COV-2 virus causing COVID-19 disease worldwide, one future direction in particular cannot be ignored. Messenger RNA (mRNA) is smaller than plasmid DNA and should be easier

to incorporate into PNPs. Currently the mRNA is loaded into liposomes for the Pfizer biotech vaccine. At the early stages of the pandemic there were issues delivering the vaccine because many of the recipient destinations were not equipped to store the vaccines at -80 °C and some nations remain unable to distribute the vaccine to all their substituents.[55] The PIHC-PNPs that were created in Chapter two can be stored at -20 °C for weeks. Naturally this technology would be of interest to explore.

The emergence of multidrug resistant genes in cancer cells from patients that have undergone chemotherapy is reported to be an event that proves to be fatal after prolonged treatment.[56] These genes, when transcribed, provide mRNA code for protein pumps that transport chemotherapy drugs out of the cytoplasm. The mRNA transcripts could be attacked by small interfering RNA (siRNA) molecules and prevent the protein pumps from forming and negating the chemotherapy.[57] Therefore, an opportunity exists to co-incorporate siRNA molecules into PNP with small molecules drugs like paclitaxel. There is already precedence for this effect illustrated in the work of Shen et al in 2015.[6] They used hyaluronic acid modified PCLHA-*b*-PEI to incorporate siRNA (targeting a tumor silencing gene COX2) and paclitaxel and treated cancer cells, which provided a synergistic killing effect on cancer cells.

Our particles potentially offer the aforementioned advantages because of the nature of the polymers themselves. Both lipids and block-copolymers can be amphiphilic. However, the hydrophobic portions of block co-polymer aggregates are much larger than their lipid counterparts. The Introduction briefly explained how an increase in the length of the hydrophobic block increases the driving force of self assembly. That driving force also provides the stability in the micelle state.

*5.3.2 Future directions for GNP- PNPs in drug delivery***.**

The future work related to Chapter 3 has already begun by fellow PoND researchers Talita De Francesco and Devon Richtsmeier. They are applying the synthetic strategy that was developed in Chapter 3 to create GNP-PNPs that will be used for CT imaging. As discussed in the Introduction and in Chapter 3 GNPs have been used as contrast agents in CT imaging for close to a decade. One obstacle to this application is having insufficient gold in an area to generate contrast. Future studies on how to scale up the synthesis of the GNP-PNPs would be beneficial for CT studies. Once that is complete the next phase would be to test the ability of these particles to act as contrast agents in vivo. Naturally one would want to compare the contrast signal intensity obtained in vivo from GNP-PNPs to those GNPs not incorporated into larger polymer carriers, similar to the PEG-GNPs used by Hara et al to provide contrast when they imaged prostate cancer by CT imaging.[58] Radiotherapy was briefly discussed in the Introduction and is an application which could be employed to the particles in Chapter 3. The particles in Chapter 3 are more suited to in vitro work as their surface plasmon is located mainly in the visible region of laser light.

Another avenue for future research would be to investigate co-incorporation of GNRs with paclitaxel to determine the feasibility of photothermal release of paclitaxel from GNR-PNPs in vivo. The GNR-PNPs were manufactured in Chapter 3 to show that the same strategy could be applied to GNRs as to GNPs, but the experimental variables weren't optimized to create dispersions with GNRs in every PNP. The future work would start with completion of the GNR-PNP design and cytotoxicity studies to determine if it is safe for in vivo use. Naturally an in-vivo study where irradiation of the particles occurs within a mouse body, and levels of paclitaxel in the blood and organs are monitored as a function of time such that release profiles can be generated, would be of interest to the drug delivery community.

5.3.3 The future application of GNP-PIHC-micelles

We demonstrated that the incorporation of PCL-GNPs or pDNA is possible and that assemblies of PCL-*b*-PEO and PCL-GNPs can contain GNPs and pDNA; however co-localisation to the same particles hasn't been proven sufficiently yet. In the same dispersions there were particles that contain neither pDNA or GNPs. The first future experiments will require finding a set of conditions where a majority of PNPs will contain both pDNA and PCL-AuNPs. This would be conducted with both GNPs and GNRs to create a set of conditions that would work for both rods and spheres. Both GNRs and GNPs would be used so that the resulting gold particle loaded PIHC-PNPs would have non-overlapping plasmons, enabling selective excitation of either nanoparticle in later steps. Demonstration of co-localization of pDNA and PCL-GNPs to the same PNP core has been a pitfall that we have been trying to overcome for some time. It is easy to visualize gold inside of PNPs but the low electron density of pDNA makes it invisible under the regular TEM. Electron energy loss spectroscopy has been employed to try to map Au and P elements in the particle system; however, there are several confounding factors. The first is the fact that phosphorous from DNA is difficult to see in an EELS elemental map because the pDNA is often only a few atoms thick compared to the ~50 nm worth of atoms that flank the pDNA when packaged into a PNP. That means for a given TEM cross section there may only be a handful of phosphorous atoms in the volume of a pixel while there are tens of thousands of atoms from the polymer creating noise in which the phosphorous signal can be lost. Phosphorous signals from pDNA have been observed in Chapter 5 and by other groups.[59,60] The second confounding factor is that the accelerating voltage that is used to map phosphorous in DNA is 200 KeV and requires the STEM to roster across the particles multiple times to generate an appreciable signal.[59] At this high voltage our polymer micelles decomposed and were burnt from the grid. The third

confounding factor is the number of micelles expected to contain DNA is low, calculated to be ~ 1 : 10, and doing an elemental map takes quite a lot of time, especially when the signal must be amplified by rostering over a single particle repeatedly. To overcome these factors cryoTEM should be employed to stabilize the PNPs during exposure to the beam.

Investigation of another synthetic approach with slightly different materials would be an interesting route forward as well. One could put a thiol group at the end of the P2VP-*b*-PCL polymer that binds the pDNA so that it can be used to bind the gold first, and then introduce DNA to the functionalized AuNP surface. This methodology has been used by a German group to co-localize GNPs and pDNA to make photo responsive liposomes that carry DNA.[61] This allowed them to use DLS to monitor the functionalization of the GNPs and then UV-Vis and DLS to monitor the attachment of DNA to the functionalized GNPs.[61] In principle this methodology could be applied to our polymer materials. In 2018 Wang et al created particles very similar to our desired particles amidst this thesis work and represents the first non-sequence specific DNA nano carrier capable of photothermal release. However, their lipid formulation has several disadvantages in comparison with our proposed particles.[61] The first of which is inclusion of a plethora of non-approved FDA materials, one of which is TAT peptide derived from HIV. This remains positively charged with a zeta potential of + 36.4 mV. Introducing positively charged material inside cells creates its own potential danger.[61] Moreover, the TAT peptide, while not being entirely sequence specific, can't be extended and thus will only be able to accommodate pDNA of certain sizes. Our equivalent P2VP-*b*-PCL system would not be charged at physiological pH and the polymers can be polymerized at different lengths to accommodate plasmids of different sizes.

The next step is to investigate the release of the particles in-vitro. It would be necessary to reconfirm the photo triggered release of pDNA from GNP-PIHC-PNPs before beginning Radiation

Assisted Selective Transformation (RAST) studies. The cellular uptake efficiency of these particles would need to be confirmed as well.

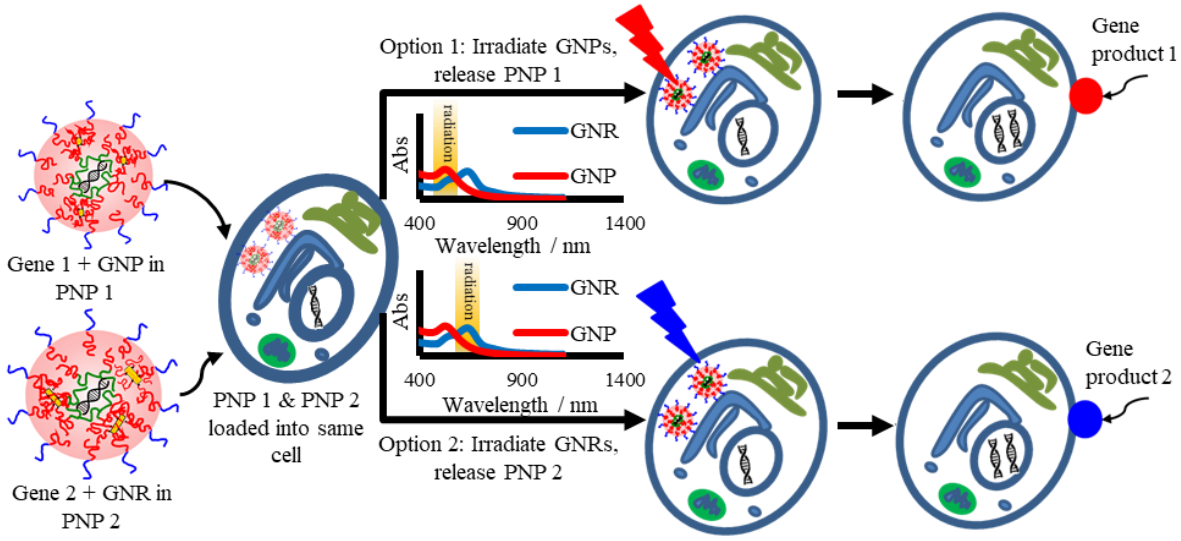

Figure 5.1. Schematic illustrating the core concepts of RAST.

Once co-incorporation, photothermal release, and cell uptake conditions have been optimized RAST experiments could begin. Theoretically cells could be dosed with a mixture of GNP-PIHC-PNPs and GNR-PIHC-PNPs that contain a plasmid that codes for red fluorescent protein in the GNP-PIHC-PNPs and a plasmid that codes for blue fluorescent protein in the GNR-PIHC-PNP respectively. This is illustrated in the left-hand side of Figure 5.1. The next step would be sorting cells that contain the PNPs from those that do not using flow cytometry. In 2010 Zucker et al showed sorting cells without TiO_2 nanoparticles from cells with TiO_2 nanoparticles is possible.[62] A 2019 paper by the Al-Syed group showed they could identify both GNPs and GNRs inside cells that act like the TiO_2 nanoparticles and increase side scatter.[62,63] This would allow us to have a sample of cells that each contain at least one PNP. Then the sample containing the cells

could be irradiated with light of wavelengths that match either option 1, the spherical GNPs, or option 2, the GNRs. The plates can then be read by a plate reader to determine the amount of fluorescence observed in both the RFP and BFP channels. The amount of fluorescence seen from each protein per given surface area could be plotted against time for each of the two conditions to determine if there is selective transfection from the plasmid in one PNP over another in each condition. The state-of-the-art 3D bioprinting technology tries to print already differentiated cells into a matrix that binds them after placement. This could allow for a new approach wherein totipotent cells could be grown and inoculated with PNPs containing genetic elements that cause differentiation. Each PNP would incorporate a different genetic element and GNP with non-overlapping plasmons. Then a light source could roster across the cells and select which genes to turn on by releasing that PNP before the others.

5.4 References

1. Arscott, P. G., Ma, C., Wenner, J. R. & Bloomfield, V. A. DNA condensation by cobalt hexaammine(III) in alcohol-water mixtures: Dielectric constant and other solvent effects. *Biopolymers* **36**, 345–364 (1995).

2. Nakano, S. ichi & Sugimoto, N. The structural stability and catalytic activity of DNA and RNA oligonucleotides in the presence of organic solvents. *Biophys. Rev.* **8**, 11–23 (2016).

3. Arcella, A. et al. Structure and properties of DNA in apolar solvents. *J. Phys. Chem. B* **118**, 8540–8548 (2014).

4. Liu, Z., Zhang, Z., Zhou, C. & Jiao, Y. Hydrophobic modifications of cationic polymers for gene delivery. *Prog. Polym. Sci.* **35**, 1144–1162 (2010).

5. Mahut, M., Gargano, A., Schuchnigg, H., Lindner, W. & Lämmerhofer, M. Chemoaffinity material for plasmid DNA analysis by high-performance liquid chromatography with condition-dependent switching between isoform and topoisomer selectivity. *Anal. Chem.* **85**, 2913–2920 (2013).

6. Shen, Y. et al. Co-delivery of siRNA and paclitaxel into cancer cells by hyaluronic acid modified redox-sensitive disulfide-crosslinked PLGA-PEI nanoparticles. *RSC Adv.* **5**, 46464–46479 (2015).

7. Alshamsan, A. et al. Formulation and delivery of siRNA by oleic acid and stearic acid modified polyethylenimine. *Mol. Pharm.* **6**, 121–133 (2009).

8. Biswas, S., Deshpande, P. P., Navarro, G., Dodwadkar, N. S. & Torchilin, V. P. Lipid modified triblock PAMAM-based nanocarriers for siRNA drug co-delivery. *Biomaterials.* **34**, 1289–1301 (2013).

9. Bromberg, L., Alakhov, V. Y. & Hatton, T. A. Self-assembling pluronic®-modified polycations in gene delivery. *Curr. Opin. Colloid Interface Sci.* **11**, 217–223 (2006).

10. Li, Y. et al. Targeted co-delivery of PTX and TR3 siRNA by PTP peptide modified dendrimer for the treatment of pancreatic cancer. *Small* **13**, 1–9 (2017).

11. Li, Y. et al. Toroidal packaging of pDNA into block ionomer micelles exerting promoted in vivo gene expression. *Biomacromolecules* **16**, 2664–2671 (2015).

12. Bains, A., Cao, Y., Kly, S., Wulff, J. E. & Moffitt, M. G. Controlling structure and function of polymeric drug delivery nanoparticles using microfluidics. *Mol. Pharm.* **14**, 2595–2606 (2017).

13. Yusuf, H. et al. A hierarchical self-assembly route to three-dimensional polymer−quantum dot photonic arrays. *Langmuir.* **23**, 5251–5254 (2007).

14. Huang, Y., Moini Jazani, A., Howell, E. P., Oh, J. K. & Moffitt, M. G. Controlled microfluidic synthesis of biological stimuli-responsive polymer nanoparticles. *ACS Appl. Mater. Interfaces.* **12**, 177–190 (2020).

15. Wang, C., Sinton, D. & Moffitt, M. G. Flow-directed block copolymer micelle morphologies via microfluidic self-assembly. *J. Am. Chem. Soc.* **133**, 18853–18864

(2011).

16. Jensen, D., Cao, Y., Lu, C., Wulff, J. E. & Moffitt, M. G. Microfluidic encapsulation of SN-38 in block copolymer nanoparticles: effect of hydrophobic block composition on loading and release properties. *Can. J. Chem.* **97**, 337–343 (2019).

17. Kim, J. et al. Microfluidic approaches for gene delivery and gene therapy. *Lab Chip* **11**, 3941–3948 (2011).

18. Shepherd, S. J., Issadore, D. & Mitchell, M. J. Microfluidic formulation of nanoparticles for biomedical applications. *Biomaterials.* **274**, 120826 (2021).

19. Digiacomo, L. et al. Cationic lipid/DNA complexes manufactured by microfluidics and bulk self-assembly exhibit different transfection behavior. *Biochem. Biophys. Res. Commun.* **503**, 508–512 (2018).

20. Wilson, D. R. et al. Continuous microfluidic assembly of biodegradable poly(Beta-amino ester)/DNA nanoparticles for enhanced gene delivery. *J. Biomed. Mater. Res. - Part A* **105**, 1813–1825 (2017).

21. Grigsby, C. L. & Leong, K. W. Balancing protection and release of DNA: Tools to address a bottleneck of non-viral gene delivery. *J. R. Soc. Interface* **7**, 67–82 (2010).

22. Debus, H., Beck-broichsitter, M. & Kissel, T. Lab on a chip optimized preparation of pDNA / poly (ethylene imine) polyplexes using a microfluidic system, 2498–2506 (2012) .

23. Xu, Z., Lu, C., Riordon, J., Sinton, D. & Moffitt, M. G. Microfluidic manufacturing of polymeric nanoparticles: Comparing flow control of multiscale structure in single-phase staggered herringbone and two-phase reactors. *Langmuir.* **32**, 12781–12789 (2016).

24. Kaufman, R. J. Overview of vector design for mammalian gene expression. *Appl. Biochem. Biotechnol. - Part B Mol. Biotechnol.* **16**, 151–160 (2000).

25. Ajdari, N., Vyas, C., Bogan, S. L., Lwaleed, B. A. & Cousins, B. G. Gold nanoparticle interactions in human blood: a model evaluation. *Nanomedicine Nanotechnology, Biol. Med.* **13**, 1531–1542 (2017).

26. Chen, Y. S., Hung, Y. C., Liau, I. & Huang, G. S. Assessment of the in vivo toxicity of gold nanoparticles. *Nanoscale Res. Lett.* **4**, 858–864 (2009).

27. Neshatian, M., Chung, S., Yohan, D., Yang, C. & Chithrani, D. B. Determining the size dependence of colloidal gold nanoparticle uptake in a tumor-like interface (hypoxic). *Colloids Interface Sci. Commun.* **1**, 57–61 (2014).

28. Ajdari, N., Vyas, C., Bogan, S. L., Lwaleed, B. A. & Cousins, B. G. Gold nanoparticle interactions in human blood: A model evaluation. *Nanomedicine Nanotechnology, Biol. Med.* **13**, 1531–1542 (2017).

29. Rehman, M. U., Jawaid, P. & Kondo, T. Dual effects of nanoparticles on radiation therapy: as radiosensitizers and radioprotectors. *Radiat. Environ. Med.* **5**, 40–45 (2016).

30. Gu, X., Li, D. D., Yeoh, G. H., Taylor, R. A. & Timchenko, V. Heat generation in

irradiated gold nanoparticle solutions for hyperthermia applications. *Processes* **9**, 1–19 (2021).

31. Cormode, D. P., Naha, P. C. & Fayad, Z. A. Nanoparticle contrast agents for computed tomography: A focus on micelles. *Contrast Media Mol. Imaging* **9**, 37–52 (2014).

32. Sobczak-Kupiec, A. *et al.* Gold nanoparticles as a modifying agent of ceramic-polymer composites. *Arch. Metall. Mater.* **59**, 1005–1009 (2014).

33. Dichello, G. A. et al. Preparation of liposomes containing small gold nanoparticles using electrostatic interactions. *Eur. J. Pharm. Sci.* **105**, 55–63 (2017).

34. Amgoth, C., Suman Joshi, D. S. D., Dharmapuri, G. & Lakavathu, M. Self-assembled block copolymer [(BenzA)-b-(PCL)] micelles to orient randomly distributed AuNPs into hollow core-shell morphology and its role as payload for nanomedicines. *Mater. Sci. Eng. C* **92**, 790–799 (2018).

35. Jain, S., Hirst, D. G. & O'Sullivan, J. M. Gold nanoparticles as novel agents for cancer therapy. *Br. J. Radiol.* **85**, 101–113 (2012).

36. Ghosh, P., Han, G., De, M., Kim, C. K. & Rotello, V. M. Gold nanoparticles in delivery applications. *Adv. Drug Deliv. Rev.* **60**, 1307–1315 (2008).

37. Joh, D. Y. et al. Selective Targeting of Brain Tumors with Gold Nanoparticle-Induced Radiosensitization. *PLOS ONE.* **8**, (2013).

38. Egli, S. et al. Biocompatible functionalization of polymersome surfaces: A new approach to surface immobilization and cell targeting using polymersomes. *J. Am. Chem. Soc.* **133**, 4476–4483 (2011).

39. Mesbahi, A. A review on gold nanoparticles radiosensitization effect in radiation therapy of cancer. *Reports Pract. Oncol. Radiother.* **15**, 176–180 (2010).

40. Azzam, T. & Eisenberg, A. Monolayer-protected gold nanoparticles by the self-assembly of micellar poly(ethylene oxide)-b-Poly(ε-caprolactone) block copolymer. *Langmuir.* **23**, 2126–2132 (2007).

41. Dai, Y., Ren, T., Wang, Y. & Zhang, X. Polyion complex micelles to stabilize gold nanoparticles for catalytic reduction of 4-nitrophenol. *Gold Bull.* **51**, 21–26 (2018).

42. Sengani, M., Mihai, A. & Rajeswari, V. D. OpenNano recent trends and methodologies in gold nanoparticle synthesis:A prospective review on drug delivery aspect. *OpenNano* **2**, 37–46 (2017).

43. Lin, W. et al. pH-responsive unimolecular micelle-gold nanoparticles-drug nanohybrid system for cancer theranostics. *Acta Biomater.* **58**, 455–465 (2017).

44. Al Zaki, A. et al. Gold-loaded polymeric micelles for computed tomography-guided radiation therapy treatment and radiosensitization. *ACS Nano* **8**, 104–112 (2014).

45. Minozzi, M., Nanni, D. & Spagnolo, P. tert -Dodecanethiol. in *Encyclopedia of Reagents for Organic Synthesis* (John Wiley & Sons, Ltd, 2008).

46. Nishiya, T. & Lam, R. T. T. Mechanistic study on toxicity of positively charged liposomes containing stearylamine to blood: use of carboxymethyl chitin to reduce toxicity. *Colloids Surfaces B Biointerfaces.* **1**, 213–219 (1993).

47. Barber, A., Kly, S., Moffitt, M. G., Rand, L. & Ranville, J. F. Coupling single particle ICP-MS with field-flow fractionation for characterizing metal nanoparticles contained in nanoplastic colloids. *Environ. Sci. Nano* **7**, 514–524 (2020).

48. Alkilany, A. M., Abulateefeh, S. R. & Murphy, C. J. Facile functionalization of gold nanoparticles with PLGA polymer brushes and efficient encapsulation into PLGA nanoparticles: Toward spatially precise bioimaging of polymeric nanoparticles. *Part. Part. Syst. Charact.* **36**, 1–8 (2019).

49. Zeng, F., Lee, H. & Allen, C. Epidermal growth factor-conjugated poly(ethylene glycol)-block-poly(δ-valerolactone) copolymer micelles for targeted delivery of chemotherapeutics. *Bioconjug. Chem.* **17**, 399–409 (2006).

50. Azzam, T. & Eisenberg, A. Monolayer-protected gold nanoparticles by the self-assembly of micellar poly(ethylene oxide)-b-poly(E-caprolactone) block copolymer. *Langmuir*, **23**, 2126–2132 (2007).

51. Rich. 基因的改变NIH Public Access. *Bone*, **23**, 1–7 (2009).

52. Kettler, K., Veltman, K., van de Meent, D., van Wezel, A. & Hendriks, A. J. Cellular uptake of nanoparticles as determined by particle properties, experimental conditions, and cell type. *Environ. Toxicol. Chem.* **33**, 481–492 (2014).

53. Coleman, B. R. & Moffitt, M. G. Amphiphilic inorganic nanoparticles with mixed polymer brush layers of variable composition: Bridging the paradigms of block copolymer and nanoparticle self-assembly. *Chem. Mater.* **30**, 2474–2482 (2018).

54. Bains, A., Cao, Y. & Moffitt, M. G. Multiscale control of hierarchical structure in crystalline block copolymer nanoparticles using microfluidics. *Macromol. Rapid Commun.* **36**, 2000–2005 (2015).

55. Uddin, M. N. & Roni, M. A. Challenges of storage and stability of mRNA-Based COVID-19 Vaccines. *Vaccines* **9**, 1033 (2021).

56. Gao, Y. et al. PH/Redox Dual-responsive polyplex with effective endosomal escape for codelivery of siRNA and doxorubicin against drug-resistant cancer cells. *ACS Appl. Mater. Interfaces.* **11**, 16296–16310 (2019).

57. Chen, K., Huang, Y. H. & Chen, J. L. Understanding and targeting cancer stem cells: Therapeutic implications and challenges. *Acta Pharmacol. Sin.* **34**, 732–740 (2013).

58. Hara, D. et al. Prostate Cancer Targeted X-Ray Fluorescence Imaging via gold nanoparticles functionalized with prostate-specific membrane antigen (PSMA). *Int. J. Radiat. Oncol. Biol. Phys.* **111**, 220–232 (2021).

59. Leapman, R. D. & Rizzo, N. W. Towards single atom analysis of biological structures. *Ultramicroscopy.* **78**, 251–268 (1999).

60. Leapman, R. D. & Hunt, J. A. Comparison of detection limits for EELS and EDXS. *Microsc. Microanal. Microstruct.* **2**, 231–244 (1991).

61. Wang, P. et al. Thermo-triggered release of CRISPR-Cas9 system by lipid-encapsulated gold nanoparticles for tumor therapy. *Angew. Chem. Int. Ed.* **57**, 1491–1496 (2018).

62. Zucker, R. M., Massaro, E. J., Sanders, K. M., Degn, L. L. & Boyes, W. K. Detection of TiO2 nanoparticles in cells by flow cytometry. *Cytometry. A* **77**, 677–685 (2010).

63. Wu, Y., Ali, M. R. K., Dansby, K. & El-Sayed, M. A. Improving the flow cytometry-based detection of the cellular uptake of gold nanoparticles. *Anal. Chem.* (2019)

Appendix A

Chapter 2 Supporting Information

S2.1 Supporting Information

Sample static light scattering data for CWC determination; Number intensity distributions for bulk and microfluidic PIHC micelles from CONTIN analysis of DLS data; 2-week PIHC micelle size

and poldispersity stability data; LSCFM images of DAPI/DiI-labelled PIHC micelles deposited from an aqueous dispersion without cells; cell viability data from MDA-MB-231 cells dosed with PIHC micelles; and a table of actual flow rates.

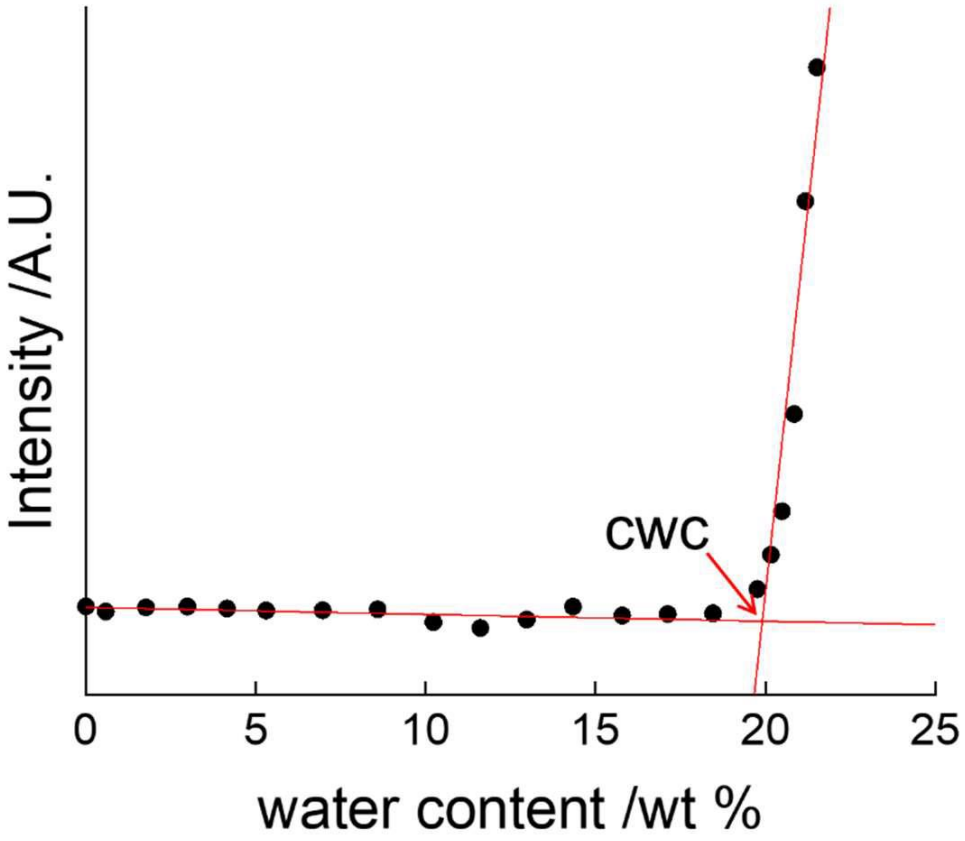

Figure S2.1. Critical water concentration (CWC) determination of PCL-b-PEG copolymer only (without PCL-pDNA) at the copolymer concentration and solvent composition of microfluidic PIHC micelle formation using static light scattering. Mean CWC and standard error (19.2 ± 0.3 wt

%) were calculated from triplicate experiments; for each experiment, the CWC value was determined using linear regression of "baseline" and "rise" regions as shown.

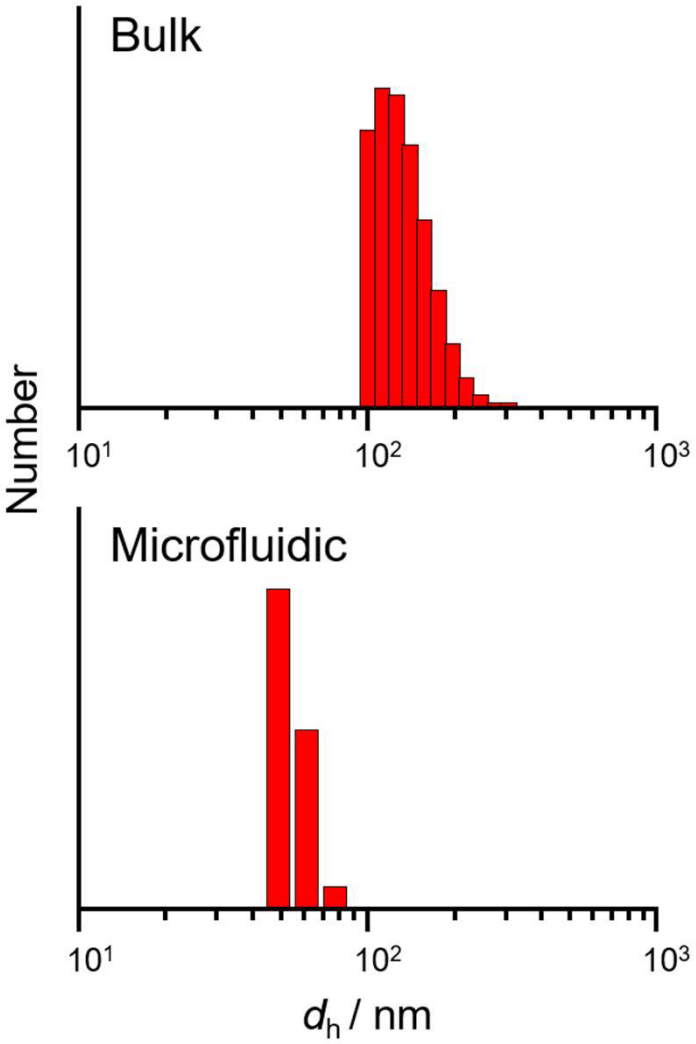

Figure S2.2. DLS number distributions (CONTIN analysis) of bulk (top) and microfluidic (bottom) PIHC micelle data shown in Figure 4.7B. In contrast to the intensity distribution of the microfluidic PIHC micelle sample (weighted by scattered light intensity) in which both smaller and larger particle populations are present (Figure 4.7B, bottom), only the smaller particle population is observed in the number distribution (bottom).

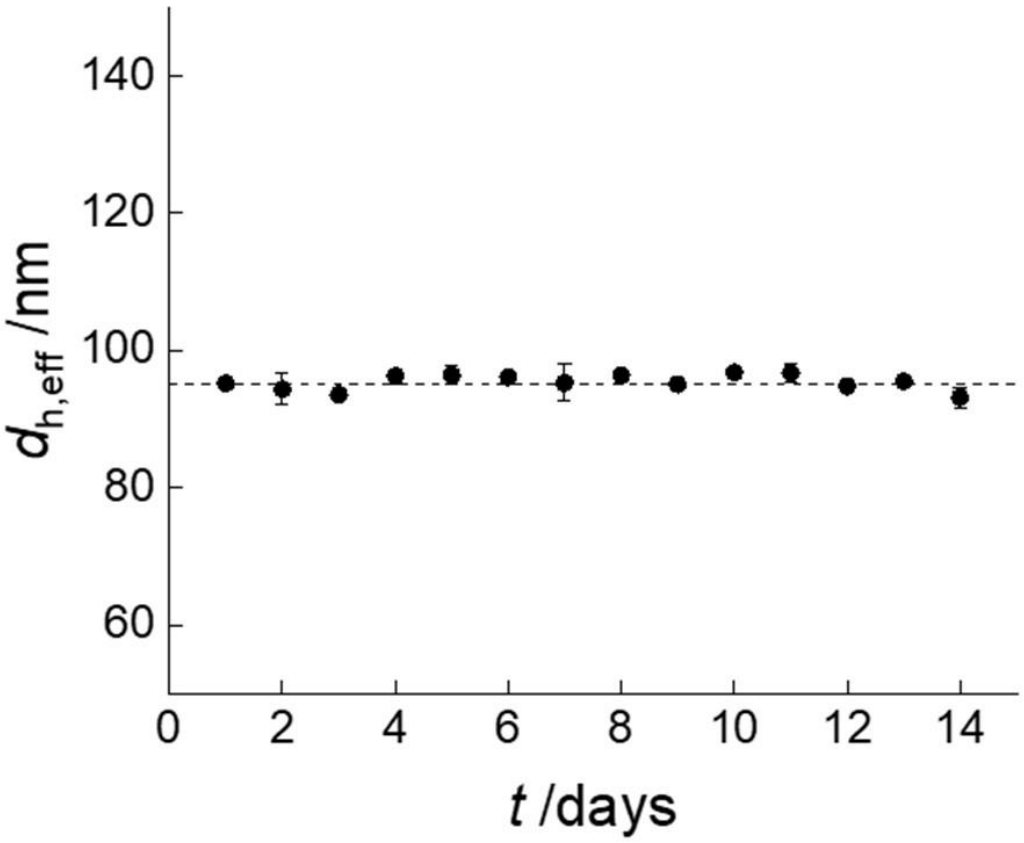

Figure S2.3. Size stability data for microfluidic PIHC micelle measured by DLS over two weeks for a single sample. The dashed horizontal line indicates the initial t = 1 day measurement. Insignificant deviation from the initial size over 14 days indicates good stability over this time period.

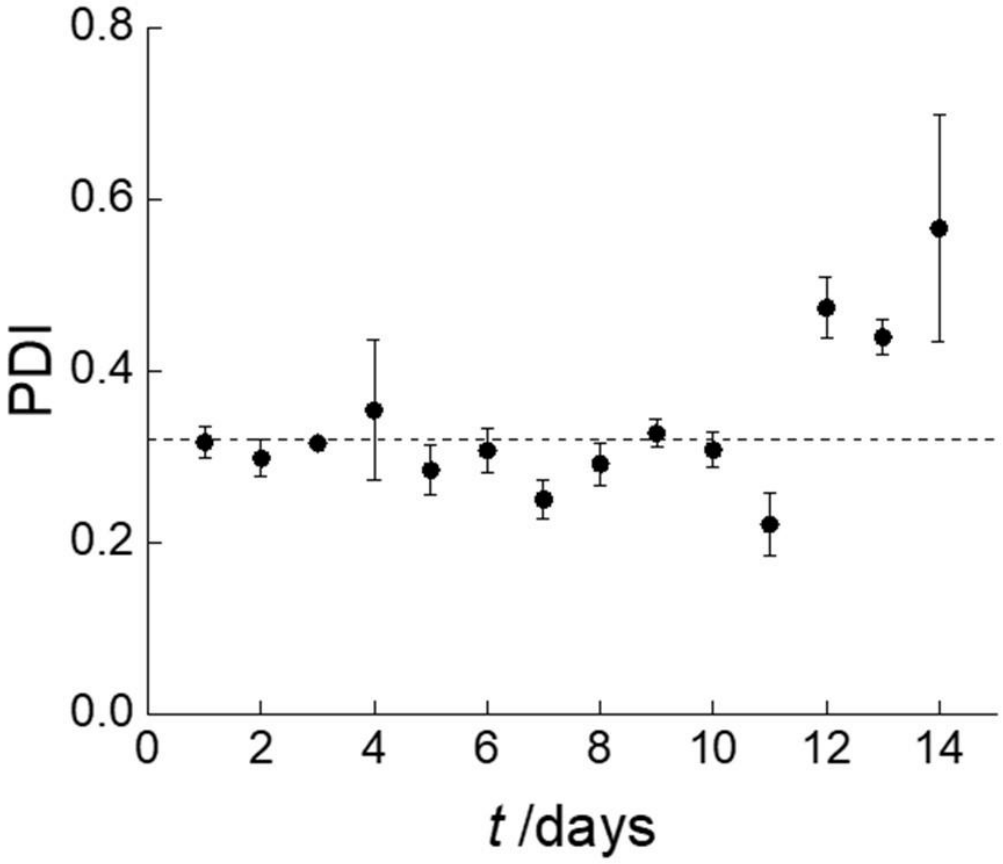

Figure S2.4. Polydispersity stability data for microfluidic PIHC micelle measured by DLS over two weeks for a single sample. The dashed horizontal line indicates the initial t = 1 day measurement. Insignificant deviation from the initial polydispersity was observed over the first 12 days.

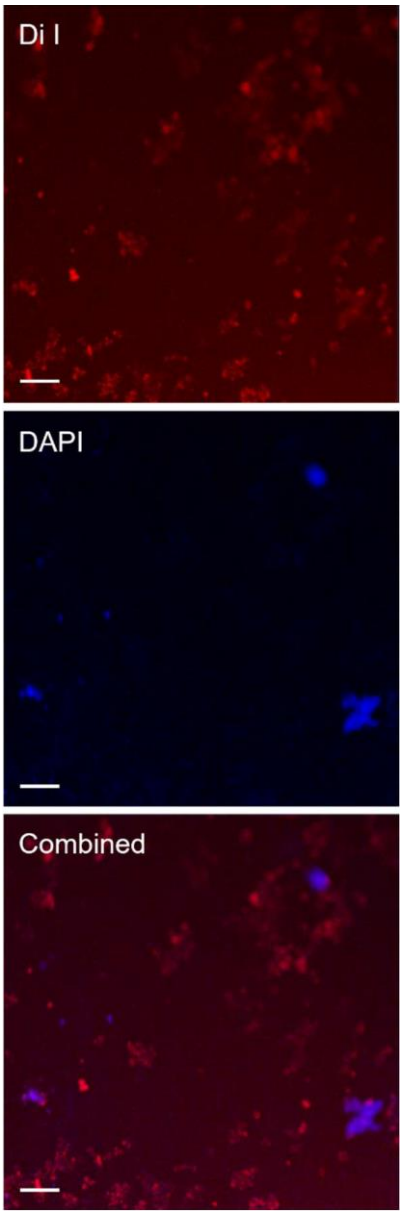

Figure S2.5. Fluorescence imaging data showing DAPI/DiI-labeled PIHC micelles deposited from an aqueous dispersion. Encapsulated pDNA was labelled with DAPI (blue) and PCL cores of the micelles were labelled with DiI (red). The red fluorescence channel (DiI) shows a greater number of fluorescent regions that the blue fluorescence channel (DAPI), indicating that some micelles do not contain pDNA. The overlay of red and blue channels (combined) shows co-localization between blue and red fluorescence, indicating that all pDNA is associated with micelles. Scale bars are 10 μm.

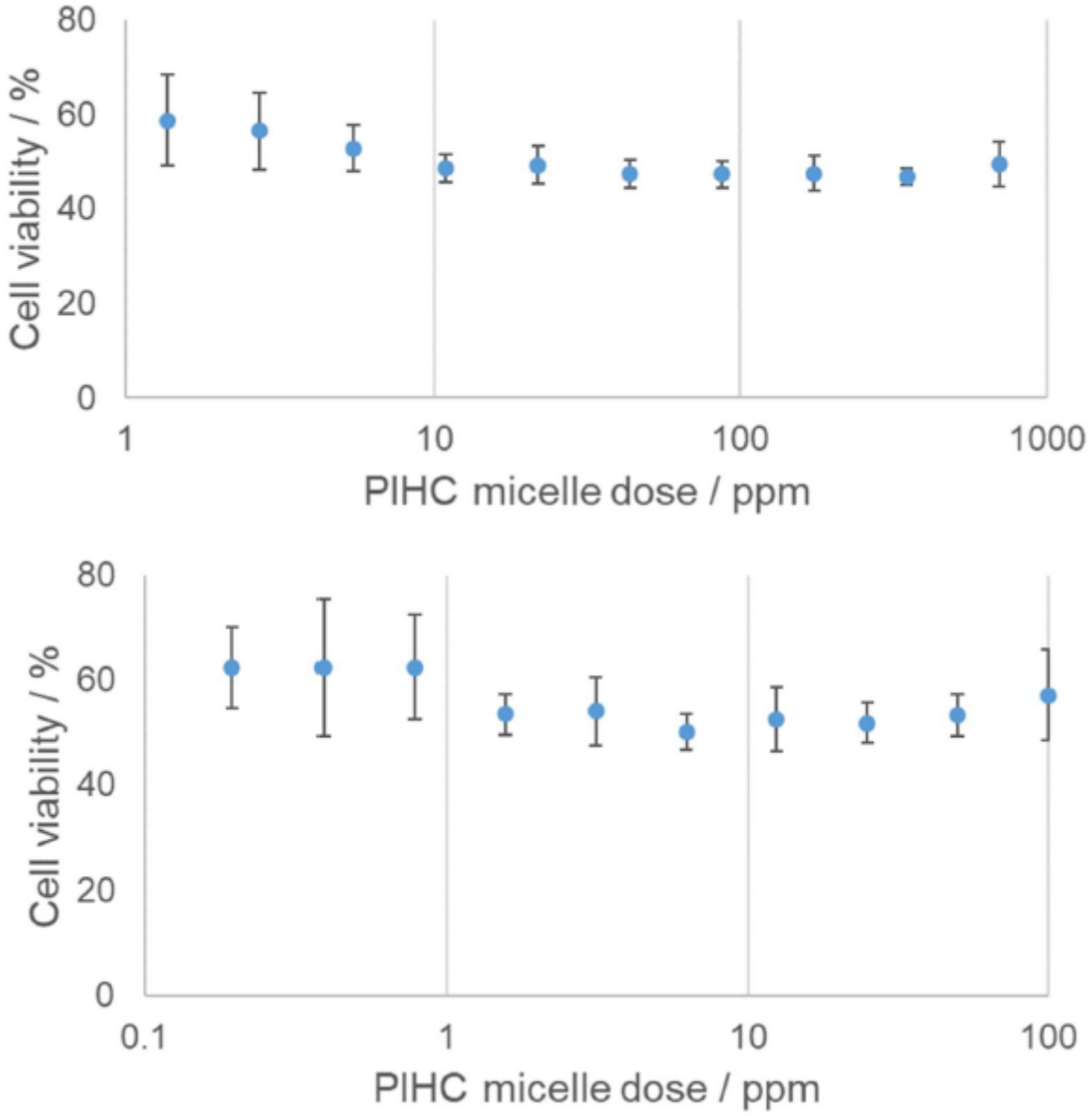

Figure S2.6. Cell viability of MDA-MB-231 cells with various dosing levels of PIHC micelles. Absence of dose dependence over 4 orders of magnitude of dosing levels indicates no cytotoxic effect of the PIHC micelles.

Table S2.1. Actual Flow Rates of Various Preparations of PIHC Micelles within the Two-Phase Segmented Microfluidic Reactor Described in the Main Text.

PIHC micelles	Trial #	Q_{gas} (µL / min)	Q_{gas} / Q_{liq}	Q_{total} (µL / min)
Figure 7A	1	103	1.03	203
	2	100	1.00	200
	3	105	1.05	205
Figure 7B, 8, 9, 10	1	108	1.08	208
	2	106	1.06	206
	3	102	1.02	202
Figure 11	1	104	1.04	204

a) The nominal flow rate for all experiments was 200 µL / min.

b)The liquid flow rate was assumed to be the sum of the three flow rate readings set on the syringe pump before running.

Appendix B

Chapter 3 Supporting Information

S3.1 Supporting Information

Schematic of the microfluidic reactor; table of actual microfluidic flow rates; size distributions from TEM images of GNPs and GNRs before and after functionalization with PCL-SH; CONTIN size distributions from DLS data of various GNP-PNP samples; TEM and DLS data for PEG-GNP control sample; GFAA calibration curve.

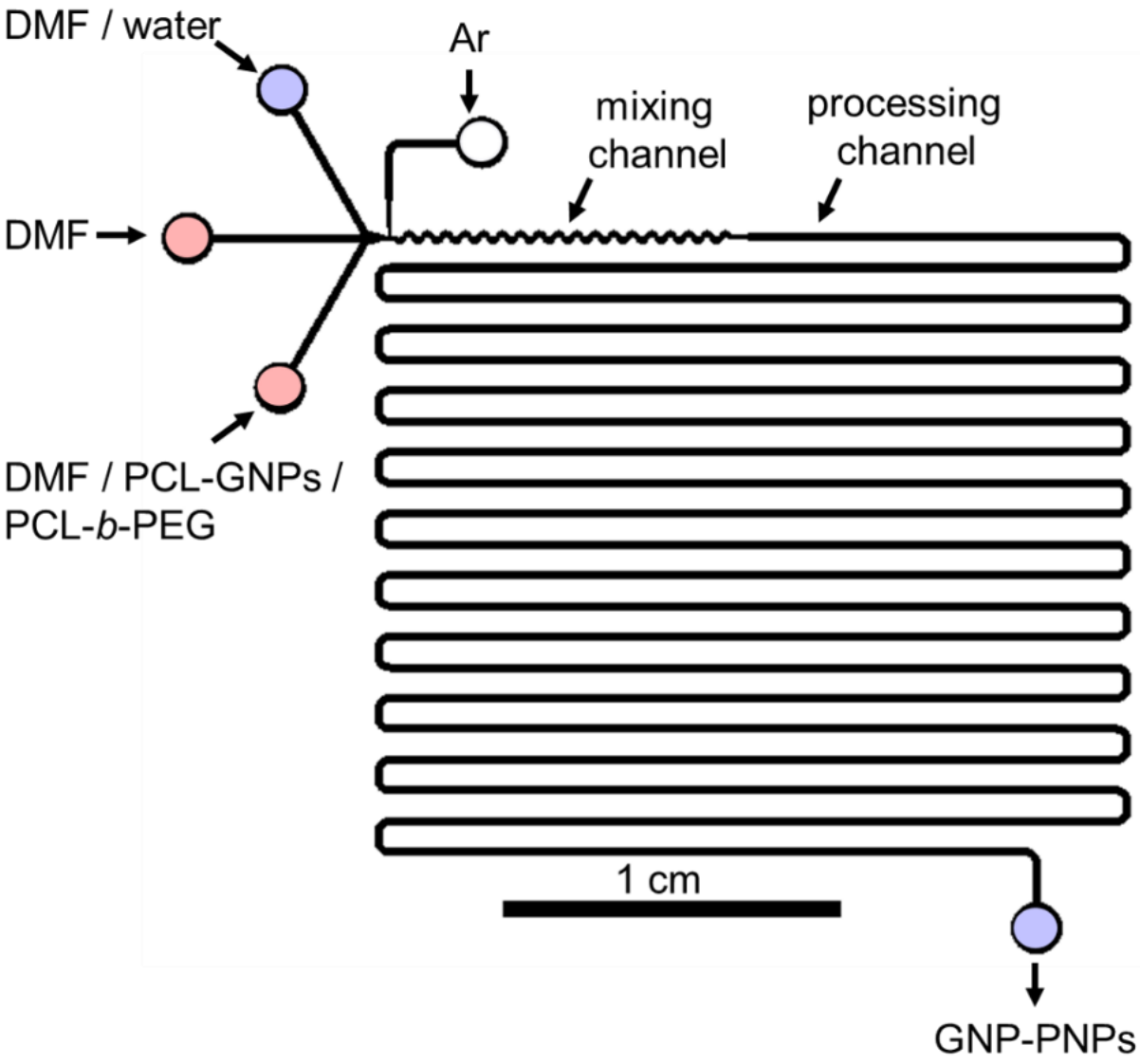

Figure S3.1. Schematic of the two-phase, gas-liquid microfluidic reactor used to produce some of the GNP-PNP samples described in the main text.

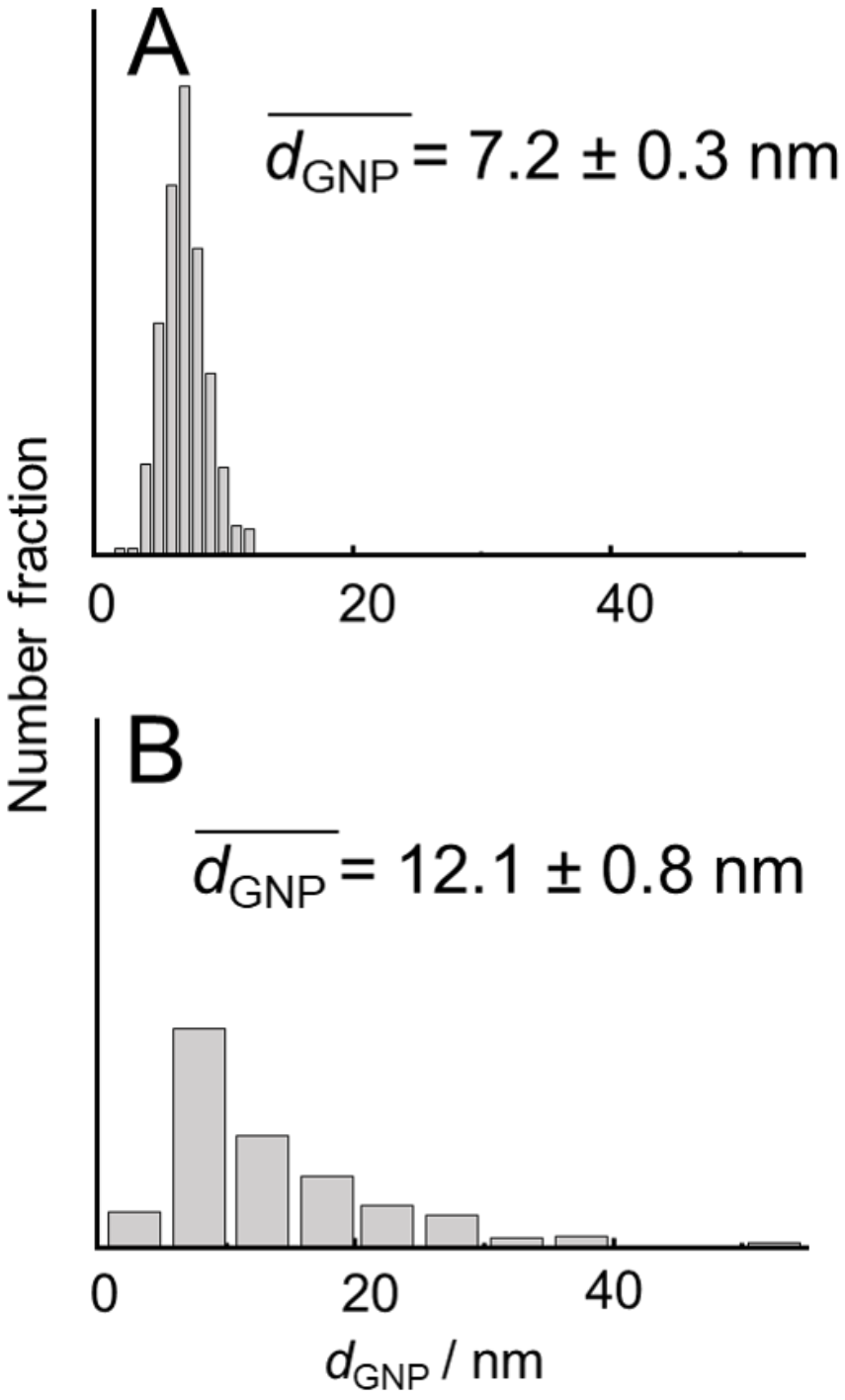

Figure S3.2. Number distributions and mean values of GNP diameters from TEM images of GNPs before (A) and after (B) PCL-SH functionalization.

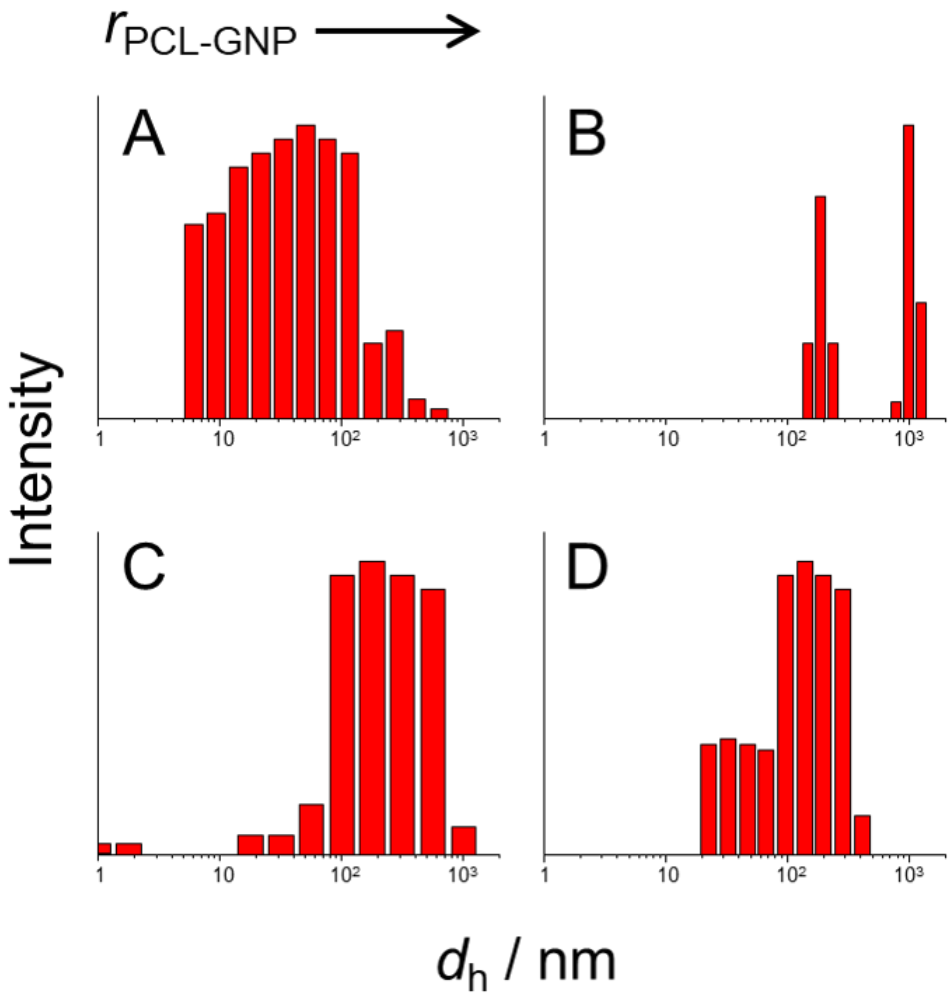

Figure S3.3. Effect of PCL-GNP/PCL-*b*-PEG ratio (w/w), $r_{PCL-GNP}$, on CONTIN distributions of hydrodynamic diameters of GNP-PNPs prepared using the bulk method. The distributions were determined from DLS measurements of GNP-PNPs prepared at (A) $r_{PCL-GNP}$ = 2, (B) $r_{PCL-GNP}$ = 10, (C) $r_{PCL-GNP}$ = 50, and (D) $r_{PCL-GNP}$ = 100.

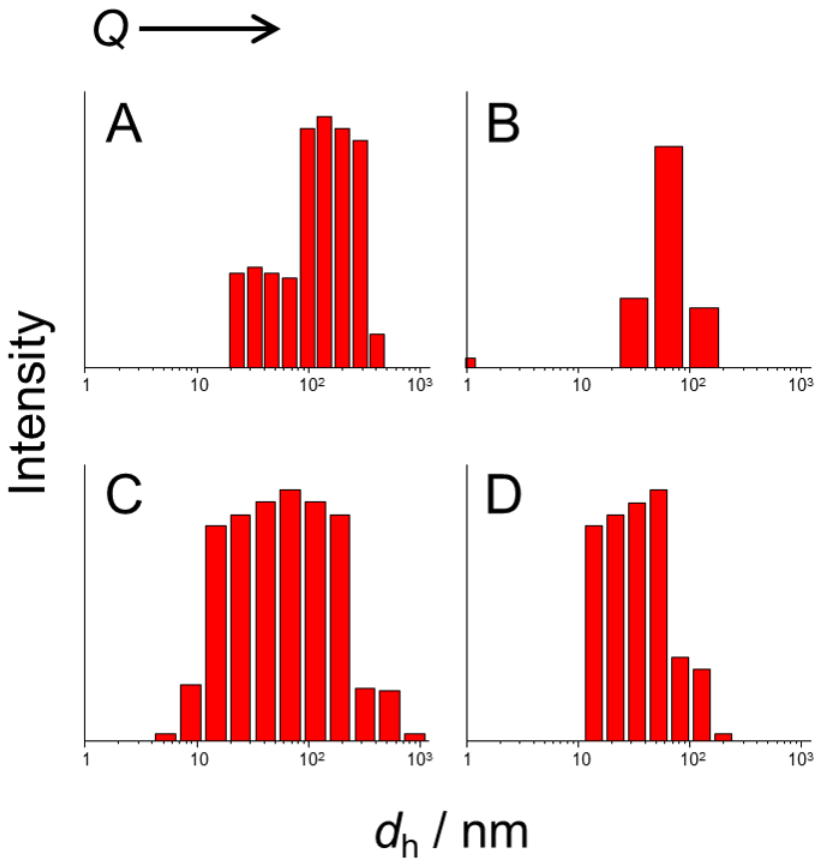

Figure S3.4. Effect of flow rate, *Q*, on CONTIN distributions of hydrodynamic diameters of GNP-PNPs prepared at a PCL-GNP/PCL-*b*-PEG ratio (w/w), $r_{PCL\text{-}GNP}$ = 100. The distributions were determined from DLS measurements of GNP-PNPs prepared at the following flow rates, where all samples were prepared using the microfluidic method except *Q* = 0 µL/min, which denotes the bulk method: (A) *Q* = 0 µL/min (bulk), (B) *Q* = 100 µL/min, (C) *Q* = 200 µL/min, and (D) *Q* = 400 µL/min.

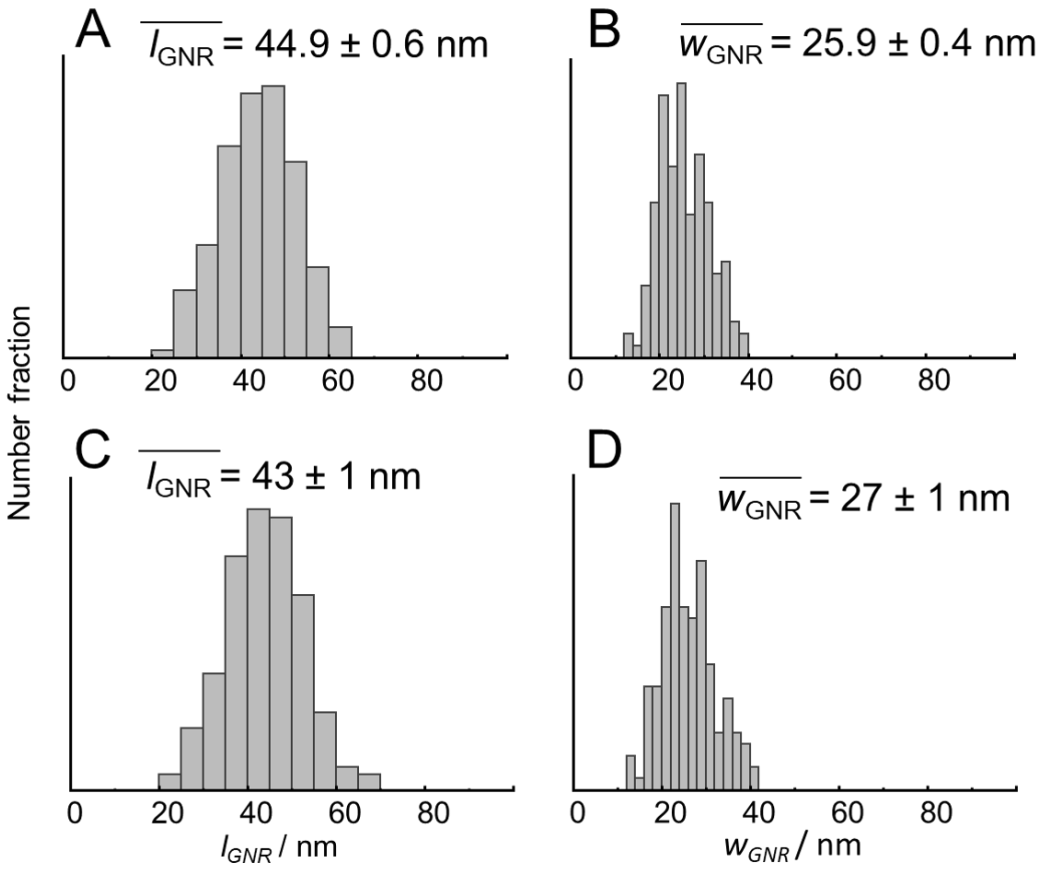

Figure S3.5. Number distributions and mean values of GNR lengths (A, C) and widths (B, D) from TEM images of GNRs before (A,B) and after (C,D) PCL-SH functionalization.

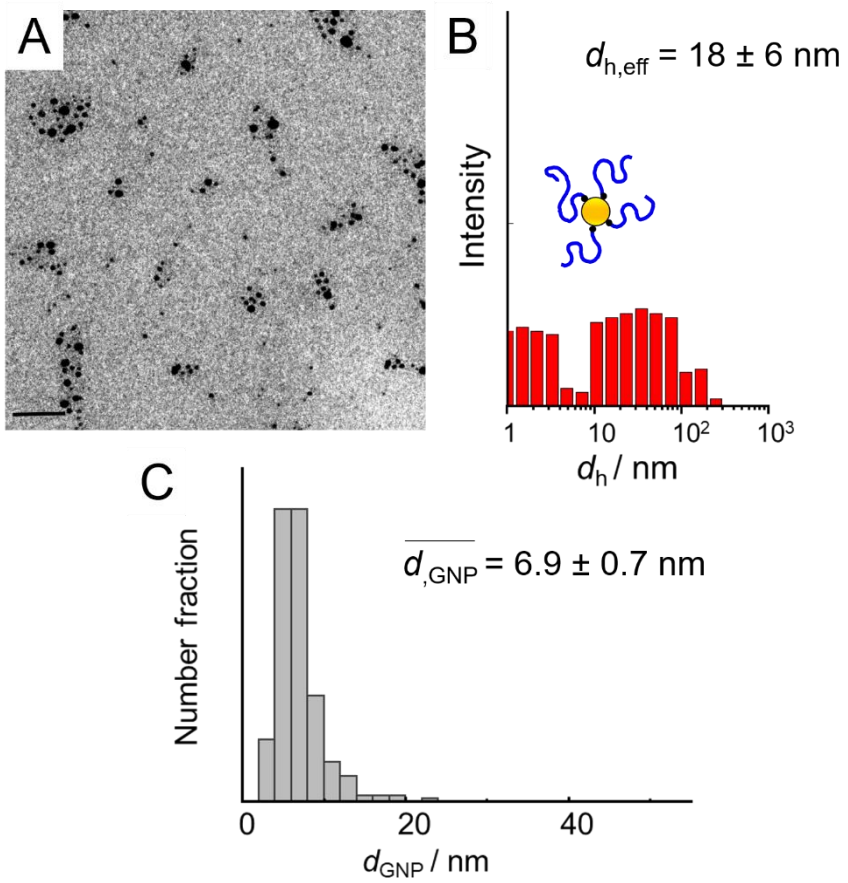

Figure S3.6. TEM and DLS data for PEG-GNP control sample. (A) TEM image and (B) DLS analysis, including CONTIN hydrodynamic size distributions and mean effective hydrodynamic diameters, $d_{h,eff}$, from cumulant analysis for PEG-GNPs in water. (C) Number distributions and mean values of PEG-GNP core diameters from TEM images. Scale bar in TEM image is 50 nm.

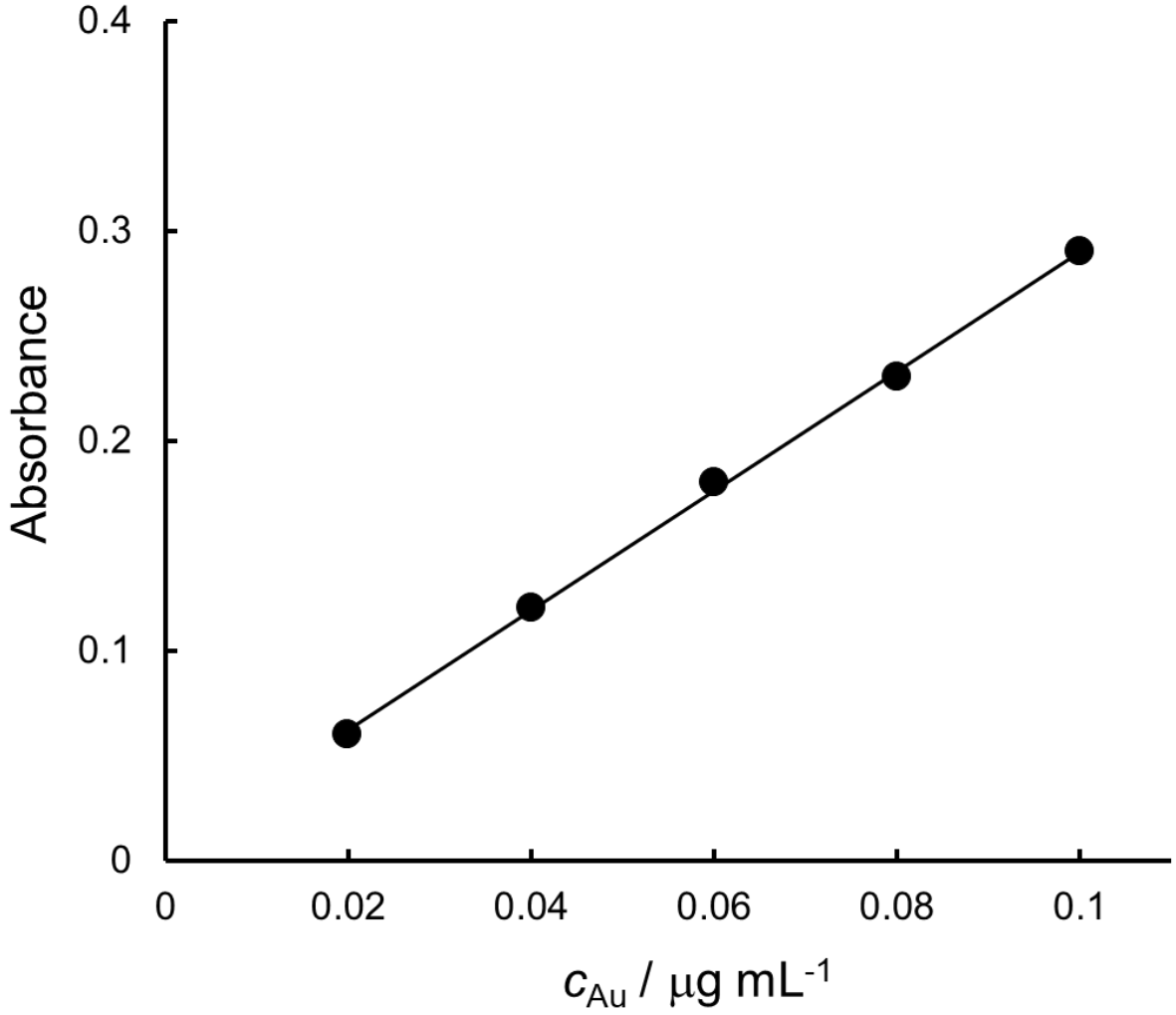

Figure S3.7. GFAA calibration curve for analysis of cell uptake of GNPs determined using gold standard solutions.

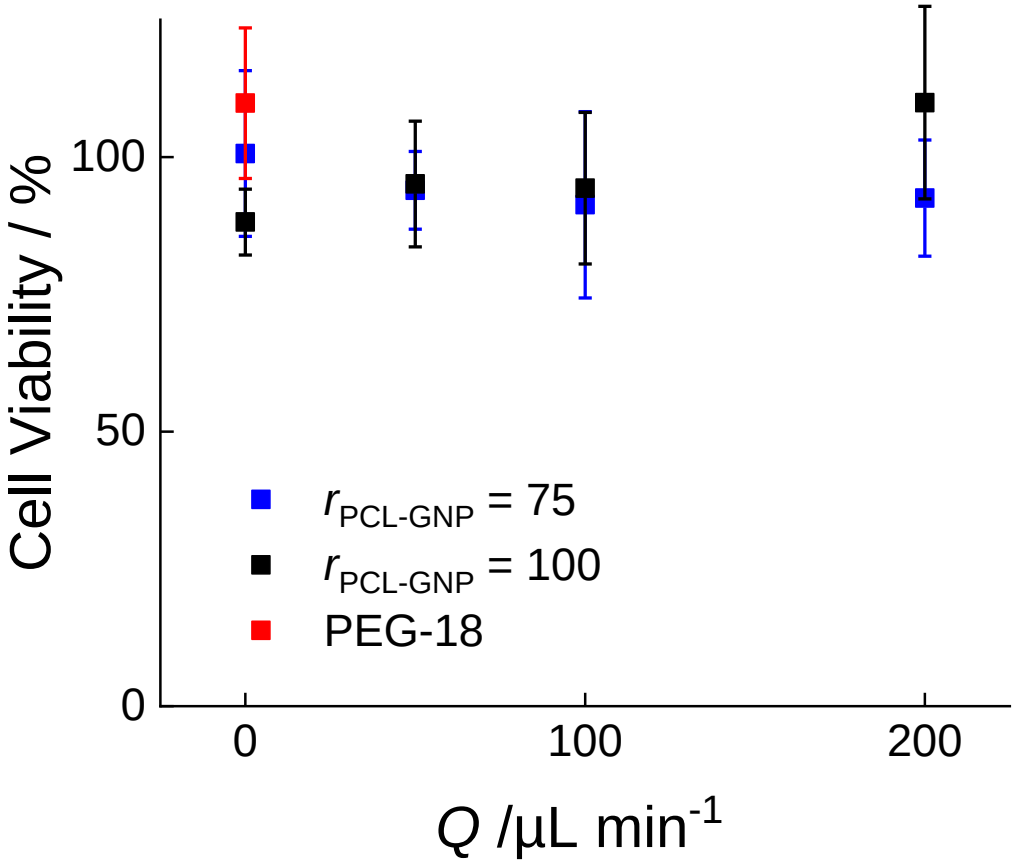

Figure S3.8 Cell viability of MDA-MB-231 cells with various dosed at 500 nM gold of GNP-PNPs or PEG-GNPs. Absence of cell indicates no cytotoxic effect of the GNP-PNPs at this dosing level.

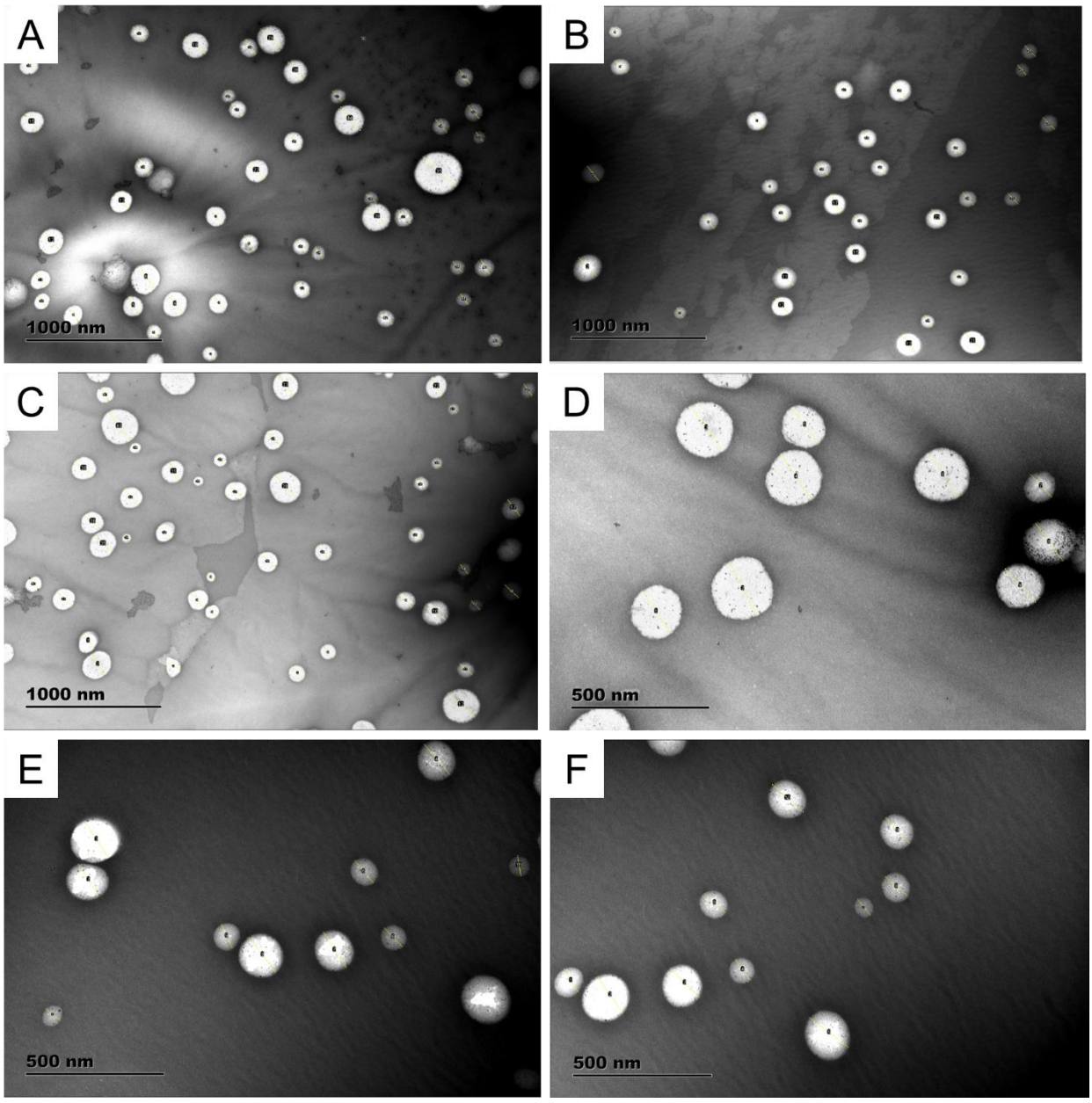

Figure S3.9. A portion of the annotated TEM images of $r_{PCL\text{-}GNP}$ = 75 bulk condition used for TEM statistics.

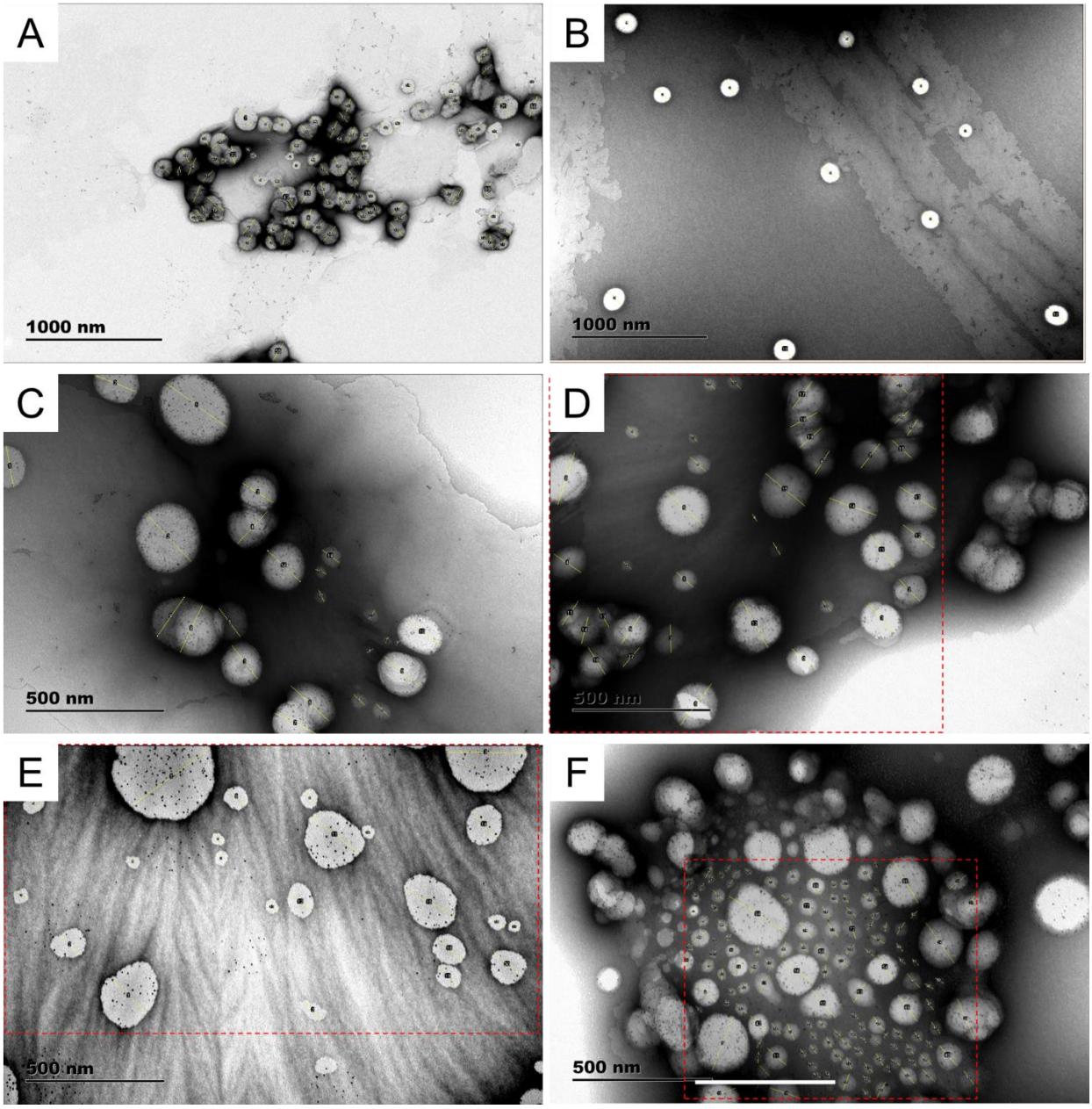

Figure S3.10. A portion of the annotated TEM images of $r_{PCL\text{-}GNP}$ = 75 Q = 50µL/min condition used for TEM statistics.

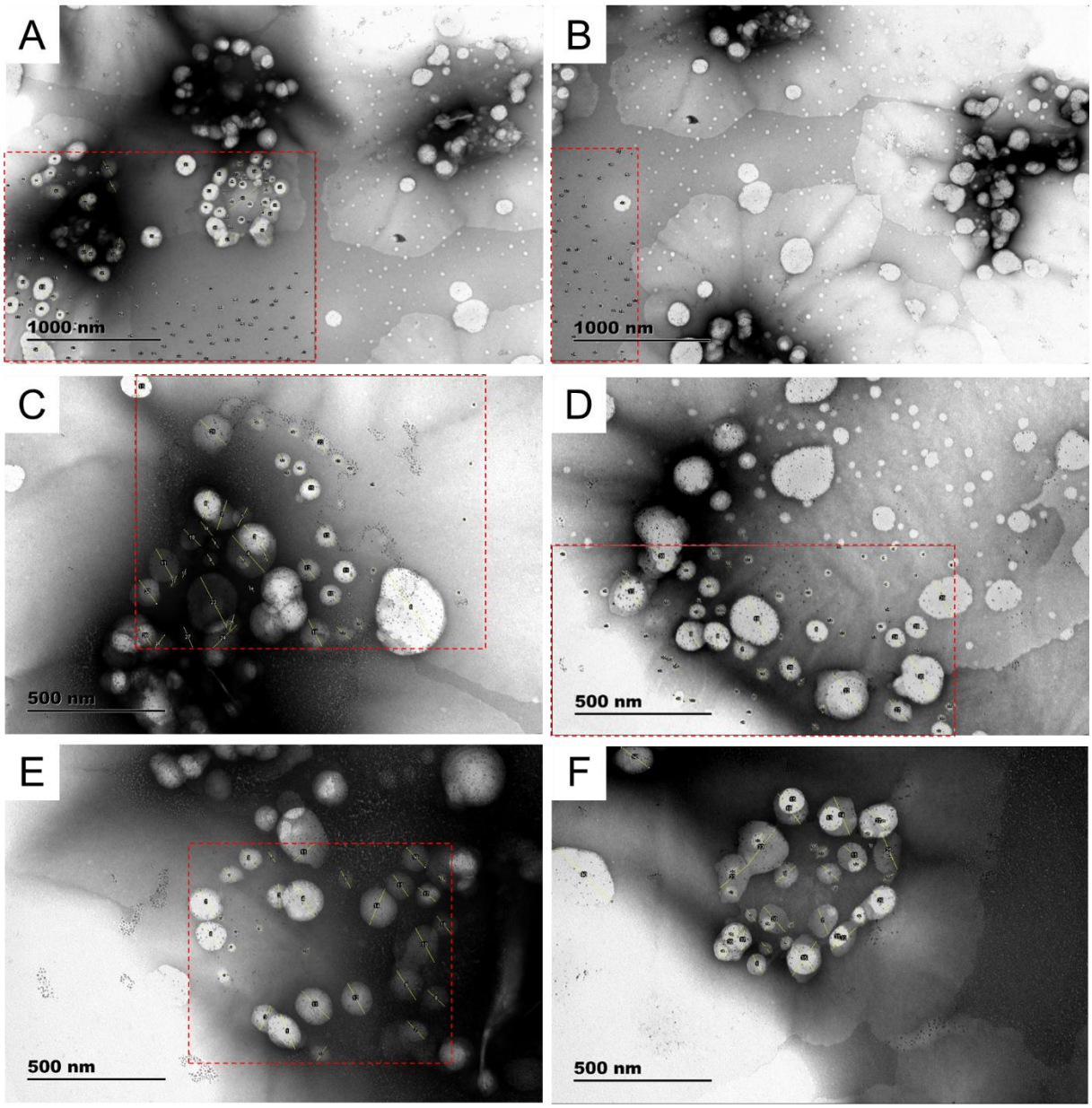

Figure S3.11. A portion of the annotated TEM images of $r_{PCL\text{-}GNP}$ = 75 Q = 100µL/min condition used for TEM statistics.

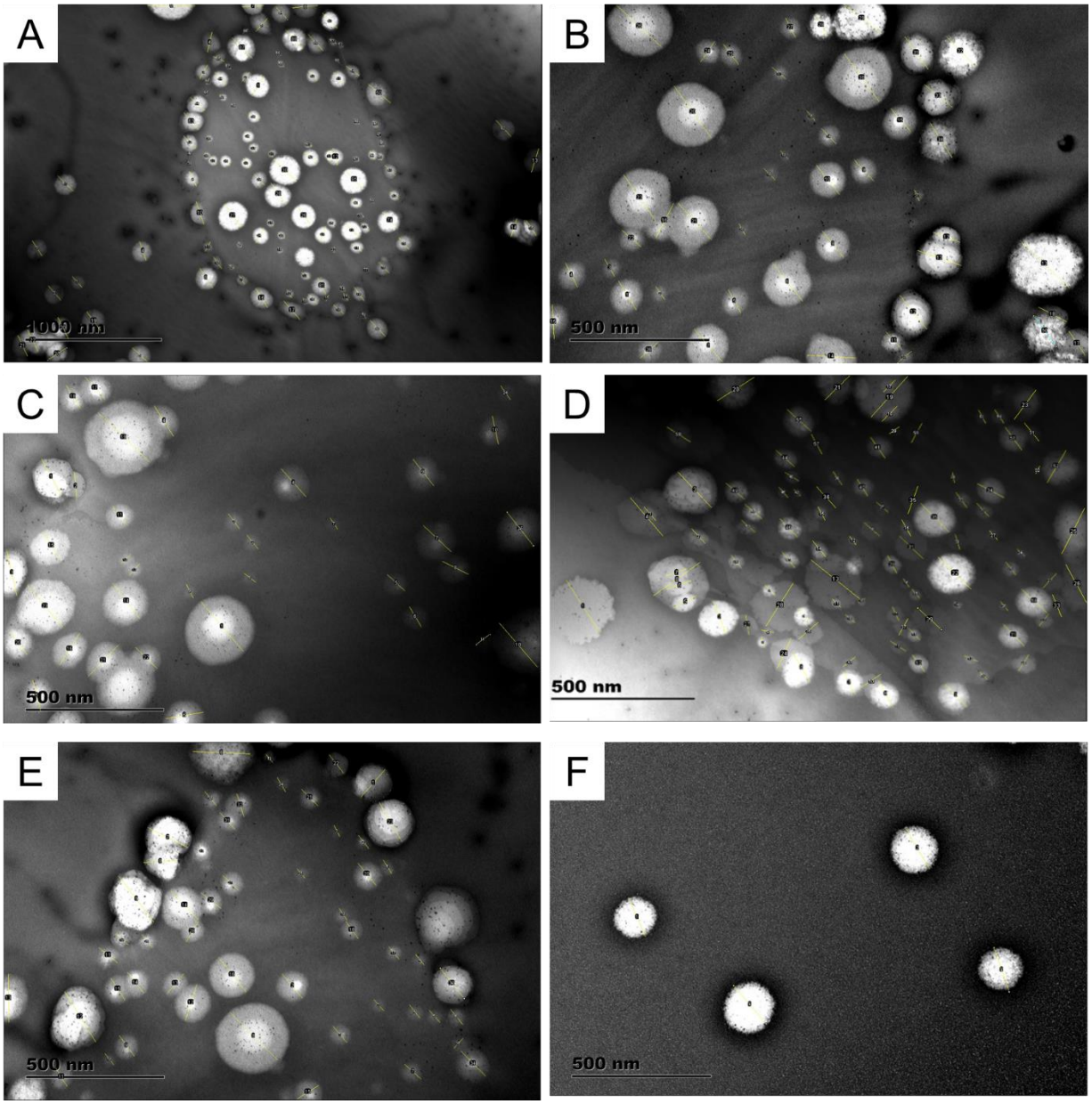

Figure S3.12. A portion of the annotated TEM images of $r_{PCL\text{-}GNP}$ = 75 Q = 200µL/min condition used for TEM statistics.

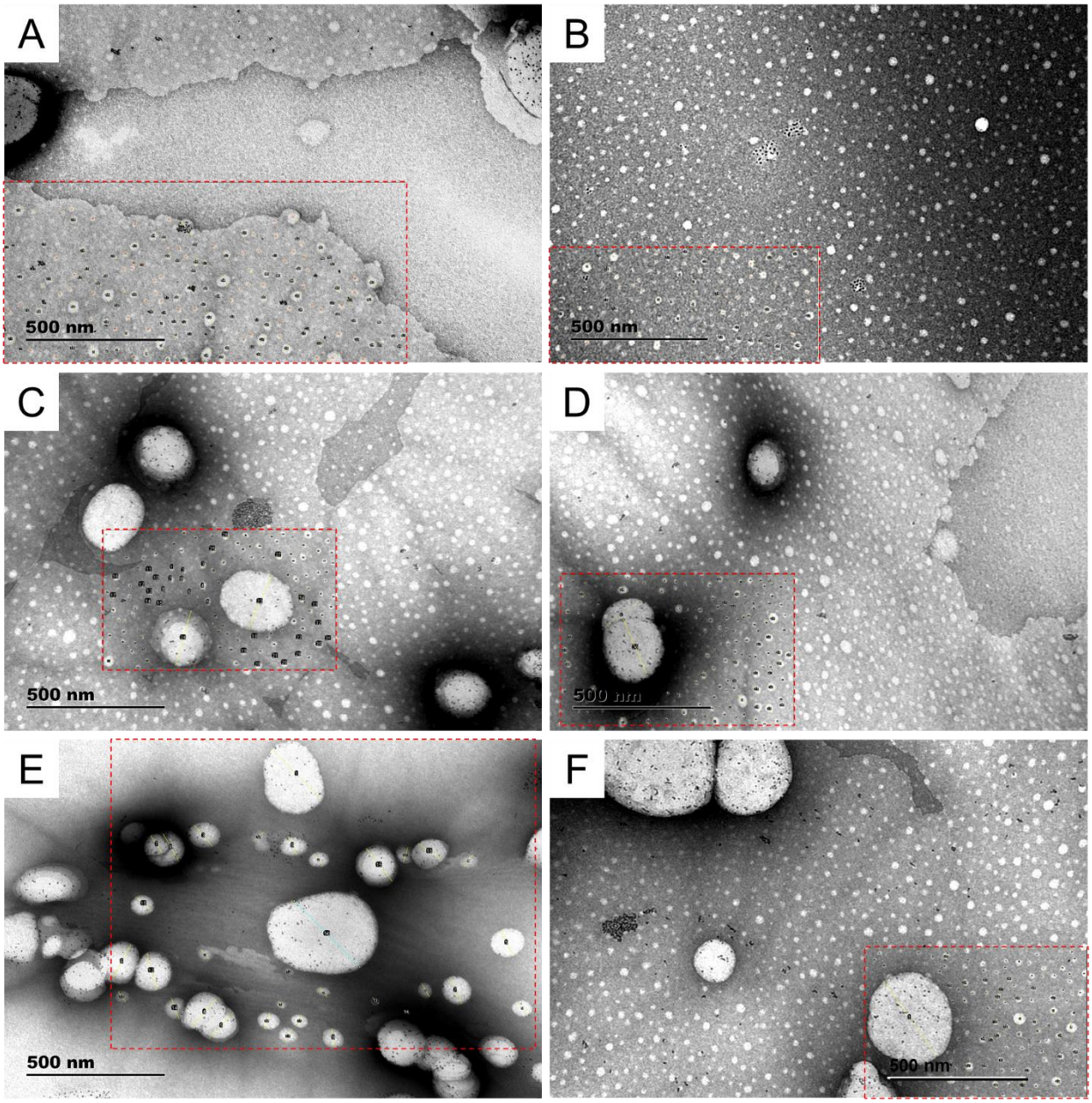

Figure S3.13. A portion of the annotated TEM images of $r_{PCL\text{-}GNP}$ = 100 bulk condition used for TEM statistics.

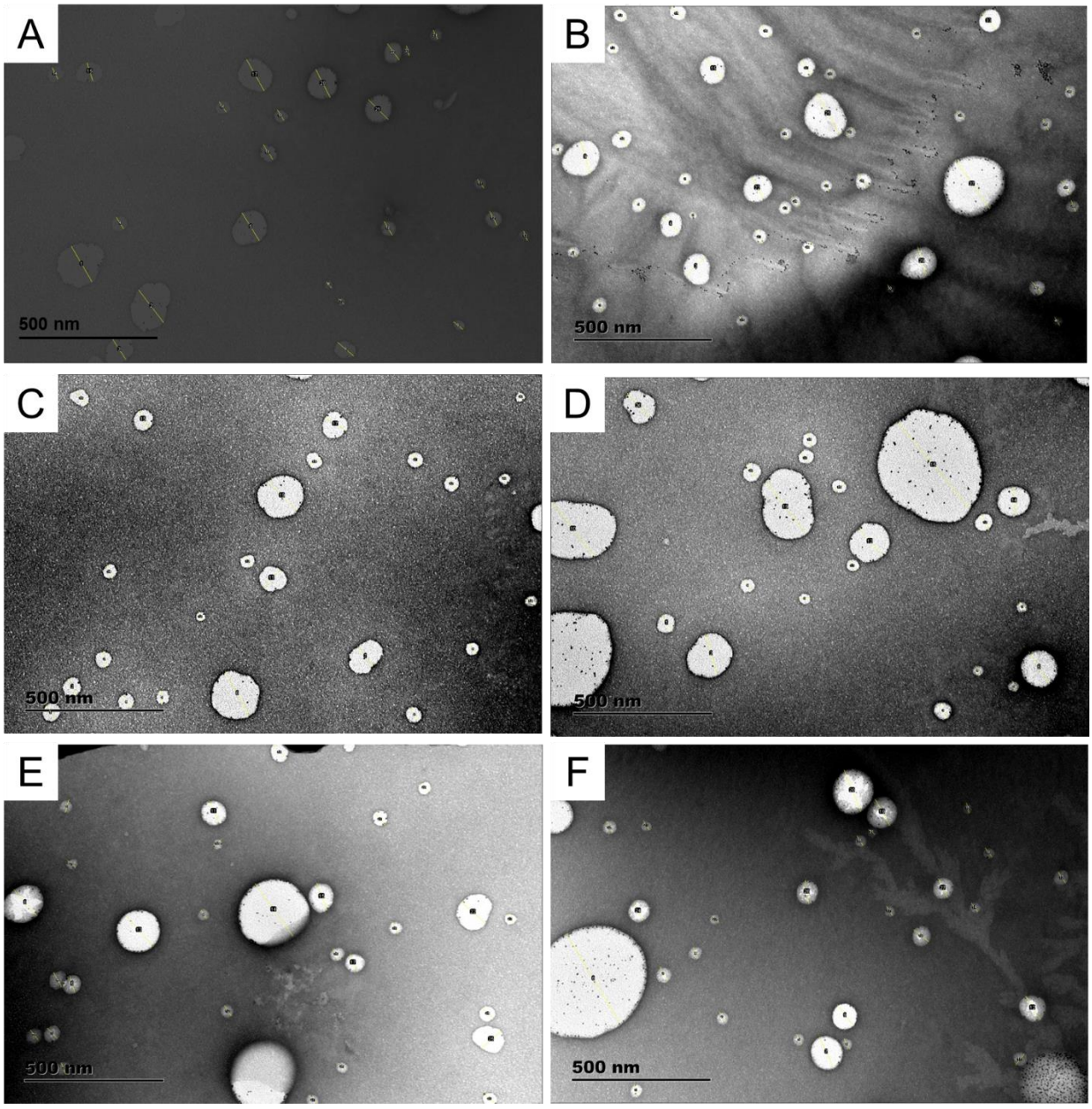

Figure S3.14. A portion of the annotated TEM images of $r_{PCL\text{-}GNP}$ = 100 Q = 50µL/min condition used for TEM statistics.

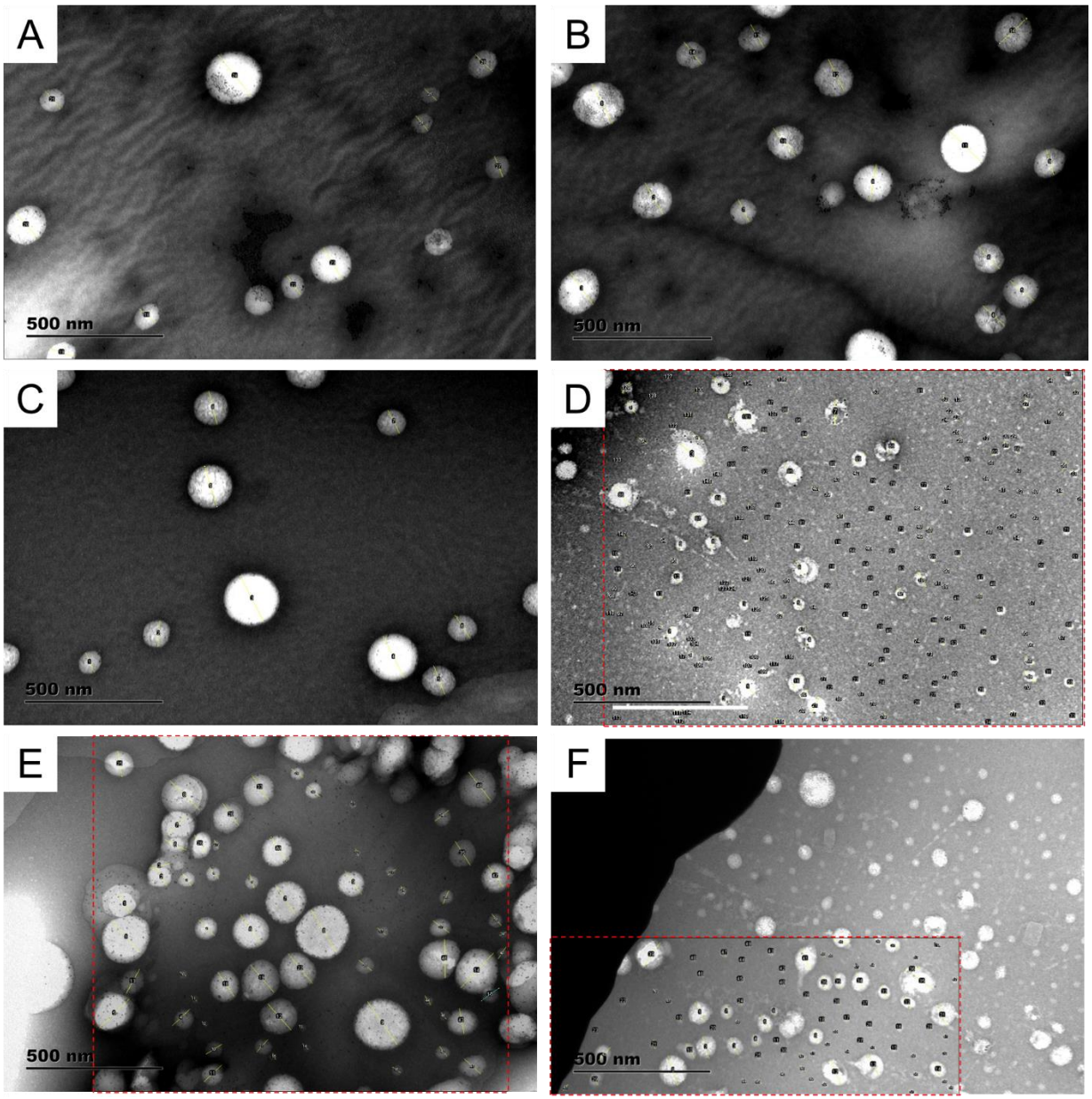

Figure S3.15. A portion of the annotated TEM images of $r_{PCL\text{-}GNP}$ = 100 Q = 100µL/min condition used for TEM statistics.

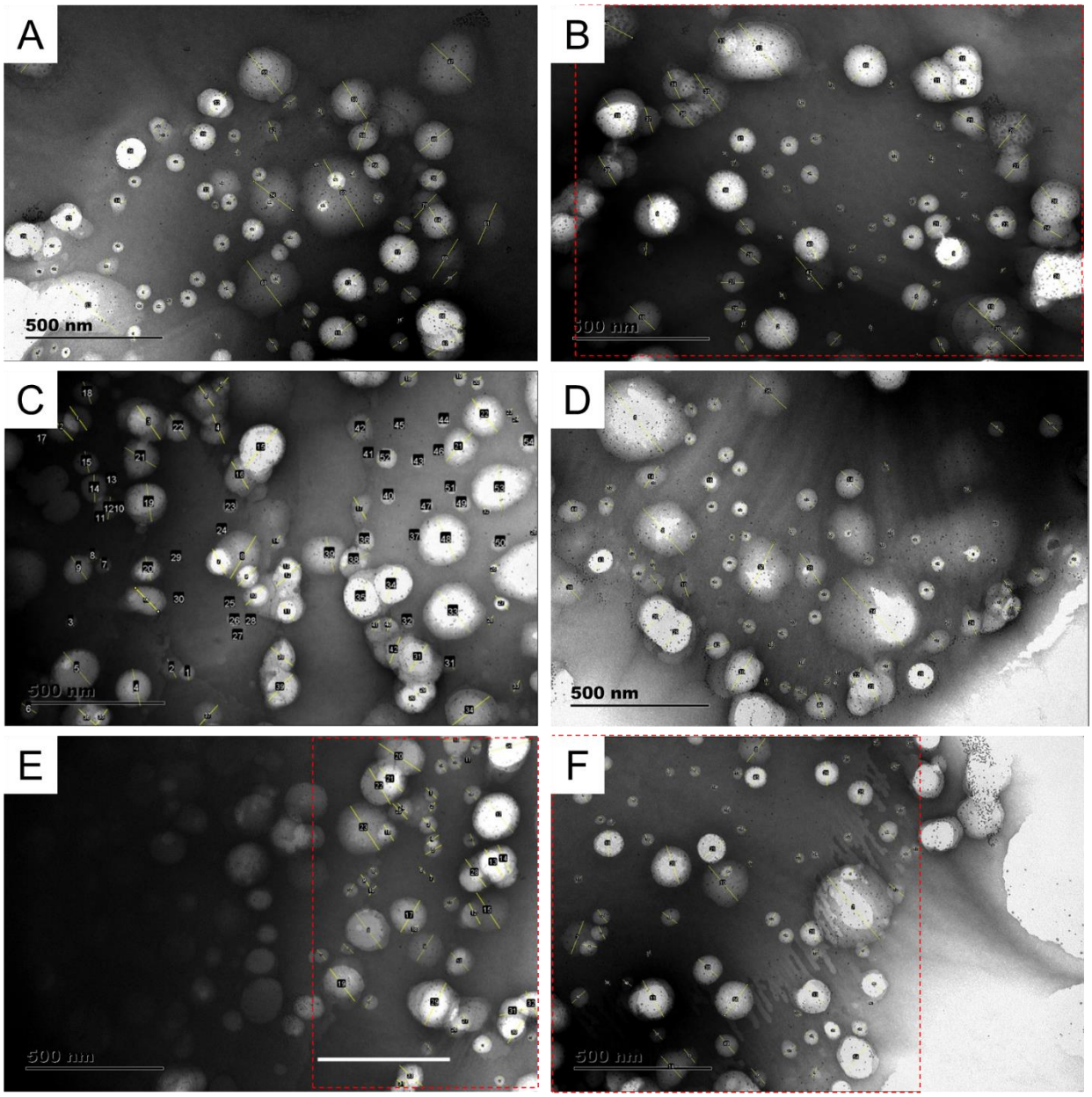

Figure S3.16. A portion of the annotated TEM images of $r_{PCL\text{-}GNP}$ = 100 Q = 200µL/min condition used for TEM statistics.

Table S3.1. Actual Flow Rates of Various Preparations of GNP-PNPs within the Two-Phase Segmented Microfluidic Reactor Described in the Main Text. $r_{PCL\text{-}GNP}$ = 75

Experiments	Nominal flow rate (µL / min)	Q_{gas} (µL / min)	Q_{liq}[a] (µL / min)	Q_{gas} / Q_{liq}	Q_{total} (µL / min)
Figure 3.6 A, 3.10 A, 3.11 B, 3.11 I, S3.8, S3.10	50	22	25	0.88	47
		27		1.08	52
		25		1.00	50
Figure 3.6 A, 3.10 A, 3.11 C, 3.11 I, S3.8, S3.11	100	51	50	1.02	101
		53		1.06	103
		51		1.02	101
Figure 3.6 A, 3.10 A, 3.11 D, 3.11 I, S3.8, S3.12	200	101	100	1.01	201
		105		1.05	205
		110		1.10	210

[a] The liquid flow rate was assumed to be the sum of the three flow rate readings set on the syringe pump before running.

Table S3.2. Actual Flow Rates of Various Preparations of GNP-PNPs within the Two-Phase Segmented Microfluidic Reactor Described in the Main Text. $r_{PCL\text{-}GNP}$ = 100

Experiments	Nominal flow rate (µL / min)	Q_{gas} (µL / min)	Q_{liq}[a] (µL / min)	Q_{gas} / Q_{liq}	Q_{total} (µL / min)
Figure 3.6 B, 3.10 B, 3.11 F, 3.11 I, S3.8, S3.14	50	25	25	1.00	50
		22		0.88	47
		26		1.04	51
Figure 3.6 B, 3.10 B, 3.11 G, 3.11 I, S3.8, S3.15	100	50	50	1.00	100
		52		0.95	102
		55		1.10	105
Figure 3.6 B, 3.10 B, 3.11 H, 3.11 I, S3.8, S3.16	200	105	100	1.05	205
		107		1.07	207
		110		1.10	210
Figure 3.6 C	400	205	200	1.03	405
		209		1.05	409
		215		1.08	415

[a] The liquid flow rate was assumed to be the sum of the three flow rate readings set on the syringe pump before running.

Appendix C

Chapter 4 Supporting Information

S4.1 Supporting Information

Schematic of release procedure for isolating pDNA from PCL-pDNA polyplexes; table describing on-chip steady state solvent compositions for all microfluidic samples; and tables of actual flow rates for all microfluidic samples.

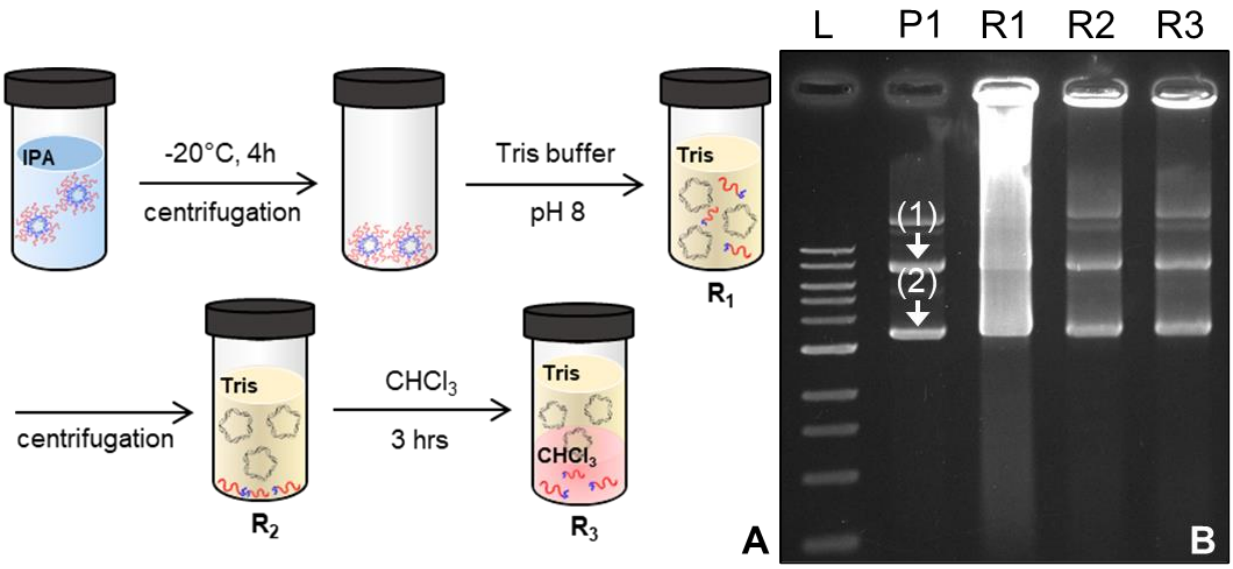

Figure S4.1. Schematic illustrating the release of pDNA from functionalized PCL-pDNA. (A) Diagram of release protocol. (B) Agarose gel electrophoresis image of a 1kb DNA ladder (lane L), untreated pDNA standard (P_1), pDNA after release purification step 1 (lane R_1), pDNA after release purification step 2 (lane R_2), and pDNA after release purification step 3 (lane R_3). Lanes P_1, R_1, R_2, and R_3 show bands associated with open circular (1) and supercoiled (2) forms.

Table S4.1. Experimental Conditions and Assessment of SC-pDNA Retention for All Samples Described in the Main Text.

Sample #	Description	% dioxane (w/w)	% H_2O (w/w)	% CH_3COOH (w/w)	% THF (w/w)	Q_{total} (µL / min)	SC-pDNA retained?
M1	pUC18, mixed solvent (Figures 4.2, 4.6)	90	10	-	-	99.7	✓
M2						208	**X**
M3						406	**X**
M4	pUC18, water (Figure 4.3)	-	100	-	-	94.3	✓
M5						206	✓
M6						395	✓
M7	PCL-pUC18, mixed solvent (Figure 4.6)	86	2	9	3	109	✓
M8						207	✓
M9						408	✓
M10	pDSK519, mixed solvent (Figure 4.7)	90	10	-	-	107	**X**
M11						205	**X**
M12						398	**X**
M13	pRK290, mixed solvent (Figure 4.7)	90	10	-	-	107	**X**
M14						205	**X**
M15						398	**X**

Table S2. Actual Flow Rates for All Samples within the Two-Phase Segmented Microfluidic Reactor Described in the Main Text.

Sample #	Description	Q_{gas} (µL / min)	Q_{gas}/Q_{liq}	Q_{total} (µL / min)
M1	pUC18, mixed solvent (Figures 4.2, 4.6)	49.8	0.997	99.7
M2		108	1.08	208
M3		205	1.02	406
M4	pUC18, water (Figure 4.3)	44.2	0.883	94.3
M5		106	1.06	206
M6		195	0.973	395
M7	PCL-pUC18, mixed solvent (Figure 4.6)	59	1.18	109
M8		107	1.07	207
M9		207	1.03	408
M10	pDSK519, mixed solvent (Figure 4.7)	57	1.14	107
M11		105	1.05	205
M12		198	0.990	398
M13	pRK290, mixed solvent (Figure 4.7)	57	1.14	107
M14		105	1.05	205
M15		198	0.990	398

a) The nominal flow rates were varied as 100, 200, and 400 µL / min (trials 1, 2, and 3 respectively) for all experiments.

b) The liquid flow rate was assumed to be the sum of the three flow rate readings set on the syringe pump before running.

Appendix D

Permissions

Figure 1.5: **Reprinted with permission from {**Zhang, L. & Eisenberg, A. Multiple Morphologies of "Crew-Cut" Aggregates of Polystyrene-b-poly(acrylic acid) Block Copolymers. Science. **268**, 5218 (1995)**}. Copyright {1995} Science**

Figure 1.6: Reprinted with permission from {Zhang, L. & Eisenberg, A. Multiple morphologies and characteristics of "crew-cut" micelle-like aggregates of polystyrene-b-poly (acrylic acid) diblock copolymers in aqueous solutions. J. Am. Chem. Soc. **118**, 3168–3181 (1996)**}. Copyright {1996} American Chemical Society**

Figure 1.7